JAN 25 2007

REPORT DOCUMENTATION PAGE

Form Approved
OMB No. 0704-0188

PLEASE DO NOT RETURN YOUR FORM TO THE ABOVE ADDRESS.

1. REPORT DATE *(DD-MM-YYYY)*	2. REPORT TYPE	3. DATES COVERED *(From - To)*
14-11-2006	THESIS	

4. TITLE AND SUBTITLE
A QUANTITATIVE SPECTROSCOPIC COMPARISON OF DISTANT AND NEARBY TYPE IA SUPERNOVAE

5a. CONTRACT NUMBER

5b. GRANT NUMBER

5c. PROGRAM ELEMENT NUMBER

6. AUTHOR(S)
1ST LT BRONDER TIMOTHY J

5d. PROJECT NUMBER

5e. TASK NUMBER

5f. WORK UNIT NUMBER

7. PERFORMING ORGANIZATION NAME(S) AND ADDRESS(ES)
UNIVERSITY OF OXFORD AT EXETER COLLEGE

8. PERFORMING ORGANIZATION REPORT NUMBER
CI07-0016

9. SPONSORING/MONITORING AGENCY NAME(S) AND ADDRESS(ES)
THE DEPARTMENT OF THE AIR FORCE
AFIT/ENEL, BLDG 16
2275 D STREET
WPAFB OH 45433

10. SPONSOR/MONITOR'S ACRONYM(S)

11. SPONSOR/MONITOR'S REPORT NUMBER(S)

12. DISTRIBUTION/AVAILABILITY STATEMENT
Unlimited distribution
In Accordance With AFI 35-205/AFIT Sup 1

13. SUPPLEMENTARY NOTES

14. ABSTRACT

15. SUBJECT TERMS

16. SECURITY CLASSIFICATION OF:			17. LIMITATION OF ABSTRACT	18. NUMBER OF PAGES	19a. NAME OF RESPONSIBLE PERSON
a. REPORT	b. ABSTRACT	c. THIS PAGE		208	19b. TELEPHONE NUMBER *(Include area code)*

A Quantitative Spectroscopic Comparison of Distant and Nearby Type Ia Supernovae

Tests for Homogeneity and Implications for Cosmology

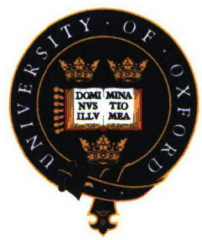

T. Justin Bronder

Exeter College

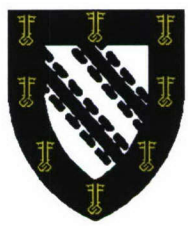

A thesis submitted in candidature for the degree of

Doctor of Philosophy

at the

University of Oxford

Michaelmas Term 2006

Declaration

I declare that no part of this thesis has been accepted, or is currently being submitted, for any degree or diploma or certificate or any other qualification in this University or elsewhere.

This thesis is the result of my own work unless otherwise stated.

This work is self-contained analysis done in parallel with the main cosmological goals of the Supernova Legacy Survey (SNLS). The spectra in the primary data set presented here were observed at the Gemini Telescopes in queue mode by the Gemini staff during Gemini North programs GN-2003B-Q-9, GN-2004A-Q-19, GN-2004B-Q-15, GN-2005A-Q-11, GN-2005B-Q-7, GN-2006A-Q-7 and Gemini South programs GS-2003B-Q-8, GS-2004A-Q-11, GS-2004B-Q-31, GS-2005A-Q-11, and GS-2005B-Q-6. The telescope settings for each observation were finalised by the author and other SNLS members using the Gemini PhaseII software. All of these spectra were reduced by the author with routines written with the IRAF software. IRAF is distributed by the National Optical Astronomy Observatories which are operated by the Association of Universities for Research in Astronomy, Inc., under cooperative aggremeent with the National Science Foundation. The Gemini-specific IRAF package[1] was also used.

The photometric data for these objects was provided by other collaboration members (primarily Mark Sullivan, Kathy Perrett, and Alex Conley at the University of Toronto) which was necessary as direct access to the Canada-France-Hawaii Telescope pixel data was not available.

The secondary set of SNLS spectra were observed with the European Southern Observatory (ESO) Very Large Telescope (VLT) by the staff at this telescope. The observation setup and reduction of this data was completed by collaboration members at the Laboratoire d'Astrophysique de Marseille.

All of the other spectroscopic data used in this thesis was assembled from the literature - the appropriate citations for these spectra are made in the text.

The measurements and calculations discussed in Chapter 2, Chapter 3 and Chapter 4 were completed with programs written by the author in IDL. The routines in these programs are from the IDL version 6.0 library and the IDL Astronomy User's Library[2]. The figures displayed in this thesis were also generated with IDL.

The code used to fit cosmological models (i.e. Ω_M and Ω_Λ) to the supernovae from the primary data set in § 4.5 was written by Ariel Goobar (Stockholm University).

This thesis was prepared using the LaTeX 2_ϵ typesetting package; the bibliography was created using BibTeX.

The views expressed in this thesis are those of the author and do not reflect the official policy or position of the United States Air Force, the Department of Defense, or the US Government.

[1] see `http://www.gemini.edu/sciops/data/dataSoftware.html`

[2] `http://idlastro.gsfc.nasa.gov/`

THE VIEWS EXPRESSED IN THIS ARTICLE ARE THOSE OF THE AUTHOR AND DO NOT REFLECT THE OFFICIAL POLICY OR POSITION OF THE UNITED STATES AIR FORCE, DEPARTMENT OF DEFENSE, OR THE U.S. GOVERNMENT.

Acknowledgements

A sincere thanks is owed to Alberta Holaday and her son, Bart, whose generosity made my time at Exeter College and Oxford possible.

I am also deeply indebted to my supervisor, Isobel Hook, whose patience and guidance were invaluable; the counsel she consistently provided made this thesis a reality.

This research would not have been possible without the dedicated queue observing completed by the staff and scientists at the Gemini Telescopes, especially Inger Jørgensen, Kathy Roth, Percy Gomez, and Marcel Bergmann. The contributions of the CFHT observations team have also been invaluable to every aspect of the work carried out by the Supernova Legacy Survey.

The stimulating discussions and contributions by the SNLS collaborators - Mark Sullivan, Andy Howell, Alex Conley, Kathy Perrett, Stéphane Basa, Reynald Pain, Don Neill, Julien Guy, and Pierre Astier (just to name a few!) - have been essential to this research and the support from the SNLS team meant a great deal throughout my time as a DPhil student.

This research also benefitted from the assistance offered by The European Union Type Ia SNe RTN; particularly from the 'young researchers' from this organisation whose aid and opinions were always helpful.

Closer to home, the talented DPhil students and distinguished post-docs, researchers, and professors at Oxford University ensured that this thesis was completed in a challenging and enlightening academic environment. The discussions over Stellar Coffee meetings, astrophysics colloquia, graduate lectures, cups of tea and pints of beer were a wonderful part of this entire experience. I would particularly like to thank Paul Taylor, David Brown, Francisco Forster, Ryan Houghton, Tim Goodsall, and Caroline van Breukelen who all graciously volunteered their time to help proofread this work.

Most of all, my most heartfelt gratitude goes out to my wife, who has made all of this worthwhile.

Now, there is a law written in the darkest of the Books of Life, and it is this: If you look at a thing nine hundred and ninety-nine times, you are perfectly safe; if you look at it the thousandth time, you are in frightful danger of seeing it for the first time.

G.K. Chesterton, from *The Napoleon of Notting Hill*

Support and Facilities Used

This work was funded by the Alberta Bart Holaday Scholarship to Exeter College. An extension to this program, in both time and funding, was granted with generous assistance from Dr. Lavin and the US Air Force Academy Graduate Studies Programs Office, permission from the appropriate staff from the Air Force Institute of Technology and the Air Force Personnel Center, and from Dr. Bart Holaday and the Exeter College Development Office.

This research is based on spectroscopic observations obtained at the Gemini Observatory, which is operated by the Association of Universities for Research in Astronomy, Inc., under a cooperative agreement with the National Science Foundation on behalf of the Gemini partnership: the National Science Foundation (US), the Particle Physics and Astronomy Research Council (UK), the National Research Council (Canada), CONICYT (Chile), the Australian Research Council (Australia), CNPq (Brazil), and CONICET (Argentina).

Academic travel to Gemini North in Hawaii in April 2004 was supported with a grant from the Dean of the Faculty and the Graduate Studies Programs Office at the US Air Force Academy. The Oxford Astrophysics department supported travel to SNLS meetings at the LPNHE in Paris, France, in February 2004 and May 2006, and attendance at the Royal Astronomical Society National Astronomy Meetings in 2005 and 2006. The European Union Research Training Network for Type Ia supernovae also supported travel to many meetings, including the International conference '1604-2004 Supernovae as Cosmological Lighthouses' in Padova, Italy, the EU RTN Young Researchers Meeting in Stockholm, Sweden, in June 2005, and the International Astrophysical Conference in Cefalu, Italy, in June 2006.

A Quantitative Spectroscopic Comparison of Distant and Nearby Type Ia Supernovae:
Tests for Homogeneity and Implications for Cosmology

T. Justin Bronder, Exeter College

Submitted for the Degree of Doctor of Philosophy, Michaelmas Term 2006

Abstract

This thesis presents quantitative analysis of spectra from 130 high-redshift ($z_{\mathrm{median}} = 0.63$) Type Ia supernovae. This extensive set of distant SNe is comprised of a primary set of objects observed at the Gemini telescopes for the ongoing Supernova Legacy Survey (SNLS), a secondary set observed at the Very Large Telescope for the SNLS, and a tertiary set of high-z spectra from the literature. All work on the reduction and identification of the spectra in the primary data set (including spectra from a total of 124 SNe candidates observed between August 2003 and May 2006) was completed by the author. Rest-frame equivalent width and CaII H&K ejection velocity measurements are made on these distant SNe Ia spectra, with methods tailored to the specific considerations of high-z data.

The results from this analysis were compared to corresponding measurements from a set of 167 SNe Ia spectra from 24 nearby objects from the literature to investigate the homogeneity of SNe Ia across a wide range of redshifts ($0.001 \lesssim z \lesssim 1.0$). This comparison provides a quantitative indicator for possible evolutionary effects in the population of high-z SNe surveyed for cosmology. A statistical comparison of the spectroscopic features of the high-z SNe and the trends exhibited in the nearby objects finds a less than 2σ difference for all of the measurements considered here. These results also indicate that there are no systematic changes due to redshift in this SNe sample. The dependence of SNe Ia spectroscopic properties on host galaxy type is also investigated and found to be similar for nearby and distant objects. These results are discussed briefly in the context of the physical understanding and cosmological implications of SNe Ia.

A new correlation between SNe Ia peak magnitudes and the strength of a specific SiII absorption feature (near 4000 Å, measured within ± 7 days of maximum light) is also presented. The application of this correlation to high-z SNe reduces the dispersion in estimated distance modulus values by nearly 30%. This improvement is of the order of the photometric-based corrections that are used currently to standardise SNe Ia magnitudes for cosmology.

A Quantitative Spectroscopic Comparison of Distant and Nearby Type Ia Supernovae:
Tests for Homogeneity and Implications for Cosmology

T. Justin Bronder, Exeter College

Submitted for the Degree of Doctor of Philosophy, Michaelmas Term 2006

Abstract

This thesis presents quantitative analysis of spectra from 130 high-redshift ($z_{\rm median} = 0.63$) Type Ia supernovae. This extensive set of distant SNe is comprised of a primary set of objects observed at the Gemini telescopes for the ongoing Supernova Legacy Survey (SNLS), a secondary set observed at the Very Large Telescope for the SNLS, and a tertiary set of high-z spectra from the literature. All work on the reduction and identification of the spectra in the primary data set (including spectra from a total of 124 SNe candidates observed between August 2003 and May 2006) was completed by the author. Rest-frame equivalent width and CaII H&K ejection velocity measurements are made on these distant SNe Ia spectra, with methods tailored to the specific considerations of high-z data.

The results from this analysis were compared to corresponding measurements from a set of 167 SNe Ia spectra from 24 nearby objects from the literature to investigate the homogeneity of SNe Ia across a wide range of redshifts ($0.001 \lesssim z \lesssim 1.0$). This comparison provides a quantitative indicator for possible evolutionary effects in the population of high-z SNe surveyed for cosmology. A statistical comparison of the spectroscopic features of the high-z SNe and the trends exhibited in the nearby objects finds a less than 2σ difference for all of the measurements considered here. These results also indicate that there are no systematic changes due to redshift in this SNe sample. The dependence of SNe Ia spectroscopic properties on host galaxy type is also investigated and found to be similar for nearby and distant objects. These results are discussed briefly in the context of the physical understanding and cosmological implications of SNe Ia.

A new correlation between SNe Ia peak magnitudes and the strength of a specific SiII absorption feature (near 4000 Å, measured within ± 7 days of maximum light) is also presented. The application of this correlation to high-z SNe reduces the dispersion in estimated distance modulus values by nearly 30%. This improvement is of the order of the photometric-based corrections that are used currently to standardise SNe Ia magnitudes for cosmology.

Contents

List of Figures

List of Tables

Chapter 1

Introduction

1.1 Type Ia Supernovae — Definition and Classification

The cataclysmic events that are now known as supernovae (SNe) have been at the center of many revolutions in astronomical theory. The well-recorded supernovae of 1006 and 1054 animated astronomical interest worldwide and were regarded by many as terrible omens heralding royal deaths and famine. The similarly spectacular events of 1572 and 1604 captured the interest of such famous astronomers as Tycho Brahe — who coined the term still in use today by referring to the 1572 event as a 'stella nova' — and Johannes Kepler. The 1604 event was also seen as a sign of sorts by a certain middle-aged professor in Padua, Italy. For this astronomer, none other than Galileo Galilei, the nova was not an astrological harbinger, but rather it was an empirical clue that would help him overthrow the Aristotelian cosmology that had captivated the western scientific world for nearly two millennia (North, 1994). The light from this particular supernova can thus be considered as one of the sparks that ignited the modern scientific era.

In present times, observations of supernovae continue to improve our understanding of the Universe. In the first half of the 20^{th} century, Edwin Hubble established that our Universe is expanding; coupled with solutions to Einstein's field equations of general relativity and the later discovery of the Cosmic Microwave Background (CMB) radiation, this discovery would establish the Big Bang theory of the creation and evolution of the Universe. At one point, this theory seemed to fail to predict the amount of heavy elements in the Universe. This was rectified by the prediction and observation of the creation of these elements in the explosive stellar deaths

that cause supernovae [e.g. Burbidge, Burbidge, Fowler & Hoyle (1957)]. Recently, surveys of distant 'Type Ia' supernovae (SNe Ia) have indicated that the rate of the expansion of the Universe is increasing due to the dominating presence of a repulsive 'dark energy' such as Einstein's cosmological constant (Λ).

When the characteristics of SNe were first studied spectroscopically, these objects were initially separated into two groups. These groups were based on observation and not on any physical mechanism. Supernovae that did not display any features attributed to hydrogen (Hα or Hβ) were designated as 'Type I', while those that did display H lines were classified as 'Type II' (Minkowski, 1941). As technology and the corresponding signal-to-noise ratios (S/N) of observations improved, the Type I designation was sub-divided to accommodate different classes of these hydrogen-deficient objects. Supernovae displaying intermediate mass elements (IME) — specifically silicon (SiIIλ6347, λ6371) — were designated as 'Type Ia' while the other Type I objects were classified as 'Type Ib'/'Type Ic' according to the presence/absence of helium (Harkness & Wheeler, 1990).

Our understanding of these objects has improved since these initial efforts at categorising supernovae. It is now known that Type II, Type Ib, and Type Ic SNe are caused by the core-collapse and explosion of massive stars. Type Ia SNe, on the other hand, are the result of a very different physical system — the thermonuclear runaway under degenerate conditions of carbon-oxygen (C+O) white dwarfs (WD) (Nomoto, Thielemann, & Yokoi, 1984). Despite the lack of a physical basis for SN nomenclature, this classification scheme has remained the standard, evolving along with advancements in observational capabilities and with larger data sets.

This adaptive trend continues through the present day, as specific sub-classes of SNe Ia have been revealed and continue to be refined. Type Ia supernovae do appear to be the most homogenous class of SNe [see Filippenko (1997) for a review], but the (observationally) identified sub-classes within this population can be broadly defined as 'overluminous' and 'underluminous' SNe Ia in addition to the 'normal' events. The former are brighter ($\sim$ 0.5 B' magnitudes) than the typical SNe and exhibit less absorption from IME at pre-maximum epochs. The latter are substantially dimmer ($\sim 2.0 - 3.0$ B' magnitudes) than all other SNe Ia and display excess absorption in their spectra than their 'normal' counterparts. The archetypes

for these SNe Ia sub-classes are generally considered to be SN 1991T (Filippenko *et al.*, 1992a) and SN 1991bg (Filippenko *et al.*, 1992b) for the over- and underluminous SNe, respectively. These SNe Ia sub-types will be discussed in more detail in the next section and throughout this thesis.

1.2 Type Ia Supernovae — Spectra and Light Curves

The physical causes for the observed characteristics of Type Ia SNe are fairly well understood [see reviews by Branch & Tammann (1992); Filippenko (1997); Hillebrandt & Niemeyer (2000) and references therein]. The most accepted explanation is that a C+O WD gains matter (through accretion or via a merger with another WD) and exceeds the Chandrasekhar mass[1] ($M_{\rm CH} \sim 1.39 M_{\odot}$); this increases pressure and temperature to ignite carbon and oxygen near its core and result in a thermonuclear runaway. This burning propagates through the WD and releases enough energy to disrupt the star (total kinetic energy is $\approx 10^{51}$ ergs) in a brilliant display which radiates more than 10^{10} times more brightly than our sun.

Before the star is destroyed, varying stages of nuclear statistical equilibrium (NSE) are reached at different radii as the burning front engulfs the star from the inside out; the energy and heat generated by this burning causes the star to expand as this happens. In regions where the nuclear burning time-scales are shorter than the convective time-scale for expansion, nucleosynthesis can continue to the formation of iron-peak elements such as ^{56}Ni. In the most dense ($\rho \gtrsim 3.0 \cdot 10^{8} \mathrm{g/cm^3}$) of these regions, electron captures drive these processes to the formation of stable ^{58}Ni and ^{54}Fe. Large amounts of material (particularly in the layers outside of the core C+O region) do not reach this end point, and the burning instead results in the formation of large amounts of IME such as calcium, silicon, and magnesium [see Arnett (1996) for detailed specifics]. The amount of ^{56}Ni produced is particularly important, as the radioactive decay of this element subsuquently powers the lightcurve and photometric evolution of each SN Ia. Note that most of the energy generated in this explosive nucleosynthesis is gained by burning up to the IME; thus the total amount of burning, regardless of the final product, is what determines just how much energy is ultimately released to unbind the progenitor star.

[1] There is still some debate about this mass limit. Discussions by Livne & Arnett (1995) (for example) propose sub-Chandrasekhar progenitors where thermonuclear runaway is induced by He detonation on the outer layers of the star. The mass at ignition could also be well over $M_{\rm ch}$ due to rotation effects [e.g., Yoon & Langer (2004)] or from WD mergers [e.g., Fisher *et al.* (1999)].

The ejecta from this explosion expand homologously so $v_{\rm ej} \sim \frac{r}{t}$ (where $v_{\rm ej}$ is the velocity of the ejecta, r is the radius away from the center of the SN, and t is the time since explosion). As the ejecta expands, the corresponding changes in opacity (i.e., toward being optically thin) allow observers, over time, to observe elements that are moving at lower velocities and which were synthesised deeper in the progenitor during thermonuclear runaway. A 'cartoon' summary in Figure 1.1 illustrates how the observed spectrum is formed. Spectroscopic observations essentially sample photons that have interacted with the line formation regions from different ions in the expanding SN ejecta. In most approximations of SNe Ia spectra, these are small regions defined in areas of the atmosphere where the photons have been Doppler shifted to be in resonance with the line in question (Sobolev, 1960). These regions are wavelength-dependent and thus occur at different respective optical depths (and different depths in real space due to the homologous expasion) that are constantly moving down through the ejecta as it expands. Theoretical models of the energetics and nucleosynthesis of these objects can be constrained with comparisons to the spectra of SNe Ia because these observations illuminate the composition of the SNe Ia (from the outside-in) over time. This combination of observation and theory has substantiated the general outline of the progenitor (PG) scenario and explosion mechanism summarised here. Many specifics (i.e., the WD mass at ignition, the location of the ignition point(s), the velocity of the burning front, rotation and magnetic field effects) are still a matter of much contention [e.g., Hillebrandt & Niemeyer (2000) and references therein] and will continue to be refined as observational constraints and computing capabilities continue to improve [see e.g., Roepke *et al.* (2006); Baron *et al.* (2006); Branch *et al.* (2006) for recent developments in different aspects of SNe Ia modelling].

Even with these existing uncertainties, the observed characteristics of a majority of these SNe Ia spectra are remarkably homogenous, as Fig. 1.2 illustrates. These spectra are representative of most normal SNe Ia near peak luminosity ($L_{\rm peak}$); they show large absorption features from different IME, including CaII, SiII, SII, and MgII. The Doppler-broadened, P Cygni profiles of the individual lines blend together to create these large features. The objects shown in Fig. 1.2 — SN 1981B (Branch *et al.*, 1983), SN 1989B (Barbon *et al.*, 1990; Wells *et al.*, 1994), SN 1992A (Kirshner *et al.*, 1993) and SN 1994D (Patat *et al.*, 1996) — exhibit the spectroscopic features that are most consistently observed in SNe Ia. Spectroscopically similar

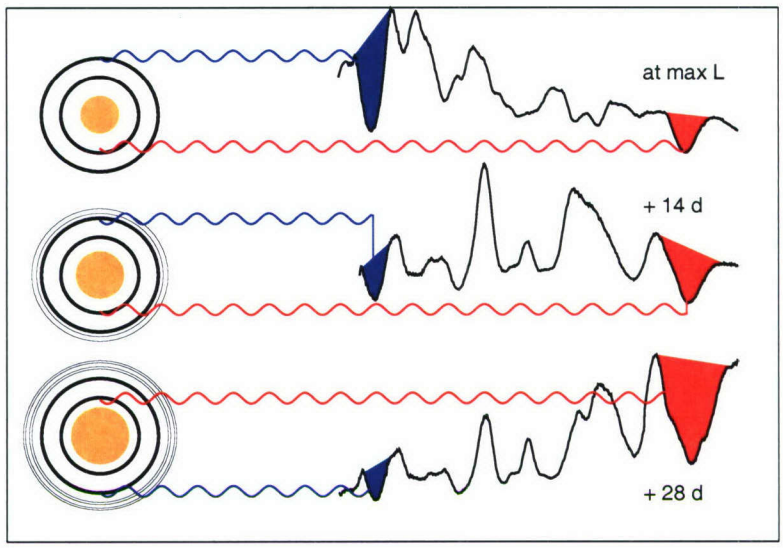

Figure 1.1: A cartoon illustration of how the observed spectroscopic features in SNe Ia spectra originate. The spectra on the right-hand side of this figure are from observations of SN 1981B (from 3500 - 6500 Å) at (from top to bottom) $t = 0, t = 14$, and $t = 28$ days past maximum luminosity. The solid circles on the left-hand side of this illustration represent where the effective photosphere is located at the wavelength of the observed photons in the SNe explosion at these epochs. Over time, the density (and subsequent opacity) changes move this layer to encompass deeper layers of the ejecta so that different products of the thermonuclear reactions that destroyed the progenitor WD are visible.

objects are often referred to as 'Branch normal' or 'core normal' SNe[2] (Branch *et al.*, 2006).

The overluminous Type Ia sub-type is defined by possessing spectra similar to SN 1991T (see Figure 1.3); this object displayed very weak absorptions from IME at epochs before L_{peak} (Filippenko *et al.*, 1992a; Phillips *et al.*, 1992), but had strong contributions from FeIII. At later epochs the spectrum looked much more like a typical core normal SNe. A handful of these objects have been observed to date, with some, such as SN 1999aa[3] (Garavini *et al.*, 2004), displaying a shift from a 1991T-like to a core normal spectrum even earlier. The fact that the spectra of these objects evolve to look more like the normal SNe seems to imply that these objects form part of a continuum of SNe Ia (Branch *et al.*, 2006) rather than an entirely different class [see discussion in Hatano *et al.* (2002)], although the presence of ^{56}Ni in the early time spectra (Mazzali, Danziger, & Turatto, 1995) could mean that a completely different explosion mechanism is at work in these objects. Regardless of which description is more valid, the

[2]Throughout this thesis, the term 'core normal' will be used to refer to this class of the most homogenous SNe Ia.

[3]These particular SNe Ia sub-types are often referred to in the literature as '1991T/1999aa'-like objects. For simplicity, the only the title '1991T'-like will be used in this thesis to refer to these particular SNe.

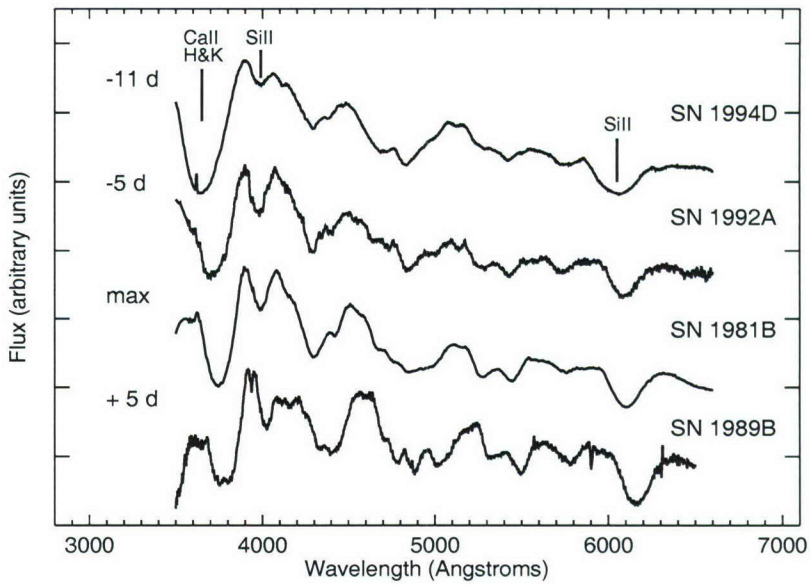

Figure 1.2: A comparison of spectra from representative core normal Type Ia SNe near maximum light. The two labelled SiII absorptions are the primary features that distinguish these objects from core-collapse Type Ib or Type Ic SNe. The source publications for these spectra are listed in Table 2.14.

observed differences in their spectra appear to be an indication of higher temperatures and more energetic thermonculear explosions (Mazzali, Danziger, & Turatto, 1995; Fisher *et al.*, 1999).

The underluminous, or 1991bg-like SNe show increased absorption at optical wavelengths (see Figure 1.3) and are much redder than core normal SNe (Filippenko *et al.*, 1992b; Turatto *et al.*, 1996). The spectroscopic differences in these objects are attributed to absorption from (primarily) TiII. The expansion velocities of the ejecta are also lower than typical Type Ia SNe (Benetti *et al.*, 2005). This evidence indicates that SNe of this sub-class are less energetic and produce much less ^{56}Ni than the rest of the SNe Ia population (Mazzali *et al.*, 1997).

From a photometric perspective, the primary quantity of importance is the amount of ^{56}Ni synthesised during thermonuclear runaway. As described by 'Arnett's Rule' (Arnett, Branch, & Wheeler, 1985), the luminosity of a Type Ia SN is governed by the instantaneous rate of energy deposition from radioactive decays in the expanding ejecta. This is due to the effects of the decay of ^{56}Ni to ^{56}Co and, subequently, to ^{56}Fe [isotopes with a half-life of 6.1 and 77.1 days (Arnett, 1996), respectively], which deposits gamma rays and positrons into the surrounding ejecta. The energy of these photons is then reduced during interactions with electrons, which

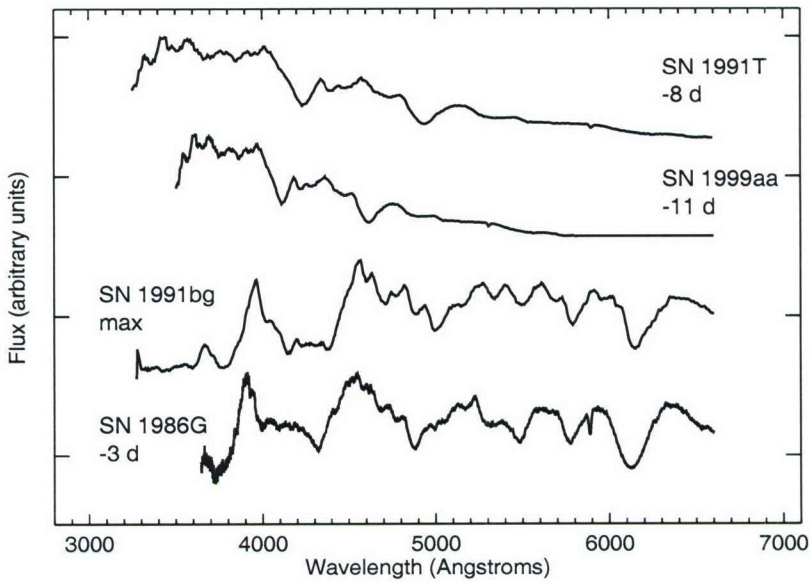

Figure 1.3: Representative spectra of the 'overluminous' and 'underluminous' Type Ia SNe sub-types. The two spectra at the top of this plot (SNe 1991T & 1999aa) are from objects that are slightly brighter than most normal Type Ia SNe. These spectra lack the dominant absorptions from IME that are usually found in pre-maximum SNe Ia spectra (see Fig. 1.2). At later epochs these '1991T-like' objects display spectra that are much more similar to core normal SNe Ia. The two '1991bg-like' spectra at the bottom of this figure are from SNe that are substantially less luminous than normal SNe and have larger absorption features due to contributions from elements such as TiII (see Table 2.14 for the sources of these spectra).

take place primarily (in the case of γ-rays) via Klein-Nishina scattering (Arnett, 1996). After these interactions have decreased the γ-ray energies to optical wavelengths, these photons then escape the photosphere to be observed as the opacity dictates. Positrons, produced mainly by the decay of ^{56}Co in the second step of this process, scatter and then annihilate to give off additional γ-rays that deposit their energy in the ejecta.

Within the context of this description of SNe Ia physics, thermonuclear explosions which produce more ^{56}Ni should result in brighter SNe Ia. These brighter SNe have also been observed to have broader, or more slowly decreasing, lightcurves [e.g., Fig. 1.4, reprinted from Hamuy *et al.* (1996c)]. At first this seems counterintuitive, as a more energetic explosion should cause the ejecta to expand faster, to dissipate the deposited energy from ^{56}Ni more quickly, and thus to exhibit a lightcurve declining more rapidly than a less energetic event. This apparent contradiction is an opacity effect. The iron-peak elements synthesised in the explosion result in excess line blanketing which allows the ejecta to stay optically thick for longer (Hoeflich *et al.*,

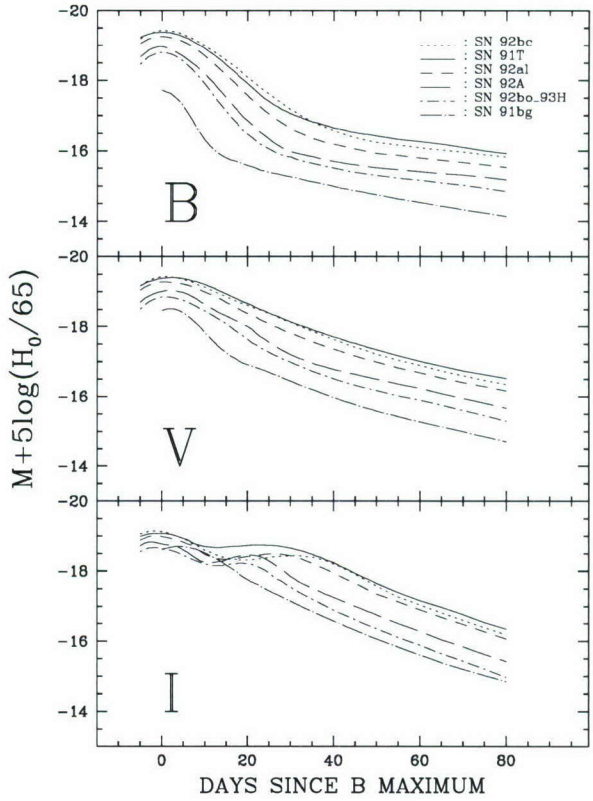

Figure 1.4: Type Ia SNe lightcurves from a sample of nearby objects. These lightcurves clearly show an intrinsic scatter in the peak magnitudes of SNe Ia. The trend for brighter SNe (such as SN 1991T) to have broader lightcurves is also clear in the B' and V' bands. This trend has been well-studied and is considered to be primarily an effect from the different amount of ^{56}Ni in each SN. The brighter-broader relation is also the basis for the methods that 'standardise' SNe Ia luminosties for cosmological distance estimates [Figure re-printed from Hamuy *et al.* (1996c)].

1996; Mazzali *et al.*, 2001). Thus the amount ^{56}Ni — as well as stable Fe and Ni — determines the width of the lightcurve. This brighter-broader relation has been firmly established with numerous SNe Ia lightcurves, as Figure 1.4 illustrates, and has important implications for the use of these luminous objects as 'standardisable' distance indicators for cosmology. This is discussed further in § 1.3.2.1 and § 1.3.3.

1.3 Type Ia Supernovae — Surveys & Cosmology

1.3.1 Cosmology — A Brief Review

The science of modern cosmology can essentially be defined as the application of the theory of general relativity to describe the large scale structure and evolution of the Universe. The starting point for this study is the cosmological principle, which states that (on sufficiently large scales) the Universe is both homogeneous and isotropic. That is, there are neither preferred locations nor preferred directions in space. The most general space-time metric that describes a path length in a Universe obeying this principle is the Robertson-Walker metric:

$$ds^2 = dt^2 - a(t)^2\left[\frac{dr^2}{1-\kappa r^2} + r^2(d\theta^2 + \sin^2\theta d\phi^2)\right]. \tag{1.1}$$

The variables r, θ, and ϕ are comoving (spherical polar) coordinates, t is the proper time, $a(t)$ is the scale factor that describes the relative expansion of the Universe at time t and has units of length. κ is the curvature parameter that describes whether the geometry of the Universe is 'closed' ($\kappa = +1$), 'open' ($\kappa = -1$), or 'flat' ($\kappa = 0$). Incorporating this metric into Einstein's field equations - with the additional assumption that the content of the Universe behaves as a perfect fluid - results in the Friedmann equations which describe the dynamics of the Universe:

$$\frac{\ddot{a}}{a} = -\frac{4\pi G}{3}(\rho + 3p) + \frac{\Lambda}{3}, \tag{1.2}$$

$$\left(\frac{\dot{a}}{a}\right)^2 = \frac{8\pi G\rho}{3} - \frac{\kappa}{a^2} + \frac{\Lambda}{3}. \tag{1.3}$$

Here, ρ and p represent the density and pressure of this 'perfect fluid', G is the gravitational constant, and Λ is the 'cosmological constant'. This last parameter was introduced by Einstein specifically to address the apparent contradiction between the dynamical nature of these solutions and static Universe that was preferred at that time. This parameter acts to counteract gravity and is also referred to as dark energy. The observational evidence that was later provided by Edwin Hubble (using redshift data from Vesto Slipher) and Penzias and Wilson effectively overturned this assumption of a static Universe, leading Einstein to comment to George Gamow that Λ was his 'biggest blunder' (Gamow, 1970).

The expansion rate of the dynamic Universe is defined by the 'Hubble parameter', H, which is just the left-hand side of Equation 1.3,

$$H^2 = \left(\frac{\dot{a}}{a}\right)^2. \tag{1.4}$$

Another useful parameter is the 'critical density' (ρ_{crit}), which is defined as the density required for the geometry of a matter-only universe to be flat.

$$\rho_{\rm crit} = \frac{3H^2}{8\pi G}. \tag{1.5}$$

The curvature of the Universe will thus be closed, open, or flat if ρ_{crit} is greater than, equal to, or less than 1 (respectively). The matter and dark energy contributions to the dynamics of the Universe from Eq. 1.3 can thus be described as fractions of this critical density, Ω, so that

$$\Omega_i = \frac{\rho}{\rho_{\rm crit}} = \frac{8\pi G}{3H^2}\rho_i, \tag{1.6}$$

for each component, i, of the total density. This parameterisation of these components enables a direct connection between the total energy density and the spatial geometry to be simply expressed as

$$\Omega_\kappa = 1 - \Omega_{\rm tot} = 1 - (\Omega_M + \Omega_\Lambda) \tag{1.7}$$

for a Universe with matter and dark energy contributions only.

Within the framework of this Friedmann-Robertson-Walker (FRW) description of the Universe, the values of the energy density and curvature parameter govern the geometry and expansion of the Universe. These parameters can also be estimated observationally. For this analysis, distance estimates to observed astronomical objects are needed. These distances are not measured directly; rather, some fraction of emitted flux from these sources is observed here on Earth. This flux (F) is related to the luminosity (L) and distance (d) to a source (ignoring the expansion of space momentarily) as

$$F = \frac{L}{4\pi d^2}. \tag{1.8}$$

If this relation is applied to a comoving grid (which more accurately describes the expanding distances in the Universe), then Eq. 1.8 changes to accommodate the 'luminosity distance', d_L, to these sources:

$$F = \frac{L}{4\pi d_L^2}. \tag{1.9}$$

This d_L is dependent on the expansion history of the Universe. The Robertson-Walker metric and Friedmann equations can describe this dependence, as a function of redshift, H, κ, Ω_M, and Ω_Λ (working backward from the present day, $z = 0$):

$$d_L = \frac{(1+z)c}{H_0|\kappa|^{1/2}} S\langle |\kappa|^{1/2} \int_0^z [\kappa(1+z')^2 + \Omega_M(1+z')^3 + \Omega_\Lambda]^{-1/2} dz' \rangle \tag{1.10}$$

where the '0' subscript refers to the parameter at the present time, t_0. The value of the function $S\langle\chi\rangle$ takes various forms based on the curvature κ:

$$S\langle\chi\rangle = \begin{cases} \sin\langle\chi\rangle & \kappa < 0 \\ \chi & \kappa = 0 \\ \sinh\langle\chi\rangle & \kappa > 0 \end{cases}$$

In observing distant luminous sources, astronomers do not usually work with observed flux or intrinsic luminosity, so d_L cannot be directly measured as well. Rather, the apparent magnitude, m, and the absolute magnitude, M (the apparent magnitude an object would have if placed at a standard distance of 10 parsecs), are the parameters that are utilised in astronomical observations. The value of the difference between these parameters, $m - M$, is referred to as the 'distance modulus', μ. At cosmological distances, the correlation between the distance modulus, magnitudes, and luminosity distance is

$$\mu(z) = m(z) - M = 5 \log d_L(z; \Omega_M, \Omega_\Lambda, H_0) + 25 \tag{1.11}$$

Here, the complete equation for $d_L(z; \Omega_M, \Omega_\Lambda, H_0)$ was defined in Eq. 1.10. In light of these relations, the utility of bright objects with absolute magnitudes that are known intrinsically — so-called 'standard candles' — to determining cosmological parameters is apparent. Observations of these standard candles (combined with estimations of their redshifts) can chart

μ values at increasing z in a plot called a 'Hubble diagram'; the relation in Eq. 1.11 is then exploited to estimate the best fit Ω_M and Ω_Λ values to this z-μ correlation and constrain these important cosmological parameters.

1.3.2 Type Ia Supernovae Surveys — A Brief Review

1.3.2.1 'Standardisable Candles'

Unfortunately, centuries of astronomical observations have yet to yield a perfect 'standard candle' that is observable to cosmological distances. Type Ia supernovae are bright enough to be observed at large redshifts, with peak M values (in B') near -19.3, but the intrinsic scatter in their properties (which has been noted previously in this introduction) means that they are not quite the standard class of objects required for this purpose. However, as Figure 1.4 illustrates, there is an apparent relation between the width of their lightcurves and their peak magnitudes. Such a relation was initially proposed by Pskovskii (1977), who posited that the slope of the lightcurve just after maximum light corresponded to the peak luminosity for SNe Ia. This correlation was refined by Phillips (1993), who noted that the peak magnitudes of SNe Ia have a linear relation to the total decrease in magnitudes 15 days after maximum light, a quantity dubbed '$\Delta_{m_{15}}$'. This relation empirically summarises the observation that intrinsically brighter SNe Ia have 'wider' or slower-declining lightcurves. The application of this $\Delta_{m_{15}}$ relation to different SNe Ia lightcurves 'normalises' the maximum luminosities of these events and significantly reduces the observed dispersion in their peak magnitudes. This adjustment essentially accounts for the difference in ^{56}Ni synthesised between SNe Ia and thus treats these objects as 'standardisable candles', where this primary parameter accounts for a majority of the dispersion in their peak magnitudes. Currently, a range of parameters, which were all derived empirically on large sets of nearby Type Ia SNe [such as the Calán/Tololo Survey (Hamuy *et al.*, 1996b)] have been established that can be used to normalise the lightcurve shape and luminosity of a given SN Ia.

The methods that are used most frequently include an updated version of the $\Delta_{m_{15}}$ measurement (Phillips *et al.*, 1999), the timescale-stretch, s, parameterisation defined by Goldhaber *et al.* (2001), and the Multi-Lightcurve Shape (MLCS) method discussed by Riess, Press, & Kirshner (1996). The $\Delta_{m_{15}}$ lightcurve measurement is linearly related to the peak magni-

tude of SNe Ia (Phillips *et al.*, 1999), while methods using s stretch an empirically derived standard lightcurve along the time axis to map onto an observed lightcurve. The size of this stretch is proportional to the peak magnitude of the event. The MLCS techniques combine the brighter SNe-slower declining lightcurve relation with the similar colour relations (i.e., intrinsically brighter SNe are more blue) to determine the luminosity and line-of-sight extinction for these events.

These methods all utilise a parallel approach — the empirically-derived $\Delta_{m_{15}}$, s, or MLCS relation is employed as a means to adjust (i.e., standardise) the measured SNe Ia magnitudes and thus reduce the scatter ($\sigma_{M_{\rm peak}}$) in the peak magnitudes of these objects. This standardisation reduces the measured $\sigma_{M_{\rm peak}}$ by a factor of ~ 2 [from a value of ~ 0.25 to ~ 0.12, e.g., (Phillips *et al.*, 1999)]. This increases the precision in the luminosity-distance (d_L) estimates of SNe Ia enough that surveys out to high redshifts (high-z; i.e., $z \gtrsim 0.5$) can discriminate between different cosmological models more effectively. However, the discovery and follow up of the large numbers of distant SNe that are required for this analysis does not provide an easy goal to accomplish.

1.3.2.2 High-z Surveys — Setup and Results

Observing high redshift transient objects within the bounds of telescope schedules set months in advance proved to be a major hurdle in capturing appreciable numbers of Type Ia SNe[4] at high-z when such surveys began in the 1990's. A more systematic method of working within set telescope schedules was demonstrated successfully by 1994 [e.g., Perlmutter *et al.* (1997)]. This method used scheduled observations of specific fields near the end of one dark run to generate reference images that were subsequently compared to search images taken in the same field during the next dark run. Transient objects that displayed photometric behaviour similar to distant SNe Ia were identified in these search images and observed spectroscopically by larger telescopes (this spectroscopic time was pre-scheduled to coordinate with the photometric observations) to firmly identify these SNe candidates. This type of search cadence helped two survey teams — the Supernova Cosmology Project (SCP) and the High-z Supernova Search Team (HzSST) — build the first large sets of distant SNe. The results presented from these

[4]For example, the pioneering work by Nørgaard-Nielsen *et al.* (1989) discovered one confirmed Type Ia SNe at $z = 0.31$ after two years of observing efforts.

high-z Type Ia SNe surveys (Riess *et al.*, 1998a; Perlmutter *et al.*, 1999) provided the first evidence for dark energy. In Riess *et al.* (1998a), a set of 16 high-z SNe in the redshift range $0.16 \leq z \leq 0.62$ (combined with 34 nearby SNe Ia) estimated $\Omega_M = 0.28 \pm 0.10$ [for an assumed flat ($\Omega_{\rm tot} = 1$) Universe]. Perlmutter *et al.* (1999) presented results with a larger set of 42 SNe at $0.18 \leq z \leq 0.83$ that had a similar conclusion, $\Omega_M = 0.28^{+0.09}_{-0.08}({\rm stat})^{+0.05}_{-0.04}({\rm sys})$. More details on the methods used to reach these results are presented in the next section, § 1.3.3.

These cosmological results have been supported by the expanded SNe Ia surveys from these teams. Tonry *et al.* (2003) (HzSST) and Knop *et al.* (2003) (SCP) used search setups similar to the initial (successful) high-z surveys and observed additional SNe Ia in the redshift ranges $0.3 \leq z \leq 1.3$ (8 objects) and $0.36 \leq z \leq 0.86$ (11), respectively. These data sets narrowed the matter energy density down to $\Omega_M = 0.28 \pm 0.05$ (Tonry *et al.*, 2003) and $\Omega_M = 0.25^{+0.07}_{-0.06}({\rm stat}) \pm 0.04({\rm sys})$ (Knop *et al.*, 2003). More focused surveys, with the ability to identify and observe larger numbers of distant supernovae, were necessary for the next advancements in SNe Ia cosmology. Efforts such as the Institute for Astronomy (IfA, at the University of Hawaii-Manoa) Deep Survey both found and followed SNe Ia with survey images taken in multiple filters of a 2.5 deg^2 field every 2-3 weeks for nearly 5 months. Barris *et al.* (2004) spectroscopically identified 23 SNe candidates at $0.34 \leq z \leq 1.03$ that were initially noted in the IfA Deep images; this doubled the amount of SNe at $z > 0.7$ that had been published up to that point.

This enhanced survey method, where large CCD's are used to repeatedly image small fields (and thus generate deep images) in multiple bands, is the foundation for two of the most ambitious surveys to date — the Supernova Legacy Survey [SNLS, (Pritchet, 2005)][5] and ESSENCE [Equation of State SupErNovae trace Cosmic Expansion, (Matheson *et al.*, 2005)]. The details of these two surveys are discussed in Chapter 2. These latest surveys are designed not only to measure the contributions of dark energy density in our Universe, but primarily to clarify its physical nature with estimates of its 'equation of state'. This parameter — which was also estimated in the other surveys that were briefly mentioned here — will be discussed in more detail in § 1.3.4.

[5] see `http://www.cfht.hawaii.edu/Science/CFHLS/`

1.3.3 Estimating Cosmological Parameters with Type Ia Supernovae

As a more specific example of how 'standardisable candles' are used, consider the first year results from the SNLS (Astier *et al.*, 2006), where the SNe Ia magnitudes were normalised with the s parameter. This stretches the observed lightcurve to fit onto an empirical SN Ia template and adjusts M accordingly, so that the left-hand side of Equation 1.11 becomes

$$\mu = m(z) - M + \alpha(s-1) + \beta \cdot c. \tag{1.12}$$

Here, α and β are coefficients that are adjusted to give the best fits when solving for cosmological parameters and c is another term derived from fits to the lightcurve of each individual SN and accounts for colour differences among the objects. This adjustment, like the $\Delta_{m_{15}}$ or MLCS-based methods, reduces the observed scatter in SNe Ia magnitudes by a factor of ~ 2 and facilitates the estimation of cosmological parameters with SNe Ia observations.

The SNLS and other SNe Ia survey teams assemble a large amount of photometric and spectroscopic data in order to identify these objects and to measure their redshifts (z) and magnitudes (which are measured over many epochs and then interpolated to give an observed peak magnitude). These observations also provide the selected $\Delta_{m_{15}}$, s, or MLCS lightcurve shape parameter of choice. For simplicity in this illustration, the standardisation parameter will be referred to as δ_{LC} as a generic term that represents the lightcurve shape-luminosity correction used by these surveys. The cosmological parameters Ω_M and Ω_Λ are then estimated by minimising the χ^2 fit of the distance modulus (adjusted with the lightcurve shape parameter so that $\mu = m - M + \delta_{LC}$) to the cosmological model. Mathematically, this χ^2 minimisation takes the following form[6]:

$$\chi^2 = \sum \frac{(m - M + \delta_{LC} - 5\log d_L(z;\Omega_M,\Omega_\Lambda,H_0))^2}{\sigma^2}. \tag{1.13}$$

This equation is minimised with respect to M, Ω_M, Ω_Λ, and any coefficients in δ_{LC} (i.e., α and β in the SNLS case from Equation 1.12). For these high-z fits, the value of H_0 is assumed (for the SNLS fits, $H_0 = 70.0$ km/s Mpc^{-1} was used); only M is dependent on this value so

[6] Again, this is a general equation that illustrates how the results of 'Type Ia SNe' cosmology are calculated. The actual components of the terms in δ_{LC} and σ^2 will vary specific to the methods and assumptions of each SNe survey.

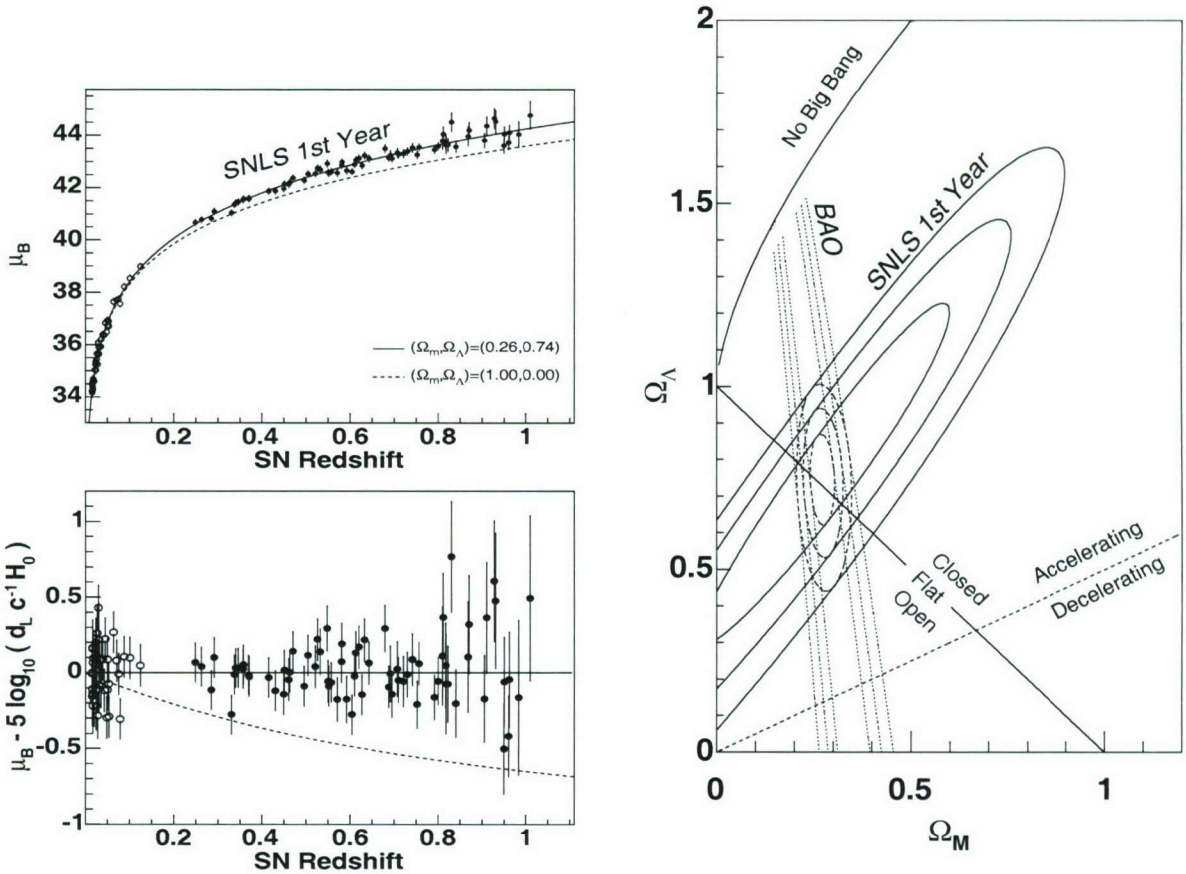

Figure 1.5: First year cosmology results from a survey of distant high-z SNe by the SuperNova Legacy Survey (Astier *et al.*, 2006). The plot on the left (top) is a 'Hubble diagram' that shows how the distance moduli measured for these SNe compares to different cosmologies. Below this plot is a close-up image of the residuals from these cosmological fits; the results from this set of SNe, combined with constraints from BAO estimates (see the figure to the right), indicate that our Universe is spatially flat and dominated by dark energy. The image on the right shows the 1σ, 2σ, and 3σ probability contours of different Ω_M and Ω_Λ values from BAO measurements (Eisenstein *et al.*, 2005) and SNLS results (with dotted and solid lines, respectively). The dashed lines represent the joint confidence contours from these two sources.

any variance in this particular parameter is absorbed in M. The σ^2 in the denominator of this equation represents the errors in the observed and derived SNe parameters as well as the intrinsic dispersion in Type Ia magnitudes [e.g., Astier *et al.* (2006)]. Note that this requires the consideration of the covariance of the errors of the parameters from the lightcurve fits (m, s, and c in this example) and any biases induced in minimising μ with respect to the δ_{LC} coefficients; this is a complex part of this analysis and must be dealt with very carefully. The results of this exercise are usually presented in a Hubble diagram (see Figure 1.5) that displays the μ-z relationship from the observed SNe and different cosmologies.

The final fits from this process give a range of values for Ω_M and Ω_Λ for a given set of SNe. The best-fit cosmology from the SNe Ia data can be constrained further by considering the results from other sources. These include large scale structure (LSS) constraints on the baryon acoustic oscillation (BAO) peak (Eisenstein *et al.*, 2005), which estimates $\Omega_{\rm M}$, and cosmic microwave background (CMB) observations (Spergel *et al.*, 2003, 2006), which give precise estimates of $\Omega_{\rm tot}$. Note that these constraints are all made within the context of Cold Dark Matter (CDM) cosmologies, which appear to supported by all observations to date. By matching the probability contours of the cosmological parameters estimated from these different sources, a holistic or 'concordance model' of the Universe has been determined. The results of the recent estimation of these parameters with distant SNe observed by the SuperNova Legacy Survey are displayed in Figure 1.5. This concordance model indicates that our Universe is spatially flat and accelerating; the direct evidence for the latter is that the distant SNe Ia are dimmer than what is expected in a matter-only Universe. The estimated values of the matter and dark energy content (under the assumption $\Omega_{\rm tot} = 1$) are $\Omega_M = 0.263 \pm 0.042({\rm stat}) \pm 0.032({\rm sys})$ and $\Omega_\Lambda = 0.737 \pm 0.042({\rm stat}) \pm 0.032({\rm sys})$ (Astier *et al.*, 2006), implying that the Universe is dominated by the dark energy behind this acceleration. This particular conclusion from SNe Ia cosmology has generated one of the most heated discussions in astrophysics in recent years and could have profound implications for our understanding of the fundamental physics at work in the Universe (Carroll, Press, & Turner, 1992; Leibundgut, 2001).

1.3.4 Type Ia Supernovae and the Dark Energy Equation of State

This brief overview of SNe Ia and cosmology illustrated how Ω_M and Ω_Λ have been estimated with high-z SNe Ia surveys. The question remains, however, as to what is the physical nature of the dark energy that appears to be driving the accelerated expansion of the Universe. If the Universe is assumed to behave like a perfect isotropic fluid undergoing adiabatic expansion (i.e., maintaining the assumptions for the Robertson-Walker and Friedmann equations listed in Equations 1.1 - 1.3), then the following description of the relationship between the pressure and density of the various energy components in the Universe can be derived:

$$\dot{\rho} + \frac{\dot{a}}{a}[3\rho + 3p] = 0. \tag{1.14}$$

where a is the scale factor as before. The equation of state parameter, w, for these components can be defined (taking c as 1) as:

$$w \equiv \frac{p}{\rho}. \tag{1.15}$$

If dark energy plays the same role as the cosmological constant proposed (and later retracted) by Einstein, then it will not evolve with time and the corresponding equation of state will be $w = -1$. From a particle physics or quantum mechanical standpoint, such a true cosmological constant could be due to the latent energy of the vacuum. However, there are some significant discrepancies between the energy density from the vacuum energy calculated from the standard model of particle physics and the measured dark energy density; the two differ by roughly 120 orders of magnitude[7]. Other descriptions of dark energy have thus been proposed [such as 'quintessence, e.g., Caldwell, Rahul, & Steinhardt (1988)] that correspond to a range of negative w values [see Leibundgut (2001); Carroll (2004); Evans *et al.* (2005), and references therein] which all result in accelerated expansion as long as $w \leq -1/3$.

The value of w can be estimated from the observationally-constrained cosmological energy densities by again considering how these parameters correlate with luminosity distance; in a FRW Universe with the assumption that $\Omega_{\rm tot} = 1$ and $\dot{w} = 0$, this estimation (i.e., Eq. 1.10) can be expressed as

$$d_L = \frac{(1+z)c}{H_0}\left(\int_0^z [\Omega_M(1+z')^3 + (1-\Omega_M)(1+z')^{3(1+w)}]^{-1/2} dz'\right). \tag{1.16}$$

Garnavich *et al.* (1998) completed this exercise with the initial HzSST results and estimated at 95% confidence that $w \leq -0.60$; the initial estimates from the SCP — $w \leq -0.80$ — were in agreement with this conclusion. This value has continued to drift toward more negative values with the SNe observations that followed these initial surveys (Knop *et al.*, 2003; Riess *et al.*, 2004); the most recent updates by the SNLS placed w at $w = -1.023 \pm 0.090(\text{sys}) \pm 0.054(\text{stat})$ when the SNe Ia constraints were combined with SDSS baryon acoustic observation results and an assumed flat universe and time-invariant w. The latest CMB observations support this result (Spergel *et al.*, 2006), but further analysis and constraints are needed for this parameter

[7]This is the famous 'cosmological constant problem'; see Carroll (2004) (and references therein) for a recent discussion on this topic.

if the physics behind dark energy are to be fully explored[8].

1.3.5 Systematics and Uncertainties

These methods of constraining cosmological parameters with SNe Ia observations rely on several assumptions. The most important of these is that, within the locally observed dispersion, all SNe have similar peak absolute magnitudes. With this assumption alone (i.e., no corrections for the lightcurve width-brightness relations) high-z SNe Ia surveys indicate that our Universe is dominated by a repulsive dark energy. If M is systematically different or (more generally) subject to any evolution in the high redshift environment, then all of the conclusions from SNe Ia-based surveys are immediately spurious. The distant SNe Ia would need to be systematically less luminous than their low-z counterparts by only ~ 0.25 magnitudes to undermine the current, accepted conclusions from SNe Ia surveys.

The exact value of the SNe Ia peak magnitude is less important, as any errors from calibrating M in the local sample are degenerate with the variance in the assumed value of H_0. This is clear from the SNLS cosmology summary in § 1.3.3, where M was treated as a free parameter. This technique will completely break down if there is a significant difference in M between the local and distant SNe.

There is certainly some cause for concern with regards to this issue of SN evolution. The intrinsic scatter in peak magnitudes, the different SNe Ia sub–types, the environmental dependence of SN characteristics (see § 3.2.6), and the lack of complete physical understanding of these objects imply that SNe from different environments may lack the assumed homogeneity that makes them standardisable candles. In defense of this assumption, a very wide range of factors that could affect SNe Ia physics — such as progenitor ages and host environment metallicities — have already been probed with the extensive observations made of SNe locally. Nearby Type Ia SNe surveys have a vast array of information at their disposal to investigate any significant changes in SNe Ia properties. Between photometric observations in multiple bands, spectroscopy, comparisons of rise-times and peak-to-tail ratios, and other measurements, there are many avenues available to test the 'standardisable' homogeneity of these objects; none of which have turned up strong evidence to reject this important assumption about their peak magnitudes. This observational evidence has also been supported in many respects by the

[8]In Chapter 2, an outline of the SNLS and ESSENCE plans to increase the precision on w are detailed.

various models that have been built to investigate SNe Ia physics [see Hillebrandt & Niemeyer (2000) for a review]. These theoretical exercises have yet to fully and self consistently describe the physics behind the observed SNe Ia diversity, but neither have they provided sound evidence for a systematic dimming of high-z SNe.

There are additional sources of systematic effects that could be at the root of the observed diminution in SNe magnitudes and which are not intrinsic to the SNe themselves. The most probable of these is extinction from dust, either within or between SN host galaxies. The issue of galactic reddening has been addressed on numerous occasions by the SNe survey teams [e.g., Riess, Press, & Kirshner (1996); Perlmutter *et al.* (1999); Phillips *et al.* (1999) and others] with different methods, and their results have indicated that distant SNe may be more blue than the local sample; this hints at a selection effect (since bluer SNe Ia are brighter) and is the opposite trend from what could cause dimming of high-z objects. The idea of an intergalactic 'grey' dust has also been proposed to account for the distant SNe Ia results (Aguirre, 1999; Aguirre & Haimann, 2000), but specific fits for these grey dust scenarios with high-z SNe in Riess *et al.* (2004) illustrated that this hypothesis fits the observed data poorly. The light from these objects could also be perturbed via gravitational lensing, but this has been shown to be a negligible effect [on the order of 3% (Perlmutter *et al.*, 1999)].

Another important expectation is that the empirical lightcurve shape-luminosity relation is an accurate parameterisation of the primary factor that affects SNe Ia peak luminosity. Certainly there are other parameters at work that contribute to the photometric and spectroscopic behaviour of SNe Ia. The applicability of the empirical lightcurve shape-luminosity relations to cosmology requires that these factors are both minimal compared to the main luminosity-lightcurve shape relation and are not systematically different at the wide range of redshifts probed by these surveys. It is also possible that any slight evolutionary changes in the scatter of SNe Ia luminosities could be well within the range of diversity that is already accounted for in the SNe Ia lightcurve shape-luminosity correlations.

Despite the large amount of references to these issues in the literature, these alternative explanations still need to be tested as thoroughly as possible. The currently accepted implication of the apparent dimming of SNe Ia at high-z is that Einstein's 'biggest blunder' must be re-introduced to quantify our current understanding of the Universe. This is supported by

other, independent observations that do not utilise SNe, (Spergel *et al.*, 2003, 2006; Eisenstein *et al.*, 2005), and is an important development that demands the utmost scrutiny of every facet of SNe Ia physics and cosmology. This thesis will present new methods and results that attempt to address these issues with quantitative comparisons of low-z and high-z spectra from Type Ia supernovae.

1.4 Spectroscopic Studies of Type Ia Supernovae

The spectra of SNe Ia have already been very well studied. Although their 'standardisable' photometric properties have been of the most utility for cosmological studies, it is the spectra that reveal more details about the chemical composition of these objects and more subtle characteristics of the SNe. Furthermore, spectroscopy provides another parameter space to study and to improve the understanding of the physics of Type Ia SNe. A few properties in particular have been the subject of the majority of the discussion with regards to SNe Ia spectroscopy.

The first spectroscopic measurements to provide evidence of an intrinsic difference between Type Ia SNe were the ejection velocities ($v_{\rm ej}$) inferred from the blueshift of various SNe absorption features (Branch *et al.*, 1988). These measurements, which explore the kinetic energy and distribution of elements in the expanding SN ejecta, have also been shown to correlate to the luminosity of these objects (Wells *et al.*, 1994; Fisher *et al.*, 1995). More recently, Benetti *et al.* (2005) used cluster analysis of measurements of the decline rate of SNe Ia $v_{\rm ej}$ to yield a new way of grouping low-z SNe. This empirical classification scheme provides evidence of the role of different explosion mechanisms in SNe Ia diversity. Hook *et al.* (2005), Blondin *et al.* (2006), and Balland *et al.* (2006) addressed the important issue of evolution with a comparison of SNe Ia velocities from objects at different redshifts and found that the measured velocities were comparable in all of the SNe, regardless of z.

Spectra with sufficiently high S/N can also be used in comparisons with synthetic spectra to provide information about the physics of SNe Ia explosions — such as the distribution of IME and temperature structure in these events [e.g., Branch *et al.* (1983); Jeffery *et al.* (1992); Turatto *et al.* (1996); Garavini *et al.* (2004); Mazzali & Lucy (1993)]. These models have been invaluable in identifying the various elements expressed in the absorption and emission

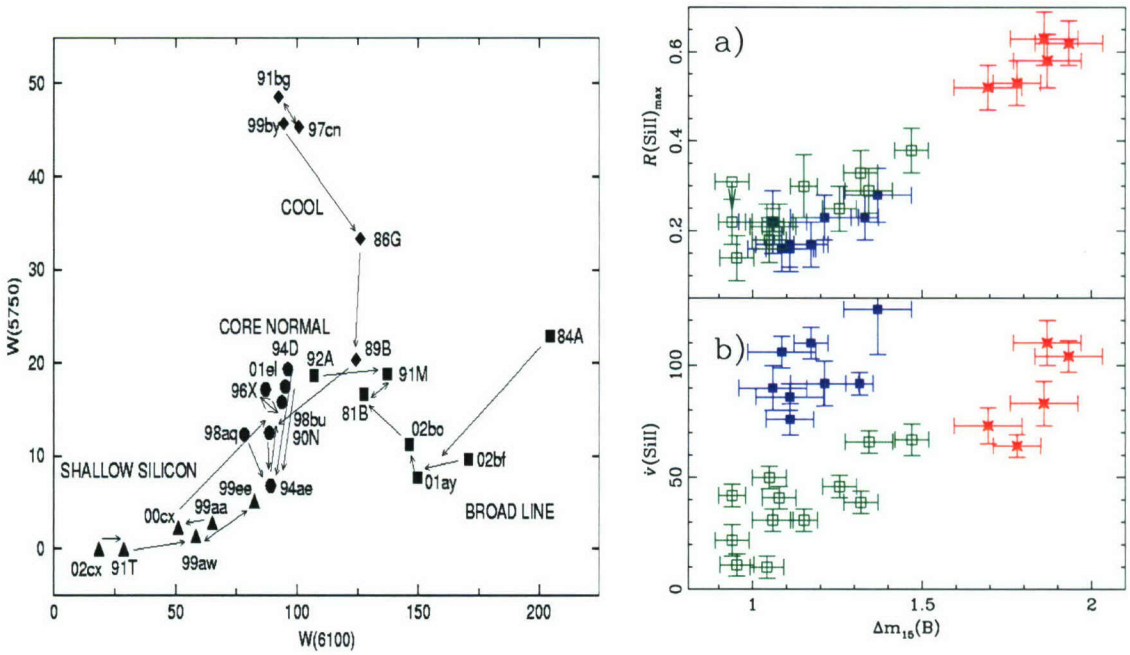

Figure 1.6: Figures from Branch *et al.* (2006) (*left*) and Benetti *et al.* (2005) (*right*). The figure on the left compares nearby SNe Ia according to the equivalent width of the two SiII features near 5800 Å and 6100Å. This comparison reveals a temperature/luminosity sequence in SNe Ia as these objects are progressively cooler and dimmer along the y-axis in this plot. On the right is a figure comparing the velocity gradient and $\Re$\{SiII\} spectroscopic measurements to the photometric $\Delta_{m_{15}}$ parameter for a similar set of local SNe. The different coloured groups were determined with statistical analysis of these measurements and may also reveal a possible continuum of SNe Ia properties based on the explosion mechanism of each SN.

features in SNe spectra, which is necessary to narrow down the possible explosion mechanisms and progenitor scenarios of these objects. Nugent *et al.* (1995b) discovered evidence for a spectroscopic based sequence in SNe Ia peak luminosities with a comparison of the line depths of the SiII features observed near 5800 Å and 6100 Å — this is known as the '$\Re$\{SiII\}' parameter. Spectral synthesis models (Nugent *et al.*, 1995a) demonstrated that this sequence may be based on temperature differences as the burning front propagates through the SNe Ia after C+O ignition.

Other publications have expanded on the Nugent $\Re$\{SiII\} sequence and found other empirical parameters that connect the photometric and spectroscopic behaviour of SNe Ia. Folatelli (2004) (F04 hereafter) defined SNe Ia-specific equivalent width (EW) measurements (see § 3.1.1) and illustrated how they differentiate between Type Ia subtypes and correlate to $\Delta_{m_{15}}$ values. Garavini *et al.* (2006) also used the Folatelli EW measurements to study a small sam-

ple high-z objects for the Supernova Cosmology Project (SCP). Hachinger, Mazzali, & Benetti (2006) illustrated additional empirical EW-$\Delta_{m_{15}}$ correlations and explored connections between these EW measurements and the velocity-gradient SNe classification scheme from Benetti *et al.* (2005). Branch *et al.* (2006) presents additional evidence for a temperature or explosion mechanism sequence in SNe Ia with comparisons of different low-z objects in EW-space.

An example of the quantitative comparisons of low-z SNe that have been made with these spectroscopic measurements [specifically from (Benetti *et al.*, 2005; Branch *et al.*, 2006)] is shown in Fig. 1.6. The left panel in this figure compares SNe Ia according to the equivalent width of the two SiII features near 5800 Å and 6100Å (the same features used in the $\Re\{\text{SiII}\}$ parameter). With just these two measurements, this parameter space would not be particularly enlightening. However, the established temperatures and luminosities in these objects (which were determined independently from the EW measurements in this plot) have been used to label the range of hot/bright to cool/dim SNe; the combination of these identifications with the apparent groups in this parameter space indicates how the different temperatures and luminosities of these SNe Ia are manifested in the absorption features of their specra. This study also addresses the question of whether the dispersion in SNe Ia characteristics is reflected in the existence of discrete sub-groups of SNe or if it corresponds to a continuum of SNe Ia properties. Branch *et al.* (2006) suggested that Fig. 1.6 supports the latter.

To the right in Figure 1.6 is an illustration comparing the velocity gradient and $\Re\{\text{SiII}\}$ spectroscopic measurements to the photometric $\Delta_{m_{15}}$ parameter for a similar set of nearby SNe. The velocity gradients were determined by the total decrease in the measured blueshifts of the SiII absorption features over the entire range of available observations for the set of low-z objects plotted here. The different, colour-coded groups were determined via cluster analysis of these velocity measurements. As in the neighboring plot, these labels also correspond to the physical characteristics of these SNe - the red squares indicate 'faint' SNe Ia (the same objects found at the top of the neighboring plot) while the blue and green squares mark 'high velocity gradient' (HVG) and 'slow velocity gradient' (SVG) SNe categories from Benetti *et al.* (2005), respectively. These statistically-derived categories indicate that there is a possible continuum of SNe Ia properties between overluminous [i.e., 'shallow silicon' in the terminology of the Branch *et al.* (2006) figure] objects through the core normal SNe as both types of SNe are interspersed

among the Benetti *et al.* (2005) HVG and SVG groups. The implications of these sequences for the understanding of the nature of the explosion mechanisms in SNe Ia is still under discussion, but all of these parameters illustrate how quantitative spectroscopic measurements can be used to explore the factors that affect both the heterogeneity and homogeneity of SNe Ia.

1.5 Spectroscopy, Homogenity, and Cosmology

Type Ia supernovae are the most useful distance indicators for cosmology that are currently available, but they are not perfect standard candles. The lightcurve shape-luminosity dependencies that have been established empirically enable a one-parameter correction which appears to account for most of the observed differences in SNe Ia. These corrections reduce the scatter of their peak magnitudes enough for precise analysis of cosmological parameters. Spectroscopic studies of these objects have revealed additional information on the extent of the physical differences and similarities among SNe Ia. These studies have not presented conclusive evidence to reject the homogeneity of SNe that is necessary to apply these lightcurve shape corrections. Despite these advances, the continued use of these objects as cosmological probes hinges on a more complete understanding and categorisation of the heterogeneity of SNe across the vast range of environments and redshifts that are probed by high-z surveys. Thus it is important to fully quantify any differences between the two SNe samples.

Another consideration for cosmology is that high-z surveys may sample SNe Ia from vastly different environments than are observed locally. For example, high-z SNe could be drawn from younger environments that have more active star formation and may have systematically different metallicities than the SNe hosts observed locally. These environments have been shown to host brighter and bluer SNe in nearby Type Ia surveys [e.g., Ivanov, Hamuy, & Pinto (2000)]. To ensure that this possible difference is not causing any bias in high-z SNe surveys, host-morphology correlations must be investigated in the distant SNe to ensure these objects are consistent within the dispersion of SNe Ia properties established locally.

Type Ia evolution is a major concern for SNe Ia cosmology; this possibility cannot be refuted until our understanding of SNe Ia physics and progenitors is complete, but the lack of any significant differences between the nearby and distant populations would be another positive step toward addressing this concern. A quantitative study of spectra will provide a

way to compare SNe Ia from different redshifts for just this purpose. Unfortunately, nearly all of the methods described in the literature (see § 1.4) are not feasible for investigating the SNe Ia observed at high-z due to the observation and survey constraints imposed on this data.

By utilising SNe observed at the Gemini telescope for the SNLS as a primary data set, the analysis in this thesis will show techniques that, unlike the other published methods, are tailored to maximise the amount of information available from high-z SNe spectra. These measurements will be used on the largest set of SNe Ia spectra studied to date to investigate, quantitatively, the homogeneity of these objects across the entire redshift range sampled for SNe cosmology. The correlations between SNe Ia properties and host morphology will also be studied. The results of these various comparisons will be evaluated statistically to firmly identify any significant or systematic differences in SNe observed at different redshifts. This investigation of SNe Ia spectra will serve as an extensive appraisal of the assumptions behind the cosmological use of these 'standardisable' distance indicators.

The complete details on the observation, data reduction, and object identification for the SNe data sets used in this analysis is presented in Chapter 2. For the data discussed in § 2.1 to § 2.4, these reductions and identifications were completed by the author for the observational cosmology goals of the SNLS. The high-z spectra summarised in § 2.5 were reduced by SNLS collaborators and the spectra presented in § 2.7 are from the literature. In § 3.1 the motivation for using EW and $v_{\rm ej}$ measurements is presented. The techniques for and results from applying these measurements to the low-z SNe Ia are discussed throughout § 3.2. A parallel discussion, with regards to the same analysis on the high-z SNe data, follows in § 3.3, with particular attention to the systematic effects that are present in these spectra. The results of these measurements are statistically investigated throughout Chapter 4 and the implications of this investigation for SNe Ia physics and cosmology are discussed in § 4.3 - § 4.5. In Chapter 5 some recommendations for future quantitative spectroscopic analysis are presented.

Chapter 2

Supernova Legacy Survey High Redshift Spectra and Additional Data Sets

The Superova Legacy Survey is a multi-year project that will observe several hundred SNe Ia in the redshift range $0.3 \lesssim z \lesssim 1.0$ in order to determine the equation of state of dark energy. As shown in Ch. 1, the value of this relation will help determine if this dark energy is indeed the time-invariant vacuum energy of Einstein's cosmological constant or an energy that varies with time, such as the slowly varying scalar fields described by models such as quintessence. Over the five-year tenure of the Legacy Survey, a sample of approximately 500 well-measured SNe Ia at high-z, combined with published results from local SNe Ia surveys (another 400 objects), will provide a definitive sample of these objects in the redshift range where w is most sensitive. This will allow this parameter to be determined to a precision of ± 0.04. Simulations predict that achieving this precision on the dark energy equation of state will differentiate between $w > -0.8$ (the value predicted by models such as quintessence) and $w = -1.0$ (the time-invariant cosmological constant) at more than 3σ.

The SNLS has two main components. First, potential SNe Ia candidates are identified and followed up with extensive photometry as the Deep component of the ongoing Canada-France-Hawaii Telescope Legacy Survey (CFHTLS). The most promising Type Ia candidates in the desired redshift range are then observed spectroscopically at the Gemini (North and South)

Telescopes, the VLT, or Keck. The consistency of this survey — with regards to methods, observed fields, depth of observations, instruments used, and data reduction steps — means that the SNLS data will be the most homogenous set of high-z SNe Ia to date. The first year results from the survey [see Ch. 1 & Astier *et al.* (2006)] demonstrate the early success the SNLS has had in achieving its scientific goals. The analysis presented in this thesis and other SNLS publications (Conley *et al.*, 2006; Howell *et al.*, 2006; Neil *et al.*, 2006; Sullivan *et al.*, 2006b; Bronder *et al.*, 2006) makes use of the large amount of SNLS data for additional investigations into the physics of Type Ia supernovae.

2.1 SNLS — Target Selection and Photometry

Full details of the methods used for SNLS candidate selection and observation can be found in Sullivan *et al.* (2006a) and Howell et al. (2005) (H05, hereafter) respectively. Additional SNLS overviews are presented by Howell (2005) and Pritchet (2005). In summary, the SNLS is a 'rolling search' survey; the Canada-France-Hawaii Telescope Legacy Survey (CFHTLS), utilizing the Megacam wide field imager, acquires real time lightcurves of possible SNe by repeatedly imaging four, one square-degree fields up to every four days (in the observers' frame). This imaging is completed in a combination of g',r',i', and z' filters to provide thorough color coverage. The Elixir reduction pipeline (Magnier & Cuillandre, 2004) is used to reduce these observations in real time. The magnitude and color information from these real-time lightcurves is then used to determine photometric redshifts ('photo-z') for each transient object; these assist in prioritizing the most likely SNe Ia candidates for spectroscopy [see Sullivan *et al.* (2006a)]. These initial photo-z fits are made after two or three epochs and can accurately predict a candidate's redshift, phase, and likelihood of being an SN Ia (Sullivan *et al.*, 2006a). The photo-z predictions also allow the spectroscopic observations to be timed to coincide with the epoch of maximum luminosity for likely Type Ia SNe. This is important as these objects are more easily identified at epochs near maximum light (H05). All of the reduction steps for this real-time imaging and analysis are completed by other SNLS collaboration members and at CFHT.

The four fields observed by Megacam are summarised in Table 2.1. The imaging done in these fields (the Deep portion of the CFHTLS) reaches down to an i' magnitude of 24.5.

Field	RA (2000)	Dec (2000)
D1	02:26:00.00	-04:30:00.0
D2	10:00:28.60	+02:12:21.0
D3	14:19:28.01	+52:40:41.0
D4	22:15:31.67	-17:44:05.07

Table 2.1: The four 1 square degree 'Deep' fields of the Canada France Hawaii Telescope Legacy survey.

Each field is observed over a 6 month window each year, resulting in complete light curves of supernovae candidates and high survey efficiency. The large size of the Megacam field also means that these supernovae light curves can be followed for newly discovered objects while completing late-time coverage of previously discovered candidates. An example of the real-time identification of an SNLS supernova candidate is shown in Figure 2.1. After complete lightcurves are available, all of the photometric data is used to generate a re-calibrated and parameterised lightcurve for further analysis. An overview of the complete process that generates these final lightcurves can be found in § 3 and § 4 of Astier *et al.* (2006). This final photometry is paired with the redshift and object identification information from spectroscopic observations to compute the lightcurve shape-magnitude correction (s, see § 1.3) and color values necessary to use these 'standardisable' candles for cosmology (Astier *et al.*, 2006).

2.2 SNLS — Spectroscopy

The SNLS spectroscopic observations are made at 8m-class telescopes with the intention of firmly identifying SNe candidates and estimating their redshifts. The 'rolling search' method locates over 40 potential Type Ia candidates monthly, and the generous time allocations at the Gemini and the VLT telescopes enables the final confirmation of a large number of these candidates. Spectroscopic time at Keck-I and Keck-II has also been used for the SNLS in each year of the survey to compliment the principal observations done at Gemini and the VLT. To date, the SNLS has been granted 60 hours per semester for six semesters at Gemini (Program IDs: GN-2003B-Q-9, GN-2004A-Q-19, GS-2004A-Q-11, GN-2004B-Q-16, GS-2004B-Q-31, GN-2005A-Q-11, GS-2005A-Q-11, GN-2005B-Q-7, GS-2005B-Q-6, GN-2006A-Q-7, GN-2006B-Q-7 — PI I. Hook) along with similar time at the VLT (PI R. Pain).

The majority of the faintest candidates are observed at the Gemini Telescopes (see § 2.3);

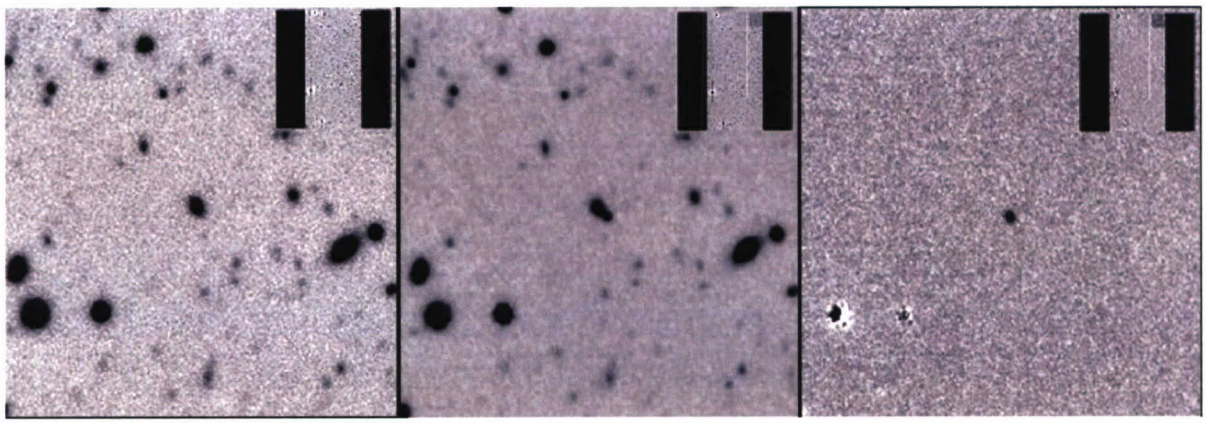

Figure 2.1: Example Megacam images of a possible supernova. Each box is an image in the i' filter measuring 19" by 19". The first two images (from left) are matching sections from Megacam observations at different epochs. The reference image (far left) is psf-matched to the epoch image in the center and then subtracted to produce the difference image on the far right. The difference image is searched for transient objects that may be supernovae. The two small blurs on the bottom of the difference image are subtraction errors due to saturation from foreground objects, while the remaining object in the center is a viable SN candidate. The flux of this brightening object is compared to the flux at the same location in the reference image to provide the percentage increase estimates that are used to both identify possible SNe and constrain host galaxy contamination in objects that are observed spectroscopically (see § 2.4.4.4).

all of these SNLS objects were reduced and classified by the author and are presented here. This SNLS Gemini data thus makes up the primary high-z data set for this thesis. The VLT data, as it was reduced by other SNLS collaborators at different institutions, is considered a secondary set of high-z spectra for this analysis. This set is very useful as these spectra help complete the redshift coverage of the SNe analysed here. The following sections detail the observation, reduction, redshift identification, and object classification of the spectra in these large data sets.

2.3 Gemini Spectroscopic Data — Observations

Longslit spectra of SNLS SN candidates were taken at the Gemini telescopes with the Gemini Multi-Object Spectrograph [GMOS, Hook *et al.* (2004)]. The setup for these observations was defined by the author and other collaboration members with the Gemini Phase-II software. The observations were then carried out by Gemini staff in 'queue mode'. A slit width of 0.75" was used with a central wavelength of 680 nm or 720 nm were used for all observations. The decision on which central wavelength to use was based on the estimated (photo-z) redshift of

each candidate so as to optimise the instrument settings for observing the distinguishing SNe Ia spectral features (see § 1.1). A central wavelength of 680 nm was used for candidates up to $z = 0.4$ to acquire SiII — near 4000 and 6150 Å — whilst the 720 nm setting was used for higher-z candidates to observe CaII H&K and SiII. The slit angle for each observation is chosen to include the host galaxy wherever possible because the features of the host spectrum provide primary indication of the redshift of each candidate (§ 2.4.3). These high-redshift candidates were faint (typical i' magnitudes ranged from 21.8 to 24.5), and required exposure times of 1 to 2 hours over two to four exposures. The GMOS R400 grating (400 lines/mm) and the GG455_G0305 or OG515_G0306 Gemini order-sorting filters (for the 680 and 720 nm central wavelengths, respectively) were used, resulting in a dispersion of 1.34 Å per binned pixel and a resolution of 6.9 Å. This setup gives a spatial resolution of 0.1454" per binned pixel (for 2x2 detector binning). The effective wavelength coverage was 4650 Å to 8900 Å (for the 680 nm setting) and 5100 Å to 9300 Å (for the 720 nm setting). The Gemini observations are made in two modes — 'Nod & Shuffle' or 'Classical' — described in § 2.3.1 and § 2.3.2, respectively.

To handle the large amount of possible SNe tracked by the SNLS, the collaboration has devised an internal SN naming convention. The SNLS nomenclature is necessary as the typical International Astronomical Union (IAU) naming convention for supernovae does not work well for projects on the scale of this survey. To avoid any confusing re-naming of the real-time SNLS analysis, a unified naming scheme is used for all SNLS SNe candidates. Each object is given one name which is retained regardless of its final classification. This convention uses six characters for each object. The first two are numbers that correspond to the year (after 2000) of a candidate's discovery. The third and fourth characters signify the field that an object is discovered in (see Table 2.1). The last two characters begin at 'aa' for the first candidate discovered (for any given year and field) and continue through 'az' for the 26^{th} candidate; the 27^{th} candidate is then named 'ba'. An example name is '03D1as'. These names are used throughout this thesis for the objects observed by the SNLS. The complete list of objects observed at Gemini and reduced by the author during the first 3 years of the SNLS presented in Tables 2.2, 2.3, 2.4, 2.5, 2.6, and 2.7. These observations are divided up into SNLS 'years' that were set by the timeline of SNLS publications. The data presented in H05 and Astier *et al.* (2006) is considered SNLS Year 1 data and covers objects observed from the beginning of

the survey in August 2003 through to October 2004. The Year 2 data spans November 2004 through November 2005, and the Year 3 data includes all other objects to date.

SN[a]	RA (2000)	Dec (2000)	UT Date[b]	Exp.[c]	Mode[d]	λ^{e}_{cent}	IQ[f]	Mag (i')[g]	$\%^{h}_{inc}$
03D1as	02:24:24.520	-04:21:40.19	2003-09-27	6000	N&S	720	0.41	23.96	1475
03D1ax	02:24:23.320	-04:43:14.41	2003-09-29	2400	C	720	0.61	23.16	65
03D1bk	02:26:27.410	-04:32:11.99	2003-09-28	4800	N&S	720	0.47	23.95	83
03D1cj	02:26:25.081	-04:12:39.89	2003-10-26	5400	N&S	720	0.57	24.11	76
03D1cm	02:24:55.288	-04:23:03.68	2003-10-27	5400	N&S	720	0.72	23.77	1568
03D1co	02:26:16.238	-04:56:05.76	2003-11-01	7200	N&S	720	0.84	23.64	188
03D1ew	02:24:14.088	-04:39:56.98	2003-12-21	7200	N&S	720	0.71	23.76	1661
03D1fp	02:26:03.073	-04:08:02.02	2003-12-26	7200	N&S	720	0.55	23.86	30
03D1fq	02:26:55.683	-04:18:08.10	2003-12-24	5400	N&S	720	0.48	23.59	41
03D4cj	22:16:06.660	-17:42:16.72	2003-08-26	2700	C	680	0.83	21.85	¿10000
03D4ck	22:15:08.910	-17:56:02.17	2003-08-27	2400	C	680	0.46	22.78	1905
03D4cn	22:16:34.600	-17:16:13.55	2003-08-27	4800	C	720	0.46	23.81	49
03D4cy	22:13:40.460	-17:40:53.90	2003-09-26	5400	N&S	720	0.59	24.19	149
03D4cz	22:16:41.870	-17:55:34.54	2003-09-27	3600	C	720	0.41	24.41	15
03D4fd	22:16:14.471	-17:23:44.37	2003-10-24	3600	N&S	720	0.67	23.61	321
03D4fe	22:16:08.844	-17:55:19.21	2003-10-24	3600	N&S	720	0.48	23.58	66
03D4gl	22:14:44.177	-17:31:44.47	2003-10-29	3600	N&S	720	0.63	23.43	121
04D1de	02:26:35.925	-04:25:21.65	2004-08-17	7200	N&S	720	0.51	23.63	56
04D1dr	02:27:23.905	-04:51:27.43	2004-08-14	5400	N&S	720	0.57	24.28	72
04D1hd	02:26:08.850	-04:06:35.22	2004-09-13	2400	C	680	0.85	22.16	1254
04D1ho	02:24:44.856	-04:39:15.55	2004-09-16	3600	C	720	0.59	23.13	24
04D1hy	02:24:08.678	-04:49:52.22	2004-09-11	5400	N&S	720	0.73	23.53	996

Table 2.2: Observed properties and telescope settings for SNLS SNe candidates observed during the first year of SNLS operations.
a — SNLS candidate name
b — UT date of spectroscopy
c — total exposure time in seconds
d — Nod & Shuffle (N&S) or Classical (C) observing mode
e — central wavelength, Å
f — seeing in arcseconds
g — i'_{AB} at the time of spectroscopy
h — percent increase, in flux, over the host galaxy background in a 1.10" aperture; this value is estimated from the final lightcurve fits to the SNe and interpolated to the date of spectroscopy

SN[a]	RA (2000)	Dec (2000)	UT Date[b]	Exp.[c]	Mode[d]	λ^{e}_{cent}	IQ[f]	Mag (i')[g]	$\%^{h}_{inc}$
04D1jf	02:25:18.914	-04:49:09.05	2004-10-13	2400	C	680	0.92	22.94	19
04D1ln	02:25:53.482	-04:27:03.75	2004-10-17	2400	C	680	0.62	22.80	29
04D1ow	02:26:42.708	-04:18:22.55	2004-11-08	5400	N&S	720	0.69	23.87	4201
04D2aa	10:02:02.100	+02:40:51.76	2004-01-23	7320	N&S	720	0.58	24.19	n/a
04D2ad	10:00:08.093	+02:39:01.40	2004-01-22	7320	N&S	720	0.54	24.17	n/a
04D2ae	10:01:52.414	+02:13:21.11	2004-01-21	5490	N&S	720	0.75	23.64	100
04D3aa	14:16:49.935	+52:45:31.12	2004-01-30	5400	N&S	720	1.02	24.05	12
04D3ae	14:22:21.569	+52:21:39.21	2004-01-25	2400	C	680	0.94	23.10	196
04D3ax	14:22:39.072	+52:51:52.57	2004-01-28	5400	N&S	720	1.30	24.95	246
04D3bf	14:17:45.096	+52:28:04.31	2004-02-17	2700	C	680	0.90	23.16	46
04D3dd	14:17:48.431	+52:28:14.72	2004-04-25	5400	N&S	720	0.59	24.06	375
04D3de	14:22:13.503	+52:17:09.71	2004-04-27	7200	N&S	720	0.57	24.01	651
04D3fj	14:19:50.703	+52:41:31.84	2004-04-28	7200	N&S	720	0.72	24.19	108
04D3fq	14:16:57.906	+52:22:46.53	2004-04-26	5400	N&S	720	0.97	23.04	1056
04D3gu	14:22:07.359	+52:38:54.60	2004-05-22	4800	C	720	1.03	22.60	6
04D3gx	14:20:13.678	+52:16:58.60	2004-05-21	7200	N&S	720	0.40	24.38	2439
04D3hn	14:22:06.878	+52:13:43.46	2004-05-22	4800	C	720	0.47	22.94	14
04D3kr	14:16:35.937	+52:28:44.20	2004-06-16	2400	C	680	0.82	21.60	156
04D3lp	14:19:50.927	+52:30:11.85	2004-05-27	5400	N&S	720	0.52	24.45	78
04D3lu	14:21:08.009	+52:58:29.74	2004-06-23	3600	N&S	720	0.84	23.49	17
04D3mk	14:19:25.830	+53:09:49.56	2004-06-19	4320	N&S	720	1.25	23.27	86
04D3ml	14:16:39.107	+53:05:35.66	2004-06-20	3600	N&S	720	0.41	23.90	2252
04D3nc	14:16:18.224	+52:16:26.09	2004-07-13	2400	C	720	0.66	23.39	149
04D3nh	14:22:26.729	+52:20:00.92	2004-06-23	1800	C	680	0.80	21.66	199
04D3nq	14:20:19.193	+53:09:15.90	2004-07-14	1500	C	680	0.61	21.03	¿10000
04D3nr	14:22:38.526	+52:38:55.89	2004-07-15	7200	N&S	720	0.69	24.40	2300
04D3ny	14:18:56.332	+52:11:15.06	2004-07-10	5400	N&S	720	0.79	23.23	203

Table 2.3: Observed properties and telescope settings for SNLS SNe candidates observed during the first year of SNLS operations. Headings a to h correspond to the same notes as in Table 2.2

SN[a]	RA (2000)	Dec (2000)	UT Date[b]	Exp.[c]	Mode[d]	λ^{e}_{cent}	IQ[f]	Mag (i')[g]	$\%^{h}_{inc}$
04D3oe	14:19:39.381	+52:33:14.21	2004-07-11	3600	N&S	720	0.62	23.21	28
04D3og	14:20:39.748	+53:01:15.02	2004-07-19	2700	C	720	1.10	21.81	151
04D3pd	14:22:33.506	+52:13:47.77	2004-07-18	3600	N&S	720	0.83	23.34	72
04D4dm	22:15:25.470	-17:14:42.71	2004-07-18	3600	N&S	720	0.96	23.55	123
04D4ec	22:16:29.286	-18:11:04.13	2004-07-19	3600	N&S	720	0.70	23.08	37
04D4ft	22:14:31.097	-17:40:19.74	2004-08-12	3600	C	720	0.67	23.21	78
04D4gg	22:16:09.268	-17:17:39.98	2004-08-16	3600	C	720	0.81	23.03	30
04D4hu	22:15:36.193	-17:50:19.81	2004-09-18	5400	N&S	720	0.52	23.45	84
04D4hx	22:13:40.587	-17:23:03.35	2004-09-16	5400	N&S	720	0.73	24.15	25
04D4ic	22:14:21.841	-17:56:36.43	2004-09-12	5160	N&S	720	0.69	23.34	231
04D4ih	22:17:17.041	-17:40:38.74	2004-10-07	5400	N&S	720	0.52	23.95	41
04D4ii	22:15:55.645	-17:39:27.09	2004-09-15	7200	N&S	720	0.45	23.86	57
04D4im	22:15:00.885	-17:23:45.84	2004-10-10	7200	N&S	720	0.44	23.23	18
04D4jy	22:13:51.605	-17:24:18.13	2004-10-14	8881	N&S	720	0.77	24.08	1779
04D4kn	22:15:04.324	-17:19:45.05	2004-10-19	5400	N&S	720	0.60	23.74	97

Table 2.4: Observed properties and telescope settings for SNLS SNe candidates observed during the first year of SNLS operations. Headings a to h correspond to the same notes as in Table 2.2

SN[a]	RA (2000)	Dec (2000)	UT Date[b]	Exp.[c]	Mode[d]	λ^{e}_{cent}	IQ[f]	Mag (i')[g]	$\%^{h}_{inc}$
04D1pu	02:27:28.437	-04:44:41.71	2004-12-12	7200	N&S	720	0.49	24.08	39
04D2mh	09:59:45.872	+02:08:27.94	2005-01-09	2400	C	720	1.0	22.90	730
04D2mj	10:00:36.535	+02:34:37.44	2005-01-09	3600	N&S	720	0.62	23.19	54
05D1az	02:25:12.492	-04:36:08.17	2005-09-04	5400	N&S	720	0.63	23.78	1246
05D1by	02:24:35.448	-04:12:04.16	2005-09-03	5400	N&S	720	0.62	23.56	9
05D1bz	02:25:00.685	-04:12:00.74	2005-09-02	7200	N&S	720	0.88	23.96	4310
05D1cc	02:26:31.173	-04:09:53.40	2005-09-05	3600	N&S	720	0.46	23.18	114
			2005-09-06	1800			0.83	23.18	114
05D1ee	02:24:46.766	-04:00:01.86	2005-10-31	3600	N&S	720	0.59	23.24	25
05D1ej	02:26:06.317	-04:43:45.79	2005-10-27	3600	N&S	720	0.47	22.83	15
05D1em	02:24:05.503	-04:56:23.35	2005-11-05	3600	N&S	720	0.62	23.71	476
			2005-11-06	1800			0.57	23.71	9524
05D1eo	02:25:23.116	-04:38:33.36	2005-10-27	5400	N&S	720	0.39	23.75	21
05D1er	02:25:41.466	-04:00:16.32	2005-10-28	7200	N&S	720	0.55	23.99	94
05D1kl	02:24:33.544	-04:19:08.33	2005-12-31	5400	N&S	720	0.59	23.61	247
05D2ab	10:01:50.833	+02:06:23.02	2005-01-09	1800	C	680	0.67	21.83	263
05D2ah	10:01:28.704	+01:51:46.18	2005-01-09	1800	C	680	0.96	20.83	1017
05D2ck	10:00:45.203	+02:34:22.13	2005-02-16	5400	N&S	720	0.65	23.88	7592
05D2ja	10:00:03.809	+02:17:36.12	2005-05-07	5400	C	680	0.94	22.15	115
05D3ax	14:19:17.595	+52:41:15.07	2005-02-11	5400	N&S	720	0.45	23.40	342
05D3bt	14:18:35.980	+52:54:55.95	2005-03-06	3600	C	720	0.84	23.52	71
05D3cf	14:16:53.369	+52:20:42.47	2005-03-08	3600	C	720	0.69	22.96	94
05D3ci	14:21:48.085	+52:26:43.33	2005-03-09	5400	N&S	720	0.76	23.03	70
05D3cq	14:18:46.173	+53:07:55.55	2005-04-11	5400	N&S	720	0.64	24.10	156
05D3cx	14:21:06.560	+52:45:01.70	2005-04-09	5400	N&S	720	0.50	23.52	65
05D3jq	14:21:45.462	+53:01:47.53	2005-06-04	5400	N&S	720	0.60	23.36	30
05D3ki	14:21:16.341	+52:35:42.47	2005-05-14	5400	N&S	720	0.67	n/a	n/a
05D3km	14:22:38.298	+53:04:01.14	2005-06-04	5400	N&S	720	1.0	23.89	536
05D3kp	14:20:02.952	+52:16:15.28	2005-06-03	5400	N&S	720	0.81	23.36	7848
05D3kt	14:19:53.730	+52:44:34.64	2005-06-03	5400	N&S	720	0.82	23.53	141

Table 2.5: Observed properties and telescope settings for SNLS SNe candidates observed during the second year of SNLS operations. Headings a to h correspond to the same notes as in Table 2.2

SN[a]	RA (2000)	Dec (2000)	UT Date[b]	Exp.[c]	Mode[d]	λ^{e}_{cent}	IQ[f]	Mag (i')[g]	$\%^{h}_{inc}$
05D3lb	14:17:31.775	+53:10:04.38	2005-06-05	5400	N&S	720	0.51	23.38	192
05D3lc	14:22:22.902	+52:28:44.11	2005-06-06	3600	C	720	0.63	22.67	17
05D3lw	14:17:44.021	+53:06:24.98	2005-07-01	7200	N&S	720	0.45	24.41	170
05D3mn	14:18:45.206	+52:19:23.56	2005-07-12	7200	N&S	720	0.77	23.31	77
05D3mh	14:18:59.805	+52:40:03.50	2005-07-10	7200	N&S	720	0.54	23.50	30
05D3mq	14:19:00.398	+52:23:06.81	2005-08-03	1800	C	680	0.71	21.48	4748
05D3mx	14:22:09.078	+52:13:09.35	2005-07-30	2700	C	680	0.83	23.10	$\geq$10000
05D4av	22:14:10.515	-17:54:42.67	2005-07-10	3600	N&S	720	0.53	23.2	77
05D3ne	14:21:02.946	+52:29:43.92	2005-07-14	2700	C	680	0.85	20.48	1074
05D4bm	22:17:04.621	-17:40:39.45	2005-07-11	3600	C	680	0.55	22.04	144
05D4bo	22:16:44.630	-17:20:12.37	2005-07-10	5400	N&S	720	0.63	24.01	305
			2005-07-14	1800			0.43	23.95	233
05D4ca	22:14:11.350	-17:48:15.47	2005-08-02	2700	C	720	0.63	22.24	156
05D4cn	22:13:31.454	-17:17:19.92	2005-08-02	5400	N&S	720	0.70	23.30	82
05D4dt	22:14:25.851	-17:40:16.03	2005-09-02	3600	N&S	720	0.55	22.62	20
05D4dx	22:13:39.387	-18:03:20.99	2005-09-06	5400	N&S	720	0.47	23.14	39
05D4dy	22:15:30.102	-18:12:55.54	2005-09-06	5400	N&S	720	0.53	23.87	684
05D4fn	22:17:01.076	-17:49:25.16	2005-10-08	7200	N&S	720	0.65	23.86	4474
05D4fo	22:15:20.925	-17:16:05.25	2005-10-07	3600	N&S	720	0.77	22.47	1845
05D4gw	22:14:47.365	-17:31:54.99	2005-11-05	5400	N&S	720	0.46	23.69	283

Table 2.6: Observed properties and telescope settings for SNLS SNe candidates observed during the second year of SNLS operations
Headings a to h correspond to the same notes as in Table 2.2

SN[a]	RA (2000)	Dec (2000)	UT Date[b]	Exp.[c]	Mode[d]	λ^{e}_{cent}	IQ[f]	Mag (i')[g]	$\%^{h}_{inc}$
05D1hn	02:24:36.254	-04:10:54.94	2005-12-04	2700	C	680	0.63	20.86	249
05D1ju	02:26:57.303	-04:08:02.78	2005-12-27	7200	N&S	720	0.50	24.04	91
05D1ka	02:24:58.945	-04:34:28.56	2005-12-28	5400	N&S	720	0.86	23.21	1059
05D2nt	10:00:58.234	+02:22:21.62	2005-12-26	5400	N&S	720	0.69	23.46	340
05D2ob	09:59:00.705	+01:50:56.62	2005-12-28	5400	N&S	720	0.73	24.22	242
05D4hn	22:17:13.545	-17:54:45.40	2005-12-01	5400	N&S	720	0.50	23.50	474
06D3bz	14:17:10.044	+53:01:29.31	2006-02-08	3600	N&S	720	0.71	23.20	115
06D3cb	14:20:43.536	+52:11:28.11	2006-02-03	5400	N&S	720	0.88	23.61	213
06D3cc	14:17:31.604	+52:54:44.79	2006-02-02	5400	N&S	720	0.58	23.55	99
06D3cl	14:22:15.106	+52:16:41.53	2006-03-06	5400	N&S	720	0.61	23.75	264
06D3cn	14:19:25.826	+52:38:27.78	2006-03-06	1800	C	680	0.40	21.26	372
06D3du	14:21:18.563	+53:03:27.10	2006-05-24	5400	N&S	720	0.45	24.27	54
06D3dz	14:18:14.731	+52:56:23.11	2006-05-02	2400	C	680	0.98	22.19	66

Table 2.7: Observed properties and telescope settings for SNLS SNe candidates observed during the third year of SNLS operations. Headings a to h correspond to the same notes as in Table 2.2

2.3.1 Nod & Shuffle Observations

Most of the SNLS observations at the Gemini telescopes are taken in the Nod and Shuffle mode (Glazebrook and Bland-Hawthorne, 2001). This setup enables more accurate sky subtraction than a normal spectroscopic obsevation by nodding frequently (every 60 seconds) between two positions along the slit. The charge on the CCD detectors is simultaneously shuffled between the illuminated science region of the CCD and an unilluminated storage region so both the object and its immediate sky background are imaged on the same pixels and slit position. This requires the use of a shorter N&S specific slit in order to provide an unilluminated region for charge storage. During the reduction of N&S data, systematics such as pixel response, sky fringing, slit irregularities, and any temporal sky variations are canceled out by subtracting the sky spectrum from the object spectrum. This method works well towards the red-end of the spectrum (where sky light is more dominant) and for the SNLS data it was particularly useful for candidates at magnitudes greater than $i' > 23.0$ and observed with the 720 nm central wavelength. Typical nod distances for this method range from less than an arcsecond to a few arcseconds. A smaller nod distance allows for more accurate offsets during nodding, but in order to avoid nodding onto a candidate's host, or any other object, larger nod distances were often required.

There are a few drawbacks to this method. The noise in sky-subtracted N&S images is higher by a factor of up to $\sqrt{2}$ compared to normally reduced long-slit spectra, as the sky is subtracted pixel-by-pixel rather than by an estimate along the entire slit. Each nod cycle can add up to approximately 24 seconds of overhead time to every N&S image. For a typical 1800 second observation, with 15 (60 second) nod cycles, these overheads add an extra 360 seconds. The extra overhead time is often minimised by choosing a small nod distance, or by employing the Electronic N&S mode. The GMOS instrument requires the use of an On-Instrument Wavefront Sensor (OIWFS), which provides image motion compensation ('fast guiding') and higher order corrections. During a normal N&S observation, this sensor physically moves during each nod cycle. The Electronic N&S mode avoids this by electronically changing the position that the OIWFS guides around instead of physically moving the sensor. This decreases the overheads for a N&S observation by nearly 200 seconds (for an 1800 second exposure), but is only available for smaller nod distances (up to 2.0 arcseconds).

Nod and Shuffle observations also suffer from charge traps, which appear as low-level horizontal (along the dispersion axis) stripes with a width of 1 pixel and a length of up to nearly 200 pixels in each image. These charge traps are caused by small detector defects that are magnified by the repeated charge shuffling in N&S mode. These traps appear at the same location on the CCD, so simply moving the detector vertically (along the spatial axis) between exposures enabled these errors to be identified and rejected. These small offsets are completed with the detector translation assembly (DTA), whose primary purpose is flexure compensation during each exposure. The DTA offsets are always set to cover an even number (between 2 and 10) of pixels.

2.3.2 Classical Observations

For Classical observations, the instrument setup is essentially the same as in N&S mode. However, the full long slit, as opposed to the shorter N&S slit, is used. The telescope is not nodded during exposures, but small telescope offsets are employed between images. These Classical observations avoid the additional overheads needed for N&S observations, but are subject to additional systematic effects during sky-subtraction. With the shorter overheads required for the Classical mode, this technique is the best method to observe brighter objects. Candidates with i' magnitudes less than 23.0 typically warrant Classical observations.

2.4 Gemini Spectroscopic Data — Reduction

2.4.1 Nod & Shuffle Reduction

All of the data reduction was completed with the Gemini/GMOS IRAF image reduction software. SNLS teams at Oxford and Toronto reduced all of the data with tailored IRAF pipelines. The independent reductions were made to double-check for any systematic differences or errors in these pipelines. Additionally, the use of two independent pipelines enabled SNLS members to reach a stronger consensus on the classifications and redshifts of SNe candidates. This is because the use of different sized windows when extracting the 2D spectra or the opinions of different observers can illuminate important, but subtle, details in high redshift spectra. The results from both reduction pipelines were in very close agreement. A detailed summary of the reductions completed on the primary Gemini data set from the first year of SNLS observaions

at Toronto can be found in H05. The Oxford reductions, which were completed by the author, are briefly described here.

A section of a raw science image from a GMOS N&S observation is shown in Figure 2.2. All of these raw images for a given object were first bias-corrected using a master bias specific to N&S observations. The images were then flat-fielded with flat images taken at the beginning and end of the observations for each object. The flat-fielding also removes fringing, which is a particular problem at the red end of the GMOS CCDs. With the N&S mode, the sky subtraction for each image was done by subtracting the separate images that are imaged on the same detector. This step effectively removes many systematic effects during this step. This N&S sky subtraction produces a set of 'positive' and 'negative' image pairs which correspond to the subtractions done at each nod position. The negative images are inverted, and then all images from an observation are combined into one science frame with a median combining operation. This final combination has to account for the different position of the positive object traces on each image, which differ along the spatial axis due to the DTA offsets. The DTA offsets, when paired with a proper rejection algorithm, enable the removal of charge traps at this stage (see § 2.3.1). These steps result in a final, two-dimensional N&S spectrum. An example of a final spectrum is displayed in Figure 2.3.

After combining all of the images, the spectrum from the object is extracted. The size and location of the extraction window, along with the other parameters for this step, are set to maximise the SN signal and minimise any flux from the host galaxy when extracting the object. Additional extractions which maximise the host signal are also made so that the host features can be used to make a precise redshift estimate. The GMOS acquisition images are referenced to check the spatial orientation of the SN and host to aid these window settings. The extracted signal is calibrated along the wavelength axis with a solution derived from CuAr arc lamps taken every Gemini queue run. The final flux calibration is based on a flux standard from a standard star observed in each semester of Gemini observations.

Although the N&S process minimises the systematic error associated with sky subtraction, the sky background is still the dominant source of noise in these spectra. Before the N&S sky subtraction step, a region of the sky background is extracted from each image. These extractions are added together in quadrature and then calibrated to provide an error spectrum

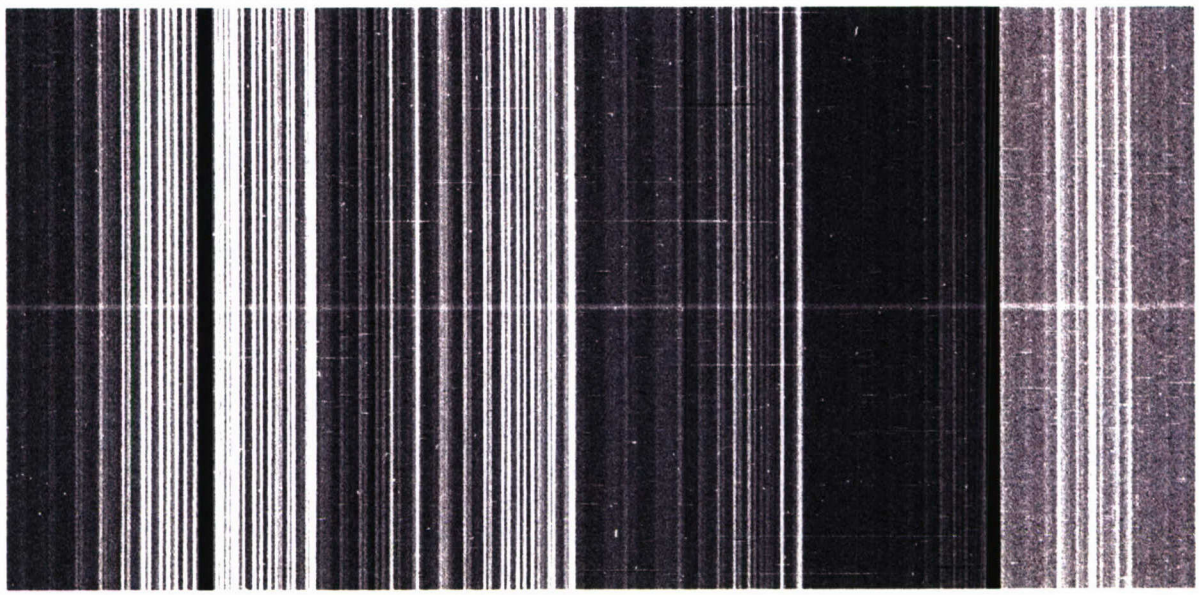

Figure 2.2: A portion of a science image observed in N&S mode at Gemini north. This image is 1480 pixels by 770 pixels (binned) and (entire detector measures 3108 pixels by 2304 pixels). The spatial direction is along the vertical axis here, and the dispersion direction is horizontal running right to left (shortest wavelengths to the right). With the dispersion and spatial resolution of the instrument settings for this N&S observation (see § 2.3), this image measures approximately 1983.2 Å by 111.96". The signal from the SN candidate is visible in the middle of the image. The two gaps between the GMOS CCD's are visible as the dark vertical bands and the other vertical lines are due to the sky background. The thin horizontal stripes are the charge traps that are removed by using the DTA to offset the telescope between exposures.

for each object.

Finally, the extracted, calibrated spectrum is corrected for atmospheric effects and gaps between the three GMOS CCDs. Telluric features are identified in the same standard star image that is used for flux calibration. The location, shape, and magnitude of these features is determined and superimposed on a flat spectrum to create a telluric correction template that is scaled to the calibrated flux from the extracted spectrum. The adjusted telluric template is then added back to the extracted spectrum to complete this correction. The detector regions on either side of the chip gaps (which cover 38 out of 3108 total pixels on the detector) are used to interpolate over these gaps for a final correction.

2.4.2 Classical Reduction

The observations with the Classical setup are reduced slightly differently than the typical methods of longslit spectroscopic reductions. After bias correction and flat fielding, pairs of

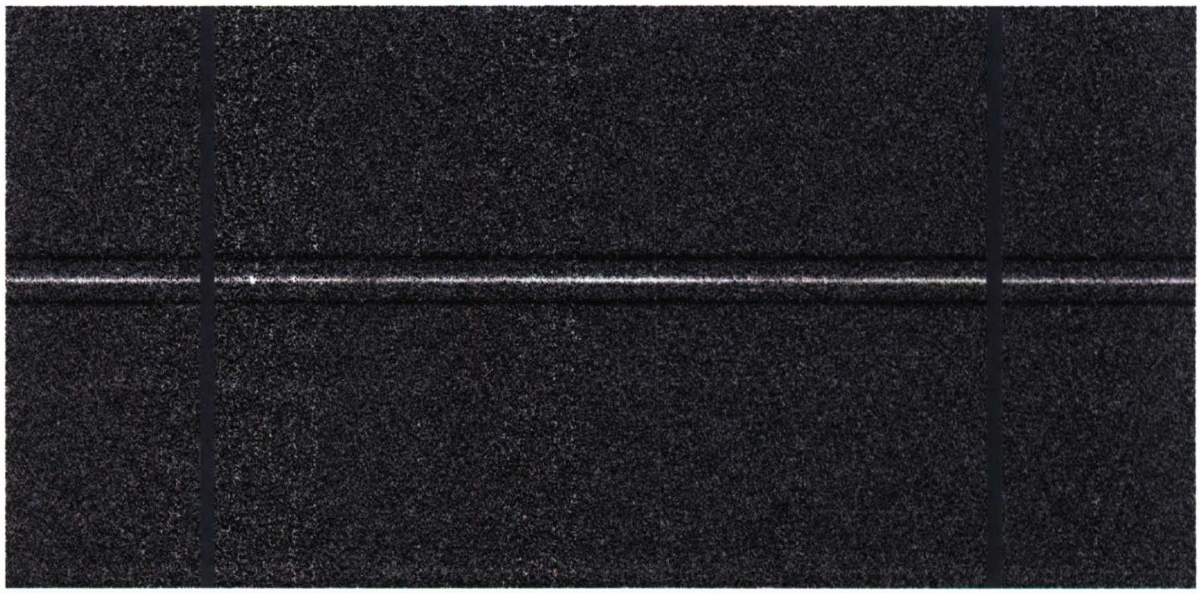

Figure 2.3: A portion of a science image observed in N&S mode at Gemini north, after bias correction, flat-fielding, sky subtraction, and combining all images. This image is the same size as Figure 2.2 — 1480 pixels by 770 pixels. The N&S shuffle sky subtraction has left negative traces of the object around the positive signal in the center of this image. The small, bright spot just to the right of the first chip gap is a thin emission feature from the host galaxy of this object which will be used to estimate its redshift.

images from each object are subtracted from each other to mimic the systematics-free sky subtraction of a N&S observation. All the images from an observation are then combined. The distances of the telescope offsets also have to be accounted for when combining these images. The combined image is then wavelength calibrated and the signal from the object is extracted. The extraction window and other parameters are set to minimise the host galaxy contamination in the object spectrum as much as possible. The telluric features and chip gaps are corrected as in the N&S reduction.

2.4.3 Redshift Estimation

Although both the photo-z real-time photometric data and final parameterised light-curves can help identify the SNLS SNe candidates, ultimately only spectroscopic observations can firmly identify a transient object as a Type Ia SNe and accurately measure its redshift. The latter is estimated (whenever possible) from narrow emission or absorption features from the host galaxy. These are visible against the broad SN features if both a candidate and its host contribute flux to the final spectrum. A spectrum from the galaxy itself is also used if it is

separated enough from the candidate to allow the extraction of two spectra. The location of these features allows estimation of redshifts to a precision of approximately ±0.001 by matching a template of the possible spectroscopic features to those observed in the host or object.

If no host features are clear, then a combination of final photometric data and supernovae template fits to the spectrum (see § 2.4.4) are used to constrain an object's redshift. If the final results from these two sources give a clear indication of the type and redshift of an object, then the z can usually be approximated to ±0.01 (Hook *et al.*, 2005). Without any host features or a clear indication of the object classification, the redshift of a candidate cannot be estimated with any precision.

2.4.4 Object Identification with Quantitative SNe Template Fits

For distant objects, reduced signal-to-noise, host contamination, reddening, and uncertainty in redshift can all make the visual identification of SNe-specific spectroscopic features extremely difficult. In order to standardise the identification process of SNLS candidates in light of these difficulties, an automated χ^2 matching program was used. This program [a slightly edited version of the algorithm defined in Howell & Wang (2002) and H05] compares an observed spectrum against nearby SNe template spectra that are varied over redshift and reddening space. A variable amount of host galaxy flux (from different host galaxy types) is also subtracted from the observed flux to assist in identifying the object. At a given redshift and for the given spectra, the code computes the reduced χ^2, given by

$$\chi^2 = \sum \frac{[O(\lambda) - aT(\lambda; z)10^{cA_\lambda} - bG(\lambda; z)]^2}{\sigma(\lambda)^2}. \tag{2.1}$$

Here O is the observed spectrum, T is the SN template spectrum, G is the host galaxy template, A_λ is the reddening law, σ is the error in the observed spectrum. The constants a, b, and c are all varied to give the best fit in template, host galaxy, and reddening space. The summation sign in this equation reflects the fact that the code iterates through all the available template SNe and then finds the best-fitting parameters simultaneously. These parameters were all restricted based on all of the available information for an object. The criteria used for these restrictions are described in the next few sections. A list of the best matching SN templates and the corresponding host galaxy templates, redshifts, and reddening amounts is produced by

this program to provide the user with a quantitative idea of which parameters fit an observed spectrum best. The final decision on the identification of an SNLS SNe candidate is then made by the user based on the input from these fits. This process can never be fully automated as the opinion of an experienced observer is necessary to discern the more qualitative aspects of these purely quantitative fits.

2.4.4.1 Template Fitting: Reddening constraints

The reddening was modelled with the reddening law of Cardelli *et al.* (1989), with $R_{\rm v} = 3.1$ (where $R_{\rm v} = A_{\rm v}/E(B-V)$). This value of $R_{\rm v}$ was fixed, while the amount of extinction ($A_{\rm v}$) was allowed to vary from -2.0 to 2.0 (in magnitudes of visual extinction) for most fits. The negative values here correspond to making the template spectrum more blue, which was necessary as some of the template spectra had not been de-reddened. This parameter provides an example of why the process can never be fully automated, as certain amounts of reddening for specific spectra are nonsensical from a physical standpoint. For example, a low reduced χ^2 fit may be achieved by making an object known to be intrinsically red, such as a sub-luminous 1991bg-like SNe Ia, brighter and more blue by a significant amount. Such a spectrum does not correspond to any known physical object, so the user will have reject this template match regardless of how well the χ^2 value compares to other fits.

2.4.4.2 Template Fitting: Redshift constraints

The redshift was determined, whenever possible, by the identification of the narrow emission and absorption features from the host galaxy, as described in § 2.4.3. The range on this value for the χ^2 fits was then allowed to vary based on the uncertainty of the z estimate. Objects with a redshift based on clearly identified host features had an associated uncertainty in this estimate of about ± 0.001 (in most cases). In all other cases, the redshift parameters were set to cover a wide range in z to enable the program to find the best appropriate fits in z and object-type space. If a consensus type was reached, the fits would be repeated over a shorter redshift range, with smaller redshift steps, to yield the quoted uncertainty (generally ± 0.01 in z).

2.4.4.3 Template Fitting: Host Galaxy constraints

The identified host features were used to narrow down the galaxy template input into the χ^2 matching algorithm. For example, absorption from H&K or the 4000 Å break are indicators of an early-type E or S0 galaxy, while emission from H or O signify a late type or star-forming host. The library of template host galaxies includes spectra from Kinney *et al.* (1996), which have been smoothed over 21 pixels and have had their narrow features removed. The identified host galaxy features were removed from the observed SN candidates before running this matching program as well.

2.4.4.4 Template Fitting: Host Galaxy 'Contamination' constraints

The limits on the amount of host galaxy template subtracted from a SN candidate spectrum (b in Eq. 2.1) were estimated from the extensive photometry available for each SNLS object. In summary, the thorough photometric coverage from CFHT allows the percent increase, in flux, of a candidate over its host to be estimated. These percent increase amounts are calculated in real time to help prioritise SNe candidates, but a more accurate value is calculated after the full, parameterised lightcurve has been estimated. The flux values from this final photometric data are interpolated to the epoch of spectroscopy to improve the real time percent increase calculation. This interpolated value is then used to approximate the final amount of host flux present in the observed spectrum.

Each object in the SNLS sample has an epoch of non-detection before the SN lightcurve begins to rise. This epoch is used as a baseline from which the percent increase, calculated in observed flux through a 1.10" (diameter) circular aperture of an SN over its host galaxy, is estimated. These estimates are completed by the SNLS collaborators that have access to the CFHT pixel data. This value, $PI_{\rm phot}$, is calculated in real time and then later adjusted with the information from the final light curve; only these final values are discussed here. This percentage is converted into a fractional increase $FI_{\rm phot}$ (where $FI_{\rm phot} = \frac{PI_{\rm phot}}{100}$). The increased flux at the position of the supernova candidate can thus be defined as

$$FI_{\rm phot} = \frac{f_{\rm SN_p}}{f_{\rm gal_p}}, \tag{2.2}$$

where $f_{\rm SN_p}$ and $f_{\rm gal_p}$ are the fraction of supernova and host flux in this photometric aperture,

calculated in the observed i'. The amount of flux from both the numerator and denominator of this estimation will be reduced by slit losses when the object is observed by GMOS. To quantify the effects of these slit losses, the throughput of the SN and host signal is estimated. The throughput of SN flux can be approximated by modelling the object's signal as a point spread function (PSF) with a full width at half-maximum equal to the seeing (as measured on the night of spectroscopy) and then integrating this 2-dimensional Gaussian through a 'rectangular' aperture with a 'width' equal to the 0.75" GMOS slit and a 'length' given by the extraction window input in IRAF during the data reduction. To estimate the host flux through the slit, the spatial profile of the host was assumed to be flat over the entire aperture. The throughput of host flux, with the 'flat' background assumption, is then simply given by the ratio of the spectroscopic 'rectangular' aperture to the 1.10" diameter photometric aperture. If these throughput adjustments are then multiplied by the initial, photometrically-determined fractional increase, a spectroscopic equivalent, $FI_{\rm spec}$, is expressed as

$$FI_{\rm spec} = \frac{f_{\rm SN_s}}{f_{\rm gal_s}} = \frac{T_{\rm SN}}{T_{\rm gal}} \cdot FI_{\rm phot} \tag{2.3}$$

where $f_{\rm SN_s}$ and $f_{\rm gal_s}$ are the supernova and host flux that are observed spectroscopically, accounting for the transmission coefficients $T_{\rm SN}$ and $T_{\rm gal}$ which estimate the throughput for the SN and host, respectively, through the spectroscopic slit. The final spectrum then contains flux from both sources, and the fraction of contamination from host light is then

$$FC_{\rm spec} = \frac{f_{\rm gal_s}}{f_{\rm SN_s}} + f_{\rm gal_s} = \frac{1}{1 + FI_{\rm spec}} = \frac{1}{1 + \frac{T_{\rm SN}}{T_{\rm gal}} \cdot FI_{\rm phot}}, \tag{2.4}$$

where $f_{\rm gal_s}$, the galaxy flux through the spectroscopic slit, and $f_{\rm gal_p}$ (from Eq. 2.2), are easily related by the $T_{\rm gal}$ coefficient (the same holds for $f_{\rm SN_s}$ and $f_{\rm SN_p}$ via $T_{\rm sn}$) from Eq. 2.3 as shown above. With the relations defined in Equations 2.2 to 2.4, the photometric estimate of percent increase $PI_{\rm phot}$ can give an approximate value of the final host contamination fraction, calculated in the observed i', of the each SN spectrum. This amount was converted back to a percent contamination, $PC_{\rm spec}$ (where $PC_{\rm spec} = 100 \times FC_{\rm spec}$), and used to set a sensible upper limit on b in Eq. 2.1.

The results of these photometric-based host galaxy contamination estimates for the SNe

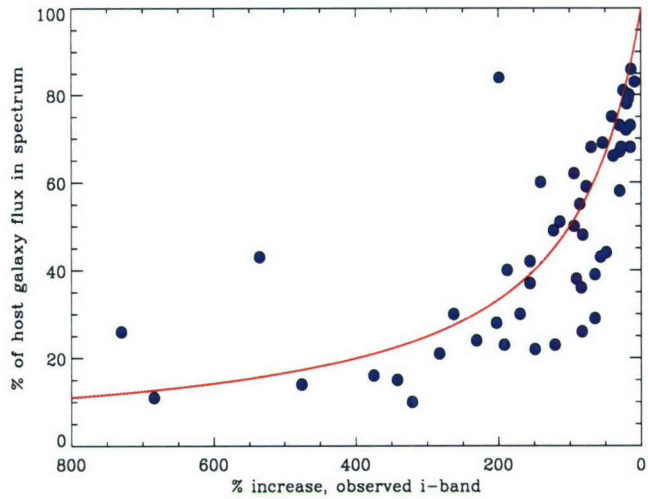

Figure 2.4: The estimated host contamination in each Type Ia SN spectrum (determined via the calculations defined in Eqs. 2.2 - 2.4) in the primary data set is shown against the percentage increase in flux (see § 2.4.4.4), computed from the final lightcurve of each SN. The trend displayed is the expected relation between these two parameters if there was a 1:1 correlation between the ratio of supernova to host flux (determined photometrically) and the amount of host flux that 'contaminates' the object's spectrum. The points below this trend illustrate that good seeing and accurate extractions can minimise the amount of host galaxy flux in the SNe spectra.

Ia in the primary data set are shown in Table 2.8. The host contamination also affects the quantitative spectroscopic measurements that are made on these high-z spectra. The specific effects of this contamination are discussed in § 3.3.3. The final amount of host galaxy contamination in the SNLS spectra ($PC_{\rm spec}$, calculated with Eqns. 2.2 - 2.4) are displayed against the photometrically estimated percent increase values ($PI_{\rm phot}$) in Figure 2.4. Also shown on this figure is predicted that would be followed if there was a 1:1 correlation between the ratio of supernova to host galaxy flux (determined photometrically) and the amount of host flux in the final spectrum. Mathematically, this expected contamination amount, $P_{\rm trend}$ is expressed as $P_{\rm trend} = \frac{1.0}{1.0+PI_{\rm phot}}$. As this plot shows, for a majority of observations the amount of host galaxy contamination in the final spectrum was lower than the expected value, even for objects with a fairly large amount of host contamination. This is not surprising as the seeing guidelines of the SNLS and the careful extractions of SNe candidate spectra are designed to yield as much signal from each SN as possible.

During the SNe identifications, the χ^2 matching program calculates the amount of host flux at each iteration with the i' filter transmission curve from CFHT Megaprime/Megacam. This ensures continuity with the derivation of the upper limit on b (i.e., the allowed amount of host

SN	PI^{a}_{phot}	PC^{b}_{spec}	SN	PI^{a}_{phot}	PC^{b}_{spec}	SN	PI^{a}_{phot}	PI^{b}_{spec}
03D1ax	65	39	04D3nh	199	84	05D2ja	115	51
03D1bk	83	26	04D3ny	203	28	05D3ax	342	15
03D1co	188	40	04D3oe	28	78	05D3cf	94	62
03D1fq	41	75	04D4dm	123	49	05D3ci	70	68
03D4cn	49	44	04D4gg	30	73	05D3cq	156	42
03D4cy	149	22	04D4hu	84	36	05D3cx	65	29
03D4cz	15	73	04D4ic	231	24	05D3jq	30	67
03D4fd	321	10	04D4ih	41	70	05D3km	536	43
03D4gl	121	23	04D4ii	57	43	05D3kt	141	60
04D1de	56	51	04D4im	18	79	05D3lc	17	79
04D1pu	39	66	05D1by	9	83	05D3lb	192	23
04D2ae	100	48	05D1cc	114	51	05D3lw	170	30
04D2mh	730	26	05D1ee	25	81	05D3mh	30	58
04D2mj	54	69	05D1ej	15	68	05D3mn	77	59
04D3bf	46	64	05D1em	476	14	05D4av	77	52
04D3dd	375	16	05D1eo	21	72	05D4bm	146	36
04D3hn	14	86	05D1er	94	50	05D4cn	82	48
04D3kr	156	37	05D1ju	91	38	05D4dt	20	78
04D3lp	78	44	05D1hn	249	26	05D4dx	39	71
04D3lu	17	80	05D1kl	247	23	05D4dy	684	11
04D3mk	86	55	05D2ab	263	30	05D4gw	283	21
04D3nc	149	33	05D2ah	1017	18	05D4hn	474	14

Table 2.8: The final host galaxy contamination estimates for the primary set of SNLS SNe Ia observed at Gemini. The amount of contamination in the final SN spectrum for each object was determined with the extensive photometric data available from the CFHTLS, the seeing during the night of spectroscopy, and the size of the extraction window used during data reduction. The seeing information is listed in Tables 2.2 - 2.7.

a — photometric percent increase determined by interpolating from the final SN lightcurve data to the date of spectroscopy, see f in Table 2.2

b — percent host galaxy contamination in the final spectrum, see § 2.4.4.4 and Equations 2.2 - 2.4.

flux) described in Equations 2.2 - 2.4. The amount of host contamination estimated by the χ^2 fits is not used in any analysis, rather, these numbers are only used to help judge which final χ^2 template matches are most realistic for a given SN candidate.

2.4.4.5 Template Fitting: Comparison SNe Templates

The comparison template SNe are selected from a large library of published, low-redshift SNe of all types. This library includes 253 Type Ia SNe spectra, 75 Type Ib/c spectra, and 47 SNII spectra. These templates cover a wide range of epochs and SN types, and have extensive wavelength coverage and high S/N. In all cases, the χ^2 matching program was run with no constraints on the template type, to avoid biasing the final results toward any initial (and po-

tentially misleading) indications of a candidate's type. The scale factor for these SN templates (a in Eq. 2.1) was allowed to range up to 2.0 for all fits.

2.4.5 Object Classification Confidence Rankings

After completing these semi-automated identifications, the final identification for each candidate was confirmed according to a Confidence Index (CI) that ranged from 0-5:

5 Certain Ia: The spectrum shows the distinctive SNe Ia absorption features, such as SiII (4000 Å or 6150 Å) or S (near 5400 Å). At the higher redshifts of SNLS candidates, the latter two features are often shifted out of the observed spectral range, so SiII λ4000 is the primary indicator that an object is a Type Ia.

4 Highly probable Ia: The spectrum matches that of a Type Ia and does not match other SN types, but the presence of the Ia-specific SiII and S features is ambiguous. Other evidence is used to confirm a candidate at this level, such as a Ia-matching lightcurve at the measured redshift.

3 Probable Ia: The spectrum matches a SN Ia, but other SN types (such as Type Ib/c SNe) are matched adequately as well and cannot be ruled out from the spectrum alone. These borderline classifications are due to either low S/N in the observed spectrum or because other SNe look similar at the same phase. Objects with this confidence index are still considered SNe Ia because the photometric information on these candidates is consistent with an SN Ia at the measured z. As in previous publications, [Lidman *et al.* (2005), H05] SNe at this confidence level are referred to as 'Ia*'.

2 Unknown: The type cannot be determined from the spectrum. Low S/N or a large amount of host galaxy contamination are generally the cause of the uncertainty. These objects are still most likely supernovae of some type, as the SNLS real-time lightcurves effectively screen out AGN and other variable objects. Objects with this confidence index are referred to as 'SN'.

1 Probably not a Ia: The features of the spectrum are inconsistent with those of a SN Ia and more consistent with another SN type. The exact SN type (again, due to high

noise or host flux) cannot be determined with complete certainty, but there is still enough evidence to classify these objects as likely Type Ib/c ('Ib/c') or Type II ('II') SNe.

0 Not a Ia: The spectrum is inconsistent with a SN Ia and shows clear features of another SN type. The spectrum unambiguously matches that from a core-collapse Type II or Type Ib/c SN.

These confidence levels were initially determined independently for each candidate by both the author and other SNLS collaborators. A final opinion on the confidence level and type was then reached by a consensus opinion between the two groups. Note objects 04D3gx† and 04D3nc† in Table 2.9 for the only instances where the CI presented in this thesis differs from previous SNLS publications. The reduced χ^2 matches to low-z SNe Ia were simply not as conclusive with the author's final spectra for these objects as the corresponding reductions by SNLS collaborators at the University of Toronto. A full presentation of the spectra reduced and identified by the author is given in Appendix A. The derived properties - the final redshift and object identifications - of the SNe reduced by the author are listed below in Table 2.9. In summary, this thesis includes spectra from 124 objects observed from the beginning of SNLS operations at Gemini (August 2003) through May 2006. From this sample, 84 candidates were confirmed as SNe Ia at a median z of 0.707. An additional 5 objects were confirmed as core collapse supernova.

Table 2.9: Final redshift estimates and object classifications for SNLS SNe candidates that were reduced and identified by the author. The cases where the object type or redshift could not be estimated are marked '...'.

SN	z^{a}	σ_z^{a}	CI[b]	Template[c]	z from[d]
03D1as	0.872	0.001	2 - SN	...	[OII]
03D1ax	0.497	0.001	5 - Ia	1996X -2	[OII], H&K
03D1bk	0.866	0.001	5 - Ia	1994D +2	H&K, Hβ, Hγ
03D1cj	0.364	0.001	1 - Ib/c	1994I +1	Hα, [OII]

continued on next page

Table 2.9

(continued)

SN	z[a]	σ_z[a]	CI[b]	Template[c]	z from[d]
03D1cm	0.87	0.01	4 - Ia	1999bp +1	SN
03D1co	0.68	0.01	5 - Ia	1994D -2	SN
03D1ew	0.868	0.001	5 - Ia	1999ee -2	[OII]
03D1fp	0.270	0.001	0 - II	1987K +7	Hα, SII
03D1fq	0.78	0.02	4 - Ia	1994D -4	SN
03D4cj	0.271	0.001	5 - Ia	1991T -8	[OIII], Hα
03D4ck	0.189	0.001	0 - II	1979C +7	Hα, Hβ
03D4cn	0.818	0.001	4 - Ia	2002bo -2	[OII], [OIII], Hβ
03D4cy	0.927	0.001	4 - Ia	1999aw +12	[OII]
03D4cz	0.695	0.001	3 - Ia*	1999av +9	H&K
03D4fd	0.792	0.001	5 - Ia	1989B -5	[OII]
03D4fe	...	...	1	...	...
03D4gl	0.56	0.01	4 - Ia	1999ee -1	SN
04D1de	0.767	0.001	3 - Ia*	1990N -7	[OII], [OIII], Hβ
04D1dr	0.640	0.001	2 - SN	...	[OII], [OIII], Hβ
04D1hd	0.368	0.001	4 - Ia	1996X -1	[OII], [OIII]
04D1ho	0.701	0.001	1 - II	1987M +7	[OII], [OIII], H&K
04D1hy	0.848	0.001	5 - Ia	1989B -5	H&K
04D1jf	0.380	0.001	2 - SN	...	[OII], [OIII], H&K
04D1ln	0.207	0.001	0 - II	1999em +9	Hα, SII
04D1ow	0.93	0.01	4 - Ia	1992A +5	SN
04D2aa	...	...	2 - SN	...	...
04D2ad	0.680	0.001	2 - SN	...	[OII], [OIII]
04D2ae	0.843	0.001	4 - Ia	1990N -7	H&K
04D3aa	0.204	0.001	0 - II	1993J +23	Hα, SII
04D3ax	0.356	0.001	1 - II	1988A +3	Hα, [OIII], SII

continued on next page

Table 2.9

(continued)

SN	z[a]	σ_z[a]	CI[b]	Template[c]	z from[d]
04D3ae	0.216	0.001	0 - II	1993W +21	Hα
04D3bf	0.156	0.001	5 - Ia	1990N +17	Hα, SII
04D3dd	1.01	0.01	4 - Ia	1999av +5	SN
04D3de	...	...	2 - SN	...	...
04D3fj	...	...	2 - SN	...	...
04D3fq	0.73	0.01	4 - Ia	1992A +3	SN
04D3gu	0.748	0.001	2 - SN	1997dd +1	[OII], H&K, Hδ
04D3gx†	0.92	0.01	2 - SN	2000cx +1	SN
04D3hn	0.551	0.001	4 - Ia	1994D -5	H&K, Hβ
04D3kr	0.337	0.001	5 - Ia	1989B -1	[OII], [OIII]
04D3lp	0.982	0.001	3 - Ia*	1999bp -2	[OII]
04D3lu	0.822	0.001	4 - Ia	1999bk +7	H&K
04D3mk	0.812	0.001	4 - Ia	1999aa -3	[OII], H&K
04D3ml	0.96	0.02	4 - Ia	1999aw +3	SN
04D3nc†	0.817	0.001	2 - SN	...	[OII]
04D3nh	0.339	0.001	5 - Ia	1992A +3	Hα, [OII]
04D3nq	0.21	0.01	5 - Ia	1998bu +11	SN
04D3nr	0.881	0.00	2 - SN	...	[OII]
04D3ny	0.81	0.01	4 - Ia	1994D +2	SN
04D3oe	0.756	0.001	4 - Ia	1999bn +2	H&K
04D3og	0.352	0.001	2 - SN	...	Hα, Hβ, [OII]
04D3pd	0.760	0.001	2 - SN	...	[OII], [OIII]
04D4dm	0.810	0.001	4 - Ia	1999ee +3	[OII]
04D4ec	0.592	0.001	2 - SN	...	[OII], [OIII]
04D4ft	0.267	0.001	2 - SN	...	Hα, Hβ
04D4gg	0.424	0.001	4 - Ia	1991T -11	[OII], [OIII], Hβ

continued on next page

Table 2.9

(continued)

SN	z[a]	σ_z[a]	CI[b]	Template[c]	z from[d]
04D4hu	0.703	0.001	4 - Ia	1999av +5	[OII], [OIII], Hβ
04D4hx	0.543	0.001	2 - SN	...	H&K
04D4ic	0.687	0.001	4 - Ia	1981B 0	[OII]
04D4ii	0.866	0.001	5 - Ia	1999bp -2	[OII]
04D4ih	0.943	0.001	3 - Ia*	1992A +9	[OII], H&K
04D4im	0.751	0.001	4 - Ia	1999aw +3	H&K, Hδ
04D4jy	0.93	0.01	3 - Ia*	1989B 0	SN
04D4kn	0.909	0.001	2 - SN	...	[OII], H&K, Hγ
04D1pu	0.639	0.001	3 - Ia*	...	[OII]
04D2mh	0.59	0.01	3 - Ia*	1996X +2	SN
04D2mj	0.513	0.001	5 - Ia	1992A -1	[OII], Hβ, [OIII]
05D1az	0.842	0.001	5 - Ia	1996X +2	probable [OII]
05D1by	0.298	0.001	5 - Ia	2002bo -1	Hα, Hβ, [OIII], SII
05D1bz	...	...	2 - SN	...	...
05D1cc	0.564	0.001	5 - Ia	1996X +7	Hβ, [OII], [OIII]
05D1ee	0.558	0.001	4 - Ia	...	H&K
05D1ej	0.312	0.001	4 - Ia	1989B -5	NII
05D1em	0.866	0.001	5 - Ia	1999ee +5	H&K
05D1eo	0.737	0.001	2 - SN	...	H&K, [OII]
05D1er	0.85	0.01	3 - Ia*	1999aa -1	SN
05D1hn	0.149	0.001	5 - Ia	2003du -7	Hα, SII, [OII]
05D1ju	0.707	0.001	3 - Ia*	1996X +7	[OII], [OIII]
05D1ka	0.857	0.001	2 - SN	...	H&K
05D1kl	0.560	0.001	3 - Ia*	1990N -7	[OII], [OIII]
05D2ab	0.323	0.001	5 - Ia	1998bu -4	Hα
05D2ah	0.184	0.001	5 - Ia	1994D -5	Hα, SII

continued on next page

Table 2.9

(continued)

SN	z[a]	σ_z[a]	CI[b]	Template[c]	z from[d]
05D2ck	0.698	0.001	5 - Ia	1992A +6	H&K
05D2ja	0.303	0.001	5 - Ia	1999aw +16	Hα, SII, [OIII]
05D2nt	0.757	0.001	4 - Ia	1999ee +3	[OII],Hβ, [OIII]
05D2ob	0.924	0.001	4 - Ia	1989B -1	[OII]
05D3ax	0.643	0.001	5 - Ia	1999aw +12	[OII], [OIII]
05D3bt	0.462	0.001	2 - SN	...	Hβ, [OII], [OIII]
05D3cf	0.419	0.001	4 - Ia	1999be +19	Hβ, [OII], [OIII]
05D3ci	0.515	0.001	5 - Ia	1992A -5	[OII], H&K
05D3cq	0.890	0.001	3 - Ia*	1999ao +5	Hβ, [OII]
05D3cx	0.805	0.001	4 - Ia	1999bk +7	possible [OII]
05D3jq	0.579	0.001	4 - Ia	2000E +5	Hβ, Hγ, [OII]
05D3ki	0.965	0.001	2 - SN	...	[OII]
05D3km	0.97	0.01	3 - Ia*	1999bo +1	SN
05D3kp	...	...	2 - SN	...	...
05D3kt	0.648	0.001	5 - Ia	1999ee -2	Hβ, [OII], [OIII]
05D3lb	0.647	0.001	5 - Ia	1999ee 0	Hβ, [OII], [OIII]
05D3lc	0.461	0.001	3 - SN	...	H&K
05D3lw	0.601	0.001	2 - SN	...	[OII]
05D3mn	0.760	0.001	3 - Ia*	1999av +2	possible [OII]
05D3mh	0.67	0.01	4 - Ia	1998aq -8	SN
05D3mq	0.246	0.001	5 - Ia	1992A +9	Hα
05D3mx	0.46	0.01	4 - Ia	1998bu +8	SN
05D3ne	0.169	0.001	5 - Ia	1994D -4	SDSS host spectrum
05D4av	0.509	0.001	3 - Ia*	2002bo -4	[OII]
05D4bm	0.375	0.001	5 - Ia	1996X -1	Hβ, [OII], [OIII]
05D4bo[‡]	...	...	...	...	...

continued on next page

Table 2.9

(continued)

SN	z^a	σ_z^a	CI[b]	Template[c]	z from[d]
05D4ca	0.607	0.001	2 - SN	1988A +3	Hβ, [OII], [OIII]
05D4cn	0.763	0.001	3 - Ia*	2002bo -1	[OII], H&K
05D4dt	0.407	0.001	4 - Ia	1994D -2	Hα,[OII], H&K, Hβ, [OIII]
05D4dx	0.793	0.001	3 - Ia*	1992A +5	H&K, Hδ
05D4dy	0.79	0.01	4 - Ia	1994D +2	SN
05D4fn	0.4	0.1	2 - SN	...	SN
05D4fo	0.373	0.001	5 - SN	1994D -2	Hα, H&K
05D4gw	0.808	0.001	4 - Ia	1999bp -2	[OII]
05D4hn	0.842	0.001	4 - Ia	1981B 0	[OII], [OIII]
06D3bz	0.72	0.01	4 - Ia	1989B -1	SN
06D3cb	...	...	2 - SN	...	...
06D3cc	0.9	0.1	3 - Ia*	1990N -7	...
06D3cl	0.555	0.001	2 - SN	...	[OII],[OIII],Hβ
06D3cn	0.818	0.001	5 - Ia	1996X -1	[OII],[OIII],Hβ
06D3du	1.0	0.1	2 - SN	...	SN
06D3dz	0.294	0.001	1 - Ib/c	1983V +18	Hα,SII

a - redshift and uncertainty; redshifts identified with the host galaxy features are (in general) accurate to ± 0.001 while redshifts identified with template matches are (in general) accurate to ± 0.01

b - SN Confidence Index (CI) and estimated object type (see § 2.4.5).

c - best match low-z SN spectrum and epoch

d - the observed host galaxy features used to estimate the redshift (where applicable), otherwise the 'SN' abbreviation for SN template match is indicated

† the final CI on this object differs from that published in H05

‡ the S/N in this object was so low that no identifyable signal could be extracted from the final 2D spectrum

2.5 VLT Spectroscopic Data

2.5.1 VLT Observations

Additional high redshift SNe spectra were observed for the SNLS with the Very Large Telescope. Observations at the VLT have a shorter setup time than at Gemini, so for more efficient use of telescope time the majority of lower redshift candidates ($z < 0.8$) were observed there. The N&S capabilities at Gemini make it more well suited for dimmer candidates, providing another reason why brighter (or, similarly, more nearby) objects are generally sent to the VLT. The VLT observations are made by VLT staff in service mode with the long slit setting of the FORS1 or FORS2 spectrograph. Either the 300V or 300I grism is used, with a slit width set to 0.2" greater than the seeing. Exposure times range from 1500s (over 2 exposures) to up to 3750s (over 5 exposures) for the faintest candidates.

Currently, 221 SN candidates have been observed at the VLT and over 100 of these have been identified as Type Ia SN or probable Type Ia SN. Due to some restrictions on the availability of these spectra [they are currently being prepared for publication, Basa *et al.* (2006)] only a sub-sample of the SNe observed during the first year of the SNLS at the VLT were considered for analysis in this thesis. The selection and observation of these objects is very similar to the primary set of Gemini spectra, but as these objects were not reduced by the author they are defined as a secondary data set here.

2.5.2 VLT Data Reduction

Reductions of VLT FORS1 images were made with an automatic pipeline based on the ESO/FORS1 standard pipeline. These reductions were completed by SNLS collaborators at the Laboratoire d' Astrophysique de Marseille and the steps they use in this process are summarised here for completeness. This reduction method first removes cosmic rays by applying a median filter to deviant pixels. Next, master bias and flat field images are computed from the median of the individual input frames. Wavelength calibrations are made with standard arc lamps and two-dimensional modeling of the dispersion relation. Flux calibrations are made by applying the Horne algorithm (Horne, 1986) during the standard star extraction (Basa *et al.*, 2006). The science frames are then bias subtracted, flat fielded, and wavelength calibrated. The flux calibration is then performed, which corrects the science images for both atmospheric extinction

effects and wavelength-dependent instrument transmission. These steps prepare the science frame for the extraction of the candidate and host spectra. This extraction is completed with the Horne algorithm for each individual frame, and an error spectrum for each exposure is extracted as well. These individual extractions are then combined for the final spectrum. The observed properties for these VLT spectra are summarised in Table 2.10.

2.5.3 Redshift Estimation and Object Classification

As with the Gemini data set, the redshift measurements for the VLT data were obtained from emission and absorption features from the host galaxy spectrum for every possible candidate. In cases where no host galaxy spectrum could be extracted and no host features were visible, the redshift was estimated by fitting spectroscopic templates to the observed spectrum. These template fits were quantified with an algorithm similar to that described in § 2.4.4 and ranked according to the same confidence level scheme [see Lidman *et al.* (2005)]. The final determination of these derived properties for the VLT data was also reached with a consensus opinion from SNLS members.

The VLT objects that were available from the first year of SNLS observations and that were classified as probable SNe Ia or higher (CI $\geq$ 3) were included in this thesis. A more strict cut with regards to host contamination was also made to the VLT data because these spectra were extracted from their corresponding 2D science frames with (in nearly every case) larger extraction windows (compared to the Gemini data reductions) by other SNLS collaborators. This meant that the final amount of host contamination (see § 2.4.4.4) was computed with $T_{\rm SN} = T_{\rm gal}$ (Eq. 2.3) and was also more uncertain (from the author's perspective) than the comparable primary Gemini spectra. The VLT objects that had a flux increase over their host galaxies (computed via interpolating from the final lightcurve data) of less than 100% were removed from any additional spectroscopic analysis. The final set of VLT spectra that met this criteria are listed below in Table 2.10. This data adds another 20 SNe Ia at a median redshift of $z = 0.634$ to the already large primary data set. Note that SNLS SN 04D1ow was observed at Gemini North as well. As expected, the median z is slightly lower than the median z of the SNLS objects observed with Gemini.

SN[a]	RA (2000)	Dec (2000)	UT Date[b]	Exp.[c]	Mag (i')[d]	$\%^{e}_{inc}$	z[f]	CI[g]
03D1dt	02:26:31.200	-04:03:08.51	2003/11/29	3750	23.5	$\geq$10000	0.612(0.001)	5 - Ia
04D1aj	02:25:53.982	-04:59:40.50	2004/01/19	3750	24.1	1000	0.721(0.001)	3 - Ia*
04D1ff	02:25:38.599	-04:54:09.30	2004/09/10	3750	23.7	422	0.86(0.01)	5 - Ia
04D1hx	02:24:42.481	-04:47:24.78	2004/09/19	3750	25.8	148	0.560(0.001)	5 - Ia
04D1hk	02:24:46.002	-04:24:03.94	2004/09/21	3750	23.4	172	0.634(0.001)	3 - Ia*
04D1ks	02:24:09.525	-04:58:43.05	2004/10/10	2250	23.3	1920	0.78(0.01)	5 - Ia
04D1ow†	02:26:42.712	-04:18:22.44	2004/11/13	3600	23.8	4837	0.92(0.01)	5 - Ia
04D2al	10:01:52.482	+02:09:51.25	2004/01/25	3750	23.8	175	0.83(0.01)	4 - Ia
04D2an	10:00:52.332	+02:02:28.73	2004/01/21	3750	23.5	2348	0.62(0.01)	5 - Ia
04D2ca	10:01:20.514	+02:20:21.76	2004/03/22	3750	23.8	111	0.83(0.01)	3 - Ia*
04D2cf	10:01:56.110	+01:52:46.40	2004/03/22	3750	22.2	130	0.368(0.001)	5 - Ia
04D2cw	10:01:22.787	+02:11:55.31	2004/03/20	3750	23.7	200	0.568(0.001)	3 - Ia*
04D2fp	09:59:28.162	+02:19:15.58	2004/04/14	3750	22.4	153	0.416(0.001)	5 - Ia
04D2fs	10:00:22.110	+01:45:55.70	2004/04/14	3750	22.2	1015	0.357(0.001)	5 - Ia
04D2gp	09:59:20.400	+02:30:31.88	2004/04/19	3750	23.6	1580	0.71(0.01)	5 - Ia
04D4bk	22:15:07.689	-18:03:37.09	2004/07/11	3750	23.9	3178	0.85(0.02)	3 - Ia*
04D4bq	22:14:49.391	-17:49:39.36	2004/07/15	3750	23.5	1000	0.55(0.01)	5 - Ia
04D4fx	22:16:38.130	-18:03:58.61	2004/08/11	3750	23.7	537	0.629(0.01)	5 - Ia
04D4hf	22:16:57.912	-17:41:13.34	2004/08/20	3750	24.3	1773	0.93(0.01)	3 - Ia*
04D4id	22:16:21.441	-17:13:45.08	2004/09/19	3750	23.5	520	0.77(0.01)	4 - Ia
04D4jr	22:14:14.332	-17:21:01.10	2004/10/11	2250	22.7	3983	0.49(0.01)	5 - Ia

Table 2.10: Observed properties of a sample of SNLS SNe candidates observed during the first year of SNLS operations (at the VLT); November 2003 through November 2004.
a — SNLS candidate name
b — UT date of spectroscopy
c — total exposure time in seconds
d — i'_{AB} at the time of spectroscopy
e — percent increase, in flux, over the host galaxy background in a 1.10" aperture
f — redshift (σ_z in parentheses)
g — SNe confidence index (CI) and estimated object type (see § 2.4.5)
† — this SN was also observed with the Gemini North telescope for the SNLS

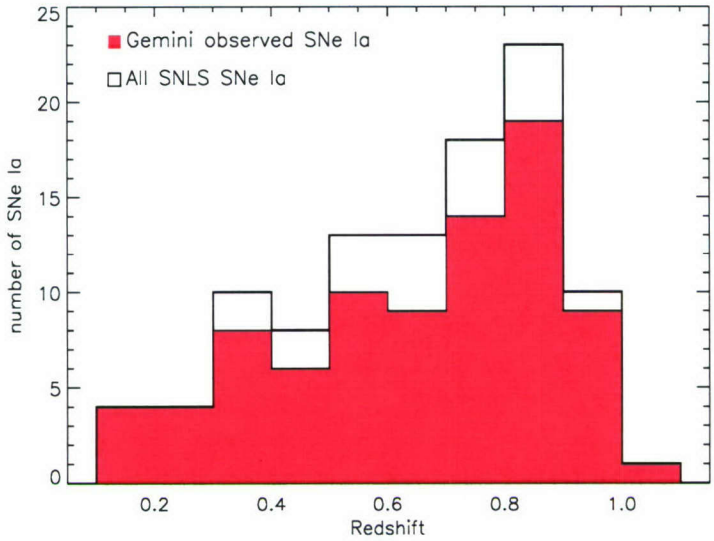

Figure 2.5: The redshift distribution of confirmed Type Ia SNe from the primary (Gemini-observed) and secondary (VLT-observed) data sets. This data includes spectra from 104 high-z SNe Ia ($z_{\rm med} = 0.703$) and is the largest set of distant supernovae to be studied in such detail.

2.6 SNLS — Summary

In total, 124 SNe candidates were observed at the Gemini telescopes from August 2003 through May 2006 for the SNLS. All of these objects were reduced and identified by the author and are displayed in Appendix A. The final redshift estimates and object identifications were reached with a consensus opinion from SNLS collaborators. The complete list of observed properties from these objects can be found in Tables 2.2 — 2.7. The derived properties and object identifications for this primary data set are listed in Table 2.9. Objects from this data set were considered confirmed SNe Ia and selected for further analysis if their final CI was 3 or greater. This mimics the selection of the SNe Ia for the first year SNLS cosmology (Astier *et al.*, 2006) and includes 84 objects at a median redshift of $z = 0.707$. The secondary set of VLT SNe Ia adds an additional 20 confirmed SNe Ia to this sample. The redshift distribution of this large and homogenous high-z sample is shown in Figure 2.5. The median z of the entire sample of 104 SNe Ia is 0.703.

The complete photometric data from SNLS objects is ultimately paired with the object and redshift identifications to produce final, parameterised lightcurves. This work is completed by other SNLS collaborators and is described in detail in Astier *et al.* (2006). The lightcurves are fitted in two or more bands with the SALT lightcurve model (Guy *et al.*, 2005), which returns

the rest frame B' magnitude m_B (at maximum), the lightcurve shape-luminosity parameter s, and a color parameter c that accounts for both intrinsic SN color differences and reddening from dust. These parameters are then used to determine the distance modulus, μ, as in Equation 1.12 during cosmological analysis. The final estimates of the photometric properties for the SNe considered in this thesis are summarised below in Tables 2.11 and 2.12.

SN	m_B^a	μ^b	s^c	c^d
03D1ax	22.95 (0.01)	42.18 (0.03)	0.89 (0.010)	-0.04 (0.02)
03D1cm	24.46 (0.06)	44.09 (0.30)	1.17 (0.06)	-0.03 (0.14)
03D1co	24.09 (0.03)	43.39 (0.08)	0.97 (0.03)	-0.02 (0.04)
03D1ew	24.35 (0.07)	43.87 (0.34)	1.02 (0.04)	-0.1 (0.16)
03D4cn	24.65 (0.05)	43.53 (0.3)	0.74 (0.05)	0.02 (0.15)
03D4cy	24.71 (0.10)	44.55 (0.38)	1.03 (0.05)	-0.3 (0.17)
03D4fd	24.21 (0.02)	43.35 (0.07)	0.91 (0.03)	0.02 (0.04)
03D4gl	23.26 (0.02)	42.46 (0.07)	0.95 (0.03)	0.03 (0.02)
04D2fp	22.52 (0.01)	41.77 (0.02)	0.96 (0.01)	0.00 (0.01)
04D2fs	22.42 (0.01)	41.44 (0.01)	0.94 (0.01)	0.12 (0.00)
04D2gp	24.15 (0.04)	43.23 (0.12)	0.80 (0.01)	-0.05 (0.06)
04D3dd	25.12 (0.19)	44.67 (0.53)	1.08 (0.07)	-0.07 (0.20)
04D3fq	24.12 (0.02)	43.28 (0.07)	0.90 (0.01)	0.00 (0.03)
04D3kr	21.96 (0.01)	41.25 (0.01)	1.06 (0.01)	0.07 (0.01)
04D3ny	24.27 (0.05)	43.69 (0.3)	1.00 (0.08)	-0.06 (0.15)
04D4bk	24.31 (0.03)	43.47 (0.18)	1.04 (0.05)	0.14 (0.09)
04D4bq	23.36 (0.02)	42.48 (0.05)	0.99 (0.02)	0.11 (0.02)
04D4dm	24.39 (0.04)	43.95 (0.26)	1.00 (0.05)	-0.16 (0.15)

Table 2.11: The final photometric properties of the confirmed SNe Ia from the first year of SNLS observations that are discussed in this thesis. These values were initially presented in Astier *et al.* (2006) and are re-printed here as they will be used in the discussion of SNe cosmology in § 4.5.
a — rest-frame B' magnitude at maximum luminosity, computed from lightcurve fits (Sullivan, 2006c)
b — distance modulus, computed with $H_0 = 70.0$ km/s Mpc^{-1} [see (Astier *et al.*, 2006) and Eq. 1.12]
c — lightcurve shape-luminosity *stretch* parameter, see Astier *et al.* (2006) and Guy *et al.* (2005)
d — color parameter; accounts for both host reddening and intrinsic SNe color differences, computed using SALT (Guy *et al.*, 2005)

2.7 Additional Supernovae Spectra

2.7.1 High Redshift Spectra

Additional high-z SNe Ia spectra from the ESSENCE and SCP surveys were also used to investigate the homogeneity of distant SNe. These data sets were analysed as published and

SN	m_B^a	SN	m_B^a
03D1bk	24.17 (0.04)	05D1kl	24.16 (0.01)
04D1de	24.12 (0.02)	05D2ab	22.00 (0.01)
04D1hd	22.15 (0.01)	05D2ah	20.76 (0.01)
04D1hy	24.19 (0.02)	05D2ck	24.44 (0.03)
04D1ow	24.23 (0.04)	05D3cx	23.78 (0.02)
04D2ae	24.33 (0.04)	05D3lb	23.85 (0.01)
04D2mh	23.44 (0.01)	05D3mh	24.02 (0.01)
04D3mk	24.33 (0.02)	05D3mn	24.01 (0.01)
04D4hu	23.87 (0.01)	05D3mq	21.47 (0.01)
04D4ic	24.15 (0.03)	05D4av	23.56 (0.01)
04D4ii	24.19 (0.03)	05D4bm	22.18 (0.01)
05D1az	24.13 (0.02)	05D4cn	24.05 (0.01)
05D1em	24.24 (0.01)	05D4dy	24.53 (0.01)
05D1er	24.52 (0.03)	05D4gw	24.40 (0.02)
05D1ju	24.55 (0.02)		

Table 2.12: The computed B' peak magnitudes of SNe Ia observed with the SNLS that were not presented in Astier *et al.* (2006). These values were estimated with the final parameterised lightcurve fits by SNLS collaborators at the University of Toronto. They are unpublished and should be considered as 'preliminary' values only.
a — rest-frame B' magnitude at maximum luminosity, computed from lightcurve fits (Sullivan, 2006c).

thus make up a tertiary set of data for this thesis; the reader is directed to the source papers for details of the acquisition, reduction, and identification of these spectra. Including these spectra ensures that the entire data set studied in this thesis closely matches the entire catalog of Type Ia surveys on which the evidence for the accelerating universe is based. Because of the observation and reduction differences between these data sets and the primary set of SNLS data, only objects with the most confident z and object identifications were used. The histogram in Figure 2.6 illustrates the redshift distribution of these objects, which compliments the higher-z SNLS data. A short summary of the objects included from ESSENCE and SCP is displayed in Table 2.13. The observed and calibrated properties from these objects can be found in Perlmutter *et al.* (1999); Hook *et al.* (2005) (for SCP) and Matheson *et al.* (2005); Blondin *et al.* (2006) (for ESSENCE). To reiterate, every step of the observation, reduction, and analysis of these objects was completed by the authors listed in these source papers. The following sections give a brief summary of the observation, reduction, and object identification techniques of these additional surveys.

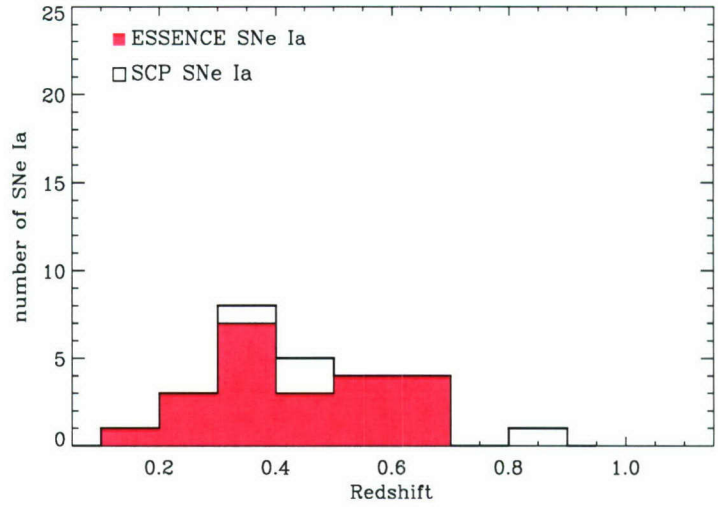

Figure 2.6: The redshift distribution of confirmed Type Ia SNe from the tertiary data set of SCP and ESSENCE spectra. The scale of this figure is the same as Fig. 2.5. Note that this data peaks at a lower redshift than the SNLS data sets in Figure 2.5. The combination of these data sets provides more complete sampling of SNe Ia at intermediate redshifts.

2.7.1.1 SCP Data

A total of 4 spectra, discovered by the SCP and with a median redshift of $z = 0.43$, were analysed for this thesis. These objects are a subset of the SNe discovered by the SCP during search campaigns in January and March 1997 [see Hook *et al.* (2005) for full details]. After being discovered in r' images from two searches on the CTIO 4m Blanco telescope, spectra of these objects were obtained during observing runs at the Keck-II 10m telescope with the LRIS spectrograph (Oke *et al.*, 1995). The 300 l/mm grating was used with the Cassegrain focus to cover a wavelength range of 5000 Å to 10000 Å with a dispersion of approximately 2.5 Å per pixel. The exposure times of these observations were in the range of 0.5 to 1.5 hours. These spectra were reduced with the IRAF spectral reduction package. The classification of these objects was done with a χ^2 matching program similar to that employed on the SNLS spectra. For a few of these objects, the angular distance between the supernova and its host galaxy was enough to enable a separate extraction of their respective spectra, but in other cases the published spectrum contains both host and supernova flux. This host flux presents an additional source of error that, unlike in the primary SNLS data set, the author did not attempt to quantify. The 8 least contaminated objects (out of a published set of 14) were

Name	z^a	effective date(s)[b]	source
1997ac	0.33	9	Perlmutter *et al.* (1999); Hook *et al.* (2005)
1997ai	0.45	5	Perlmutter *et al.* (1999); Hook *et al.* (2005)
1997am	0.416	10	Perlmutter *et al.* (1999); Hook *et al.* (2005)
1997ap	0.83	-2	Perlmutter *et al.* (1999); Hook *et al.* (2005)
2002iz	0.428	-1,19	Matheson *et al.* (2005); Blondin *et al.* (2006)
2002ja	0.33	2	Matheson *et al.* (2005); Blondin *et al.* (2006)
2002jb	0.25	-7	Matheson *et al.* (2005); Blondin *et al.* (2006)
2002js	0.54	7	Matheson *et al.* (2005); Blondin *et al.* (2006)
2002jd	0.32	-3,16,18	Matheson *et al.* (2005); Blondin *et al.* (2006)
2002jt	0.56	0	Matheson *et al.* (2005); Blondin *et al.* (2006)
2002jw	0.36	-2,19	Matheson *et al.* (2005); Blondin *et al.* (2006)
2003jo	0.53	3	Matheson *et al.* (2005); Blondin *et al.* (2006)
2003ju	0.20	-8,18	Matheson *et al.* (2005); Blondin *et al.* (2006)
2003jv	0.41	-2	Matheson *et al.* (2005); Blondin *et al.* (2006)
2003js	0.363	-5	Matheson *et al.* (2005); Blondin *et al.* (2006)
2003jw	0.296	-6	Matheson *et al.* (2005); Blondin *et al.* (2006)
2003jy	0.339	-10	Matheson *et al.* (2005); Blondin *et al.* (2006)
2003kk	0.164	-4	Matheson *et al.* (2005); Blondin *et al.* (2006)
2003kl	0.335	-3,0	Matheson *et al.* (2005); Blondin *et al.* (2006)
2003km	0.47	-12,-11	Matheson *et al.* (2005); Blondin *et al.* (2006)
2003ko	0.360	-2	Matheson *et al.* (2005); Blondin *et al.* (2006)
2003kt	0.61	4	Matheson *et al.* (2005); Blondin *et al.* (2006)
2003kq	0.62	-3	Matheson *et al.* (2005); Blondin *et al.* (2006)
2003kp	0.64	1	Matheson *et al.* (2005); Blondin *et al.* (2006)
2003le	0.56	-1	Matheson *et al.* (2005); Blondin *et al.* (2006)
2003ln	0.63	4	Matheson *et al.* (2005); Blondin *et al.* (2006)

Table 2.13: A summary of the spectra in the tertiary set of high-z SNe Ia. Only the details relevant to the analysis in this thesis are presented here.

a — as in Table 2.9, redshifts determined by host galaxy features are quoted to an accuracy of ± 0.001 while those determined from spectral template matches are quoted to an accuracy of ± 0.01
b — date relative to maximum luminosity (rest frame B', rounded off to the nearest day; the error on these values is (approximately) ± 1.0 days.

selected for this analysis.

The selection of these objects was straightforward. Objects that were separated at a large enough distance from their host to enable the extraction of two separate signals, or, had no identifiable host galaxy features, and were definitely classified as SNe Ia, were clear candidates for further analysis. This included the objects SN 1997ac, SN 1997ai, SN 1997am, and SN 1997ap. The other objects that were classified as SNe Ia from this sample were contaminated with various amounts of host flux as evidenced by narrow host features. The amount of contamination in these objects was not estimated and they were not considered for any additional

analysis here.

2.7.1.2 ESSENCE Data

The supernovae analysed from the ESSENCE project were published in Matheson *et al.* (2005). For this survey, potential Type Ia targets were selected from a large set of transient objects observed with the CTIO Blanco 4m telescope. Spectroscopic images were taken of the most likely SNe Ia candidates at a wide variety of telescopes, including the Keck I and II 10m telescopes; the 8m Very Large Telescope; the Gemini North and South 8m Observatories; the Magellan Baade and Clay 6.5m telescopes; the MMT 6.5m telescope; and the Tillinghast 1.5m telescope at the F.L. Whipple Observatory. The spectrographs used at these instruments are LRIS (Oke *et al.*, 1995) and ESI (Sheinis *et al.*, 2002), FORS1 (Appenzeller *et al.*, 1998), GMOS (Hook *et al.*, 2004), IMACS (Dressler, 2004), LDSS2 (Mulchaey, 2001), the Blue Channel (Schmidt *et al.*, 1989), and FAST (Fabricant *et al.*, 1998), respectively. These spectroscopic images were reduced with standard IRAF procedures, utilizing the optimal extraction algorithm of Horne (1986). This procedure was slightly different for the ESSENCE SNe candidates observed with the VLT, which were extracted with a method [presented by Blondin, Walsh, Leibundgut, & Sainton (2005)] based on Richardson-Lucy restoration.

The spectra were classified with a consensus opinion by the ESSENCE observers. This estimation was then assisted with automated comparisons, such as a spectral feature aging routine (Riess *et al.*, 1997) or SNe template comparisons with the SuperNova IDentification algorithm (SNID, Tonry et al. *in prep.*). A portion of the identified SNe Ia presented in Matheson *et al.* (2005) were studied by Blondin *et al.* (2006) (B06, hereafter). The B06 data set gives updated epoch information on these objects, based on light-curve fits (Prieto, Rest, & Suntzeff, 2006), that is more precise than the SNID dates given in Table 2 of Matheson *et al.* (2005). The increased precision of the epoch information is key to interpreting the results of the quantitative spectroscopic measurements presented in this thesis, so the B06 subset was used to determine which objects from Matheson *et al.* (2005) to include in this study. The issue of host galaxy contamination was not addressed in B06, as the authors 'did not have a reliable way of evaluating' this uncertainty. This error source was minimised by the 2D deconvolution extraction methods used for the VLT-observed objects in this set (Blondin,

Walsh, Leibundgut, & Sainton, 2005). A handful of these objects did exhibit some of the narrow emission and absorption features from their host galaxies and were removed from the high-z data as the total contamination is uncertain. The remaining VLT spectra from the published ESSENCE data in B06, with the updated lightcurve fits and reduced host contamination, were considered precise enough to be included in this high-z analysis. This set adds 22 SNe Ia at a median redshift of $z = 0.41$ to the large sample considered here. The author also tested the 2D deconvolution extraction method on the SNLS Gemini data. Due to the higher redshifts (and thus smaller angular separation and increased blending between the SNe and their hosts) of the SNLS objects, no significant difference was found in the limiting cases where the usual extraction method used on the SNLS spectra observed at Gemini was not optimal.

The combination of data from the 1°, 2° and 3° data sets includes 138 spectra from 130 different high-z Type Ia supernovae.

2.7.2 Low Redshift Spectra

The spectra that make up the low redshift sample in this study were selected from published sources and a majority of these spectra can be found on the online Supernova Spectrum Archive (SUSPECT, `http://bruford.nhn.ou.edu/suspect/index1.html`). The main goal of this study is to quantify the similarities and differences between high-z SNe Ia and those discovered locally, so objects with epoch and wavelength coverage that approximated the distant population of SNe Ia observed by the SNLS were selected. The spectra from different sources are available in various states of reduction and calibration. These spectra were also corrected for peculiar velocities and redshift where appropriate. All of the low-z objects that met this criteria are listed below in Table 2.14. This low-z sample includes data from 24 different objects with a total of 167 spectra.

2.7.2.1 Low Redshift Spectra — Photometric Properties

The 24 nearby Type Ia supernovae analysed in this thesis have all been observed and reduced by different survey teams. The source papers listed in Table 2.14 provide complete information on these objects. The observed properties of some of these nearby objects have previously been discussed in the literature (Perlmutter *et al.*, 1999; Phillips *et al.*, 1999; Altavilla *et al.*, 2004;

Name	effective date(s)	source
1981B	0,20	Branch et al. 1983
1986G	-5,-4,-3,0	Phillips et al. 1987
1989B	-7,-5,-3,-2,-1,3,5,8,9,11,12,13,16,17,18,19	Barbon et al. 1990, Wells et al. 1994
1990N	-14,-7,2,3,17	Mazzali et al. 1993
1991M	3	Gomez & Lopez 1998
1991T	-12,-11,-10,-8,-7,-6,0,10,15	Mazzali, Danziger, & Turatto 1995
1991bg	0,1,2	Turatto et al. 1996
1992A	-5,-1,3,5,6,7,9,11,16,17	Kirshner et al. 1993
1994D	-11,-10,-9,-8,-7,-5,-4,-2,2,4,10,11,12,13,20	Patat et al. 1996
1994Q	10	Gomez & Lopez 1998
1996X	-2,-1,0,1,2,7	Salvo et al. 2001
1997br	-9,-8,-7,-6,-4,8	Li et al. 1999
1997cn	3	Turatto et al. 1998
1998aq	-8,0,1,2,3,4,5,6,7	Branch et al. 2003
1998bu	-4,-3,-2,8,9,10,11,12,13	Capellaro et al. 2001
1999aa	-11,-3,-1,5,6	Garavini et al. 2004
1999ac	-15,-9,0,2,8,11	Garavini et al. 2004
1999aw	3,5,5,12	Strolger et al. 2002
1999by	-5,-4,-3,-2,3,4,5,6,7,8,11	Garnavich et al. 2004
1999ee	-11,-9,-8,-6,-4,-2,-1,0,3,5,7,8,9,12,14	Hamuy et al. 2002
2000E	-2,3,5,14	Valentini et al. 2003
2000cx	-4,-3,-2,-1,0,1,5,6,7,9,11	Li et al. 2001
2002bo	-14,-13,-11,-7,-6,-5,-4,-3,-2,-1,4	Benetti et al. 2004
2003du	-11,-7,13	Anupama, Sahu, & Jose 2005

Table 2.14: The low redshift spectra analysed in this thesis. The effective dates correspond to the epoch relative to maximum luminosity in the B'. The source papers for these spectra are printed in the far right column, and many are reproduced in the SUSPECT archive.

Reindl *et al.*, 2005) with slightly different results depending on the color corrections or lightcurve fits to the published photometry. To remove any systematic differences from comparing results across publications and surveys, the photometry from these supernovae was re-fitted, within the SNLS collaboration (by A. Conley), to derive the magnitudes and lightcurve shape parameters used in this analysis. These values, summarised in the first 5 columns of Table 2.15, were used when analyzing these spectra for this thesis. These parameters were derived using a template spectrum derived by A. Conley and the Cohen (2003) realization of the Landolt filters.

These re-derived photometric properties were also used to estimate the absolute peak (B') magnitudes, $M_{\mathrm{B_{peak}}}$, of these low-z SNe Ia. A new estimate of these magnitudes is of interest as the published values have (in general) already been corrected for a derived lightcurve shape-luminosity correction. In order to fully explore the homogeneity of SNe at different redshifts,

and to investige any possible spectroscopic sequences in SNe Ia (see § 1.4), an uncorrected $M_{\mathrm{B_{peak}}}$ is desired. To make this estimation, the observed magnitudes from Table 2.15 were first corrected for host galaxy reddening using the Phillips *et al.* (1999) relation. Note that in order to make the reddening estimate, the $\Delta_{m_{15}}(B)$ value is required. This is the only part of the estimate that made use of a SNe Ia lightcurve shape-luminsosity correction and is unavoidable as it provides the most accurate way of estimating effects of host extinction on these SNe Ia magnitudes. The host reddening was then converted to a B' extinction with $R_{\mathrm{B}} = 3.0$, which is approximately the median value of the different R_{B} estimates for SNe Ia in the literature. Next, the distance modulus, μ, to the host galaxy was used to convert to an absolute magnitude via $\mu = m - M$ (where m and M are the observed and absolute magnitudes, respectively). To yield the most correct distance modulus, the author researched the literature for the most reliable cepheid variable-based distances to the host galaxies of these SNe. These distances were available for 9 of the SNe in Table 2.15. Another 5 low-z SNe had reliable host distances from the *Nearby Galaxies Catalogue* (Tully, 1988). The remaining SNe did not have any independent distance constraints and were not considered for these M_{B} estimates. The errors at each of these steps were propagated through this estimate and used to provide a final error on M_{B}. The final column in Table 2.15 lists these M_{B} values for the 14 low-z SNe that had reliable, independent distance estimates and secure observed photometric properties. The errors on these estimates and the source for the independent μ values are displayed in this column as well.

2.8 Supernovae Data Sets — Conclusion

This chapter summarised the observation, reduction, and identification of a large set of distant and nearby SNe Ia spectra from 154 different objects. The combination of data from the 1°, 2° and 3° data sets includes 138 spectra from 130 different high-z Type Ia supernovae and the low-z data is comprised of 167 spectra from 24 different SNe Ia. The reduction and identification of 84 of these SNe was completed by the author for the SNLS. These spectra were all studied utilising methods tailored to the limited S/N of the high-z SNe in order to make a quantitative comparison of the spectroscopic features of SNe Ia at different redshifts and host environments. This comparison tests the assumption that the high-z SNe do form a

Name	z	MJD^{a}_{max}	m^{b}_{B}	$(B-V)^{c}_{max}$	s^{d}	M^{e}_{b}
1981b	0.0060	44671.84(0.09)	11.83(0.01)	-0.06(0.01)	0.95(0.01)	-19.58(0.22)[1]
1986g	0.0027	46560.53(0.05)	11.91(0.01)	0.83(0.01)	0.73(0.01)	...
1989b	0.0024	47564.39(0.27)	12.12(0.02)	0.30(0.02)	0.94(0.01)	-19.03(0.31)[1]
1990n	0.0034	48081.92(0.03)	12.53(0.01)	-0.09(0.01)	1.07(0.01)	-19.59(0.23)[1]
1991M	0.0072	...	...	...	...	...
1991t	0.0060	48374.25(0.04)	11.30(0.01)	-0.04(0.01)	1.05(0.01)	-20.07(0.27)[2]
1991bg	0.0030	48604.50(1.0)	14.75(0.04)	0.00(0.08)	.68(0.10)	...
1992a	0.0063	48639.71(0.02)	12.41(0.01)	-0.09(0.01)	0.85(0.01)	-18.73(0.22)[7]
1994d	0.0015	49431.41(0.01)	11.64(0.01)	-0.19(0.01)	0.84(0.01)	-19.44(0.22)[7]
1994q	0.0294	49494.35(0.90)	16.16(0.09)	-0.14(0.04	1.11(0.04)	...
1996x	0.0070	50190.65(0.10)	12.86(0.01)	-0.12(0.01)	0.90(0.01)	-19.38(0.22)[7]
1997br	0.0053	50558.57(0.03)	13.23(0.02)	0.12(0.01)	0.89(0.01)	...
1997cn	0.0162	50593.36(0.32)	18.12(0.02)	0.92(0.01)	0.89(0.02)	...
1998aq	0.0037	50930.16(0.02)	12.18(0.01)	-0.25(0.01)	0.98(0.01)	-19.87(0.23)[6]
1998bu	0.0030	50951.89(0.04)	11.97(0.01)	0.15(0.01)	0.99(0.01)	-19.18(0.26)[1]
1999aa	0.0144	51231.82(0.03)	14.59(0.01)	-0.18(0.01)	1.12(0.01)	...
1999ac	0.0095	51250.07(0.08)	13.99(0.01)	-0.08(0.01)	1.02(0.01)	...
1999aw	0.0380	51253.34(0.08)	16.59(0.01)	-0.17(0.01)	1.22(0.01)	...
1999ee	0.0114	51468.89(0.01)	14.69(0.01)	0.11(0.01)	1.05(0.01)	-19.70(0.30)[3]
2000e	0.0047	51576.44(0.03)	12.68 (0.01)	0.01(0.01)	1.03(0.01)	-20.08(0.25)[7]
2000cx†	0.0079	51752.03(0.03)	12.92(0.01)	-0.09(0.01)	0.91(0.01)	-19.44(0.44)[4]
2002bo	0.0042	52356.43(0.04)	13.82(0.01)	0.29(0.01)	0.95(0.01)	-19.04(0.46)[7]
2003du	0.0064	52766.22(0.19)	13.36(0.01)	-0.25(0.01)	1.02(0.01)	-19.53(0.45)[5]

Table 2.15: The photometric properties of the low-z spectra analysed in this thesis. The published photometry from these objects was analysed within the SNLS (A. Conley) to determine the magnitudes and lightcurve shape parameters shown here. SN 1991M did not have published photometry in B', so the parameters for this object were not determined. Also, the SNLS models did not fit the sub-luminous SN 1991bg with any accuracy (A. Conley); the values printed here for this unusual object are from Altavilla *et al.* (2004). The absolute magnitudes shown in the last column have been estimated by the author (see § 2.7.2.1).

a — date of maximum luminosity (rest-frame B')
b — maximum apparent magnitude in rest-frame B', corrected for Milky Way extinction with E(B-V) values from Schlegel et al. (1998)
c — $B-V$ color at (B') maximum luminosity
d — s values (which normalise the lightcurve shape-luminosity relation for SNe Ia), based on a fiducial $s=1.0$ Type Ia template (A. Conley)
e — absolute peak luminosities (B'), **not** adjusted for lightcurve shape-luminosity corrections — see § Section 2.7.2.1 for details. DISTANCE MODULUS SOURCES — 1: Gibson *et al.* (2000) 2: Saha *et al.* (2001) 3: Stritzinger *et al.* (2002) 4: Candia *et al.* (2003) 5: Anupama, Sahu, & Jose (2005) 6: Riess *et al.* (2005) 7: Tully (1988)
† — Note that the derived color and magnitude values for SN 2000cx are very uncertain as the spectroscopic and photometric behaviour for this unusual object was poorly described by the usual methods used to parameterise SNe Ia

homogenous class of objects with those observed locally. The methods for this analysis and the results of these measurements are presented in the following Chapter.

Chapter 3

Quantitative Spectroscopy of Nearby and Distant Type Ia Supernovae

3.1 Limitations on Analysis of High-z Spectra

The necessity of comparing the SNe observed by low and high redshift surveys was established in the introduction to this thesis (§ 1.5). However, the majority of the published low-z SNe Ia spectroscopic studies use methods that are inadequate for this comparison because of the limitations on data obtained at high-z. One such limitation is the reduced S/N of the spectra observed at higher redshifts, which is due to the smaller amount of flux received by these objects over a set observation time. This could be overcome by appropriately increasing the exposure times, but telescope availability and the large number of objects that need to be observed by ambitious surveys (such as the SNLS) set a reasonable upper limit on the S/N of distant SNe. This means that comparisons of high-z spectra to detailed synthetic models (see § 1.4) are not feasible and only the most coarse measurements are possible with any accuracy. Similarly, the large distances to these objects means that features toward the red end of their optical spectra are redshifted to regions dominated by noise from the sky background. Overcoming this noise would require even more exaggerated exposure times and observations in the infrared. Measurements in this redder wavelength range [such as the $\Re\{\mathrm{SiII}\}$ parameter (Nugent *et al.*,

1995a) or the EW measurements from Branch *et al.* (2006) and Hachinger, Mazzali, & Benetti (2006)] are thus not practical for the majority of high-z data.

Another restraint imposed by the cosmological goals of most high-z surveys is the epoch coverage of the observations of SNe candidates. To maximise the number of objects spectroscopically confirmed as SNe Ia, these surveys observe SN candidates (in general) only once. Supernova spectra are a complex expression of the physical state of the photosphere that is highly dependent on epoch (§ 1.2). This single epoch of observation thus bars any investigation into the evolution of these features as measurements made at one particular epoch cannot be extrapolated to other times with any certainty. Due to this constraint, the spectroscopic parameters that are defined at one specific epoch [e.g.,Wells *et al.* (1994); Nugent *et al.* (1995a)], or that are defined by the change in parameters over time [e.g., F04, Benetti *et al.* (2005); Hachinger, Mazzali, & Benetti (2006)] cannot be studied in high redshift spectra.

Some successful comparisons have been made between SNe Ia spectra at high and low redshifts. Coil *et al.* (2000) visually compared two high-z spectra to low-z SNe Ia while Balland *et al.* (2006); Hook *et al.* (2005) and B06 compared $v_{\rm ej}$ measurements from a few dozen high-z SNe to nearby objects. The extent of the analysis presented in these publications and the number of objects used in these studies will be significantly improved upon in this thesis. In order to quantitatively study the homogeneity of SNe Ia at different redshifts, specific measurements that are robust to these limitations are required. This thesis addresses this issue with equivalent width and ejection velocity measurements.

3.1.1 Quantitative Spectroscopy — Equivalent Widths

F04 defined a method of measuring equivalent widths for absorption regions of specific importance to SNe Ia spectra. These measurements are essentially a shape-independent method of quantifying the strength of these features. These measurements are also fairly coarse so they can be made at a large range of S/N levels. The effects of the reddening differences between these objects will also be minimal as the supernova absorption features cover a relatively small wavelength range with regards to these effects. This EW measurement is thus useful in investigating any differences in SNe observed over a wide range of distances and instrument setups. F04 defined eight regions that contain the strongest absorption features observed in core nor-

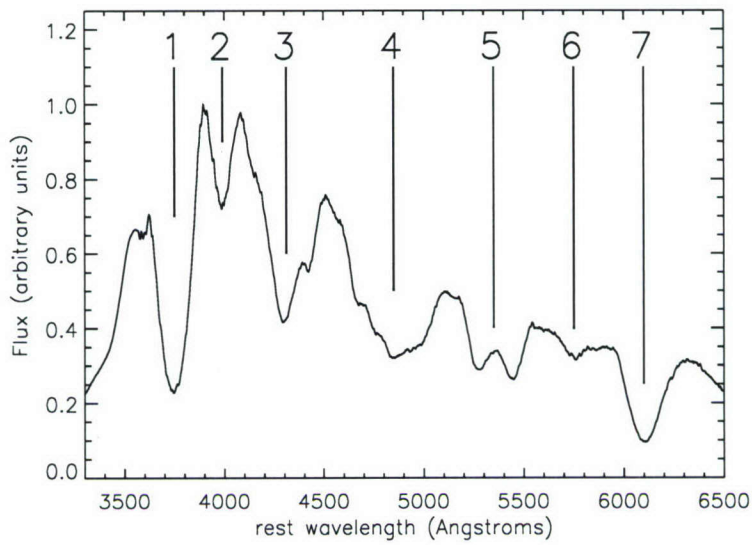

Feature #	Label	Blue-ward Limit (Å)	Red-ward Limit (Å)
1	'CaII H&K'	3500 - 3800	3900 - 4100
2	'SiII 4000'	3900 - 4000	4000 - 4150
3	'MgII'	3900 - 4150	4450 - 4700
4	'FeII'	4500 - 4700	5050 - 5550
5	'SII W'	5150 - 5300	5500 - 5700
6	'SiII 5800'	5550 - 5700	5800 - 6000
7	'SiII 6150'	5800 - 6000	6200 - 6600

Figure 3.1: The spectroscopic regions of specific interest to SNe Ia EW measurements, as defined by F04 and shown here on a core normal SN Ia near maximum light. The specific wavelength range and nomenclature for these features is summarised in the chart above.

mal SNe Ia spectra near maximum luminosity. The first seven regions, and the nomenclature used to describe them, are defined in Figure 3.1. The F04 nomenclature is used throughout this thesis. Note that this naming scheme corresponds to the ion that is thought to contribute most to the absorption in each respective wavelength region. In reality, all of these doppler-broadened features are formed from contributions of various ions; the F04 terminology is thus a straightforward way of standardising the measurement, comparison, and discussion of these spectroscopic trends.

For supernovae, the continuum needed to make the EW measurement is not well defined, so here it is estimated by making a straight line fit between the local maxima that bound each feature (F04). The following rules govern how the continuum is set:

- the pseudo-continuum is always set within the feature regions listed in Figure 3.1
- the maxima are selected to maximise the wavelength span of the measurement without intersecting the boundaries of any neighboring features
- the EW is always calculated in the rest frame

The continuum is set automatically by EW measurement programs written by the author for this study, but the user makes a final judgement on its placement to ensure that the guidelines listed above are followed. The EW is then calculated by numerically integrating underneath this 'pseudo-continuum' at every wavelength pixel $\lambda_{\rm i}$ (for all N points within the set continuum bounds)

$$EW = \sum_{\rm i=1}^{\rm N} \left(1 - \frac{f_\lambda(\lambda_{\rm i})}{f_c(\lambda_{\rm i})}\right) \Delta\lambda_{\rm i}, \tag{3.1}$$

where f_λ is the flux level of the spectrum, and f_c is the flux of the pseudo-continuum. An example EW measurement of the broad feature attributed (primarily) to CaII H&K is illustrated in Figure 3.2. The statistical uncertainty in the EW measurement is calculated by propagating the estimated uncertainties in the flux and pseudo-continuum:

$$\sigma^2_{EW} = \sum_{\rm i=1}^{\rm N} \left(\{\frac{\sigma_f(\lambda_{\rm i})}{f_c(\lambda_{\rm i})}\}^2 + \{\frac{f_\lambda(\lambda_{\rm i})}{f_c(\lambda_{\rm i})^2}\}^2 \cdot \sigma^2_{c_{\rm i}}\right) \Delta\lambda^2_{\rm i}, \tag{3.2}$$

here σ_f is the measurement uncertainty in the flux and $\sigma_{c_{\rm i}}$ is the uncertainty in the pseudo-continuum flux. The σ_{c_i} is calculated via the propagation of the correlated errors in the selection and calculation of this continuum.

In addition to the error defined in Eq. 3.2, uncertainties can be caused by variations in the extent or the slope of the pseudo-continuum. Although these errors were minimised by making the most consistent measurements in every case (see the rules outlined above), this particular measurement is still at the discretion of the observer. The range and effects of these pseudo-continuum variations were estimated by randomly shifting the continuum boundaries within $\frac{R}{4}$ Å of the selected maxima (where R is the range of the feature boundaries, see the chart in Fig. 3.1) for the feature and spectrum in question. The EW was then re-measured, and the standard deviation of these measurements (which were repeated 50 times) was accepted as an

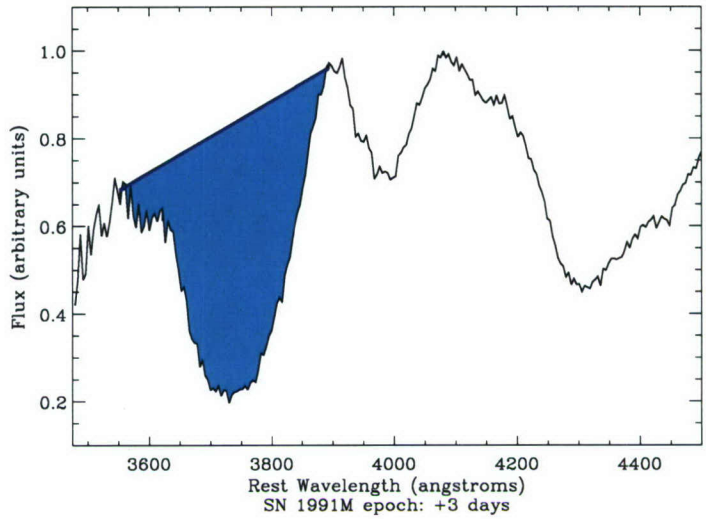

Figure 3.2: An example EW measurement on the absorption feature attributed to CaII H&K in a low-z SN spectrum. The pseudo-continuum has been set (within the bounds listed in Fig. 3.1) by the peak of local maxima around the feature in question. The EW is next calculated via Eq. 3.1 by numerically integrating at every point within these pseudo-continuum boundaries. This is the type of measurement that is possible on SNe Ia spectra at all S/N levels and is well-suited for quantifying spectroscopic features in high-z data.

approximation of this error in each EW measurement. For the high S/N spectra, the possible variations in the continuum were found to be the dominant source of error. The uncertainty in spectra with lower S/N (in general) had equal contributions from the error in possible psuedo-continuum variations and the computed error in Eq. 3.2. The high-z data was also subject to some systematic errors, so this general procedure had to be amended for these objects. These measurement techniques are described in more detail in § 3.2.1 and § 3.3.1 for the low-z and high-z data sets, respectively.

3.1.2 Quantitative Spectroscopy — CaII H&K Ejection Velocity

The distribution of the IME in the homologously expanding SN photosphere and the kinetic energy from the thermonuclear explosion are expressed in the ejection velocities measured in the SN spectrum. Measurements of the ejection velocities of the features attributed to CaII H&K, SII λ5640 and SiII λ6150 (EW features 2, 5, and 7 in this thesis, respectively) have previously been studied in both nearby (Branch *et al.*, 1988; Wells *et al.*, 1994; Fisher *et al.*, 1995; Mazzali *et al.*, 1998; Benetti *et al.*, 2005; Mazzali *et al.*, 2005) and high redshift (Blondin *et al.*, 2006; Hook *et al.*, 2005; Balland *et al.*, 2006; Garavini *et al.*, 2006) SN Ia spectra. The

kinetic energy probed by these measurements has also been shown to be connected to the peak luminosity of these objects (Wells *et al.*, 1994; Mazzali *et al.*, 1998). The redshifts of the distant objects that make up the bulk of the SNLS sample mean that the SII (near 5640 Å) and SiII (near 6150 Å) are generally not observed, so only the CaII H&K feature was studied. As with the EW analysis, these velocity measurements are available across data sets and are robust at the reduced S/N of high-z spectra.

The ejection velocity, $v_{\rm ej}$, was calculated as the blueshift of the minimum of the feature away from an estimated rest wavelength of 3945.0 Å (a weighted average of the two components of the CaII H&K feature). The contribution of other ions to the absorption in the wavelength range spanned by CaII H&K (most notably SiII), as well the intrinsic distribution of CaII in velocity space, can give this feature a 'kinked' shape with two possible minima. This shape makes it difficult to determine where the mininum of the feature is located. This difficulty is compounded by the S/N of the high-z objects, which obscure the minimum even further. To make a consistent measurement for all SNe, the minimum was located by fitting the entire feature with a Gaussian model. A linear component, determined by the slope of the pseudo-continuum fit for the EW{CaII H&K} measurement, was added to this Gaussian model to more accurately reflect the shape of this feature. This fit was weighted to the most dominant region of the absorption feature by making initial Gaussian fits within a restricted range (typically ± 25.0 Å) to the deepest, (and most often) bluest, part of the feature. The best fit parameters from this intial fit were then used as starting values for a final fit made to the entire absorption trough.

These best fits were estimated with robust non-linear least-squares fitting calculations made with the MPFIT routines (available for the IDL programming language courtesy of Craig B. Markwardt at `http://cow.physics.wisc.edu/~craigm/idl/`). The location of the minimum of the final fit, $\lambda_{\rm m}$, determined from the MPFIT routines was used to calculate $v_{\rm ej}$ as

$$v_{\rm ej} = -c \cdot \left(\frac{(\frac{\lambda_{\rm m}-\lambda_0}{\lambda_0}+1)^2 - 1}{(\frac{\lambda_{\rm m}-\lambda_0}{\lambda_0}+1)^2 + 1} \right), \tag{3.3}$$

where λ_0 is 3945.0 Å and c is the speed of light. This equation takes into account any relativistic effects at these high velocities. The uncertainties in each object's redshift were propagated through Equation 3.3 to estimate the statistical error in this calculation. The difference between

the calculated velocities from the initial and final fits was used to estimate the additional error in v_{ej} caused by the uncertainty in the selection of the appropriate minimum for this feature. As with the EW measurements, the vast differences in S/N among the objects of this study meant that some smoothing was necessary to ensure the most consistent measurements were made between the multiple data sets. The smoothing techniques and possible systematic effects are discussed in § 3.3.5.

3.2 Analysis of Low Redshift Type Ia SNe

In the previous section, two measurements were defined that can be made on high-z spectra to quantify the diversity and homogeneity of SNe Ia from different redshifts. This analysis was first carried out on the large set of low-z SNe Ia spectra that were collected for this thesis (see § 2.7.2 and Table 2.14). This set includes 167 spectra from 24 different supernovae at epochs similar to those observed by the SNLS and other high-z surveys (from day -14 to 20), relative to B' peak magnitude. These low-z results can then be compared to the same measurements on the high-z data as a preliminary, but quantitative, check for evolution.

3.2.1 Low-z Type Ia SNe — Equivalent Width Measurements

The S/N of the objects from the low-z set was high enough that the selection of the pseudo-continuum boundaries was completed as defined in § 3.1.1. Any possible effects from noise fluctuations were mitigated by setting the pseudo-continuum end-points to an average flux value that was computed over a 25 Å window around the selected maxima. An example measurement is displayed in Figure 3.2. Observed error spectra were not available for most of the objects in this nearby sample, so the uncertainty in Eq. 3.2 could not be calculated. The dominant error from the range of possible pseudo-continuum variations was estimated by randomly varying the local maxima (see § 3.1.1). This measurement technique differs slightly from previously published EW studies [F04, Hachinger, Mazzali, & Benetti (2006); Branch *et al.* (2006); Garavini *et al.* (2006)], as other observers have determined the pseudo-continuum bounds with polynomial fits to the local maxima or by re-binning the spectra. The results here are in very good agreement with these other sources. Based on the wavelength coverage available in the high-z spectra, this EW analysis is focused on EW features 1, 2, and 3 - CaII

H&K, SiII 4000, and MgII in the F04 nomenclature (EW{CaII}, EW{SiII}, & EW{MgII} hereafter).

3.2.2 Low-z Type Ia SNe — Equivalent Width Results

The results of the low-z EW measurements are listed for each spectrum in Table 3.1. These results are also plotted against rest-frame epoch (relative to B' maximum light) and displayed in Figure 3.3. A comparison between EW and epoch is the best way to study these results due to the epoch sensitivity of these measurements. Additionally, comparisons of SNe from surveys with different epoch coverage can be viewed in this parameter space only. The mean trend (and 1σ deviation) exhibited by normal SNe Ia is shown on these figures as well. This trend was derived by making EW measurements on a template core normal Type Ia SN spectrum from Nugent, Kim, & Perlmutter (2002). This template spectrum was made by combining a number of core normal spectra into a single 'grid' of flux as a function of wavelength and time for an $s \approx 1.0$ SN Ia (Nugent, Kim, & Perlmutter, 2002). The error contours on this trend were then derived by estimating the amount of error necessary for the set of low-z core normal measurements to fit this trend with a reduced χ^2 of 1.0. The mean trends for the 1991T-like and 1991bg-like objects were also measured from template Type Ia spectra (Stern *et al.*, 2004; Levan *et al.*, 2005; Nugent, 2006) that were assembled in a similar manner to the core normal spectrum of Nugent, Kim, & Perlmutter (2002). The trends for these sub-types are shown where appropriate (i.e., the top two panels of Figure 3.3 for 1991T and the bottom panel in the case of 1991bg).

3.2.2.1 Low-z Type Ia SNe — Sub-Type Identification with Equivalent Width Results

Figure 3.3 demonstrates that the core normal SNe exhibit fairly homogenous behaviour as the EW of these three features evolves with time. These EW results also clearly differentiate between the overluminous and underluminous SNe Ia sub-types. The lack of absorption from intermediate mass elements in 1991T-like objects, due to inferred higher temperatures, is clearly seen in the EW{CaII} and EW{SiII} results. Similarly, the additional absorption from (primarily) TiIII in cooler, 1991bg-like objects results in a significant difference with regards

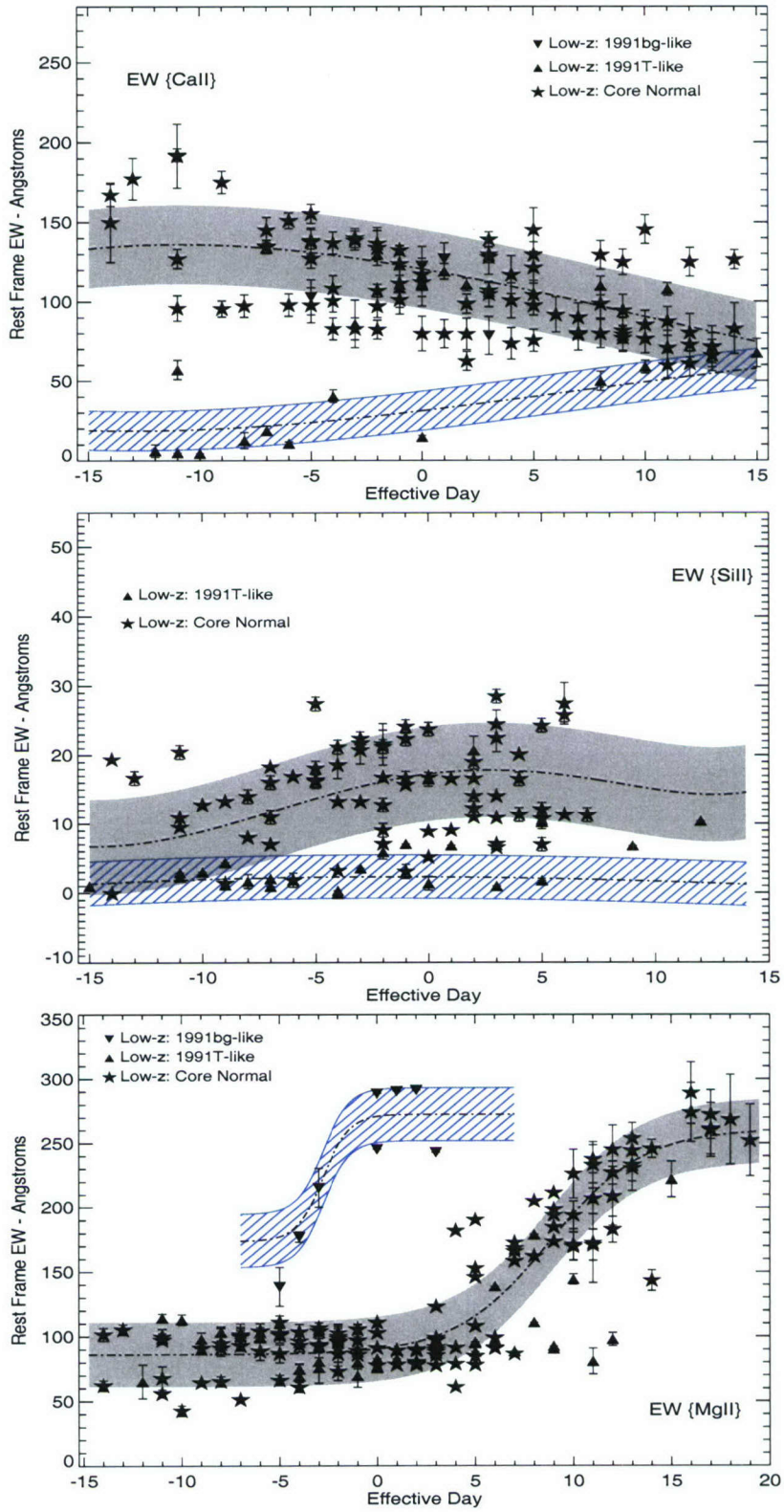

Figure 3.3: Measurements of the EW for the 'CaII H&K', 'SiII', and 'MgII' features (from top to bottom), versus rest-frame epoch, in the low-z sample. The shaded, grey region marks the mean trend and 1σ distribution of the epoch evolution of this feature in core normal objects. The striped region marks the same trend for 1991T-like objects in the EW{CaII} and EW{SiII} (top and middle panel) plots and the trend for 1991bg-like objects in the EW{MgII} plot (bottom panel). These trends were estimated with EW measurements on template SNe Ia spectra (see § 3.2.2) and the 1σ contours were computed by varying the error on the mean trends to give a reduced χ^2 fit of 1.0 to the low-z data.

to EW{MgII} measurements. These results simply repeat the qualitative and quantitative differences that have already been established for these different SNe types (Filippenko *et al.*, 1992a,b; Benetti *et al.*, 2005; Branch *et al.*, 2006). However, these results are unique as these sub-type differences were confirmed with measurements that can be repeated specifically on SNe spectra at high-z. This is very useful as previous studies of high-z spectra (Blondin *et al.*, 2006; Hook *et al.*, 2005; Balland *et al.*, 2006) have not been able to securely identify many distant SNe as belonging to either of these (broad) SNe categories. By applying these measurements to high-z spectra, it can be determined whether or not this is a true difference between the SNe populations at different redshifts or an artifact of the sample sizes, observed epochs, or the spectroscopic measurements used in these studies.

3.2.3 Low-z Type Ia SNe — EW{SiII} Spectroscopic Sequence

Note the large increase that occurs in the EW{MgII} feature range after maximum light (Fig. 3.3). This is due to the 'merging' of the SiII and MgII features. For these EW measurements, two neighboring features are considered merged once a single, uninterrupted pseudo-continuum can fit both features in question. This SiII-MgII merger is caused by additional absorption from the IME located at the regions further down in the photosphere that are revealed at later epochs. The fact that the SN 1991T-like objects exhibit this merger at later epochs than core normal SNe Ia is another indication of the different distributions of the IME in the ejecta of the SNe sub-types. F04 noted this trend - defined as the 'MgII break parameter' — and noted that it correlates with $\Delta_{m_{15}}$.

This is just one of several parameters (see § 1.4) that have been used as evidence for a spectroscopic sequence in SNe Ia. To date, however, these spectroscopic-luminosity correlations have either been made with measurements that are not possible in high-z surveys (see § 3.1) or correlate with $\Delta_{m_{15}}$ (which is itself another empirical estimator of peak luminosity) only. The results of the low-z EW measurements in this thesis were investigated for any correlations with a more fundamental parameter — the peak luminosity un-corrected for any empirical lightcurve shape calibrations. This investigation found that the EW{SiII} measurement is a new spectroscopic indicator of these luminosities, as its relation to $M_{\mathrm{B_{peak}}}$ in Figure 3.4 illustrates. This plot shows the EW{SiII} measurement, measured as close as possible to

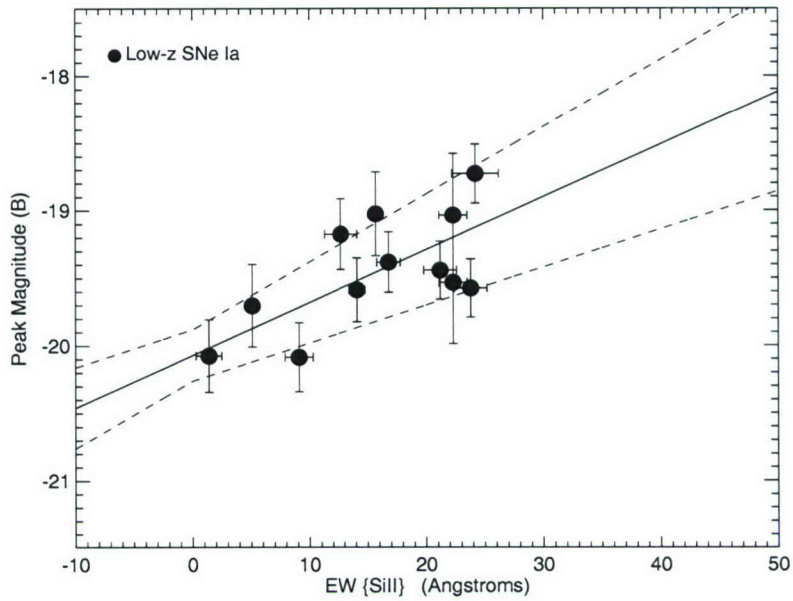

Figure 3.4: A comparison of the EW measurement of the 'SiII 4000' feature (results shown in Fig. 3.3), measured near maximum light (within ± 7.0 days), to the absolute B' peak magnitudes of SNe Ia. These magnitudes (estimated by the author, see § 2.7.2.1) have not been corrected for the lightcurve shape-luminosity relations used to standardise SNe Ia magnitudes. A linear best fit is illustrated with the solid line in this figure and the 1σ range on (based on the uncertainty in the final coefficients) is marked with the dotted lines. The significant correlation seen here reveals a new spectroscopic sequence in SNe Ia and can be used to estimate SNe Ia luminosities for cosmology.

maximum light (within ±7.0 days), compared to the absolute peak magnitudes for a sub-set of the low-z sample (see § 2.7.2.1). There is a strong (3σ, based on the Spearman rank coefficient for this trend) relationship between this EW value and $M_{\mathrm{B_{peak}}}$. Linear fits to this relation have small residuals (~ 0.25 mag.) that place this spectroscopic indicator on par with others in the literature (Wells *et al.*, 1994; Nugent *et al.*, 1995a; Bongard *et al.*, 2006). This spectroscopic sequence is also relatively free of the epoch constraints on similar sequences [Nugent *et al.* (1995a), Benetti *et al.* (2005), or F04] because EW{SiII} evolves little near maximum light; only one observation is necessary to constrain this parameter. Any EW measurement near this date (within ±7.0 days is optimal) yielded the same results for the sub-set of low-z SNe shown in Figure 3.4. The wavelength position of this measurement also makes it ideal as it is well within the wavelengths observed by SNe Ia surveys at all redshift ranges.

The linear best fit to this correlation, including errors in both $M_{\mathrm{B_{peak}}}$ and EW is

$$M_{\mathrm{B_{peak}}} = (-20.07 \pm 0.19) + (0.039 \pm 0.011) \times \mathrm{EW\{SiII\}}. \tag{3.4}$$

This relation presents a novel way to estimate SNe Ia peak absolute magnitudes with spectroscopy. The utility of this correlation for SNe Ia cosmology analysed and discussed in § 4.5.

In a rough approximation, the primary physical parameter that underlies this sequence is temperature. For an assumed Chandrasekhar mass white dwarf explosion scenario, the distribution of peak magnitudes is based primarily on the different amounts of ^{56}Ni synthesised. Although mixing may prevent ^{56}Ni from directly affecting temperature (Mazzali *et al.*, 2001), higher production of this isotope results in the release of more energy into the expanding SN photosphere. This energy, aside from powering the lightcurve, also increased the temperature within the ejecta. The successive changes in the ionisation of the IME can thus result in the appearance of a smaller amount of SiII in the spectra of hotter and brighter SNe (Nugent *et al.*, 1995a; Hatano *et al.*, 2000; Branch, 2001; Branch *et al.*, 2006). This could also be an abundance effect, as the increased amount of ^{56}Ni will be made at the expense of IME. However, near maximum light these abundance effects would not be so clearly expressed in the SNe spectra due to the influence of mixing effects and expansion opacities. The EW{SiII}-$M_{\mathrm{B_{peak}}}$ relationship thus makes sense in this simplified temperature explanation. As with most of the broad features exhibited in SNe Ia spectra near maximum light, even the fairly small absorption region considered for this EW{SiII} measurement has contributions from other elements. Additional absorption from CoII, MgII and high-velocity FeII (Tonry *et al.*, 2003; Branch *et al.*, 2006) have all been proposed to explain the appearance (depth, width, and shape) of this particular feature, so some additional spectral synthesis models are required to determine (quantitatively) how these ions affect the EW{SiII}-$M_{\mathrm{B_{peak}}}$ correlation proposed here.

3.2.4 Low-z Type Ia SNe — CaII H&K v_{ej} Measurements

The quality of the nearby SNe Ia spectra meant that no additional steps were needed to make the velocity measurements described in 3.1.2. The entire CaII H&K feature was fit consistently for all of the low-z SNe in a manner that can be repeated on the lower S/N high-z spectra. The dominant errors were found to be those induced by the range of velocities between the initial and final Gaussian fits. Even these errors were minimal for a majority of the v_{ej} measurements.

These results are in agreeement with previously published CaII H&K velocities (Wells *et al.*, 1994; Blondin *et al.*, 2006).

3.2.5 Low-z Type Ia SNe — CaII H&K v_{ej} Results

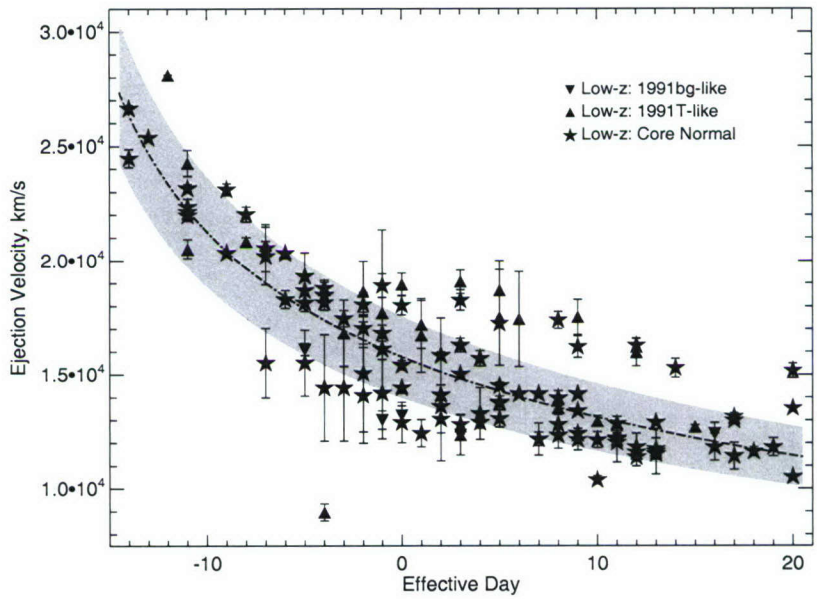

Figure 3.5: The epoch evolution of CaII H&K ejection velocities measured on low redshift SNe Ia. The expected trend, generated from fitting a model power law to the core normal data (see § 3.2.4), is illustrated with the dashed line. The grey contours denote the 1σ dispersion about this fit. The behaviour of all SNe Ia sub-types is fairly homologous with regards to this parameter.

The evolution of CaII H&K v_{ej} over epoch is shown in Figure 3.5. The mean trend was estimated by fitting a power law of the form $v \propto t^{-2/(n-1)}$ (where v is the velocity, t is the time since explosion, and n is a constant to account for the density) to all of the data points from core normal objects. This assumed relation arises from the variation of density (ρ) with velocity (v) in the ejected matter, which is also represented by the power law $\rho \propto v^{-n}t^{-3}$ [see Branch *et al.* (1988) for more detail]. The core normal objects display a broad, but homogenous, trend about this best fit and the SN sub-types are generally interspersed around it. The distribution of these results is smaller than many other spectroscopic parameters. Previous estimations of SN Ia ejection velocities implied that over-luminous objects have significantly higher velocities (Jeffery *et al.*, 1992), but the statistical analysis of SiII velocities by Benetti *et al.* (2004) suggests that these objects perhaps differ in their velocity gradients instead. The velocity

gradient measurements were not studied here as corresponding measurements are not available on the high-z set.

Table 3.1: Equivalent width and v_{ej} results — low Redshift SNe Ia (the source publication for each object is listed in Table 2.14). Measurements that could not be made due to wavelength coverage are marked with '...'.

Name	Day[a]	EW{CaII}[b*]	EW{SiII}[b*]	EW{MgII}[b*]	$v_{ej}/1000.0$[c*]
1981B	0	117.2 (6.2)	23.8 (1.4)	...	15.42 (0.20)
1981B	20	80.3 (8.1)	...	...	13.53 (0.02)
1986G	-5	102.8 (11.5)	...	177.2 (15.4)	16.11 (0.27)
1986G	-4	...	...	138.4 (4.3)	...
1986G	-3	...	...	215.3 (15.3)	...
1986G	0	...	...	245.3 (19.8)	...
1989B	-7	134.9 (4.8)	16.1 (1.4)	101.2 (5.6)	15.51 (1.52)
1989B	-5	127.2 (6.6)	16.2 (1.1)	101.1 (6.1)	15.51 (1.44)
1989B	-3	...	20.7 (3.0)	93.6 (5.9)	...
1989B	-2	...	21.6 (2.9)	102.5 (7.7)	...
1989B	-1	123.9 (11.2)	15.7 (0.5)	105.6 (3.8)	14.18 (2.00)
1989B	3	129.6 (5.8)	...	...	12.81 (0.41)
1989B	5	121.5 (11.0)	...	...	13.08 (0.38)
1989B	8	98.5 (9.7)	...	...	12.81 (0.43)
1989B	9	94.2 (10.4)	...	...	12.41 (0.22)
1989B	11	87.5 (9.9)	...	237.7 (11.9)	12.22 (0.24)
1989B	12	80.3 (12.3)	...	245.1 (19.8)	11.82 (0.60)
1989B	13	71.6 (13.0)	...	253.9 (12.0)	11.62 (0.99)
1989B	16	74.7 (7.6)	...	289.1 (24.2)	11.82 (0.60)
1989B	17	71.1 (7.2)	...	261.3 (20.3)	11.43 (0.59)
1989B	18	76.2 (10.5)	...	268.4 (35.9)	11.62 (0.20)
1989B	19	59.7 (7.9)	...	252.1 (28.6)	11.82 (0.40)
1990N	-14	167.1 (7.2)	-0.1 (0.1)	62.1 (4.1)	24.47 (0.40)

continued on next page

Table 3.1

(continued)

Name	Day[a]	EW{CaII}[b*]	EW{SiII}[b*]	EW{MgII}[b*]	$v_{ej}/1000.0$[c*]
1990N	-7	134.4 (4.9)	7.0 (0.4)	92.9 (4.0)	20.21 (1.26)
1990N	2	···	14.1 (0.7)	···	···
1990N	3	···	14.0 (0.5)	77.6 (3.0)	···
1990N	17	68.2 (8.3)	···	260.4 (21.6)	13.15 (0.18)
1991M	3	139.0 (5.3)	24.5 (2.1)	···	16.29 (0.30)
1991T	-12	6.1 (4.4)	···	65.3 (13.8)	28.11 (0.01)
1991T	-11	4.9 (0.6)	2.3 (0.4)	114.5 (4.0)	24.26 (0.58)
1991T	-10	4.5 (0.9)	3.0 (0.4)	113.0 (4.3)	···
1991T	-8	12.6 (5.4)	2.5 (0.3)	110.9 (4.6)	20.85 (0.16)
1991T	-7	18.7 (3.9)	2.0 (0.4)	100.5 (4.2)	20.69 (0.16)
1991T	-6	10.7 (1.4)	1.8 (1.2)	99.7 (4.7)	20.37 (0.03)
1991T	0	14.7 (1.8)	1.4 (1.1)	···	18.95 (0.50)
1991T	10	58.8 (4.8)	···	144.3 (4.2)	12.96 (0.24)
1991T	15	67.6 (9.3)	···	221.9 (14.4)	12.71 (0.08)
1991bg	0	122.7 (12.5)	···	···	13.21 (0.42)
1991bg	1	127.0 (10.9)	···	···	···
1991bg	2	···	···	291.4 (20.9)	···
1992A	-5	155.3 (6.2)	27.4 (1.2)	86.8 (7.7)	18.15 (0.38)
1992A	-1	101.1 (9.5)	24.2 (2.0)	88.9 (3.5)	16.12 (0.46)
1992A	3	104.7 (8.1)	28.5 (1.1)	···	15.02 (0.09)
1992A	5	97.5 (7.0)	24.3 (1.7)	···	13.80 (0.05)
1992A	6	91.7 (12.0)	25.8 (1.8)	···	14.15 (0.11)
1992A	7	89.9 (9.3)	···	···	14.15 (0.10)
1992A	9	81.7 (8.4)	···	···	14.14 (0.06)
1992A	11	···	···	233.1 (18.8)	···
1992A	16	···	···	274.0 (23.5)	···

continued on next page

Table 3.1

(continued)

Name	Day[a]	EW{CaII}[b*]	EW{SiII}[b*]	EW{MgII}[b*]	$v_{ej}/1000.0$[c*]
1992A	17	83.3 (6.5)	···	272.5 (20.0)	12.99 (0.02)
1994D	-11	192.2 (4.2)	9.5 (0.6)	55.9 (3.7)	23.16 (0.18)
1994D	-10	···	12.75 (.8)	42.6 (4.7)	···
1994D	-9	175.1 (7.5)	13.3 (0.8)	64.3 (2.2)	23.11 (0.25)
1994D	-8	···	···	65.2 (4.5)	···
1994D	-7	···	···	51.2 (2.5)	···
1994D	-5	97.7 (11.9)	16.4 (1.3)	66.2 (4.7)	18.69 (0.41)
1994D	-4	100.5 (7.0)	18.6 (2.2)	60.7 (4.8)	18.48 (0.66)
1994D	-2	97.1 (7.5)	21.2 (1.4)	73.1 (7.9)	15.05 (2.56)
1994D	2	98.6 (3.1)	19.0 (1.9)	···	15.84 (1.64)
1994D	4	73.5 (11.0)	20.1 (0.7)	···	12.90 (0.26)
1994D	10	···	···	171.1 (12.5)	···
1994D	11	59.7 (8.7)	···	172.6 (31.3)	12.02 (0.87)
1994D	12	60.8 (8.7)	···	208.7 (24.0)	11.38 (0.40)
1994D	13	66.1 (5.6)	···	230.5 (10.9)	11.74 (0.47)
1994D	20	72.1 (4.9)	···	···	10.51 (0.08)
1994Q	10	145.9 (9.6)	···	226.1 (19.2)	10.38 (0.19)
1996X	-2	···	16.8 (0.7)	86.5 (2.7)	···
1996X	-1	···	16.7 (1.1)	85.8 (3.6)	···
1996X	0	79.7 (11.7)	16.8 (1.0)	···	12.90 (0.89)
1996X	2	79.5 (10.9)	16.6 (0.9)	···	13.05 (0.60)
1996X	1	79.7 (10.0)	16.6 (0.9)	···	12.42 (0.60)
1996X	7	79.2 (10.0)	···	···	12.17 (0.30)
1997br	-9	···	4.4 (0.5)	97.9 (5.3)	···
1997br	-8	···	1.7 (1.3)	96.5 (10.3)	···
1997br	-7	···	0.9 (0.5)	102.6 (5.8)	···

continued on next page

Table 3.1

(continued)

Name	Day[a]	EW{CaII}[b*]	EW{SiII}[b*]	EW{MgII}[b*]	$v_{ej}/1000.0$[c*]
1997br	-6	···	···	99.0 (11.9)	···
1997br	-4	40.4 (4.5)	0.0 (0.1)	74.9 (4.6)	8.96 (0.37)
1997br	8	49.9 (6.2)	···	···	13.54 (0.08)
1997cn	3	78.5 (12.0)	0.1 (0.1)	243.0 (18.9)	12.36 (0.89)
1998aq	-8	···	···	91.0 (6.3)	···
1998aq	0	···	···	77.9 (9.0)	···
1998aq	1	···	···	78.3 (5.0)	···
1998aq	2	···	···	78.1 (7.0)	···
1998aq	3	···	···	89.8 (6.4)	···
1998aq	4	···	···	91.4 (5.5)	···
1998aq	5	···	···	84.9 (13.0)	···
1998aq	6	···	···	90.8 (11.4)	···
1998aq	7	···	···	86.5 (13.3)	···
1998bu	-4	82.8 (7.1)	13.2 (0.9)	93.1 (5.2)	14.42 (2.33)
1998bu	-3	82.8 (7.1)	13.2 (0.9)	92.5 (3.6)	14.42 (2.33)
1998bu	-2	82.4 (6.2)	12.7 (1.4)	95.5 (5.8)	14.09 (2.09)
1998bu	8	79.7 (9.9)	···	···	12.34 (0.58)
1998bu	9	77.0 (8.6)	···	···	12.15 (0.47)
1998bu	10	76.4 (10.0	···	194.0 (11.8)	12.14 (0.35)
1998bu	11	70.7 (11.2)	···	206.9 (12.2)	12.15 (0.24)
1998bu	12	72.6 (8.1)	···	227.0 (9.9)	11.59 (0.04)
1998bu	13	71.3 (9.5)	···	244.3 (12.8)	11.51 (0.23)
1999aa	-11	57.1 (6.3)	2.9 (0.5)	101.7 (4.5)	20.52 (0.41)
1999aa	-3	85.9 (15.4)	3.5 (0.3)	80.7 (3.4)	16.82 (1.46)
1999aa	-1	108.4 (12.6)	7.0 (0.8)	80.1 (5.3)	17.71 (3.63)
1999aa	5	···	···	94.7 (4.3)	···

continued on next page

Table 3.1

(continued)

Name	Day[a]	EW{CaII}[b*]	EW{SiII}[b*]	EW{MgII}[b*]	$v_{ej}/1000.0$[c*]
1999aa	6	···	···	138.8 (18.7)	···
1999ac	-15	···	1.0 (0.4)	61.0 (2.5)	···
1999ac	-9	···	···	83.4 (4.4)	···
1999ac	0	110.1 (7.0)	16.5 (1.2)	···	14.42 (0.11)
1999ac	2	110.7 (4.5)	20.7 (2.3)	···	14.11 (0.43)
1999ac	8	110.0 (6.4)	···	···	13.97 (0.31)
1999ac	11	107.8 (4.4)	···	275.8 (15.3)	12.84 (0.31)
1999aw	3	103.9 (9.5)	1.0 (0.2)	···	19.07 0.529
1999aw	5	115.4 (8.7)	1.8 (0.2)	···	18.69 (1.32)
1999aw	9	110.7 (4.3)	6.8 (0.6)	···	17.52 (0.77)
1999aw	12	109.4 (3.4)	10.4 (0.9)	97.9 (5.5)	15.97 (0.59)
1999ee	-11	95.8 (8.4)	···	97.2 (3.8)	21.97 (0.25)
1999ee	-9	95.5 (5.8)	1.4 (0.2)	90.8 (4.5)	20.35 (0.11)
1999ee	-8	97.3 (8.0)	···	94.5 (2.8)	22.03 (0.33)
1999ee	-6	97.9 (8.0)	1.8 (0.2)	88.6 (7.3)	20.34 (0.05)
1999ee	-4	108.4 (8.6)	3.2 (0.9)	96.4 (4.8)	18.79 (0.26)
1999ee	-2	106.9 (4.5)	7.1 (0.7)	98.4 (9.2)	18.07 (0.52)
1999ee	-1	111.5 (5.4)	3.1 (1.1)	97.0 (3.9)	18.91 (0.51)
1999ee	0	112.2 (15.1)	5.1 (0.6)	···	18.04 (0.43)
1999ee	3	106.9 (5.0)	7.0 (0.9)	···	18.26 (0.45)
1999ee	5	129.5 (8.5)	12.1 (1.5)	···	17.25 (0.14)
1999ee	7	···	···	158.4 (9.9)	···
1999ee	8	129.3 (9.5)	···	···	17.39 (0.37)
1999ee	9	124.9 (8.9)	···	···	16.22 (0.48)
1999ee	12	125.0 (9.9)	···	182.8 (10.3)	16.28 (0.32)
1999ee	14	126.5 (6.7)	···	245.7 (7.1)	15.29 (0.41)

continued on next page

Table 3.1

(continued)

Name	Day[a]	EW{CaII}[b*]	EW{SiII}[b*]	EW{MgII}[b*]	$v_{ej}/1000.0$[c*]
2000cx	-4	···	5.7 (1.1)	69.5 (9.9)	···
2000cx	-3	···	8.6 (1.3)	76.0 (12.2)	···
2000cx	-2	···	···	99.6 (9.0)	···
2000cx	-1	···	11.7 (1.7)	69.8 (9.7)	···
2000cx	0	···	9.2 (1.2)	82.7 (12.6)	···
2000cx	1	61.6 (8.6)	9.9 (1.7)	···	17.20 (1.06)
2000cx	5	54.1 (7.6)	14.3 (2.0)	···	17.51 (2.11)
2000cx	6	55.5 (6.7)	14.7 (2.0)	···	17.43 (2.09)
2000cx	7	···	13.5 (2.1)	88.5 (12.5)	···
2000cx	9	···	12.4 (1.5)	90.5 (10.4)	···
2000cx	11	···	15.3 (2.0)	80.8 (10.9)	···
2000E	-2	133.8 (11.1)	9.1 (1.2)	99.9 (6.2)	24.59 (1.16)
2000E	3	128.1 (11.9)	6.5 (0.4)	···	···
2000E	5	145.1 (14.6)	7.0 (1.2)	···	···
2000E	14	82.9 (16.7)	···	143.4 (8.1)	···
2002bo	-14	149.9 (25.9)	19.4 (0.9)	101.6 (5.3)	26.64 (0.15)
2002bo	-13	177.2 (13.4)	16.7 (1.4)	105.3 (4.3)	25.37 (0.10)
2002bo	-11	191.5 (21.0)	20.4 (1.1)	99.6 (4.0)	22.35 (0.35)
2002bo	-6	151.0 (5.2)	16.9 (0.7)	104.0 (3.3)	18.30 (0.39)
2002bo	-5	138.5 (8.8)	18.1 (1.6)	111.1 (4.5)	19.31 (1.04)
2002bo	-4	137.0 (7.4)	21.2 (1.0)	103.5 (6.1)	18.17 (0.09)
2002bo	-3	138.5 (6.1)	21.7 (0.8)	106.5 (3.3)	17.46 (0.35)
2002bo	-2	136.6 (10.4)	21.6 (3.9)	96.6 (6.3)	17.03 (0.70)
2002bo	-1	132.4 (3.9)	22.3 (1.2)	105.5 (4.5)	16.82 (0.35)
2002bo	4	116.9 (12.4)	···	···	15.71 (0.34)
2003du	-11	127.0 (6.5)	10.9 (1.0)	67.9 (9.9)	22.13 (0.25)

continued on next page

Table 3.1

(continued)

Name	Day[a]	EW{CaII}[b*]	EW{SiII}[b*]	EW{MgII}[b*]	$v_{ej}/1000.0$[c*]
2003du	-7	145.1 (8.4)	10.1 (1.4)	99.9 (10.2)	20.55 (1.03)
2003du	13	66.0 (10.6)	···	233.1 (20.6)	12.90 (0.04)

a — Rest-frame day, relative to B' max

b — Equivalent Width, Å

c — Ejection velocity, km/s

* 1σ *errors listed in parentheses*

3.2.6 Low-z Type Ia SNe — Host Galaxy Correlations

The general trend of brighter SNe and a higher dispersion of SNe Ia peak magnitudes in objects hosted by late-type galaxies is well established (Hamuy *et al.*, 1996a, 2000; Sullivan *et al.*, 2003). Yet only a few quantitative spectroscopic corollaries (Branch & van den Bergh, 1993; Branch, Romanishin, & Baron, 1996) have been made that agree or disagree with this trend. The EW and ejection velocity results from the low-z SNe studied here were analysed for this purpose. Kolmogorov-Smirnov (KS) tests were used to highlight any differences between the distribution of spectroscopic parameters measured in SNe from different host types. Because these measurements are all heavily dependent on epoch, the residuals from the EW and v_{ej} results were compared. The residual for each EW and v_{ej} value is defined as the difference between the measurement and the corresponding low-z mean trend (derived in § 3.2.2 and § 3.2.5) at the same epoch. This type of comparison essentially negates the epoch dependence of these measurements, which would obscure any other correlations in this data.

The host type for each low-z SN was grouped into the broad categories of 'E/S0', 'Early Spiral' (Sa and Sb), or 'Late Spiral' (Sc and irregular) galaxies. The published morphology (from the Nearby Galaxy Catalogue and other appropriate databases) of each SN host galaxy (based on the hosts listed in the SNe source papers, see Table 2.14) was used to determine which group was appropriate for each SN host.

The KS tests on all four of the spectroscopic measurements defined in this thesis detected

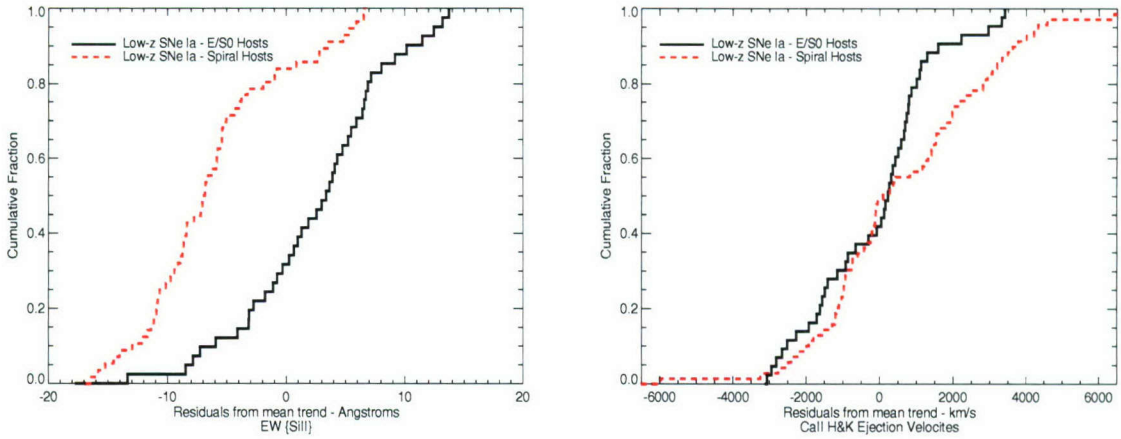

Figure 3.6: The cumulative distribution of residuals (the difference between the measured property and the estimated low-z SNe Ia core normal mean trend) from the EW{SiII} (*left*) and CaII H&K $v_{\rm ej}$ (*right*) measurements of low-z SNe from different host types. The significant differences found in these comparisons, which are useful because they can also be repeated on distant SNe, provide additional spectroscopic evidence for the correlations in SNe Ia properties and host morphology that have been established in previous low-z surveys.

interesting differences between the SNe results from E/S0 and spiral galaxies. A statistically significant difference (a probability that the two distributions were drawn from different populations at greater than 99.5% confidence) was measured for the distribution of EW{SiII} and $v_{\rm ej}$ results from the different host types. These results are shown in Figure 3.6 (for clarity, all of the SNe from the 'Early Spiral' and 'Late Spiral' hosts were grouped into one category for this plot). As discussed in § 3.2.3, the EW{SiII} measurements near maximum light show a linear correlation with peak (B') absolute magnitude. Any comparisons with this parameter can essentially be viewed as a comparison of $M_{\rm B_{peak}}$ as well. The difference between EW{SiII} measurements from different host galaxies, which show a clear bias towards lower EW (and thus higher luminosities) in spiral hosts, provides additional spectroscopic evidence for the established host galaxy trends.

The difference in the distributions of the CaII H&K ejection velocities provides further evidence of the correlations that have been noted in the literature. Branch & van den Bergh (1993) demonstrated that SNe with low SiII λ6355 ejection velocities (measured 10 days past maximum) were found preferentially in early type galaxies. This is a possible sign of the effects of progenitor age (Gallagher *et al.*, 2005) on SNe Ia characteristics, although the multidimensional nature of these objects also suggests that the explosion mechanism (Hatano *et al.*, 2000; Benetti *et al.*, 2005) or metallicity (Lentz *et al.*, 2000) may be a factor in this trend as well.

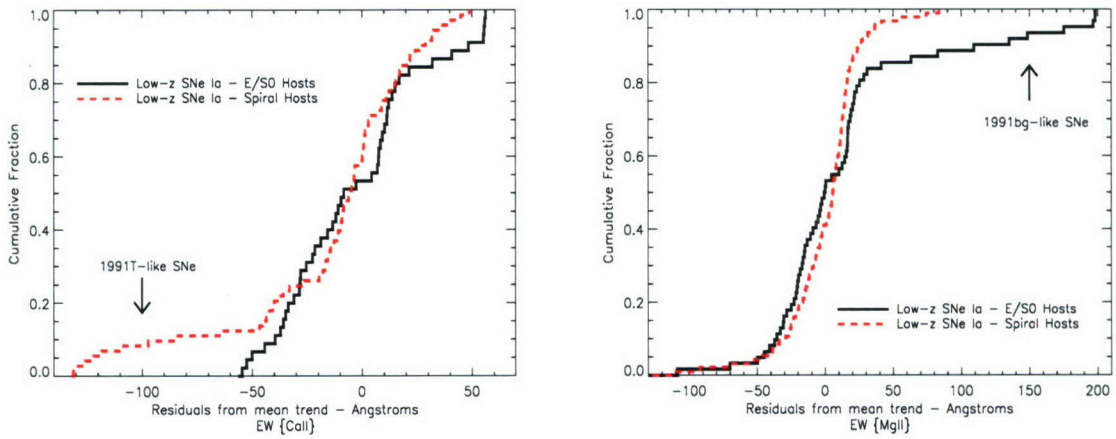

Figure 3.7: As in Fig. 3.6, the cumulative distribution of residuals from the EW{CaII} (*left*) and EW{MgII} (*right*) low-z measurements, separated according to host morphology. The contributions of 1991T-like objects are clear at the low end of the EW{CaII} results from spiral galaxies, while the upper range of the EW{MgII} results from early-type galaxies are skewed by the 1991bg-like outliers.

As Figure 3.6 illustrates, the trend for SNe with in early-type galaxies to exhibit smaller photospheric velocities is also supported by the ejection velocities measured for the CaII H&K feature. This result does not clarify the physical basis for the established trend, but it is useful as this exact test can be repeated with the spectra of distant SNe with poor epoch coverage and lower S/N (see § 4.3) .

The KS tests of the residuals from the EW{CaII} and EW{MgII} results — displayed in Figure 3.7 — did not detect a significant difference between the spectroscopic parameters from different host types. However, the prevalence of 1991T-like and 1991bg-like SNe in late and early type galaxies, respectively, is clearly exhibited in this comparison. The cumulative distributions from each host type are very similiar, but they clearly diverge at the low end for EW{CaII} and at the high end for EW{MgII} due to these overluminous and underluminous outliers.

Possible evolutionary effects in the high-z sample can be checked with similar comparisons within the distant SNe data. Although galaxy morphology is fairly broad way of classifying the different host environments that produce SNe Ia, comparisons based on host type will compare SNe from environments with more similar evolutionary histories. This may help reveal any evolutionary effects that are too subtle to discern with analysis of the SNe data as a whole. The host galaxy correlations in these quantitative spectroscopic measurements are discussed with regards to the high-z SNe in § 4.3.

3.3 Analysis of High Redshift Type Ia SNe

The utility of equivalent width and ejection velocity measurements for the quantitative analysis of Type Ia SNe was demonstrated in the previous section. These measurements are unique because they are also well suited for corresponding analysis on SNe Ia observed at high redshifts, despite the limitations imposed on these distant spectra (summarised in § 3.1). The methods and results of the EW and $v_{\rm ej}$ measurements made on the large set of high-z spectra are presented in the following sections.

3.3.1 High-z Type Ia SNe — Equivalent Width Measurements

High redshift SNe are subject to additional systematic errors from decreased S/N and contaminating flux from the host galaxy. Some additional steps are necessary to account for these errors when making EW measurements. The additional noise obscures the feature bounds enough that the correct placement of the pseudo-continuum in both the wavelength and flux axes can be uncertain. To locate the local maxima and set the pseudo-continuum, a median filter covering 60 Å (in the rest frame) was applied to the SN flux. This filter was determined to be the optimal smoothing amount (see § 3.3.2) for the spectra at the signal to noise levels sampled in the primary data set. The local maxima for each measurement were selected within this filtered spectrum using the same guidelines listed in § 3.1.1 and the EW measurement was then made with the initial, un-filtered points as Figure 3.8 shows. The points in the EW calculation (Eq. 3.1) that are most affected by sky noise can easily bias the final measurement as well. For the SNLS data set, the measurement uncertainty ($\sigma_f(\lambda_{\rm i})$) was used to weight each point so that the equivalent width was calculated as

$$EW_{\rm SNLS} = \left(\sum_{\rm i=1}^{\rm N} \left(1 - \frac{f_\lambda(\lambda_{\rm i})}{f_c(\lambda_{\rm i})} \right) \Delta\lambda_{\rm i} w_{\rm i} \right) \frac{\rm N}{\Sigma(w_{\rm i})} \tag{3.5}$$

where $w_{\rm i}$ is the weighting function at each point:

$$w_{\rm i} = 1/\sigma_f(\lambda_{\rm i})^2 \tag{3.6}$$

The statistical errors were calculated as defined in equation 3.2. The error induced by any variance in the pseudo-continuum was computed with the method described in § 3.1.1. A

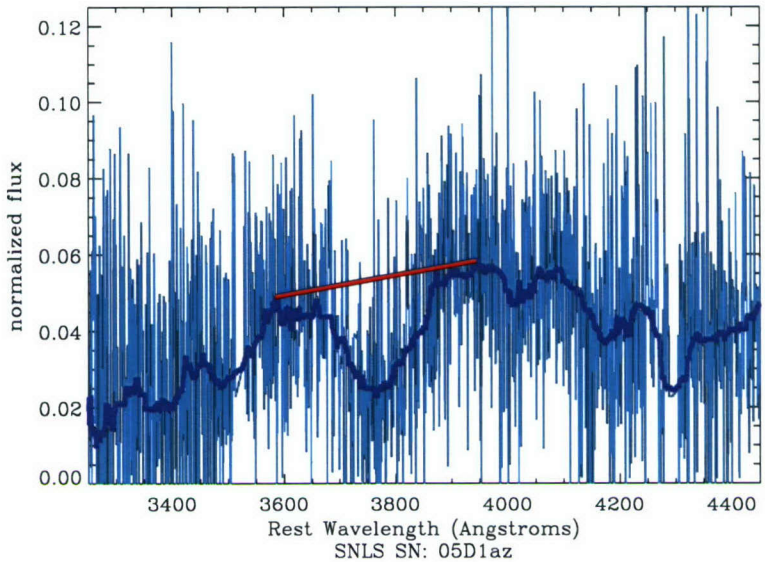

Figure 3.8: An example of an EW measurement (for EW{CaII} in this case) on a high-z SNLS object. The median filtered spectrum is plotted over the unbinned, observed spectrum. The local maxima of the feature have been found within this median filter. The EW is then computed by numerically integrating the weighted, un-filtered flux underneath the pseudo-continuum defined by the two maxima.

more detailed description of the errors caused by sky noise and host galaxy contamination is presented in the next section. For the EW measurements on the tertiary data set, which did not have available error spectra, the weighting function was approximated with a representative sky background spectrum observed at Gemini North. The statistical errors from Eq. 3.2 were not calculated for these objects, but the error from the uncertainty in the pseudo-continuum was estimated. The results from the SNLS sample showed that these two sources of error were nearly equal in most cases, so the total error for the EW measurements from the ESSENCE and SCP data sets was estimated by doubling the uncertainty estimated by varying the continuum.

There were two cases where EW measurement results from the high-z set were considered unusable for further analysis. These cases are specifically due to instrument effects. The first instance was if either the lower or upper range of an EW measurement (refer to the boundaries defined in Figure 3.1) was cut off by the end of the detector. This is sensible as any pseudo-continuum fit without complete access to the EW bounds defined for this method would be highly uncertain and inconsistent with the rest of the measurements. Similarly, any local maxima that were found at a location where a chip gap had been corrected also had to be removed. This is because the lack of real data within these pixels also makes the placement of

any psuedo-continuum endpoints too uncertain to be of any value. These two considerations removed results on a measurement-by-measurement basis and particularly affected the final set of EW{CaII} and EW{MgII} results. This high-z data set is large enough that removing the affected measurements did not seriously detract from the analysis of these sets. The results from 37 EW measurements in the primary data set, 6 measurements from the secondary set, and 5 measurements from the tertiary set were removed due to these considerations; the removals are marked with '$\cdots$' in the tables of EW results (see Tables 3.2 - 3.4). Combined with the objects that had to be removed due to excess host galaxy contamination (see § 3.3.3), this left a total of 238 measurements from 97 different high-z SNe in the final set of EW results.

3.3.2 Systematic Error in High-z Measurements I — Signal to Noise

The EW measurements made on SNe Ia spectra use a method that is dependent on the local maxima that bound each absorption feature. The sky noise affects the high-z measurements by augmenting these selected maxima. This pushes the pseudo-continuum up the flux axis and increases $f_c(\lambda_i)$ at every point in Equations 3.1 and 3.5 an results in an overestimate of the equivalent width. Appropriate smoothing of these noisy spectra can negate these systematic effects and set a more correct pseudo-continuum. A median filter was selected as an effective and straight-forward method to make this correction. The size of the filter window, effectively the smoothing amount, was selected very carefully to ensure this filtering could account for the systematic effects caused by the sky noise. If the lower S/N spectra are not filtered enough, the residual noise will continue to cause a systematically overestimated EW. On the other hand, too large of a filtering window will set the pseudo-continuum too low and have the opposite systematic effect.

The appropriate filtering amount was selected with simulations using the high S/N low-z spectra. In these simulations, spectra from the low-z sample were degraded with Gaussian-distributed noise to cover all applicable S/N levels sampled in the high-z SNe. The added noise was scaled by an average high-z error spectrum to exactly mimic the effects of the sky background. The EW was then re-calculated on each of these noisy spectra, using a median filter set to various window sizes. The deviation in each EW measurement from the true value was recorded (as a percent error, $\frac{EW_{\rm sim}-EW_{\rm true}}{EW_{\rm true}} \cdot 100$) along with the S/N in every iteration of

the simulation. The S/N was estimated as the median S/N, calculated per pixel, within the region covered by the pseudo-continuum bounds set for each specific measurement. A sample of the results of these simulations is shown in Figure 3.9. This figure shows four panels which display the results of simulated EW{MgII} measurements using different filtering amounts. The percent error in the EW measurements made with these different filtering amounts is plotted against signal-to-noise in this figure.

Each point in Figure 3.9 is from an EW measurement made during these simulations, and the large circles represent the median percent error in each integer S/N bin. In three of these panels a line at $y = 0$ is over-plotted to help illustrate any systematic effects. As expected, the distribution of the deviations from the true EW value increase at lower S/N levels in every case. The systematic effects of the noise are manifested in how evenly distributed these deviations are from the true EW value (a percent error of 0%). The systematic EW overestimate, which was expected in the measurements made with too little filtering (10 Å and 40 Å in this example), is clear in the top two panels of Fig. 3.9. The results of applying too much filtering can be seen in the bottom right panel, where a median filter over an 80 Å window has caused a slight systematic underestimate of EW values at all S/N levels. This simulation was repeated for the EW measurements of every feature studied in this thesis (as well as the $v_{\rm ej}$ measurements), and a median filter over a 60 Å window proved to be the most robust at the wide range of S/N levels covered by the high-z spectra. This is shown in the bottom left panel of Fig. 3.9 as the median percent error in these simulated measurements deviates little from 0% at all S/N levels.

3.3.2.1 Confirming Calculated Uncertainties

The simulated measurements also provided the clearest and most logical way to evaluate the calculated EW uncertainties. An illustration of this is provided in Figure 3.10. This figure shows the same results as in the bottom left panel in 3.9 — the simulated EW{MgII} measurements with a 60 Å median filter — only the absolute magnitude of the percent error for every simulation is shown. Plotted on top of these points are the actual EW{MgII} calculated errors (for the SNe in the 1° and 2° data sets), which clearly show good agreement with the uncertainties predicted by these extensive tests. This confirms that the uncertainty calculated

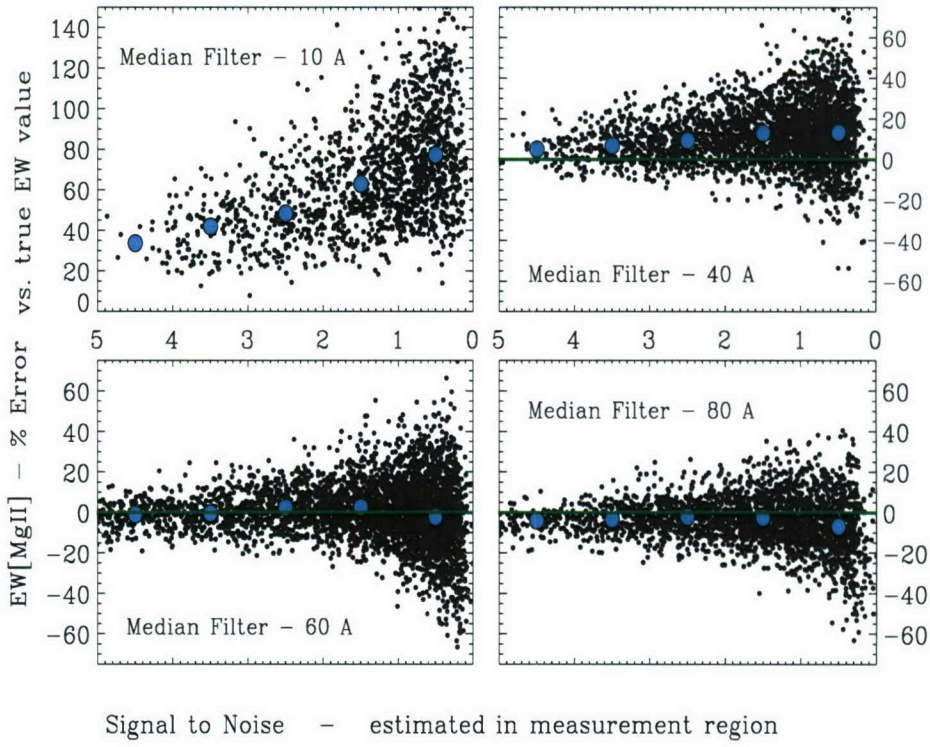

Figure 3.9: The results from simulated high-z EW{MgII} measurements on degraded low-z spectra. Each point in this figure is from an EW measurement on a template spectrum that was degraded with an error spectrum that approximated the dominant sky noise in the high-z objects. These measurements were repeated using different amounts of median filtering to determine the most robust measurement technique for the high-z data. The light coloured dots represent the median percent error in each integer S/N. The top two panels show that the 10 Å & 40 Å filtering windows were too small to effectively filter out the sky noise and resulted in systematically over-estimated EW values. The opposite is true for the measurements made with a median filter over 80 Å (bottom right panel). These simulations demonstrated that a median filter using a 60 Å window resulted in the most robust EW measurements at all S/N levels.

via Equation 3.2 is a valid estimate of the measurement errors in this particular analysis.

3.3.3 Systematic Error in High-z Measurements II — Host Galaxy Contamination

Host galaxy contamination adds another source of systematic error to the EW measurements on high-z data. In nearby objects, the angular separation between a host and SN candidate is enough that most observations are not seriously affected by host galaxy light. This is not the case with distant SNe. In previous high-z spectroscopic studies, this error has been addressed by subtracting host galaxy templates during the χ^2 SN identification process (Hook *et al.*,

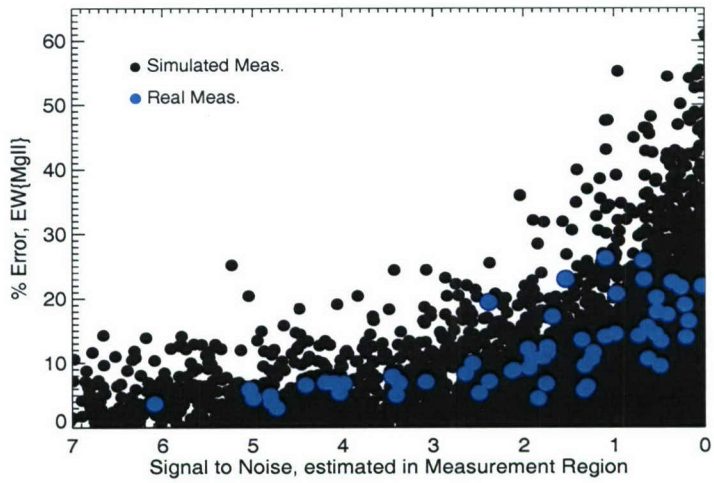

Figure 3.10: The absolute value of the percent error from each simulated EW{MgII} measurement, made with a 60 Å filter, is shown (as in Fig. 3.9) in the solid black circles. The bright blue circles are the calculated percent errors from the same measurements in the 1° and 2° data sets.

2005; Balland *et al.*, 2006) during the extraction of the SN spectrum (Blondin *et al.*, 2006), or not at all. In reality, the host contamination tends to 'wash out' the absorption troughs in SNe spectra and cause the measured strength of these features to be systematically lower than what would be seen in a spectrum free of host galaxy flux.

Generally, there has been no reliable way to evaluate the effect of this contamination (Blondin *et al.*, 2006). This is not the case for the SNLS supernovae, as § 2.4.4.4 (see Equations 2.2 - 2.4) demonstrated how the photometric data available for this data set can be used to estimate the fraction of host flux in each spectrum. With these host contamination constraints, simulations were next employed to estimate the specific effects of this contamination on the EW measurements from the primary and secondary data sets. The results of these simulations were then used to adjust the affected EW measurements to correct for this systematic error. The high S/N, low-z spectra from several different SNe Ia and template galaxies from E, S0, Sa, Sc, and starburst galaxies [from Kinney *et al.* (1996), see § 2.4.4.3] were used in this simulation.

In each run of the simulation, the range of the observed i' was shifted, specific to the redshift of each SNLS object, to where it would fall in the rest frame. All contamination calculations were made within this de-redshifted band using the i' filter transmission curve from CFHT. This was done to be consistent with the photometric estimates of the supernova and host galaxy flux ratios (§ 2.4.4.4). The flux of a host galaxy template was then scaled to

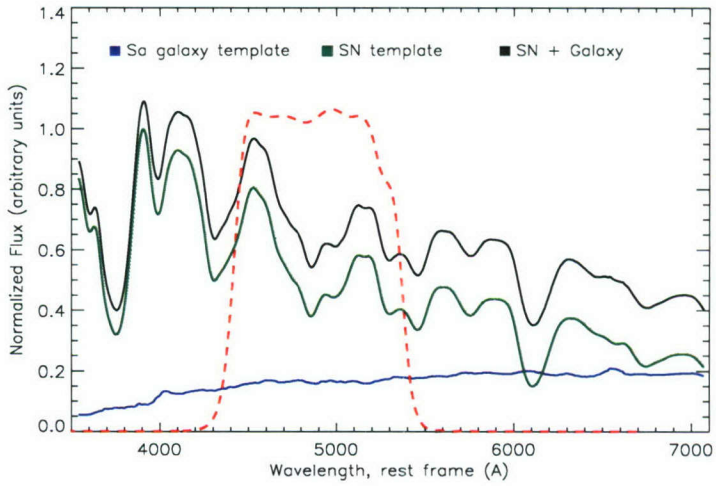

Figure 3.11: A sample iteration of the simulation used to determine the effects of host galaxy contamination for each SNLS object. The dotted lines show the transmission curve for the CFHT Megaprime instrument in the i', shifted to where this observed band would lie at the redshift of one specific SNLS object. For this case, the simulation is estimating the effects of 26% contamination from a typical Sa galaxy on an SNLS object observed at $z = 0.59$. The EW is re-measured on the contaminated spectrum at the top of this plot and compared to the 'true' measurement initially made on the uncontaminated SN spectrum. The percent error from this comparison is used to quantify the bias caused by host contamination for the case of this specific high-z object. The EW measured in this object will then be adjusted accordingly based on this information.

meet the host contamination estimated from the photometric percent increase (see Eqns. 2.2 - 2.4). The adjusted host template was added to the low-z supernova spectrum and the EW was re-measured to give the percent error caused by the specific host type and contamination amount for every EW measurement on each SNLS object. Figure 3.11 shows an example iteration of this process, which was repeated with several low-z spectra for the specific percent contamination and redshift of every contaminated SNLS object. The median value of the percent error estimates among the different low-z spectra was used as the best estimate for the contamination effects on each SNLS supernova, EW measurement, and galaxy type in question. In each instance, the entire range of effects from all different galaxy types was measured. This range was used as the uncertainty in the final EW correction, which was made based on the simulation results from one host galaxy type. This galaxy type was selected based on the observed host features in each affected SNLS spectrum (see § 2.4.4.4 for details). Each contaminated EW measurement was then adjusted by the inverse of the percent error to correct for the systematic effects caused by the host flux.

The corrections made to each EW measurement to account for this systematic error (for the

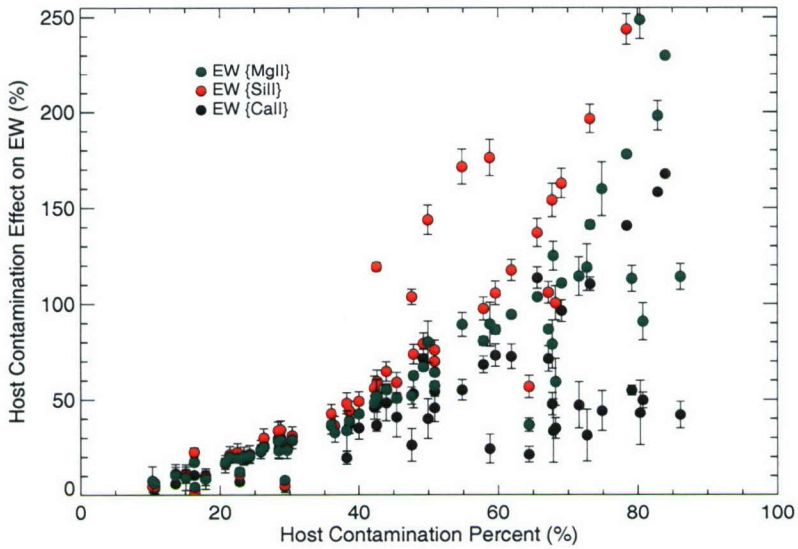

Figure 3.12: The amount of host contamination, determined from photometry (§ 2.4.4.4), for each object in the primary data set is shown on the x-axis. This contamination causes a systematic bias in each EW measurement that must be corrected for. The size of the correction for this bias, as a percent of the initialy-measured EW value, is plotted along the y-axis. The uncertainty in the selection of the correct host type is reflected in the error bars, which mark the standard deviation of the possible errors among all host templates. The different coloured points represent the different EW measurements.

1° data set) are shown in Figure 3.12, and the adjusted values are shown along with the initial EW measurements in Figures 3.13 and 3.14. In Figure 3.12 the amount of host contamination (determined photometrically, see § 2.4.4.4) is displayed along the x-axis. The values along the y-axis show the size of the correction made to each contaminated EW measurement (as a percent of the initial EW measurement value). The error bars were estimated by the standard deviation in host contamination effects across all host galaxy types. The different colours represent the three different EW measurements. The dispersion within the EW measurements in this plot is due to the effects of different host types.

The results of these simulations were used to determine that objects with greater than 65% host contamination were too biased to be included in the final analysis of this data set. This is based on the fact that at this contamination level, a majority of the high-z EW results would require adjustments greater than 100% of the measured EW (see Fig. 3.12). This amount of host flux also severely alters the shape of the SNe spectra so that the local maxima identified for each feature cannot be identified with any certainty. The combination of these effects means that the EW values from spectra with this amount of contamination are too uncertain for

further analysis. The objects listed in Table 2.8 with greater than 65% contamination were removed from the results and analysis presented in the following sections. This removed 18 objects from the primary data set. Combined with the measurements that had to be removed due to instrument effects (see § 3.3.1), measurements from a total of 54 supernovae from the primary set of SNLS SNe (out of 84 confirmed SNe Ia) were considered in the final EW analysis.

3.3.4 High-z Type Ia SNe — Equivalent Width Results

The results of the EW measurements on the high-z data sets are summarised in Tables 3.2 - 3.4 and plotted against rest-frame epoch in Figures 3.13 - 3.15 (for the 1°, 2°, and 3° data sets, respectively). The measurements that had to be adjusted for host contamination are indicated in these figures; dotted vertical lines connect these adjusted measurements with the initial EW results. The mean trends from the low-redshift normal, 1991T-like, and 1991bg-like SNe are also displayed on these figures as in Figure 3.3. A statistical comparison of the EW results from the high and low-redshift spectra and the identification of any SNe Ia sub-types (see § 3.2.2) is discussed in the next chapter.

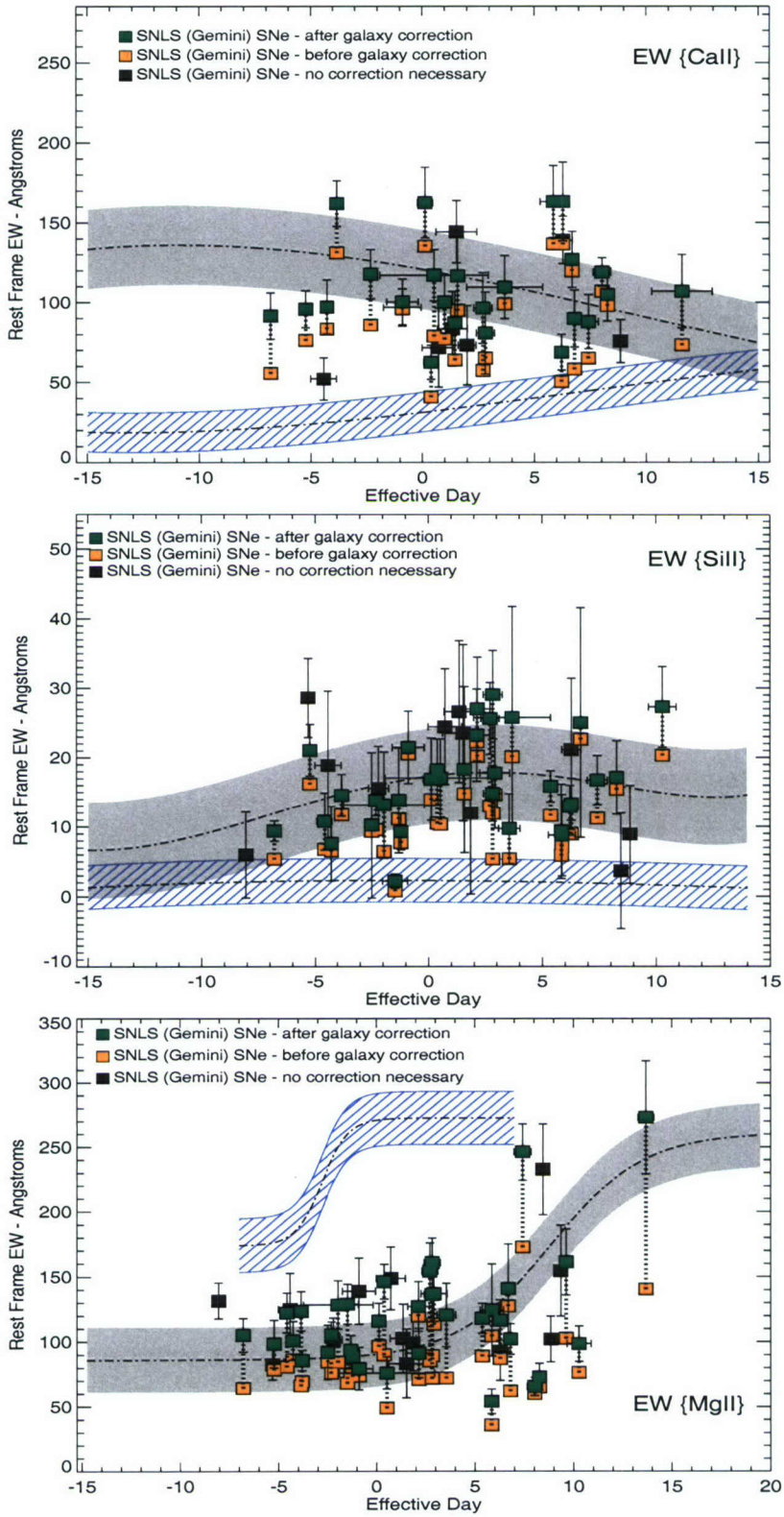

Figure 3.13: Measurements of the EW of the 'CaII H&K', 'SiII', and 'MgII' features (from top to bottom), versus rest-frame epoch, in the primary high-z sample. The shaded and striped regions are the same as in Figure 3.3. The EW measurements that did not need any correction for the systematic effects of host galaxy contamination are shown with the dark, filled squares. All of the other points illustrate the measurements that were corrected for host contamination. The adjusted EW values are connected to the corresponding initial measurements with dotted lines.

Table 3.2: Equivalent width and ejection velocity results for the primary set of high redshift SNe Ia observed by the SNLS. This set includes all of the SNLS objects (reduced by the author) that were confirmed as Type Ia SNe (a confidence index of 3 or higher; see § 2.4.4, § 2.4.5, and Table 2.9) and were subject to less than 65% contamination from their host galaxies (see § 2.4.4.4 and Table 2.8). The blank spaces in this chart ('· · · ') indicate where a measurement had to be removed due to inadequate wavelength coverage in the detector or chip gap interference (see § 3.3.1). The quoted uncertainties in the EW results include measurement errors, errors from any possible variance in the pseudo-continuum, and the uncertainty from the host galaxy contamination correction.

Name	Day[a*]	EW{CaII}[b*]	EW{SiII}[b*]	EW{MgII}[b*]	$v_{ej}^{c*}/1000.0$
03D1ax	-2.30 (0.11)	117.6(15.4)	13.8(2.0)	105.3(10.0)	11.84(0.29)
03D1bk	-5.23 (0.25)	95.7(11.6)	21.0(3.7)	98.3(18.2)	12.71(3.40)
03D1cm	-4.42 (0.59)	52.0(13.1)	14.8(10.6)	125.0(27.5)	16.98(1.81)
03D1co	7.42 (0.44)	87.8(16.9)	16.7(3.4)	246.2(21.8)	13.99(6.45)
03D1ew	1.53 (0.91)	144.2(19.5)	23.5(12.7)	83.2(26.4)	20.21(1.32)
03D4cj	-8.05 (0.01)	· · ·	5.9(6.1)	131.6(13.8)	· · ·
03D4cn	0.53 (2.42)	116.9(16.0)	17.0(5.4)	76.0(12.3)	13.85(1.14)
03D4cy	5.86 (0.59)	163.2(22.5)	8.7(5.8)	124.5(35.3)	16.38(3.22)
03D4fd	-0.88 (0.70)	100.2(14.3)	21.4(5.2)	79.4(16.4)	14.83(0.45)
03D4gl	8.27 (0.28)	104.8(16.6)	17.0(5.3)	72.9(10.4)	20.42(1.96)
04D1de	-6.80 (0.10)	91.4(14.5)	9.4(1.3)	105.1(12.9)	20.78(1.01)
04D1hd	1.85 (0.04)	· · ·	11.9(11.5)	99.1(21.4)	15.25(1.44)
04D1hy	-2.19 (0.44)	· · ·	15.5(6.0)	101.4(16.9)	16.11(2.05)
04D1ow	6.28 (0.42)	139.0(14.9)	21.1(10.2)	92.7(22.4)	14.66(3.02)

continued on next page

Table 3.2

(continued)

Name	Day[a*]	EW{CaII}[b*]	EW{SiII}[b*]	EW{MgII}[b*]	$v_{ej}^{c*}/1000.0$
04D2ae	-1.95 (1.78)	···	13.1(7.5)	128.4(18.7)	19.41(1.87)
04D2mh	1.58 (0.24)	116.5(29.1)	18.2(11.9)	···	14.41(5.15)
04D3dd	3.68 (1.69)	109.5(19.8)	30.7(15.9)	···	16.97(1.42)
04D3fq	1.35 (0.66)	83.3(23.4)	26.6(10.2)	102.5(26.2)	16.26(2.76)
04D3kr	5.37 (0.09)	···	15.8(1.8)	118.0(11.6)	14.43(1.63)
04D3lp	1.00 (0.20)	100.1(16.9)	···	···	17.62(2.28)
04D3mk	-1.47 (0.55)	···	2.2(1.0)	129.0(15.4)	12.31(2.08)
04D3ml	-0.89 (0.84)	96.8(11.6)	···	138.9(25.3)	13.06(1.53)
04D3nq	9.36 (0.04)	···	···	154.5(34.8)	···
04D3ny	2.15 (0.67)	···	26.9(7.4)	91.3(18.8)	11.23(4.32)
04D4dm	3.55 (0.47)	···	9.7(4.9)	120.6(24.5)	18.56(2.50)
04D4hu	6.22 (0.29)	68.6(11.2)	12.9(3.0)	···	···
04D4ic	2.92 (0.66)	···	17.7(7.9)	137.0(21.3)	15.92(1.69)
04D4ii	-4.58 (0.34)	···	10.7(3.9)	122.2(15.3)	19.99(3.21)
04D4jy	2.00 (0.40)	73.9(24.8)	···	···	15.34(1.48)
05D1az	8.85 (0.17)	75.6(13.5)	8.9(7.0)	102.1(17.5)	14.13(0.15)
05D1cc	6.80 (0.15)	89.7(17.9)	···	102.0(11.8)	12.79(0.58)
05D1em	6.69 (0.23)	126.8(17.7)	25.0(16.5)	140.9(34.2)	14.95(2.76)
05D1er	2.83 (0.42)	···	29.0(5.5)	160.7(18.9)	16.35(1.83)
05D1ju	6.28 (0.27)	163.2(24.6)	13.2(3.6)	116.50(15.7)	18.46(2.79)
05D1kl	-4.27 (0.21)	97.0(17.0)	7.6(5.3)	100.8(14.9)	18.92(3.56)
05D2ab	-1.30 (0.08)	···	13.8(7.5)	93.5(11.3)	15.34(3.64)
05D2ah	-2.49 (0.03)	···	10.2(10.4)	92.0(21.0)	···
05D2ck	0.730 (0.74)	71.5(24.7)	24.4(8.3)	148.7(24.0)	14.07(0.36)
05D2ja	9.63 (0.12)	···	···	161.3(25.3)	···
05D3ax	8.03 (0.39)	118.9(9.0)	···	65.6(7.2)	14.77(0.62)

continued on next page

Table 3.2

(continued)

Name	Day[a*]	EW{CaII}[b*]	EW{SiII}[b*]	EW{MgII}[b*]	$v_{ej}^{c*}/1000.0$
05D3cf	13.68 (0.41)	···	···	273.1(44.1)	···
05D3cq	11.6 (1.35)	106.9(23.1)	···	···	13.51(0.32)
05D3cx	10.28 (0.61)	···	27.2(5.7)	98.5(13.6)	10.01(0.33)
05D3km	1.46 (0.31)	87.1(19.7)	···	···	13.67(2.07)
05D3kt	-3.86 (0.30)	···	···	123.5(15.2)	18.34(2.68)
05D3lb	-1.21 (0.24)	···	9.2(2.6)	88.5(7.7)	19.16(1.35)
05D3mh	2.71 (0.40)	96.4(22.1)	25.6(4.6)	154.3(21.5)	13.43(1.79)
05D3mn	2.82 (0.40)	80.7(25.7)	14.8(3.7)	136.4(14.7)	13.88(0.24)
05D3mq	8.45 (0.07)	···	3.6(15.1)	232.8(35.2)	···
05D4av	5.84 (0.15)	···	9.3(6.7)	54.1(9.5)	···
05D4bm	-3.81 (0.05)	162.0(14.3)	14.5(2.9)	85.7(7.8)	19.98(0.99)
05D4cn	0.39 (0.32)	62.3(10.7)	18.2(4.3)	146.2(13.2)	14.10(0.57)
05D4dy	2.13 (0.55)	···	23.2(6.6)	127.1(19.2)	11.33(2.50)
05D4gw	0.13 (0.34)	162.6(22.1)	16.8(5.9)	115.8(13.8)	18.70(2.08)
05D4fo	-5.31 (0.03)	···	28.6 (5.1)	82.6 (11.7)	···

a — Rest-frame day, relative to B' max

b — Equivalent Width, Å

c — Ejection velocity, km/s

* 1σ *errors listed in parentheses*

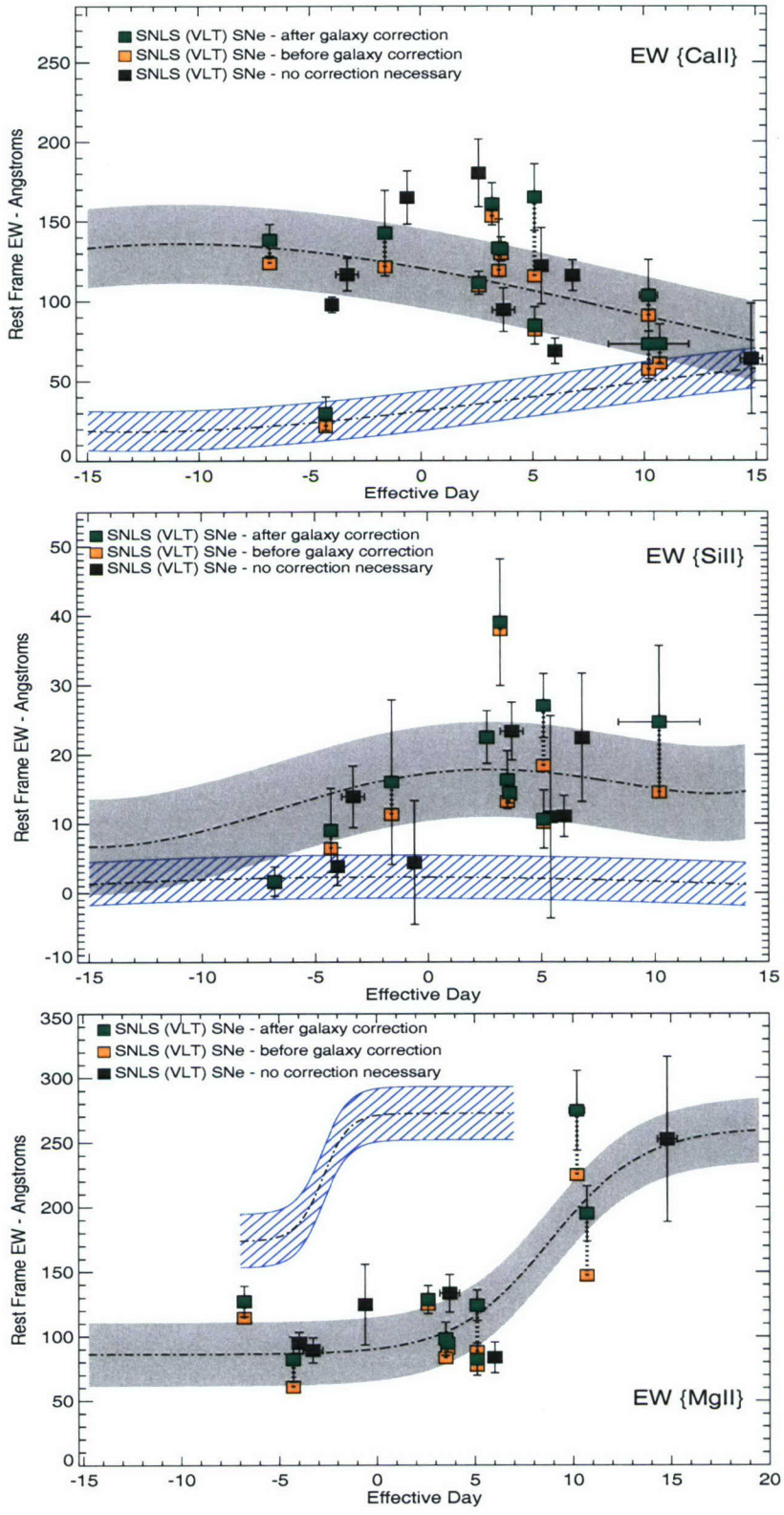

Figure 3.14: Measurements of the EW of the 'CaII H&K', 'SiII', and 'MgII' features (from top to bottom), versus rest frame epoch for the 2° set of high-z spectra (SNe observed at the VLT for the SNLS). The symbols and contours in this plot are the same as in Figure 3.13.

Table 3.3: Equivalent width and ejection velocity results for the secondary set of high redshift SNe Ia. These objects were observed by the SNLS at the VLT. The relevant information on these SNe is summarised in § 2.5 (see also Table 2.10).

Name	Day[a*]	EW{CaII}[b*]	EW{SiII}[b*]	EW{MgII}[b*]	$v_{ej}^{c*}/1000.0$
03D1dt	6.0 (0.1)	68.6(7.9)	11.0(2.9)	83.6(11.8)	14.33(3.78)
04D1aj	14.8 (0.5)	63.7(34.5)	···	252.4(63.9)	11.86(0.74)
04D1ff	3.2 (0.1)	160.9(13.2)	39.0(9.1)	···	17.08(2.12)
04D1hx	5.1 (0.1)	165.0(20.9)	27.0(4.6)	124.0(11.7)	17.63(0.22)
04D1hk	-4.3 (0.1)	29.6(10.4)	9.0(6.0)	82.0(17.6)	12.02(0.91)
04D1ks	-0.6 (0.1)	164.8(16.7)	4.3(8.9)	124.7(31.2)	17.65(1.74)
04D1ow	6.8 (0.1)	116.0(9.7)	22.4(9.2)	···	12.29(2.65)
04D2al	-1.6 (0.1)	142.6(26.9)	15.9(11.9)	···	18.83(2.49)
04D2an	-3.3 (0.5)	116.6(10.2)	13.8(4.4)	89.2(9.8)	16.39(1.79)
04D2ca	10.2 (1.8)	72.9(21.7)	24.6(11.0)	···	13.73(1.75)
04D2cf	10.7 (0.1)	73.0(12.4)	···	194.9(21.4)	11.91(0.36)
04D2cw	10.2 (0.4)	103.3(22.4)	···	274.6(30.8)	20.29(4.09)
04D2fp	3.5 (0.1)	133.1(18.1)	16.3(4.2)	98.0(12.9)	16.55(0.92)
04D2fs	3.6 (0.1)	132.5(7.5)	14.4(1.5)	94.5(6.9)	17.11(0.66)
04D2gp	3.7 (0.5)	94.5(13.6)	23.3(4.1)	133.3(14.5)	14.79(2.41)
04D4bk	5.4 (0.1)	121.9(23.8)	10.9(14.5)	···	11.18(3.19)
04D4bq	2.6 (0.1)	111.3(7.2)	22.4(3.8)	128.5(10.8)	14.89(2.07)
04D4fx	-6.8 (0.1)	138.2(9.9)	1.6(2.1)	127.1(11.9)	18.53(2.43)
04D4hf	2.6 (0.1)	180.2(21.2)	···	···	18.48(1.89)
04D4id	5.1 (0.1)	84.5(11.8)	10.5(4.4)	82.2(12.5)	14.58(2.77)
04D4jr	-4.0 (0.1)	97.7(4.9)	3.8(2.7)	94.9(8.2)	17.08(2.47)

a — c are the same as in Table 3.2.

* 1σ *errors listed in parentheses*

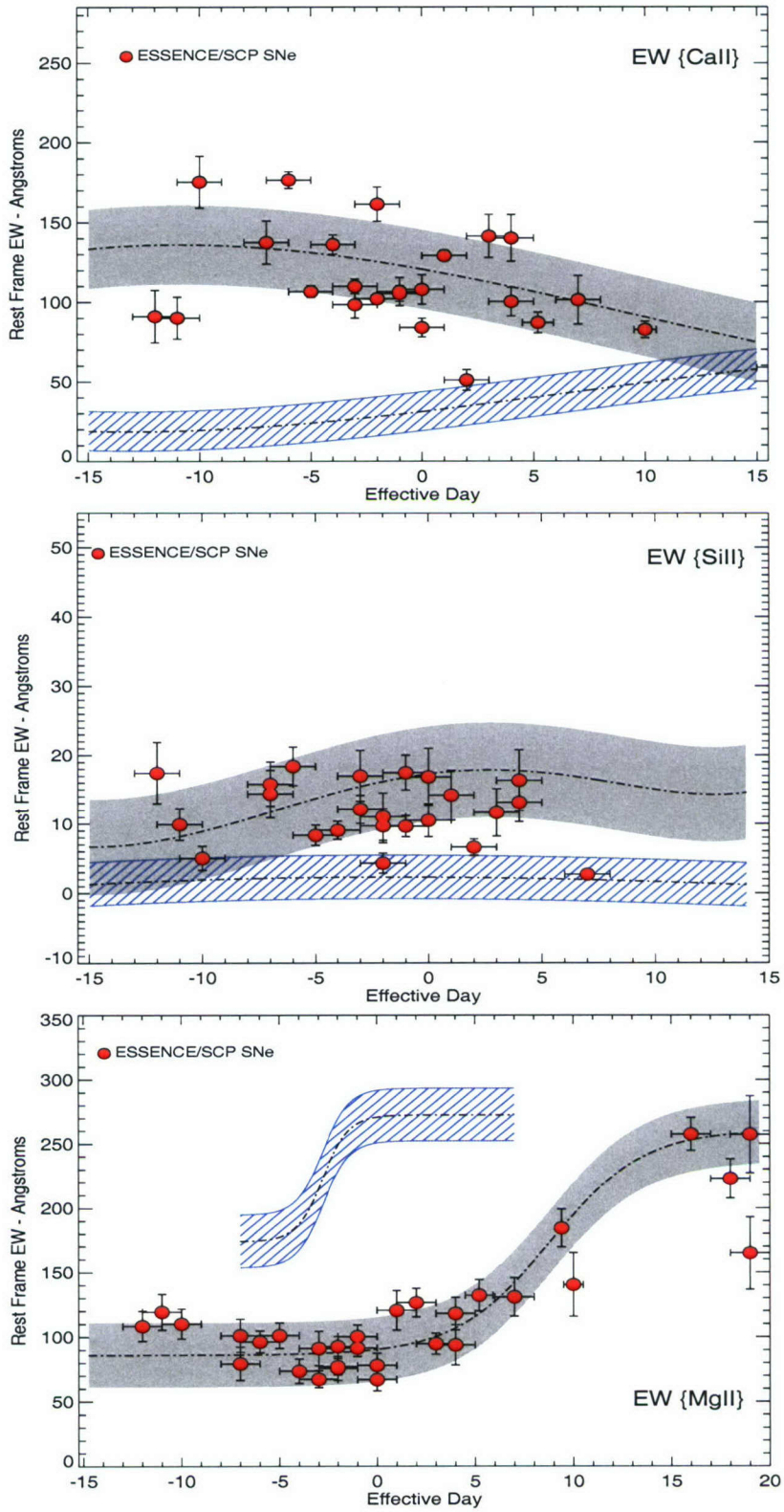

Figure 3.15: Measurements of EW for the 'CaII H&K', 'SiII', and 'MgII' features (from top to bottom), versus rest-frame epoch, in the tertiary data set of SNe observed by the SCP and ESSENCE surveys. The contours are the same as those defined in Figure 3.3 and the filled points are the high-z EW results. Unlike the results from the 1° and 2° data sets (Figures 3.13 and 3.14), these measurements were not corrected for any host galaxy contamination, as the necessary photometric information for these corrections was not available. Instead, a much more strict cut of any possibly contaminated objects was made (see § 2.7) before including these SN in this analysis.

Table 3.4: Equivalent width and ejection velocity results for the tertiary set of high redshift SNe Ia. These objects were observed by the SCP and ESSENCE collaborations. A summary of the details and sources for these spectra can be found in § 2.7 and Table 2.13.

Name	Day[a]*	EW{CaII}[b*]	EW{SiII}[b*]	EW{MgII}[b*]	v_{ej}^{c*}/1000.0
1997ai	5.2 (0.7)	···	···	···	11.98(2.0)
1997am	10.0 (0.5)	82.5(5.2)	···	140.4(24.6)	14.14(0.34)
2002iz	-1.0 (1.0)	106.5(8.8)	17.4(2.5)	100.3(8.9)	21.11(1.15)
2002iz	19.0 (1.0)	91.5(12.5)	12.4(2.5)	257.2(30.0)	13.24(.20)
2002ja	2.0 (1.0)	51.0(6.4)	6.6(1.1)	126.5(11.0)	12.06(2.47)
2002jb	-7.0 (1.0)	137.4(13.4)	14.3(3.4)	79.4(12.8)	16.31(2.27)
2002js	7.0 (1.0)	101.3(15.2)	2.7(0.1)	130.9(14.9)	13.38(1.86)
2002jd	-3.0 (1.0)	109.8(4.5)	16.9(3.7)	91.1(13.2)	15.8(2.23)
2002jd	16.0 (1.0)	58.7(6.0)	···	257.5(12.9)	13.39(2.26)
2002jt	0.0 (1.0)	107.8(9.2)	16.8(4.1)	78.1(9.3)	11.12(1.92)
2002jw	-2.0 (1.0)	102.0(3.0)	4.3(1.4)	75.7(9.3)	18.14(3.15)
2002jw	19.0 (1.0)	104.0(10.0)	···	164.7(28.1)	18.14(3.15)
2003jo	3.0 (1.0)	141.3(13.5)	11.6(3.4)	94.7(8.1)	16.10(1.93)
2003ju	18.0 (1.0)	···	6.2(2.3)	222.8(15.2)	···
2003jv	-2.0 (1.0)	···	9.7(2.4)	77.2(6.3)	···
2003js	-5.0 (1.0)	106.5(3.5)	8.3(1.5)	101.1(9.8)	19.39(1.20)
2003jw	-6.0 (1.0)	176.5(5.2)	18.3(2.8)	96.3(8.4)	17.66(0.65)
2003jy	-10.0 (1.0)	175.2(16.2)	5.0(1.7)	110.2(11.5)	20.67(0.64)
2003kk	-4.0 (1.0)	136.0(6.0)	9.0(1.3)	73.6(9.5)	18.98(1.41)
2003kl	-3.0 (1.0)	98.3(8.4)	12.1(2.0)	67.3(6.5)	17.36(1.82)
2003kl	-3.0 (1.0)	83.9(5.8)	10.5(2.4)	67.0(8.6)	17.36(1.82)
2003km	-12.0 (1.0)	91.0(16.4)	17.4(4.4)	108.4(11.5)	19.7(1.91)

continued on next page

Table 3.4

(continued)

Name	Day[a]	EW{CaII}[b*]	EW{SiII}[b*]	EW{MgII}[b*]	$v_{ej}^{c*}/1000.0$
2003km	-11.0 (1.0)	90.0(13.1)	9.9(2.2)	119.3(13.9)	20.25(2.53)
2003ko	-2.0 (1.0)	161.3(10.7)	11.0(3.4)	92.6(7.6)	21.71(1.21)
2003kt	4.0 (1.0)	140.1(14.6)	16.3(4.4)	93.8(15.5)	13.09(1.85)
2003kp	1.0 (1.0)	129.0(3.3)	14.1(3.6)	120.5(15.2)	14.22(1.74)
2003le	-1.0 (1.0)	105.3(4.8)	9.6(1.5)	91.5(6.4)	15.70(1.82)
2003ln	4.0 (1.0)	100.2(9.0)	13.1(2.7)	118.0(12.5)	14.82(2.0)

a — c are the same as in Table 3.2.

* 1σ *errors listed in parentheses*

3.3.5 High-z Type Ia SNe — CaII H&K v_{ej} Measurements

The CaII H&K v_{ej} calculation did not deviate from the low-z method defined in § 3.2.4, but the lower S/N in the high-z data meant these spectra had to be smoothed before the Gaussian fits to the CaII H&K feature could be made. The same 60 Å median filter that was used to help locate the local maxima for the high-z EW measurements (see § 3.3.2) was used for this purpose as well. The smoothed CaII H&K feature was fit with a Gaussian model as described in § 3.2.4 (see Fig. 3.16 for an example). The error spectra (when available) were used to weight these MPFIT-determined Gaussian curves. For the objects without measurement errors (the tertiary data set), an average spectrum from the sky background observed at Gemini was used as a weighting function. The statistical error in the final v_{ej} values was estimated by propagating the estimated redshift uncertainties through the velocity calculation. Additional statistical error bars were (as with the low-z spectra, see § 3.2.4) estimated by the difference between the velocity determined with the initial and final feature fits. No corrections were necessary to account for the systematic error from host galaxy contamination as this error was minimal for v_{ej} measurements made on the SNe within the 65% contamination limit defined in § 2.4.4.4.

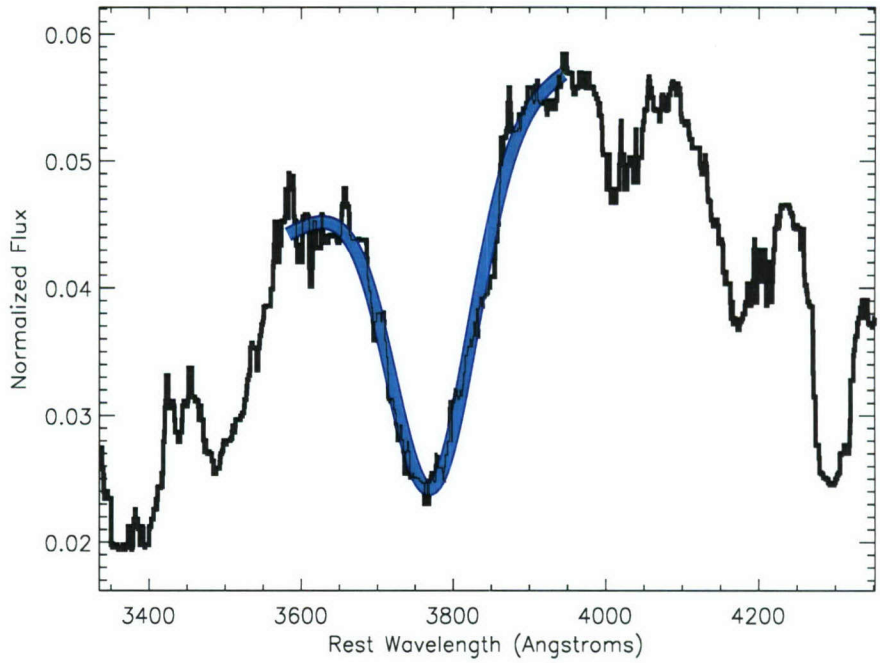

Figure 3.16: An example of a CaII H&K ejection velocity measurement on a high-z SNLS supernova. A Gaussian curve with a linear component is fit to the median filtered spectrum with the IDL MPFIT routine. A fit was made to a small ($\approx$ 50.0 Å) region near the apparent minimum of this feature to generate the initial parameters for the final fit. This final fit was then made to the entire feature and the minimum was used to estimate the blueshift of the feature for the $v_{\rm ej}$ calculation.

3.3.6 High-z Type Ia SNe CaII H&K $v_{\rm ej}$ Results

The $v_{\rm ej}$ measurements from the high-z SNe are printed in the final column of Tables 3.2, 3.3, and 3.4. These results are also displayed in Figure 3.17 below. All of the measurements appear to be in good agreement with the low-z trends. This corroborates the results from previous comparisons of SNe Ia photospheric velocities from distant and nearby supernova (Hook *et al.*, 2005; Blondin *et al.*, 2006; Balland *et al.*, 2006; Garavini *et al.*, 2006) with a data set that is larger than all of the existing high-z studies combined. The significance of these results and their implications for SNe Ia evolution are discussed in the next chapter.

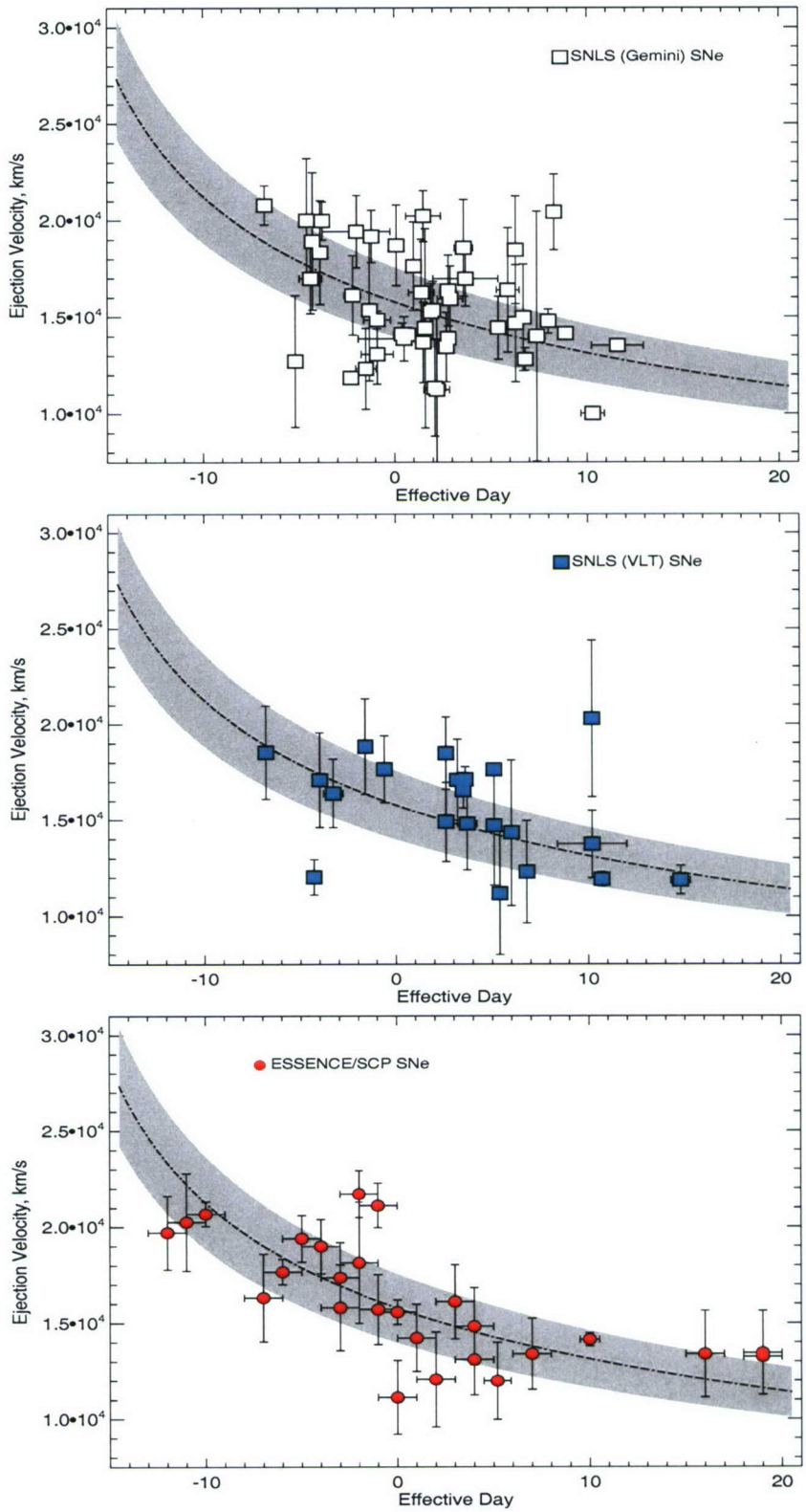

Figure 3.17: The epoch evolution of CaII H&K ejection velocities measured on high redshift SNe Ia. These results (from top to bottom) are from the 1°, 2°, and 3° high-z data sets, respectively. The expected trend (see § 3.2.4) and 1σ contours are displayed as in Figure 3.5. These results include 94 measurements from 90 different high-z objects. This large set of $v_{\rm ej}$ results appears to be consistent with the trends determined from local SNe.

Chapter 4

Comparison of Distant and Nearby Type Ia SNe – Homogeneity and Cosmology

4.1 High-z Type Ia SNe — Sub-Type Identification with Equivalent Width Results

As discussed in § 3.2.2.1, the EW measurements made on the high-z SNe can assist in the quantitative identification of any objects that fall into the two general classes of Type Ia sub-types. The EW results (corrected for systematic effects, see § 3.3.2 and § 3.3.3) from the high-z data are displayed along with the low-z SNe in Figures 4.1 and 4.2. This comparison demonstrates that a few distant SNe did appear to fit the 1991T-like or 1991bg-like trends; these objects are marked with open circles in these two figures. The results from the $v_{\rm ej}$ measurements were also investigated for any significant or interesting outliers, but due to the limited epoch coverage of the high-z sample, this particular parameter is not well suited to identifying SNe Ia sub-types. The $v_{\rm ej}$ results are displayed in Fig. 4.3. This measurement is better for investigating the bulk properties of the high-z set, which is discussed in the next section (§ 4.2).

Overluminous 1991T-like SNe Ia have less absorption from IME at certain epochs, so the high-z objects with particularly low EW measurements are quantitatively more consistent with

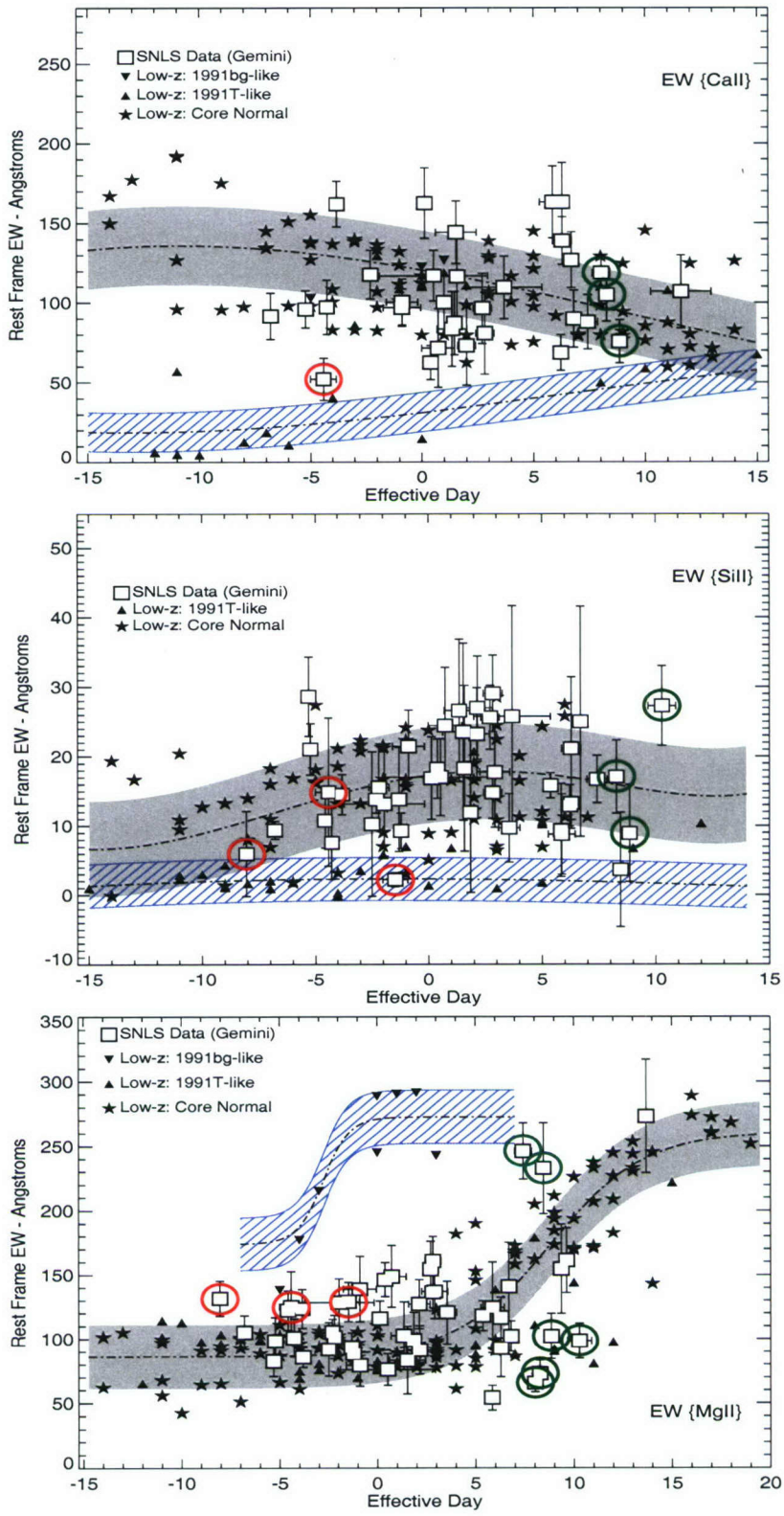

Figure 4.1: From top to bottom, measurements of EW{CaII}, EW{SiII}, and EW{MgII} from the primary set of high-z SNe (open squares) compared to the EW results from the low-z sample (filled symbols). The contours in each plot are the same as Fig. 3.3. The objects that were identified as 1991T-like SNe are circled in red. The objects circled in dark green and light green are outliers that were possible 1991T/1991bg-like (respectively) SNe that were ultimately determined to be core normal SNe Ia.

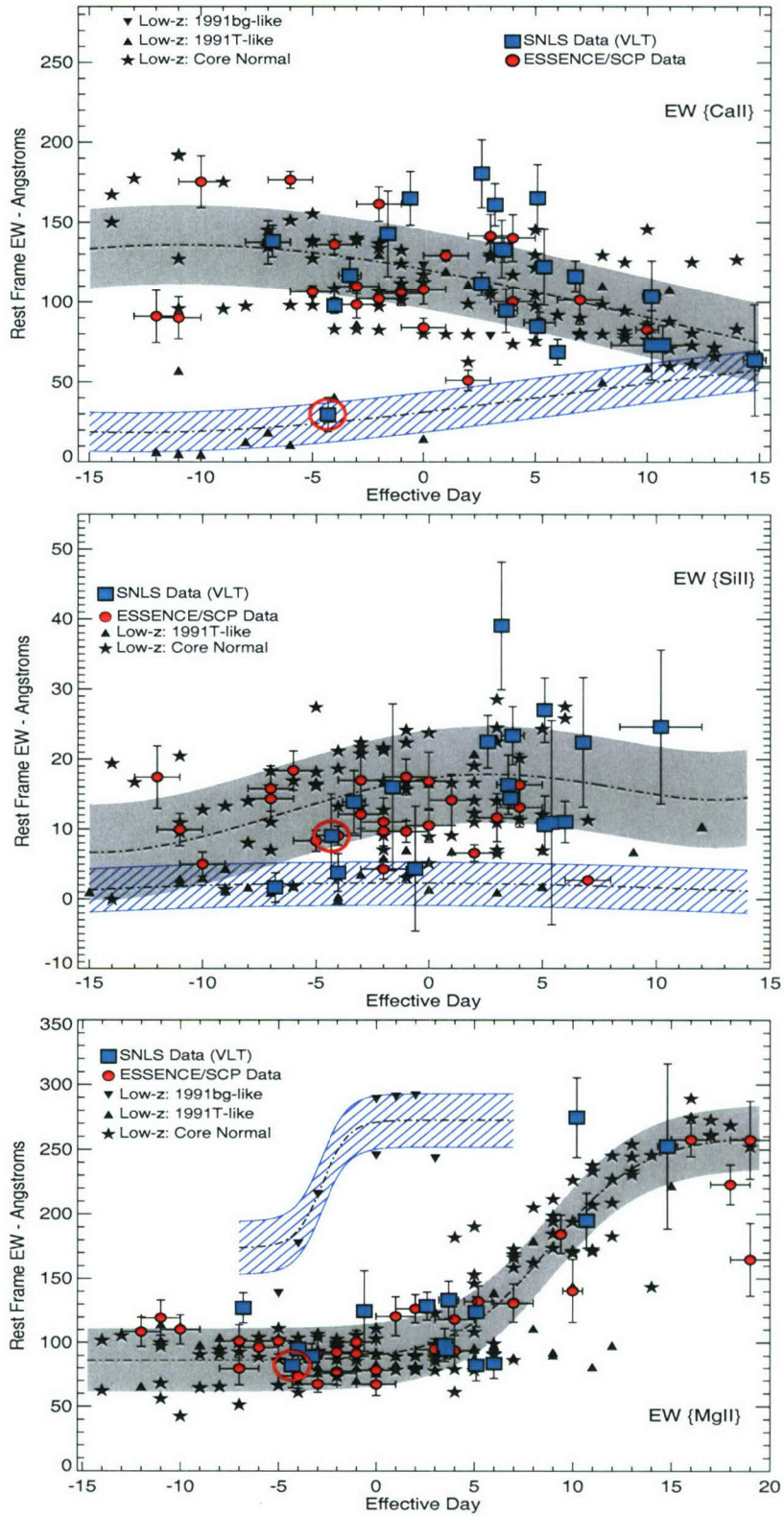

Figure 4.2: As in Figure 4.1, a comparison of EW{CaII}, EW{SiII}, and EW{MgII} results from the secondary (squares) and tertiary (circles) sets of high-z SNe. The EW results from the low-z sample (filled stars and triangles) are shown as well. The contours in each plot are the same as Fig. 3.3. The red circle indicates the SN that was determined to be spectroscopically consistent with 1991T-like SNe sub-type.

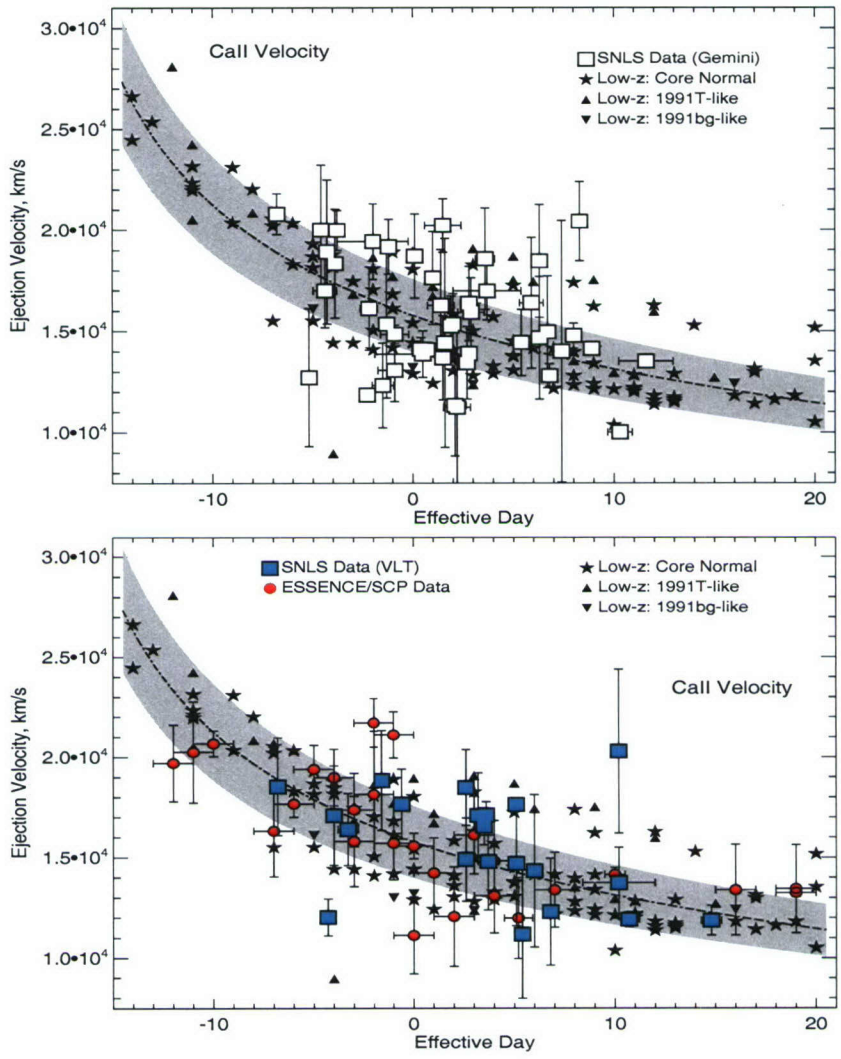

Figure 4.3: As in Figure 3.17, a comparison of the epoch evolution of the CaII H&K ejection velocity in the high-z and low-z data.

these SNe than with the core normal objects. In the primary data set, the EW measurements highlight 03D1cm (based on EW{CaII}-top, Fig. 4.1), 03D4cj, 04D3mk (based on EW{SiII}-middle, Fig. 4.1), 03D4gl, 05D1az, 05D3ax, and 05D3cx (based on EW{MgII}-bottom, Fig. 4.1) as 1991T-like candidates. The objects from this sample that were determined to be similar to the SN 1991T sub-type are marked with red circles in this figure, while the dark green circles indicate the outliers that retained a core normal SNe classification. The light green circles indicate possible 1991bg-like SNe, these are discussed later in this section. The reader is referred to Table 3.2 for the specific epoch and EW measurement results of these objects. The following paragraphs detail how these final sub-type classifications were made.

A closer look at the outliers in the EW{MgII} results shows that is not possible to firmly

identify any of them as overluminous SNe Ia. For example, SNLS SN 03D4gl has an EW{MgII} measurement that is consistent with the 1991T-like trends, but the EW{SiII} measured for this object is high enough to negate any likeness to this particular sub-type. The paramaterised lightcurve fit to this object (Astier *et al.*, 2006) resulted in an s value (0.957 ± 0.033) that is completely consistent with core normal SNe. This object thus cannot be compared to the known class of overluminous SNe Ia with any certainty and the most likely explanation is that the lower S/N in this object is at the root of its peculiarity (with regards to this EW measurement) rather than any true physical difference.

A similar conclusion can be reached about three of the other EW{MgII} outliers. In the case of 05D1az, 05D3ax and 05D3cx, the SNe Ia sub-type identification implied by the low EW{MgII} measurements is completely contradicted by a normal amount of SiII absorption in these objects. This contradiction implies that the differences between these SNe and the low-z core normal objects in this EW{MgII} parameter space is not indicative that they are overluminous SNe Ia sub-types.

Three other outliers do have additional evidence of being more like the known class of 1991T-like objects. The SNLS supernova 03D4cj displayed a smaller amount of SiII than a typical core normal object. The error bars on this measurement are relatively large (EW{SiII}$= 5.9 \pm 6.1$ Å), but the photometric data for this object supports the conclusion that it is a 1991T-like SN or even more peculiar; Astier *et al.* (2006) stated that the lightcurve from this SN was incompatible with the model used to fit all of the other SNLS SNe. The χ^2 template fits to 03D4cj also indicate that it is similar to SN 1991T.

The 1991T-like classification appears valid for SNLS supernova 03D1cm as well. This SN has a very low EW{CaII} measurement and an EW{SiII} result that (within large error bars, EW{SiII} $= 14.8 \pm 10.6$ Å) is also consistent with the low values measured in 1991T-like objects. Photometrically, 03D1cm is also more like a 1991T-like SN as it had one of the highest stretch values from the entire set of Gemini SNLS data at $s = 1.173 \pm 0.061$ (Astier *et al.*, 2006). The SNLS SN 04D3mk also had a very low, well constrained EW{SiII} value. At the epoch this object was observed, the EW{MgII} result cannot differentiate between normal and overluminous SNe and the EW{CaII} measurement was unusable as it fell on the gap between GMOS detectors (e.g., § 3.3.1). The final photometry of this object did

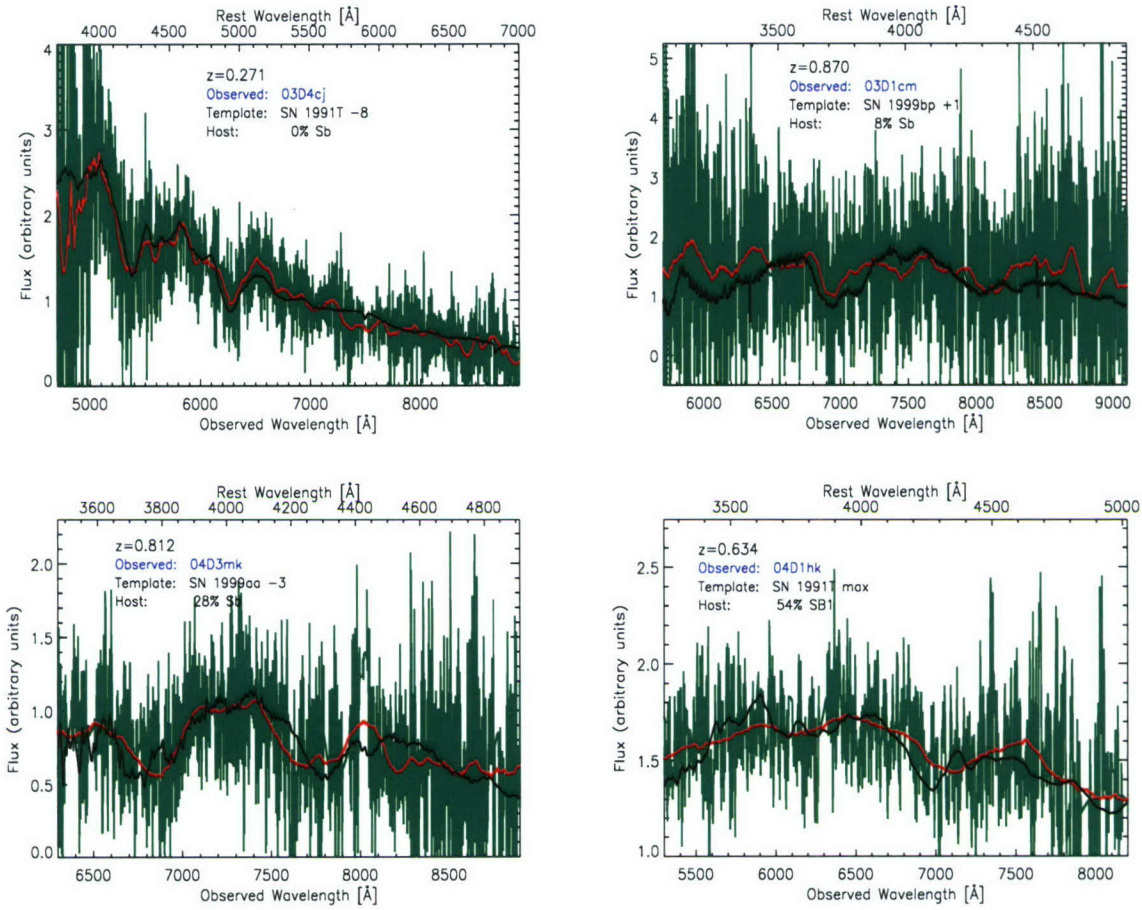

Figure 4.4: Four SNe Ia — 03D4cj, 03D1cm, 04D3mk, and 04D1hk — from the high-z data set that demonstrate a quantitative similarity to the 1991T-like SNe Ia sub-type. The green spectrum is the observed spectrum without any binning. The black spectrum is the best-fitting SN from the low-z library and the red spectrum a smoothed version of the observed spectrum. The primary evidence for the similarity of these objects to 1991T-like SNe is the EW{CaII} and EW{SiII} measurements, although in each case the χ^2 fits of the 1991T-like objects were quantitatively much better than those of core normal SNe Ia.

not reveal any photometric peculiarities, but the χ^2 template matches to 04D3mk singled out overluminous SNe Ia spectra only as the most similar low-z objects. This supports the quantitative similarities of 04D3mk to this particular SN Ia sub-type. With this evidence, SNLS objects 03D1cm and 04D3mk are the most distant supernova (at $z = 0.87$ and $z = 0.812$, respectively) to be shown to be spectroscopically similar to the 1991T-like SNe Ia sub-types. The χ^2 template matches of these three objects (and one 1991T-like SN from the 2° data set) to 1991T-like SNe are illustrated in Figure 4.4.

The SNLS SNe 03D1co and 05D3mq are marked with light green circles in the bottom panel of Fig. 4.1. These SNe are 1991bg-like candidates as their large EW{MgII} values are

more consistent with the excess absorption measured in the subluminous low-z SNe. However, these two high-z SNe had normal amounts of SiII (albeit with large error bars in the case of 05D3mq) near 4000 Å. This is a feature that has yet to be observed in any 1991bg-like SNe because it is obscured by additional absorption from TiIII and FeII. This evidence, combined with the normal photometric parameters (Astier *et al.*, 2006) derived for these objects, and the fact that spectroscopic template matches of these SNe to 1991bg-like objects resulted in poor χ^2 results, is enough to justify that these SNe are more like core normal SNe than any of the underluminous SNe observed to date.

The results from the secondary and tertiary data sets show the same general agreement with the trends from low-z core normal objects (see Figure 4.2). Only one object, the SNLS supernova 04D1hk, is consistently different from the mean trend and dispersion of the normal SNe Ia. The EW{CaII} and EW{SiII} measurements, as well as the χ^2 fits (Figure 4.4) clearly show that the spectrum from this SN is quantitatively more like a 1991T-like object. This implies that 04D1hk is the fourth SNe in this large data set to be quantified as spectroscopically similar to this SNe Ia sub-type.

The equivalent width results of this large high-z set note 4 objects (out of 96 distant supernovae with EW results, $\sim 4\%$) that are spectroscopically similar to the class of 1991T-like SNe sub-types that have been observed locally. Previous studies of distant SNe Ia have noted a similarly small percentage of these sub-types in the high-z samples; only SNe 2002iv ($z = 0.231$), 2003jn ($z = 0.33$), and 2003lh ($z = 0.56$) (Matheson *et al.*, 2005; Krisciunas *et al.*, 2005) have been shown to be quantitatively similar to 1991T or 1999aa. This is in contrast to the apparent contribution of these sub-types to the low-z SNe sample, which is roughly 10% to 20% (Li *et al.*, 2001a; Strolger *et al.*, 2002). This has been interpreted as a possible sign of evolution (Branch, 2001; Li *et al.*, 2001a,b) or of a significant difference between the nearby and distant SNe Ia populations. The identification of the 4 possible 1991T-like objects in this extensive high-z sample doubles the number of these sub-types observed at higher redshifts, but the percentage of identified 1991T-like SNe is still much lower than at low-z. It is difficult to determine the significance of this apparent discrepancy due to the unknown influence of selection effects on this particular comparison of the high-z and low-z data sets. For example, the low-z peculiar objects are often singled out for spectroscopic follow up and thus may be

over-represented in the nearby sample.

It may be that the difference between the fraction of these sub-types at different redshifts is primarily an effect of the epoch coverage differences between these data sets. SNe 1991T and 1999aa displayed unusual spectroscopic features primarily before maximum light and then evolved to look little different than core normal SNe. Within the low-z set considered in this thesis, 77% of the SNe were observed at least once during these pre-maximum epochs, compared to only 37% of the high-z sample. With the simple assumption that this factor of ~ 2 difference has reduced the number of overluminous sub-types possibly identified in the high-z sample by a similar amount, the disparity in the percentage of sub-type identifications between the two data sets is immediately minimised. The identification of these sub-types, and the general agreement between the spectroscopic parameters measured at all redshifts, demonstrates that the range of SNe spectroscopic characteristics that have been observed locally are also seen at high redshifts. The next section will address the significance of this result with a statistical comparison of these quantitative spectroscopic measurements.

4.2 Statistical Comparison of Nearby and Distant SNe Ia

The homogeneity of SNe Ia spectroscopic properties at different redshifts was tested with a statistical comparison of the EW and $v_{\rm ej}$ results of the high-z and low-z supernovae. Any differences between the high-z measurements and the low-z core normal mean trends (i.e., a low-z 'model') were initially quantified with a χ^2 test. The 4 objects that were determined to be spectroscopically similar to the 1991T-like sub-types were removed from the high-z set for this comparison and the reader is referred to § 3.2.2 and § 3.2.5 for a description on how the low-z core normal mean trends were derived. Although this comparison is not necessarily a direct test of evolution, a lack of a significant, quantitative difference from the established spectroscopic trends of these objects would be a positive indication of the homogeneity of SNe Ia across redshifts. When making these χ^2 calculations, the full uncertainties for each measurement (quoted in Tables 3.2 - 3.4) were used. The 1σ dispersion in the low-z trends was also considered by adding this error (in quadrature) to the uncertainty of each high-z measurement. The effects of the uncertainty in the estimated epoch for every high-z result was added (again, in quadrature) according to the low-z model for each measurement. The results

from these tests — which were computed for the 1° data set, the combined 2° and 3° sets, and the entire set of high-z SNe — are shown in Table 4.1.

Feature	Reduced[a] χ^2	DOF[b]	*Prob*[c]
1° Data			
EW{CaII}	1.10	30	0.67
EW{SiII}	0.47	40	$\approx$ 0.00
EW{MgII}	1.86	44	>0.999
v_{ej}	1.03	45	0.64
2° & 3° Data			
EW{CaII}	1.11	45	0.72
EW{SiII}	0.82	38	0.23
EW{MgII}	0.73	43	0.09
v_{ej}	0.92	46	0.63
All High-z Data			
EW{CaII}	1.09	76	0.73
EW{SiII}	0.63	79	$\approx$ 0.00
EW{MgII}	1.29	88	0.95
v_{ej}	0.92	89	0.31

Table 4.1: A χ^2 comparison of the spectroscopic features in high-z supernovae (as measured with EW and CaII H&K ejection velocity) and the mean trends exhibited for these quantities by local SNe Ia. These results show that there are no significant differences (i.e., greater than 2σ) between distant and nearby SNe, with the exception of the EW{MgII} feature (specifically in the 1° set of SNLS SNe).
a — χ^2/dof calculated for the measurement/data set in question and the corresponding low-z mean trend
b — degrees of freedom used when calculating the reduced χ^2, $N_{\rm datapoints} - 1$
c — probability (0.00 - 1.00) that the null hypothesis, that the high-z data are consistent with the 'model' given by the derived low-z mean trend, can be rejected.

These results confirm the general impression given by Figures 4.1, 4.2 and 4.3 — that there is no significant difference between the spectra of local core normal SNe Ia and those observed at high-z with regards to the EW and v_{ej} measurements. With the exception of the EW{MgII} results (from the primary data set only), all of these high-z measurements demonstrate a less than 2σ difference from the corresponding low-z trends.

The reality of the significant difference in EW{MgII} results is questionable. The 1° data set does not represent a significantly different group of SNe (with regards to redshift or environment sampling) than the objects contained in the remaining high-z sample, yet the EW{MgII} results in the 2° and 3° data sets did not deviate in any measureable way from the low-z trends. This suggests that this significant difference in the 1° SNe may be a statistical artifact caused by

the differences in the epoch sampling and total number of objects between the 1° and low-z data sets. Figure 3.3 shows that there are an appreciable number of low-z core normal points between 0 and +10 days past maximum (where the bulk of the outliers in the 1° are located) to help estimate the 1σ range on the empirically derived mean trend (see § 3.2.2). Yet these points are from 15 different SNe only; half of the number of 1° data set SNe in the same range. The statistical difference between the two sets could possibly be explained by an underestimate of the true amount of variance in the EW{MgII} trends due to the smaller number of low-z objects.

Another factor that may be contributing to this difference is the trend for slightly bluer, brighter objects in the SNLS SNe sample (Astier *et al.*, 2006). F04 noted that the evolution of different SNe along the mean trend for EW{MgII} correlated with decline parameter, with objects wider lightcurves making the 'jump' in EW at later times. The small group of outliers below the EW{MgII} mean trend between +5 and +10 days may just be reflecting a slightly brighter group of SNe in the high-z sample. The average s value within these SNe is just above 1.0 [this corresponds to brighter SNe, see Fig. 9 in Astier *et al.* (2006)], which supports this hypothesis. This particular comparison may just be more sensitive to this slight trend in the 1° data set than the other EW results.

It may also be possible that this EW{MgII} difference is a manifestation of some mistakes made by the author during the host galaxy contamination corrections. Recall from § 3.3.3 that the EW values for each measurement made on a spectrum contaminated with host galaxy flux had to be adjusted towards higher EW values. Another look at Figure 3.13 shows that an appreciable number of the discrepant EW{MgII} points in the 1° set are indeed the very measurements that did need a large amount of adjustment for this systematic error. If there is some mistake in the estimation or application of this systematic effect then perhaps that is the reason for the large χ^2 for this comparison. The outlying point at 7.45 days (SNLS SN 03D1co) in Fig. 3.13 in particular appears to support this hypothesis. However, the total distribution of the outlying EW{MgII} values, especially with regards to epoch, makes this suggestion slightly more spurious. There is a large group of high-z EW values in Fig. 3.13 between +5 and +10 days that, despite being adjusted for host galaxy effects, are still well below the mean trend. If the large χ^2 from these results is due to a systematic over- or under-adjustment of the host

galaxy errors then it should not show any grouping with regards to any other independent parameter, such as epoch. A quantitative look at the distribution of the outlying EW{MgII} points, based on host galaxy contamination and all other possible systematic effects, showed nothing to indicate that these particular errors are behind this possible difference in EW measurements.

If the difference between the EW{MgII} core normal mean trend and the SNe Ia measurements from the 1° high-z cannot be explained by these effects, then perhaps it is a sign of metallicity differences in these spectra. Explosion and nucleosynthesis calculations from Travaglio, Hillebrandt, & Reinecke (2005) and Roepke *et al.* (2006), which were computed by modelling thermonuclear burning by deflagration (as opposed to delayed detonation or detonation only) of a C+O WD progenitor, showed that at higher metallicities Type Ia SNe produce a significantly lower (by a factor of 10) amount of ^{24}Mg. In their results, the abundances of Si and Ca were relatively unaffected by these Z changes. Thus, it may be that the group of high-z SNe that are below the mean trend for this feature are all SNe from higher Z progenitors. The normal EW{SiII} and EW{CaII} measurements in these SNe support this explanation within the context of the results of these models. This Z deviation from the low-z SNe could also have some implications for the luminosity calibration of these objects [e.g., Timmes, Brown, & Truran (2003); Mazzali & Podsiadlowski (2006); Roepke *et al.* (2006) and § 4.4] and for the homogeneity of SNe Ia.

This explanation, however, is dependent on this particular set of theoretical calculations. Model SNe Ia spectra from progenitors of varying Z, calculated by Lentz *et al.* (2000), showed the opposite effect in the EW{MgII} measurements. The Lentz *et al.* (2000) spectra were calculated with a similar deflagration model SN [W7 from Nomoto, Thielemann, & Yokoi (1984)], with the metallicity changes approximated by scaling the number abundances of elements heavier than O in the unburned C+O layer. The final IME abundances were not published in Lentz *et al.* (2000), so they could not be compared directly to the Travaglio, Hillebrandt, & Reinecke (2005) results. Instead, the EW measurements defined in this thesis were made directly on the final Lentz *et al.* (2000) model spectra (by the author). These measurements showed that the SNe with higher Z had larger EW{MgII} measurements at pre-maximum epochs. The EW{MgII} results then evolved with epoch such that the different Z models were nearly

indistinguishable after maximum light.

Considering the competing explanations for the significant difference in the EW{MgII} results from the 1° data set and the complete lack of any EW{MgII} deviations in the 2° and 3° high-z sets, this disparity has minimal practical significance in negating the assumption of general homogeneity among SNe Ia at redshifts up to $z \approx 1.0$. Further investigation into this parameter is certainly warranted.

4.3 Redshift and Host Galaxy Correlations in High-z SNe Ia

If there are any evolutionary changes in the high-z objects, then some additional correlations between the deviations from the low-z results and redshift or host environment would be expected. These possible correlations are difficult to discern, however, as the epoch dependence of the measured spectroscopic features can easily overwhelm any of the more subtle differences between spectra. This time dependence was removed as much as possible by making comparisons of the residuals (see § 3.2.6), calculated with respect to the respective core normal SNe mean trends, of the high-z EW and $v_{\rm ej}$ measurements.

These residuals are plotted against redshift in the left-hand column in Figure 4.5. These comparisons illustrate that any differences between the EW and ejection velocity measurements in the high-z spectra and the derived low-z core normal trends do not correlate with redshift. Calculations of Spearman's ρ rank correlation and Kolmogorov-Smirnov tests on these results attest that the differences in the high-z data, with regards to z, are not significantly different than a random scatter. This provides additional evidence that the observed properties of these objects are not changing in any systematic way indicative of evolution.

On the right side of Figure 4.5, the measured differences are separated by both redshift and host galaxy type. The host types were only estimated for the spectra in the SNLS data sets that had clear host galaxy features (see Table 2.9) as described in § 2.4.4.3. The SNe from the 3° data set that had any evidence of host contamination were removed before any measurements were made (see § 2.7.1.1 and § 2.7.1.2) so there was no way to identify the host galaxies for these SNe in a manner consistent with the rest of the sample; they are not included in this particular analysis. The host type for each available object was placed into one of three broad categories; 'E/S0' for early (elliptical and S0) hosts, 'Early Spirals' for objects with spectroscopic features

similar to Sa and Sb galaxies, and 'Late Spirals' for Sc and irregular hosts. These categories are similar to classifications of SNe Ia hosts in the literature [e.g., Sullivan *et al.* (2003)] and parallel the definitions in § 3.2.6. By using the spectroscopic host features only to make these identifications [and not integrated spectra (Gallagher *et al.*, 2005) or model fits to the broad band spectra (Sullivan *et al.*, 2006b) of these galaxies, for example] these categories are not exact (particularly when discriminating between 'Early Spiral' and 'Late Spiral' hosts). These classifications are really designed as a prescriptive way to consistently organise this high-z data to search for any trends in the spectroscopic measurements that may have a physical basis within these broad definitions of host morphology. The sub-set of 1° and 2° SNe Ia with identifyable host galaxies includes 58 of the 70 total SNLS objects that were analysed (45 SNe from the 1° data set and 13 SNe from the 2° data set).

The panels to the right in Figure 4.5 illustrate that there are no redshift-based trends within the SNe results from each host type as well. The evolutionary histories of host galaxies within a given morphological category have more in common than galaxies of different classfications. The comparison of SNe Ia spectroscopic features at different redshifts but within similar host types should thus be more sensitive to any evolutionary effects than tests using the bulk properties of the high-z sample as a whole. The comparison illustrated in Fig. 4.5 does not have complete enough coverage at intermediate and high redshifts to reach a definitive conclusion on the issue of evolution, but this analysis does include the largest set of high-z SNe Ia spectroscopic measurements available and supports the assumption of SNe Ia homogeneity at high-z.

Measurement	N[a]	$\bar{x}$[b]	N[a]	$\bar{x}$[b]
Host Type		E/S0		Spiral
EW{CaII}	8	-0.6 (31.9)	30	-2.2 (36.2)
EW{SiII}	10	4.3 (7.9)	38	-1.3 (6.3)
EW{MgII}	8	16.7 (28.9)	41	1.4 (43.9)
v_{ej}	11	0.3 (2.0)	41	0.7 (3.0)

Table 4.2: The mean values of the high-z residuals (classified by host galaxy type) plotted in the right-hand column of Fig. 4.5 are listed here. The 'Early Spiral' and 'Late Spiral' groups shown in Fig. 4.5 have been grouped into one category.

a — Number of measurements

b — mean value of the residual displayed in Fig. 4.5 for the SNe from each host type. The units for the three EW measurements are Å and the units for the final row of v_{ej} results are 1000 km/s. The 1σ deviation from the mean is printed in parentheses

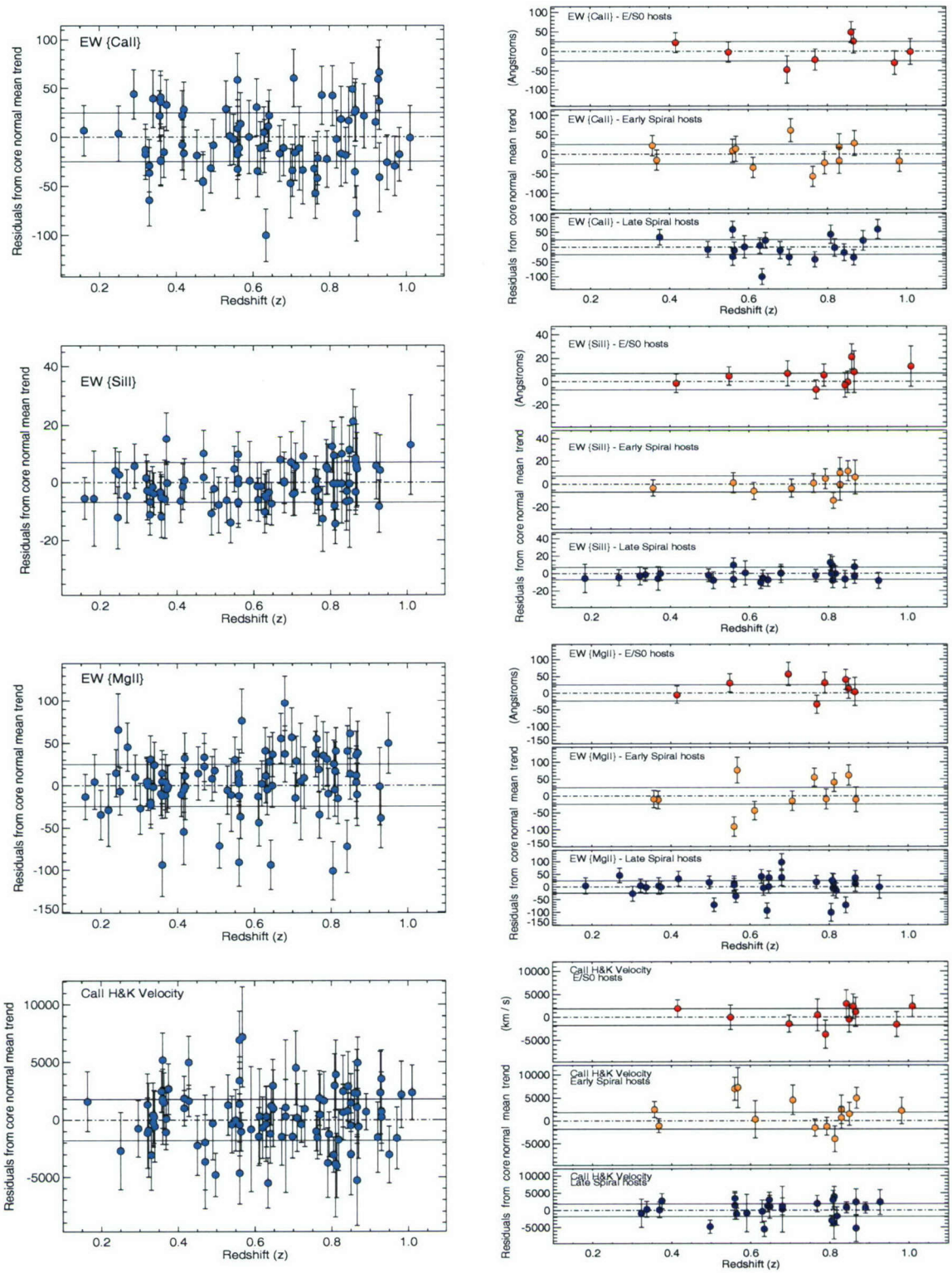

Figure 4.5: An additional check of evolution in SNe Ia. The residuals (the difference between the measured property and the low-z SNe Ia core normal mean trend) from the EW and v_{ej} measurements for all of the high-z SNe are plotted against redshift in the figures on the left. The column of figures on the right shows this same comparison, but with the results divided between the different host galaxy types. These comparisons reveal that any differences between the spectroscopic features measured at high-z and the mean trends exhibited by nearby SNe Ia do not correlate with z. The trends in the distribution of measurements within the different host types (i.e., the lower EW{SiII} results in distant late-type galaxies) are expected, based on the known correlations observed in the nearby SNe (see § 4.3).

The mean of the residuals displayed in Figure 4.5 are printed in Table 4.2. These values indicate that there are some possible trends in the high-z results based on host type as the mean values for each measurement differ between early and spiral hosts. Yet the standard deviation of these values also implies that this trend is not significant. A closer look at these results is necessary to investigate whether these (possible) correlations match those observed in the nearby SNe (see § 3.2.6). The EW{SiII} parameter is of particular interest due to its linear correlation with peak absolute magnitude. KS tests were used to expand on the impression conveyed in Table 4.2 and determine if there are any significant differences between the spectroscopic measurements from high-z SNe in different host galaxy types. In agreement with the comparison of mean values in Table 4.2, and unlike in the low-z set, none of these KS tests (see Fig. 4.6) found any highly significant differences in the high-z results from different hosts. However, a direct comparison of the cumulative distributions from the different SNe data sets — displayed in Fig. 4.7 — shows some definite similarities in the low-z and high-z results.

The distant late type galaxies host SNe that display a smaller amount of SiII than objects from early hosts and the ejection velocities measured in high-z spiral galaxies peak at higher velocities. Although this difference may not be statistically significant, this may be due to the smaller number of measurements in the high-z data. For example, the measured maximum deviation between the EW{SiII} distribution in the high-z early and late type host galaxies (KS statistic D) is $D = 0.42$. This value is comparable to the low-z result of $D = 0.60$ and would indicate a significant difference if the high-z sample was larger by only 10 measurements. Although the significance of these correlations between high-z SNe Ia characteristics and host galaxy morphology is less than that in the low-z sample, the existence of these trends cannot be refuted. This agrees with the results of Sullivan *et al.* (2006b), who used a broad-band photometric study of SNLS SNe host galaxies and found that the correlations between host galaxy type and lightcurve shape (Hamuy *et al.*, 1996a, 2000; Sullivan *et al.*, 2003) are consistent in distant and local SNe Ia.

Admittedly, these host galaxy morphology comparisons are not optimal for fully investigating SNe Ia homogeneity. The morphological categories only sum up broad trends in these host galaxies and do not encompass the subtle metallicity and stellar population variance both

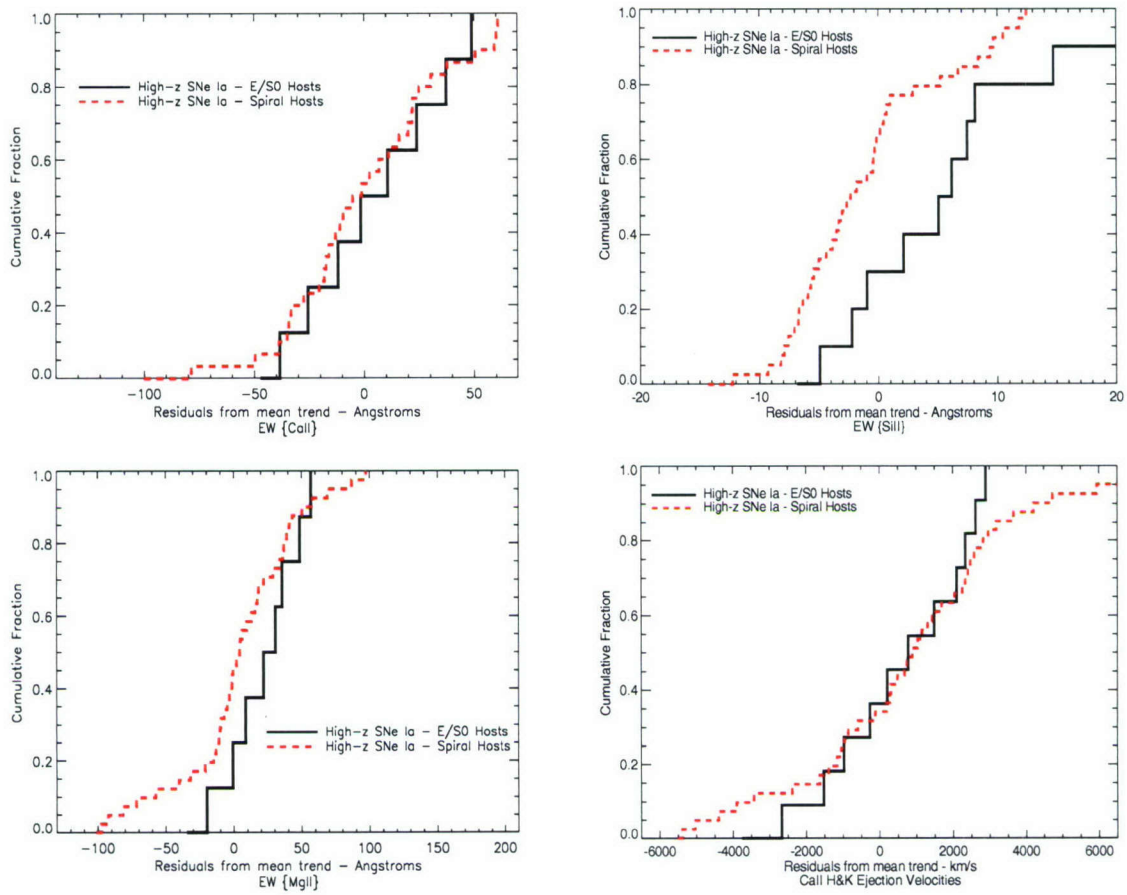

Figure 4.6: The cumulative distribution of residuals (the difference between the measured property and the estimated low-z SNe Ia core normal mean trend) from the 4 spectroscopic measurements made on the high-z data with available host galaxy information. The cumulative distribution of high-z EW{CaII} and EW{SiII} measurements are shown at the top; EW{MgII} and CaII H&K v_{ej} are shown on the bottom. KS tests on these distributions did not measure any significant differences in the measurements from different host types in this high-z set. The distributions in the EW{SiII} and v_{ej} results look very similar to the corresponding low-z comparison in Fig. 3.6.

within and between galaxies. As illustrated with the EW{MgII} results, there could be some Z effects in the high-z sample that cannot be thoroughly addressed by considering the morphology of SNe host galaxies only. Considering that the amount of information necessary to fully explore these options is not readily available for this large data set, these host type comparisons are one of the only remaining avenues for investigating SNe Ia homogeneity.

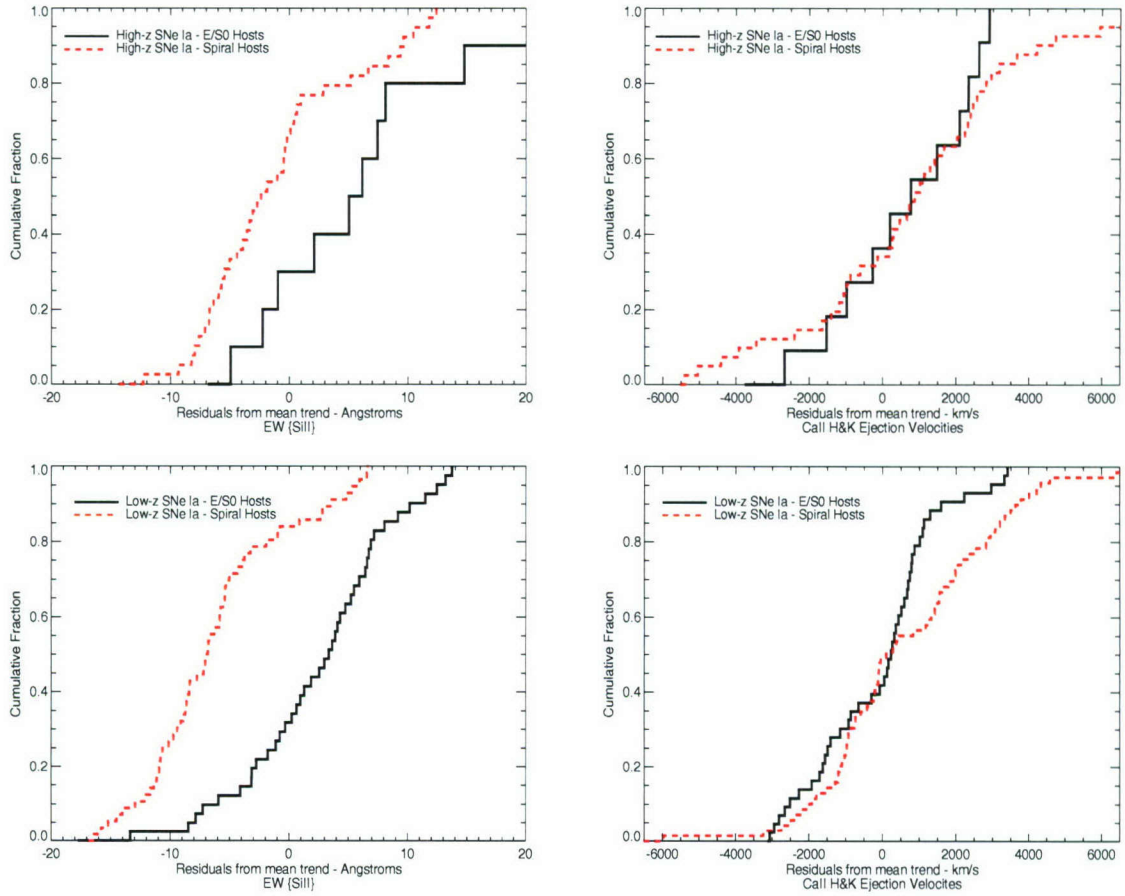

Figure 4.7: The cumulative distribution of residuals from the EW{SiII} (*left*) and CaII H&K $v_{\rm ej}$ (*right*) measurements from different host galaxy types in the high-z and low-z data. The results from the SNLS high-z SNe are on the top row and low-z data is displayed in the bottom row. Unlike the low-z SNe, these comparisons do not show a statistically significant difference, though this is most likely due to the smaller numbers of measurements in the high-z set; the general trend of lower EW{SiII} and higher $v_{\rm ej}$ in later hosts parallels the trends observed in nearby SNe.

4.4 Quantitative Spectroscopy of Distant Type Ia SNe — Physical Implications

The primary factor that affects the observed peak luminosities of Type Ia supernovae is ^{56}Ni mass [Arnett (1982); Arnett, Branch, & Wheeler (1985), and § 1.2], but the observed host environment correlations and intrinsic dispersion in $L_{\rm peak}$ are indicative of a secondary parameter which correlates to ^{56}Ni mass in SNe Ia explosions. Although a wide range of suggestions have been made with regards to this parameter, this debate may be clarified with the results from the measurements made in this thesis. The results of the theoretical work with supernovae have suggested the most likely source of this 2° parameter is either the metallicity (Z) or the

initial main sequence mass ($M_{\rm ms}$, or, similarly, the stellar population age) of the supernovae progenitors.

According to the interpretations of models by Dominguez, Hoeflich, & Straniero (2001) and Umeda *et al.* (1999) [with supporting explanations offered by Branch & van den Bergh (1993); Ivanov, Hamuy, & Pinto (2000); Gallagher *et al.* (2005)], the Z effects are small and the $M_{\rm ms}$ differences cause the observed dispersion and environment-based trends in SNe Ia. Within the framework of these explanations, the more massive progenitors evolve into carbon-oxygen white dwarfs with lower C/O ratios. This is a temperature effect as smaller stars undergo He burning at lower T [e.g., Dominguez *et al.* (1999)] and have a larger central C/O region (as the region of central He burning increases with $M_{\rm ms}$). These mass dependencies translate into different temperatures between individual supernova events once thermonuclear runaway has begun. Outside of the central (most dense) region of the WD, the division between 'complete' burning to iron group elements (including ^{56}Ni) and 'incomplete' burning to IME (which is governed by the nuclear physics considered in these models) is a very small range in temperature (near 5 x 10^9 K). Thus the final amount ^{56}Ni (at the expense of the mass of IME formed) is heavily influenced by the aforementioned temperature differences.

If this paradigm is propagated out to high-z galaxies, there are two main differences that would be measured with regards to the host morphology dependence of SNe Ia properties. The effects in SNe Ia from spiral galaxies can be estimated by assuming that at higher z these galaxies will produce supernovae from a set of generally younger progenitors with higher (and more homogenous) masses than the sample observed locally. These objects, with their higher masses and lower lifetimes, have reduced C/O ratios compared to similar SNe observed locally in addition to a more restricted range of C/O ratios. This would result in a distribution of SNe Ia luminosities that peaks slightly lower and is more homogenous than what is seen in nearby late-type galaxies. For higher redshift E/S0 hosts, the population of progenitors for the observed SNe would contain fewer of the older, smaller mass PGs than low-z early type hosts and more objects that come from younger progenitors[1] . These effects would combine to bring the distribution of SNe Ia luminosities (or EW{SiII}, as established in this thesis) between hosts

[1]The redshift and host mass range over which this trend should hold is debatable. For example, recent evidence indicates that most elliptical galaxies more massive than $10^{11} M_{solar}$ were fully formed near $z \approx 2$ (Jørgensen *et al.*, 2006). Observations in these galaxies will continue to acquire SNe from old, low-mass progenitors that are similar to those observed in any lower-mass ellipticals in the nearby sample.

closer together. This would then be expressed as a less significant difference between EW{SiII} values from different host types while still retaining the general correlations which are measured locally. This description roughly fits the results of the high-z EWSiII measurements made in this thesis, although the corresponding luminosity effect is not observed.

Conversely, Timmes, Brown, & Truran (2003) [with support from models by Travaglio, Hillebrandt, & Reinecke (2005) and others] predict that metallicity should be at the root of of this secondary SNe Ia light curve parameter. These publications indicate that an increase in progenitor metallicity could cause a reduction in the ^{56}Ni produced in SNe Ia as a result of a higher amount of ^{22}Ne in central (between 0.2 and 0.8 $M_{\odot}$) regions of the WD. In these regions, burning to NSE is assumed to take place in a regime with a constant electron fraction (Y_e). This is because the nuclear burning timescales are shorter than those for the weak interactions that would change Y_e; from conservation of mass and charge (for a given WD mass and explosion energy) arguments, the excess metals (^{22}Ne) will directly alter the final relative amounts of ^{56}Ni and other iron-peak nuclei and change the lightcurve shape and luminosity of the SNe [e.g., Mazzali *et al.* (2001); Mazzali & Podsiadlowski (2006)]. Three dimensional deflagration models by Roepke *et al.* (2006) agree with this Z dependence from the perspective of buoyancy effects, which were shown in their models to minimise the impact of the C/O ratio on the final ^{56}Ni production. These effects may be at the root of the difference in EW{MgII} results from the 1° set of high-z SNe.

The predicted effects of this dependence at different redshifts depends on how metallicity evolves with z in these SNe host galaxies. It has previously been assumed that Z should, in general, decrease with redshift as the bulk effects of stellar evolution increase the global metallicity in the Universe as it evolves. This trend does not have to describe the mean metallicity in the star forming regions of massive galaxies, however. In 'downsizing' descriptions of galaxy formation [e.g., recent discussions by Jørgensen *et al.* (2006); Alighieri, Lanzoni, & Jørgensen (2006)], the largest galaxies with the highest metallicities formed and completed a majority of star formation at $z \gg 1.0$. Thus, looking back at galaxies near $z = 1$ could sample SNe Ia hosts with higher Z than many local galaxies [e.g., Heavens, Panter, Jimenez, & Dunlop (2004)]. The former assumption implies that more distant SNe Ia would be brighter, while the opposite would be true for predictions made within the downsizing paradigm. Note

that because the SNLS is not magnitude-limited when searching SNe Ia host galaxies; even if the downsizing predictions are true this survey will still not preferentially observe the brighter high-z galaxies that would have higher metallicities. The epoch sampling and S/N of the spectra analysed in this thesis are also not well-suited for addressing metallicity effects, as any direct spectroscopic indicators of Z would not be detectable in the absorptions from IME that are observed in the spectra at epochs around maximum light. However, the significant decrease in ^{24}Mg production that is predicted for higher Z SNe Ia by Travaglio, Hillebrandt, & Reinecke (2005) and Roepke *et al.* (2006) could explain the EW{MgII} difference in the 1° data set. Any additional evidence for systematic changes in peak luminosity should have been discernible in the different tests discussed in this chapter (particularly those with the EW{SiII} measurements), yet none were found.

If the difference in the significance of the KS tests on the EW{SiII} measurements between different host galaxies at high-z (compared to what has been measured in the sample of local SNe) is indeed not a result of a smaller sample, then this result could support the Type Ia models and studies made by Dominguez, Hoeflich, & Straniero (2001); Umeda *et al.* (1999) and Gallagher *et al.* (2005). Similarly, if the significant difference in the EW{MgII} results from the 1° data set is not a statistical artifact, and if the Z of the host galaxies of the outliers can be determined to be higher than the nearby SNe, then the EW{MgII} results would support the calculations by Travaglio, Hillebrandt, & Reinecke (2005) and Roepke *et al.* (2006). A more extensive look at the host galaxies of distant SNe, paired with higher S/N spectroscopy at earlier epochs, would really be needed to yield quantitative results that would be more useful in identifying host or metallicity effects. All of these models discussed in this section also are subject to different assumptions and simplifications with regards to the physics of these objects, so applying the analytical results in this thesis within the framework of these predictions is probably premature. Still, this discussion illustrates that this type of quantitative analysis can be used to help investigate the predictions from different SNe Ia theories. Future observations, combined with more precise SNe models, will assuredly continue to improve our understanding of these 'standardisable' candles.

4.5 Quantitative Spectroscopy and Cosmology

The EW{SiII} spectroscopic sequence defined in § 3.2.3 can be used to address both SNe evolution and the cosmological implications of data from high redshift supernovae surveys. First, the validity of this relation in the high-z data needs to be verified. As discussed throughout this chapter, there is no quantitative evidence to reject the assumption that the distant SNe Ia are similar to those observed locally. No significant differences were measured between the low-z and high-z EW{SiII} measurements and both sets exhibited similar trends with regards to this measurement and host galaxy type. Supporting evidence that this specific EW{SiII} spectroscopic sequence is also similar is illustrated in Figure 4.8. In this illustration, the absolute magnitudes, uncorrected for lightcurve stretch or colour adjustments, of the SNLS high-z SNe and the low-z SNe are compared to the EW{SiII} values for each object. The value of these magnitudes were computed by solving the distance modulus equation ($\mu = m - M$) for M and are thus dependent on both the assumed cosmology and H_0. The plot in Fig. 4.8 is thus a rough estimate of the EW{SiII}-$M_{\mathrm{B_{peak}}}$ correlation in the high-z data, but it is suitable here as a simple check of the *consistency* of this relation. Within these relatively large EW error bars and uncertain magnitude errors, the SNLS supernovae are still consistent with the low-z trends in this parameter space. With the lack of evidence for any significant difference between the two SNe populations and the apparent consistency with the low-z SNe spectroscopic sequence, this EW{SiII}-$M_{\mathrm{B_{peak}}}$ correlation can be assumed to be applicable to distant SNe.

This spectroscopic parameter can next be tested as a new way to estimate the peak magnitudes of distant SNe. This is completely new as the numerous correlations between SNe Ia spectra and their photometric behavior (Wells *et al.*, 1994; Nugent *et al.*, 1995a; F04; Benetti *et al.*, 2005; Bongard *et al.*, 2006) that have been previously discussed have never actually been used for this purpose. Determining cosmological parameters with 'standardisable' candles such as Type Ia supernovae is a complicated process (summarised in § 1.3) that requires precise scrutiny of all of the errors and assumptions in both the cosmological models and the objects used as distance indicators. The straightforward application of the EW{SiII} sequence that is being tested here is a simplified version of this procedure and can be considered more of a 'proof of concept' than an independent verification of SNe Ia cosmology. The accuracy in this exercise cannot meet that of Astier *et al.* (2006) because of the smaller number of objects[2] and

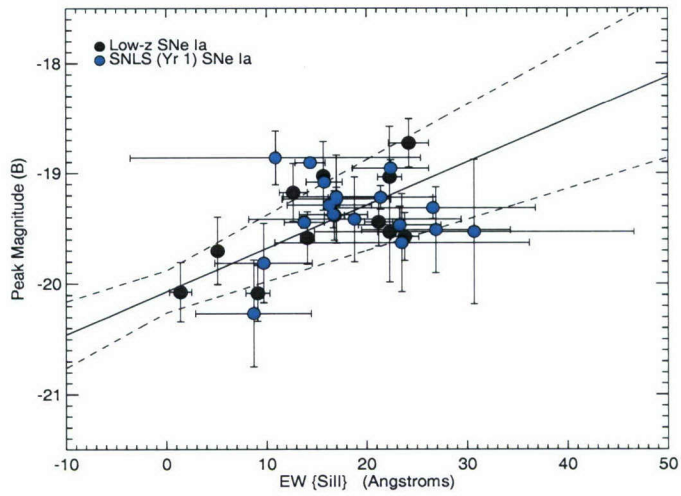

Figure 4.8: A comparison of the EW{SiII}-$M_{\mathrm{B_{peak}}}$ relationship in a sample of distant and nearby SNe Ia. The high-z data is consistent with the low-z trend (illustrated with the solid line). Combined with the additional comparisons of low and high-z spectra, this plot supports the assumption that the EW{SiII} spectroscopic sequence is a valid correlation for the high-z SNe.

the large relative errors in the high-z EW{SiII} results. Potential methods of overcoming the latter error are discussed in § 5.2.

To begin this process, the relation estimated from the low-z sample (see Eq. 3.4 in § 3.2.3 and Figure 3.4) was used to estimate the peak B' magnitudes for the SNLS SNe that were both published in the first year SNLS cosmology results and had measured EW values in this thesis. The distance modulus (μ) for these distant objects was then calculated as

$$\mu = m_{\mathrm{B}} - M_{\mathrm{B_{EW\{SiII\}}}}, \tag{4.1}$$

where m_{B} is the observed peak B'- magnitude (uncorrected for any Type Ia lightcurve-shape or colour relations) published in Astier *et al.* (2006) (re-printed in § 2.6), and $M_{\mathrm{B_{EW\{SiII\}}}}$ is the absolute magnitude estimated from the EW{SiII} relation determined with the low-z sample. The uncertainties in the linear M_{B}-EW{SiII} fit were propagated accordingly with the EW errors during this calculation. By using an m_{B} value that is not corrected for any Type Ia SNe colour or lightcurve-shape standardizations, this test implicitly assumes that the primary dispersion in SNe Ia properties is already accounted for by adjusting the peak magnitude to the value predicted in the EW{SiII} sequence. The major assumption for this test, then, is

[2]This refers to both the number of low-z objects used to derive this relation and the number of high-z objects as well. Note that the number of nearby SNe Ia used to derive the EW{SiII}-$M_{\mathrm{B_{peak}}}$ relation is still larger than the original sample of 9 SNe that Phillips (1993) used to initially define the $\Delta_{m_{15}}$ parameter.

that this spectroscopic sequence is both an accurate representation of the low-z magnitudes and is directly applicable to the distant SNe. No additional errors in this assumption were investigated here.

As an initial test, the dispersion of the distance moduli of the SNLS objects, calculated with the spectroscopic EW{SiII} parameter, about the best fit cosmology from Astier *et al.* (2006) were compared to the dispersion of SNLS SNe computed without any s or c adjustments. The m_B values from Astier *et al.* (2006) (and re-printed in Table 2.11) were used in this test. If this method accurately reflects the 'standardisable' characteristics of SNe Ia, then the residuals [about the best fit cosmology] should be smaller for the spectroscopically adjusted magnitudes. This is indeed the case, as the images on the left side of Figure 4.9 illustrate. The images on the right side of this figure display the same points, adjusted with the s and c corrections determined in the first year SNLS cosmology analysis (Astier *et al.*, 2006). The dispersion in the EW{SiII}-estimated magnitudes is 0.26 mag., compared to 0.23 mag. for the Astier *et al.* (2006) stretch and colour-corrected results. Both of these values are much improved over the 0.37 mag. dispersion from the un-corrected SNe magnitudes in this sub-set of 18 high-z SNLS SNe. For consistency, all of the low-z points from Astier *et al.* (2006) were used in these tests without any adjustments[3]. This result strengthens the case that the EW{SiII} measurement is a valid way of standardising and estimating high-z SNe Ia peak absolute magnitudes for cosmology.

A direct comparison of the cosmology results from the spectroscopically-estimated SNe magnitudes to the published results is displayed in Figure 4.10. Again, the full set of low-z SNe from Astier *et al.* (2006) are shown in this comparison. This test of correcting the distance modulus for the high-z SNe with a spectroscopic parameter results in a best fit cosmology that agrees with the parameters from the concordance model. With the small number of objects nothing more precise can be inferred about the cosmology suggested by these results. At the very least, this 'spectroscopic' Hubble diagram illustrates that an independent (and simplified) estimation of the high-z SNe luminosities provides evidence for a universe not significantly or systematically different than the currently accepted concordance model. This is another good sign that systematic errors or evolution are not the cause of the perceived dimming of distant

[3]Adjusting the low-z with this same spectroscopic sequence is also not really possible as the majority of the low-z objects with available spectra (which are included in this thesis) are too near to our own galaxy to be of any use to cosmology.

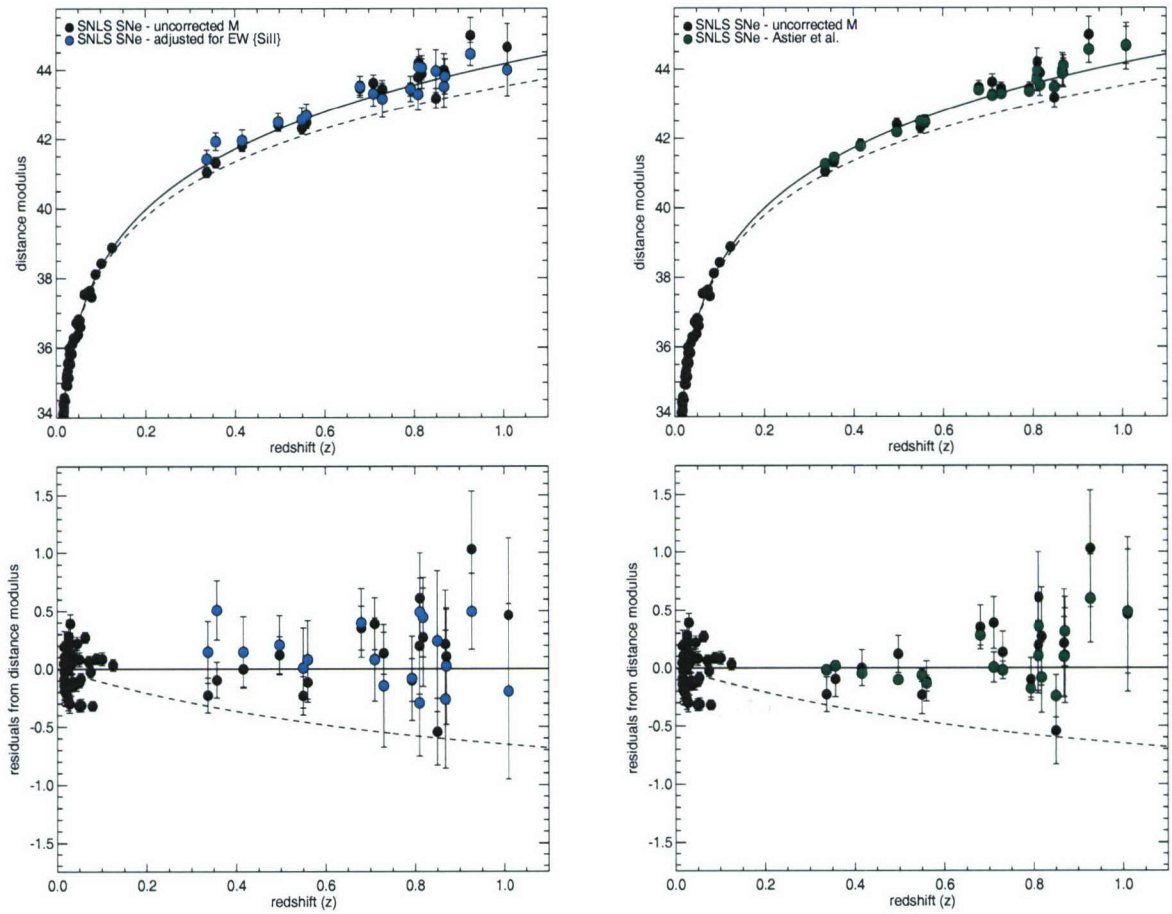

Figure 4.9: An illustration of the standardisable methods used to decrease the dispersion of SNe Ia about an assumed cosmology. The Hubble diagram on the left displays SNe Ia luminosities that were constrained with the EW{SiII} sequence, while the results on the right are from the s (stretch) and c (coloured) corrected SNe from Astier *et al.* (2006). The solid line indicates the best fit cosmology from the first year SNLS results - a spatially flat Universe with $\Omega_M = 0.263$ and $\Omega_\Lambda = 0.737$. The dashed line is the model from a flat Universe with $\Omega_M = 1.00$. The residuals about this cosmology are shown in the bottom two panels; the uncorrected high-z SNe points have a dispersion about this cosmology of 0.37 mag., while the EW{SiII} points have a dispersion of 0.26 mag.; this is comparable to the 0.23 mag. dispersion in the Astier *et al.* (2006) results.

Type Ia SNe. If the EW{SiII} relation can be further constrained in all SNe data sets, and understood more completely from a physical standpoint, then perhaps precise Hubble diagrams based on spectrosocpic estimations of SNe peak magnitudes may be feasible.

A final example of the utility of this EW{SiII} sequence to observational cosmology is presented in Figure 4.11. This figure displays a Hubble diagram using all of the high-z SNe Ia from the 1° data set (i.e., not just the SNLS year 1 results), anchored at low-z with the same SNe from Astier *et al.* (2006). The observed peak magnitudes for these objects (see Tables 2.11 and 2.12) were paired with the estimated absolute magnitudes from the EW{SiII}

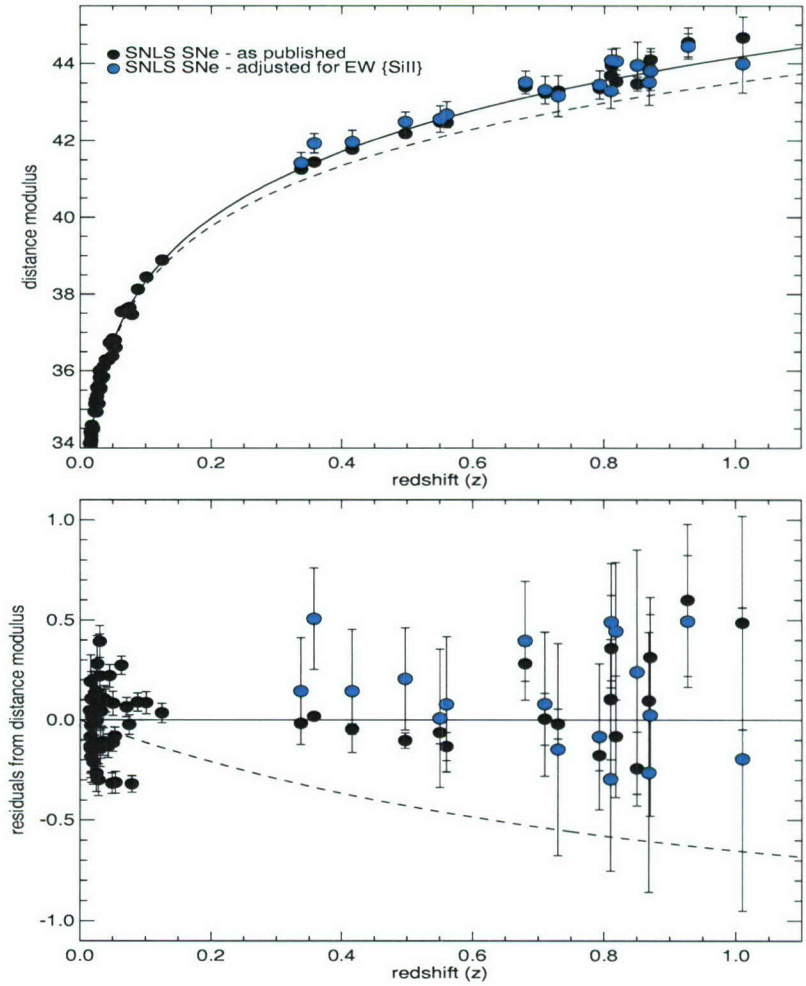

Figure 4.10: A 'proof of concept' Hubble diagram, showing the cosmology results from the SNLS compared to a test application of estimating the peak luminosities of the same high-z objects with the EW{SiII} spectroscopic sequence defined in this thesis. The best fit cosmology from Astier *et al.* (2006) is shown with the solid line ($\Omega_M = 0.26, \Omega_\Lambda = 0.74$) and the dotted line is a flat, matter dominated universe ($\Omega_M = 1.00$). This test is a simplified version of any true cosmological parameter determination that could be possible with this EW{SiII} parameter. The results from both methods are statistically similar and support the concordance model.

sequence to derive a spectroscopically corrected distance modulus for each SN. In addition to the caveats that were mentioned for the derivation of the Hubble diagrams presented in Figures 4.9 and 4.10, these results should be noted with additional caution. The m_B values for the SNe from the second and third years of the SNLS (see Table 2.12) are unpublished and are considered 'preliminary'. The sample of distant SNe from the 1° data set are also not ideal to limit the statistical errors on any derived cosmological parameters because of the uneven redshift distribution of the SNe observed at Gemini. For the SNLS, the Gemini telescopes are utilised to observe the most distant SNLS candidates; a clear result of this is the small

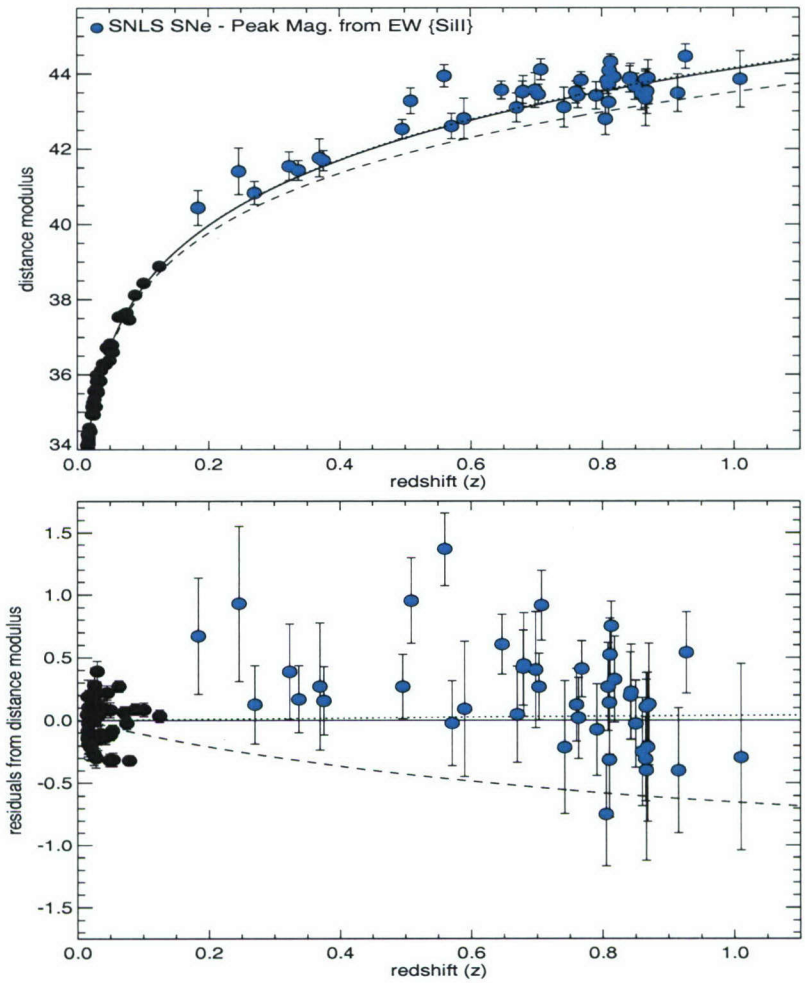

Figure 4.11: A Hubble diagram using the same low-z SNe from Astier *et al.* (2006) and high-z objects from the 1° data set with luminosities derived with the EW{SiII} sequence defined in this thesis. The solid line is the best fit cosmology to these SNe, $\Omega_M = 0.29$ and $\Omega_\Lambda = 0.71$ ($\Omega_{\rm tot} = 1.0$ was assumed). The dotted line just above this is the best fit cosmology from Astier *et al.* (2006), while the dashed line is the predicted trend from a flat Universe with $\Omega_M = 1.0$. Despite the numerous discussions of spectroscopic-photometric correlations in SNe Ia in the literature, this is the first example that derives cosmological parameters by constraining SNe magnitudes with a spectroscopic measurement.

number of objects at intermediate redshifts ($0.2 < z < 0.6$) in this final Hubble diagram. The best fit cosmology to these points, after constraining to a flat universe with $\Omega_M + \Omega_\Lambda = 1.0$, yields $\Omega_M = 0.29$ and $\Omega_\Lambda = 0.71$ ($\sigma_\Omega = 0.13$). To reiterate, this example presents a fairly simple approach to SNe Ia-based cosmology and the covariance of errors and systematics of the measurements used to derive these parameters have not been addressed. This result should be interpreted as a 'proof of concept' that illustrates how the absolute magnitudes of distant SNe may be estimated through spectroscopy, though the agreement with the concordance model of cosmology supports the results from previous SNe Ia surveys.

Chapter 5

Future Work with Distant Type Ia SNe Spectra

5.1 Recommendations for Future Spectroscopy of Type Ia SNe

The measurements completed in this thesis directly compared the largest set of high-z SNe Ia spectra studied to date with a substantial set of nearby objects. The differences in the spectroscopic features of the high-z SNe and the trends exhibited in the low-z core normal SNe – statistically estimated with χ^2 and KS tests – were found to be less than 2σ. No significant redshift-based trends were found in the high-z results and the correlations between the SNe Ia measurements and host galaxy morphology were found to be similar between the local and distant spectra as well. These results support the assumption that the SNe Ia observed at high-z are not systematically different than the objects sampled locally. This is important as this reasoning is essentially the foundation for using these supernovae as 'standardisable candles' for cosmology. Of course, the absence of proof for evolution in Type Ia SNe is not the same as proof of absence. Further study is needed to fully constrain the differences in these objects and validate or reject the accelerating Universe implied by the apparent dimming of distant SNe.

From the standpoint of the measurements made in this thesis, the continued identification of SNe Ia sub-types and investigation into the host galaxy correlations in SNe may help to narrow down the possible progenitor scenarios for SNe Ia. Similar measurements, completed

over many epochs or at different wavelength bands (Benetti *et al.*, 2005; Branch *et al.*, 2006; Hachinger, Mazzali, & Benetti, 2006), have also shown promise for classifying Type Ia SNe in a new way that may help unlock the different explosion mechanisms or explain the physics for the environment dependence of these objects. These are factors that can surely illuminate the physical differences that cause the observed dispersion in SNe Ia properties. Thus, our understanding of the causes for the dispersion in SNe Ia characteristics will be enhanced with the continued (and expanded) use of these particular quantitative methods. This is essential for the future of SNe Ia cosmology. The large numbers of objects observed by the surveys to date have effectively limited the statistical uncertainty in the cosmology results from SNe Ia Hubble diagrams. However, it is the systematic errors and uncertainties that truly limit the calculation and understanding of cosmological models. A better grasp of the specific, physical basis for SNe Ia heterogeneity is the only way to truly address these systematic concerns.

The physical description offered by EW and ejection velocity measurements has its limitations. These measurements provide a quantitative way to compare the spectroscopic characteristics of different SNe, but they cannot firmly specify the amount, distribution, and type of elements that are observed in SNe spectra. What is needed for this level of analysis is higher S/N spectra over multiple epochs that can be analysed with spectral synthesis modeling [see recent discussions by Branch *et al.* (2006); Baron *et al.* (2006)] to quantify the physical foundation for the observed SNe Ia behaviour. In particular, such measures are required to verify the predictions made by the rapidly evolving explosion models of SNe, whose synthetic spectra can only be compared in detail with observed spectra of roughly equivalent quality (Baron *et al.*, 2005). These theoretical exercises can also be paired with more detailed descriptions of host galaxies, to include estimates of metallicity and star formation history [e.g., Gallagher *et al.* (2005); Sullivan *et al.* (2006b)] in the specific SNe host regions to thoroughly differentiate the varied proposals for SNe Ia progenitor scenarios. This type of analysis would also be necessary to further the investigation of the possible Z effects noted in the EW{MgII} measurements from the 1° data set (§ 4.2).

Meeting these needs with data from ambitious surveys such as the SNLS may not be possible. This is due to the excess time that would be necessary for a Gemini or VLT observation of a high-z object to approach the required S/N for more detailed analysis. A visual example

of this limitation is displayed in Figure 5.1. At the bottom of this plot is a SNLS SN candidate observed with GMOS. This candidate (SNLS SN 05D3kt) was observed for a total of 5400 seconds with 3 N&S exposures. At an i' magnitude of 23.53 (with 0.82" seeing) and a derived redshift of $z = 0.648$, this object is very typical of the SNe in this sample. The S/N in this observation (calculated as the average S/N per pixel in the central GMOS CCD) is ≈ 3.5. This same object with a simulated S/N of three times this value (≈ 10.0) is shown at the top of this figure.

The improvement in the clarity of the large absorption features is obvious. Yet these features still require some smoothing or filtering in order to provide the detail necessary for useful application to spectral synthesis models. The effects of this smoothing on the uncertainty in the SNe features could diminish the impact of any results from the comparison of the high-z spectra to any computed model. The accuracy gained for other quantitative measurements would be improved; for example, the statistical error bars on an EW measurement would be roughly 50% smaller than in the lower S/N spectrum. This modest gain, however, would be made at the cost of approximately 8-9 times more exposure time[1]. The use of 43200 seconds to observe one SN would consume $1/5^{th}$ of the 60 hours granted (per semester) to the SNLS at Gemini North.

Considering that this extensive observation time would only minimally improve the quantitative measurements available for these spectra, it is clear that this is not a feasible option for the current crop of large scale studies of SNe Ia at cosmological distances. The strength of future analysis available from these surveys will lie in optimising the large sample size, thorough host galaxy information, and well-controlled systematics that characterise these projects. The current publications from the SNLS [H05; Sullivan *et al.* (2006a,b); Neil *et al.* (2006); Conley *et al.* (2006)] have already demonstrated these utilities and future advancements in SNe Ia understanding will be possible by continuing this analysis within context of the theoretical predictions that were discussed in § 4.4.

For example, quantitative information on high-z galaxy masses and metallicities can be used to divide up the large SNe sample by these factors and determine the validity of the

[1]This was verified by using the specific settings of the GMOS SNLS observations with the Gemini Integration Time Calculator (`http://www.gemini.edu/sciops/instruments/itc/ITCgmos.html`). It was found that increasing the exposure time by a factor of 8 for these observations was often enough to triple the S/N for any object.

proposed metallicity effects on SNe Ia luminosities (Timmes, Brown, & Truran, 2003; Mazzali & Podsiadlowski, 2006). A similar division in the SNe Ia sample, based on quantitative analysis of the spectroscopic and photometric data from these large data sets, can also be used to re-classify and re-calibrate the empirical calibrations of SNe Ia peak magnitudes. Such a re-classification or division in the data would fully expand on the observational strategy of comparing 'like versus like' that already underpins SNe Ia cosmology. This type of comparison may prove to be the best way to fully utilise the homogeneities within the SNe Ia population and to address the systematic effects that will dominate future surveys.

The higher S/N observations necessary to fully probe SNe Ia explosion physics are more likely to come from spectra of nearby objects[2] and SNe in the area known as the 'redshift desert' between $z \approx 0.05$ to $z \approx 0.35$. Observations in the latter range will provide ample numbers of supernovae at a relative brightness ($\approx 20.0 - 21.0$ in i' at peak luminosity) that will enable observations with good S/N and with more modest exposure times and smaller telescopes than those used in high-z searches. Observations toward the upper end of this region are also sampling SNe that are distant enough that to possibly be useful for additional tests of SNe Ia evolution. As a specific example, the redshift distribution and quality of spectra obtained by surveys such as the Sloan Digital Sky Survey (SDSS) II Supernova Survey[3] should provide additional data that may be better suited to this particular type of analysis. Even these growing data sets will continue to include spectra where the S/N or epoch sampling are not optimal for the suggested application of spectral synthesis models and similar studies. In this case, the quantitative techniques demonstrated in this thesis can be utilised to study and compare Type Ia supernovae.

5.2 The Possibility of a 'Spectroscopic' Hubble Diagram

These suggestions for future science with Type Ia supernovae spectra are aimed at quantifying the physical differences behind the observed inhomogeneities in their observed properties, i.e., the factors other than ^{56}Ni production that affect their peak magnitudes. An improved understanding of the physics driving the dispersion in SNe Ia characteristics is the only way

[2]The Nearby Supernova Factory `http://snfactory.lbl.gov` and Aldering *et al.* (2002) is well underway is gathering large numbers of SNe Ia observations at $0.03 < z < 0.08$.

[3]See `http://sdssdp47.fnal.gov/sdsssn/sdsssn.html` and links therein.

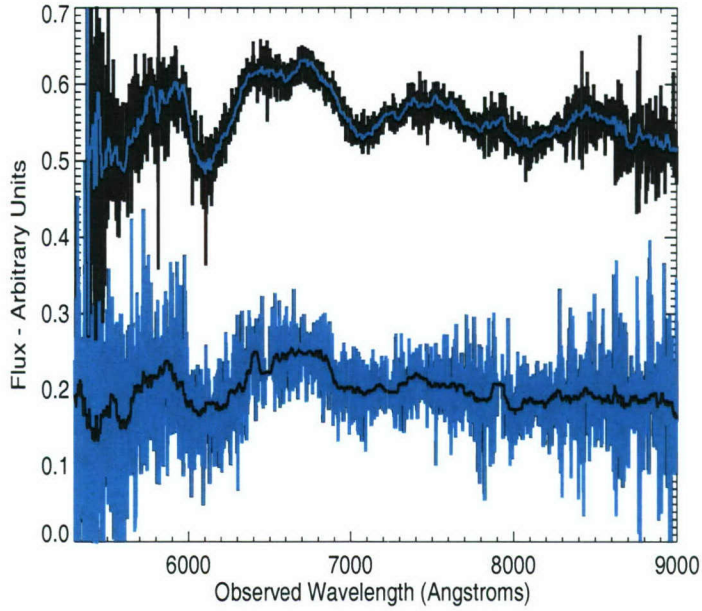

Figure 5.1: The observed spectrum for SNLS object 05D3kt is shown in blue on the bottom of this figure. At the top is a simulated version of this same spectrum with approximately 3 times higher S/N. To help compare these two spectra, the median-filtered flux from each is overplot (in black for the observed spectrum and blue for the simulated spectrum). The flux units in this plot have been normalised to arbitrary units. The improvement in S/N that is shown here would require approximately 8-9 times the exposure time utilised for the observed spectrum.

to limit the systematic errors in the SNe Ia-based derivation of cosmological parameters. This is already an important goal with regards to the current high-z SNe data set and will be even more necessary for maximising the results from larger numbers of SNe observed with projects such as the SuperNova / Acceleration Probe [SNAP, Aldering *et al.* (2002)]. As illustrated with the spectroscopically-corrected Hubble diagram in Figure 4.11, it may also be possible to directly address the cosmological implications of SNe Ia with spectroscopy. Of course, some photometry will always be required to perform this type of analysis, but as a final suggestion in this thesis an illustration of a proposed method of constraining cosmological parameters primarily with spectroscopy will be discussed.

One method for building a 'spectroscopic' Hubble diagram with SNe Ia was detailed by Riess *et al.* (1998c). This work proposed that all of the necessary information for estimating the type, luminosity, lightcurve shape, and colours for a SN could be gathered in observations over only one night with a combination of photometry and spectroscopy. A slightly different version of this proposal, based on the spectroscopic analysis techniques discussed in this thesis,

is briefly outlined in Figure 5.2. This method relies primarily on having a good S/N spectra of an SNe Ia candidate within a week of $L_{\rm peak}$ so that a solid SN identification can be made, and, if the observed object is a Type Ia, EW{SiII} can be measured. The observed spectrum, quantitatively matched to a similiar low-z template, can also provide a good estimate of redshift and epoch. If any information is available about the SN host galaxy, then the redshift and subsequent spectroscopic template fits can be improved. As discussed in § 2.4.4, the errors on redshift can be as small as (approximately) $\sigma_z = 0.01$ (without host galaxy constraints) or $\sigma_z = 0.001$ (with host constraints). The uncertainty in epoch can vary, but for a spectrum free of any major peculiarities (e.g., the unusual SN 2000cx) and decent S/N (a minimum average S/N per pixel of $\sim$ 5.0, with a preferred S/N $\sim$ 15.0 and higher), spectroscopic dating can narrow the epoch down to $\pm$3.0 days. In situations with lower S/N and z estimates this value ranges from $\pm$5.0 to $\pm$10.0 days.

With this available information from the spectrum, one photometric observation could be sufficient to estimate the observed peak luminosity ($m_{\rm peak}$). This observation will be most useful if it is made in multiple bands where SNe Ia photometric behaviour is well-constrained. With the spectroscopic estimate of the epoch and a lightcurve-shape parameter from the EW{SiII} value (this parameter corresponds to s and $\Delta_{m_{15}}$ in addition to $M_{B_{\rm peak}}$, see § 3.2.3), the uncertainty in $m_{\rm peak}$ could be close to $\sim$ 0.2 mag. This uncertainty requires additional testing to determine a more accurate range. The final step with regards to any cosmology goals would be to calculate the distance modulus μ by subtracting the EW{SiII}-estimated $M_{\rm peak}$ from $m_{\rm peak}$. The end result of this process would be the addition of a new point on an SNe Ia Hubble diagram.

The difference between this proposal and the more detailed presentation of this method in Riess *et al.* (1998c) is the use of the new EW{SiII} spectroscopic parameter instead of the $\Re${SiII} (or $\Re${CaII}) (Nugent *et al.*, 1995a) sequence. This is advantageous because the EW{SiII} measurement is not as limited by wavelength coverage as Nugent *et al.* (1995a) parameters. The S/N necessary to measure EW{SiII} with enough accuracy to estimate $M_{\rm peak}$ for cosmological purposes would have a lower limit of S/N $\sim$ 5.0 and would preferably be at least S/N $\gtrsim$ 10.0 (S/N calculated as the median S/N per pixel in the SiII wavelength region). This parameter does have some epoch constraints; the EW{SiII}-$M_{\rm peak}$ relationship is best

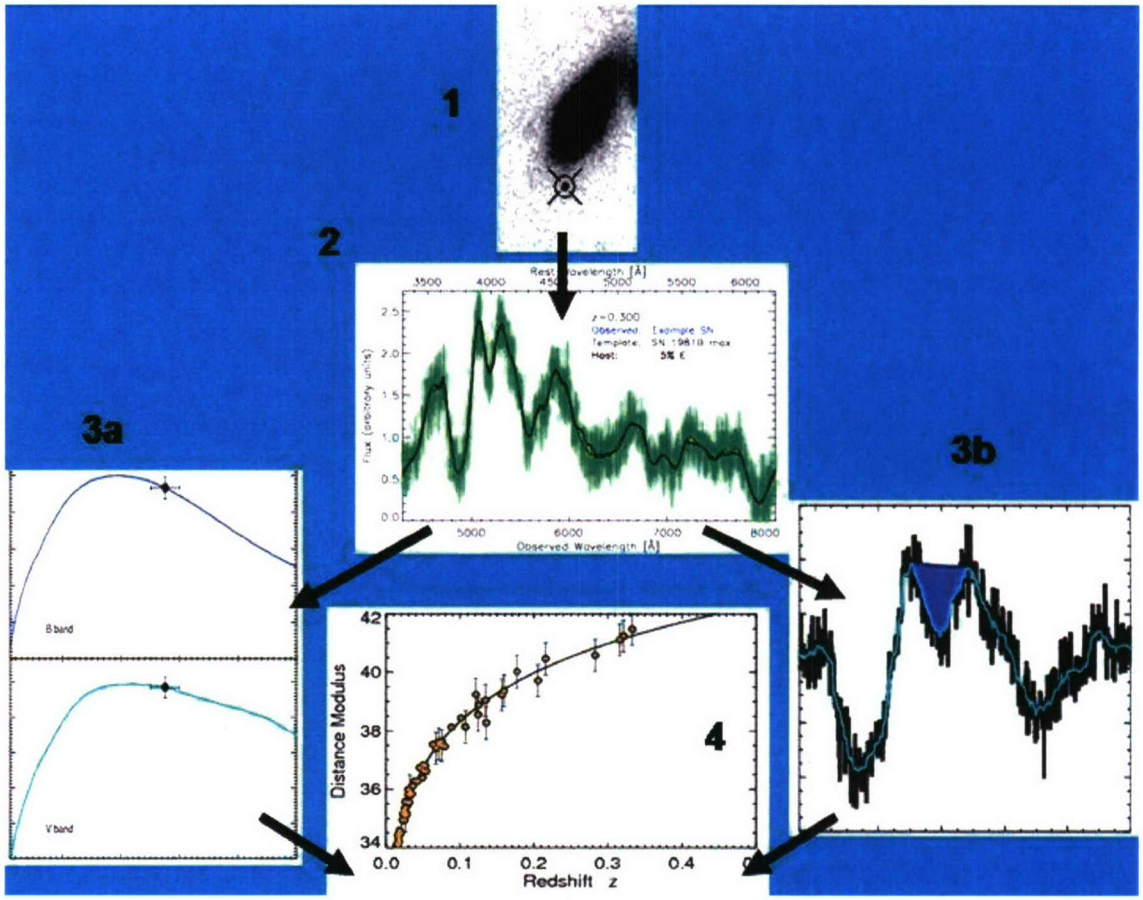

Figure 5.2: An overview of a possible method for estimating cosmological parameters primarily using spectroscopy of Type Ia SNe. A SNe Ia candidate is identified (Step 1), either through a specific search for SN transients or in another survey that serendipitously acquires these events. Next (Step 2) a spectrum of the object is observed (or, again, acquired unintentionally via a non SNe Ia-specific survey); low-z SNe templates are matched to this object to determine a spectroscopic date, redshift, and object type. Next, the object is observed photometrically (Step 3b) and the approximate (spectroscopic) date is used to constrain SNe Ia lightcurve fits which can estimate the observed peak magnitude of the event. The spectrum is used to estimate the intrinsic peak magnitude (Step 3b) based on the EW{SiII} parameter defined in this thesis. The observed peak m from the lightcurve fits and the spectroscopically constrained $M_{\rm peak}$ can estimate a distance modulus via $\mu = m - M$, the calculated μ is then plotted against the spectroscopically-confirmed z to build a Hubble diagram to test cosmological predictions.

between $\pm$7.0 days of maximum light and is not available at all after this feature disappears (see § 3.2.2). The overall errors in this suggested method are not well constrained [Riess *et al.* (1998a) quoted d_L errors of $\sim$ 10% with this technique], and additional tests would be necessary to determine just how the various uncertainties from the spectroscopically estimated parameters would propagate through the lightcurve fits and final m and μ estimates. The fact that the similar method discussed in Riess *et al.* (1998c) has not been extensively used [the d_L measurements that were made with this method for Riess *et al.* (1998a) were even removed

from Hubble diagrams in later publications] implies that there are inherent uncertainties in a spectroscopically-based technique for constraining SNe Ia distance moduli that make the extensive photometry and spectroscopy used by all other SNe sureveys a preferred alternative. This technique is being suggested in this thesis mainly to illustrate the possibilities which quantitative spectroscopy holds for addressing SNe Ia cosmology. With additional testing, this proposed method may prove to be a viable way to perform SNe-based estimations of cosmological parameters for surveys or data sets that are smaller in scope than the current SNe Ia surveys or are not specifically set up for detailed (photometric) SNe Ia coverage.

5.3 Conclusion

The old adage that 'extraordinary claims require extraordinary proof' has been used many times in response to the contribution of SNe Ia to the concordance model of cosmology. Astronomers are faced with a large (and growing) set of luminous objects that have been thoroughly studied to yield empirical correlations which appear to make Type Ia SNe precise distance indicators for cosmology. The analysis presented in this thesis, and the numerous investigations described throughout, support the 'extraordinary claims' from surveys utilising these objects and their 'standardisable' properties. Yet even the centuries of SNe observations have not yielded the evidence necessary to completely rule out other contingencies — such as evolution, metallicity effects, or some unknown systematic differences — that could explain the apparent dimming of SNe Ia at cosmological distances that has been measured in recent years.

If future studies continue to agree with the conclusions from SNe Ia surveys and if support for the concordance model continues to grow, then estimates of the dark energy equation of state and its variance with time will be the best way to explore the physical basis for the acceleration of the Universe. The precision necessary for this exercise can be enhanced, statistically, by larger SNe Ia samples. However, the systematic limitations on the measurements of this parameter require a different approach. These systematics are particularly important for the surveys that are underway and for future efforts, such as the Dark Energy Survey[4], the SDSS-II SN Survey (§ 5.1), the Joint Efficient Dark-energy Investigation[5], and SNAP (§ 5.2)[6]. A possible way to address this concern is through the continued application of the quantitative spectroscopic measurements discussed in this thesis and references within; these measurements

can continue to narrow down the SNe that appear to result from the most homogenous explosion scenarios or progenitor environments. The systematic errors on SNe Ia surveys may then be improved by comparing only the high-z and low-z objects that have a physical fraternity beyond the one parameter offered by the lightcurve shape-luminosity relations. The reciprocal advances in SNe Ia understanding that are available from the interaction of these quantitative measurements with improved spectroscopic models is another avenue that can make a breakthrough in understanding SNe Ia systematics a reality.

This thesis presented some advancements in addressing the homogeneity and systematics of Type Ia supernovae studies with analysis on the one of the largest, most distant and most consistently measured sets of SNe Ia spectra compiled in the long history of supernovae observations. This analysis answered some questions on the issue of Type Ia SNe evolution, which is perhaps the 'most serious challenge' (Li & Filippenko, 2003) to the cosmological interpretation of high-z SNe surveys. No significant, quantitative differences were found between the spectra of SNe at different redshifts, although tentative evidence of a significant difference in the spectroscopic behaviour of high-z SNe from metal rich progenitors was discussed. This work is a cautious step toward validating the implications of high-z SNe Ia observations. Yet the task of ruling out the other explanations for the apparent dimming of distant SNe and of fully understanding their physics still remains. The astrophysics community thus stands in a very similar place to Brahe, Kepler and Galileo, when they first trained their eyes and instruments on supernovae in 1572 and 1604; only the continued observations and investigations of these amazing objects can determine if we are on the cusp of a similar revolution in mankind's understanding of the Universe.

[4] `http://www.darkenergysurvey.org`
[5] `http://jedi.nhn.ou.edu/`
[6] see also `snap.lbl.gov/`

Appendix A

SNLS Gemini Spectra

Spectra from each Supernova Legacy Survey SN candidate, observed at the Gemini telescopes from the start of the survey in August 2003 through May 2006, are presented here. All of these objects were reduced and identified by the author; the final object type and confidence ranking for each SN candidate was reached via a consensus from SNLS members (see § 2.4.4 and § 2.4.5). The reader is also directed to § 2.3 and § 2.4 for the specific observational setup and data reduction steps for these spectra. These spectra are (primarily) displayed in two columns. The left-hand column (marked 'Observed') shows the observed spectrum, re-binned to 7.5 Å resolution, in dark blue with a smoothed version of the spectrum overplot in light blue. This smoothed spectrum is for illustrative purposes only and was generated with a Savitsky-Golay filter computed with a 3^{rd} degree polynomial and fit over 40 pixels of the observed spectrum. These spectra have been corrected for sky absorption and chip gaps and the host galaxy features have also been removed. These are the spectra that are input into the χ^2 template matching program. The right hand column in these figures shows the output spectrum from the best fitting SNe template, computed with this identification program. These figures (marked 'Template Fit') show the observed spectrum, adjusted for reddening and host contamination, in green. The best-fit template is overplot in black and a smoothed version of the adjusted initial spectrum is plot in red.

A.1 SNLS Supernovae Spectra - Confirmed Type Ia SNe

These spectra are from SNLS SN candidates that were confirmed as Type Ia SNe (i.e. a Confidence Index of 3, 4, or 5,). The sub-set of these objects that met the host-galaxy contamination constraints defined in § 3.3.3 were quantitatively analysed and compared to the spectra of low-z Type Ia SNe in Chapters 3, 4, and 5.

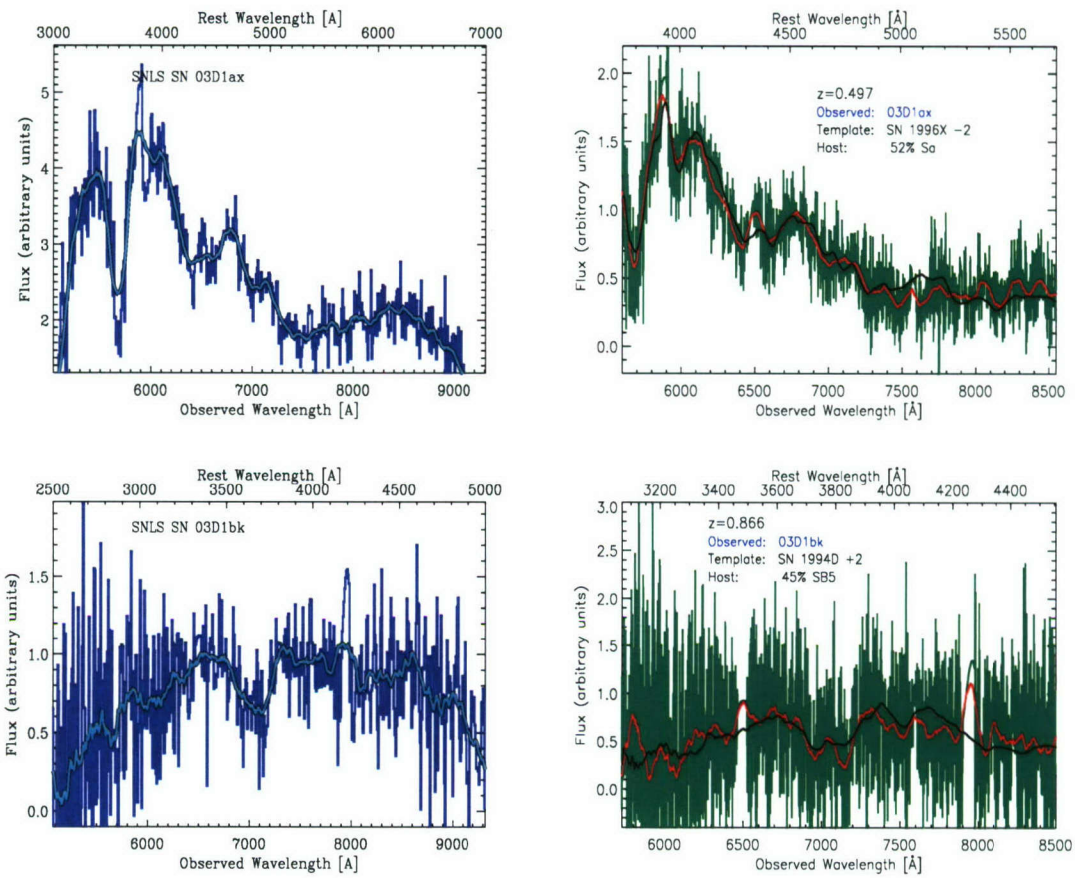

Figure A.1:
TOP: SN Ia 03D1ax **Left** - Observed spectrum **Right** - Template Fit
BOTTOM: SN Ia 03D1bk **Left** - Observed Spectrum **Right** - Template Fit

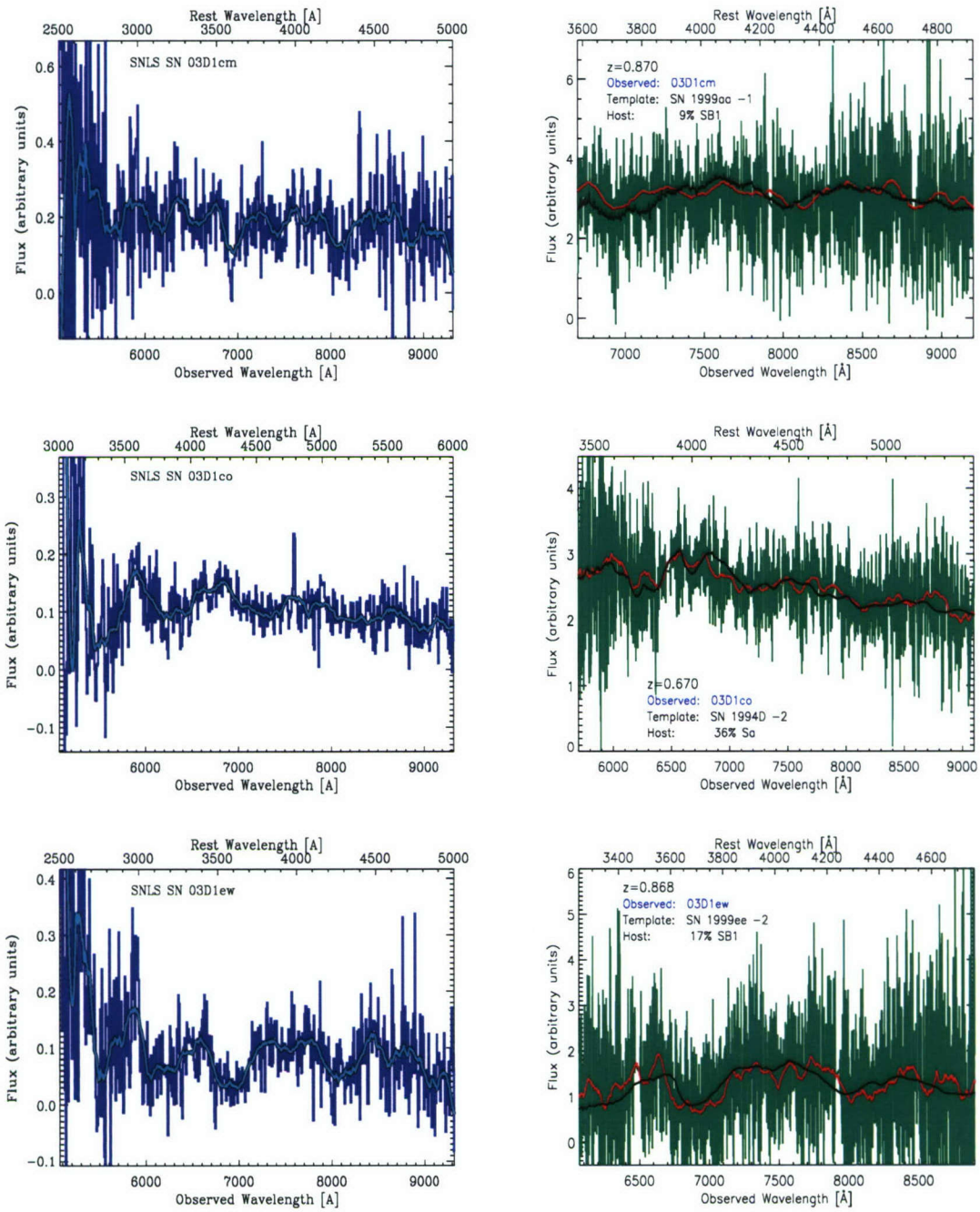

Figure A.2:

TOP:	SN Ia 03D1cm	**Left** - Observed spectrum	**Right** - Template Fit
MIDDLE:	SN Ia 03D1co	**Left** - Observed spectrum	**Right** - Template Fit
BOTTOM:	SN Ia 03D1ew	**Left** - Observed Spectrum	**Right** - Template Fit

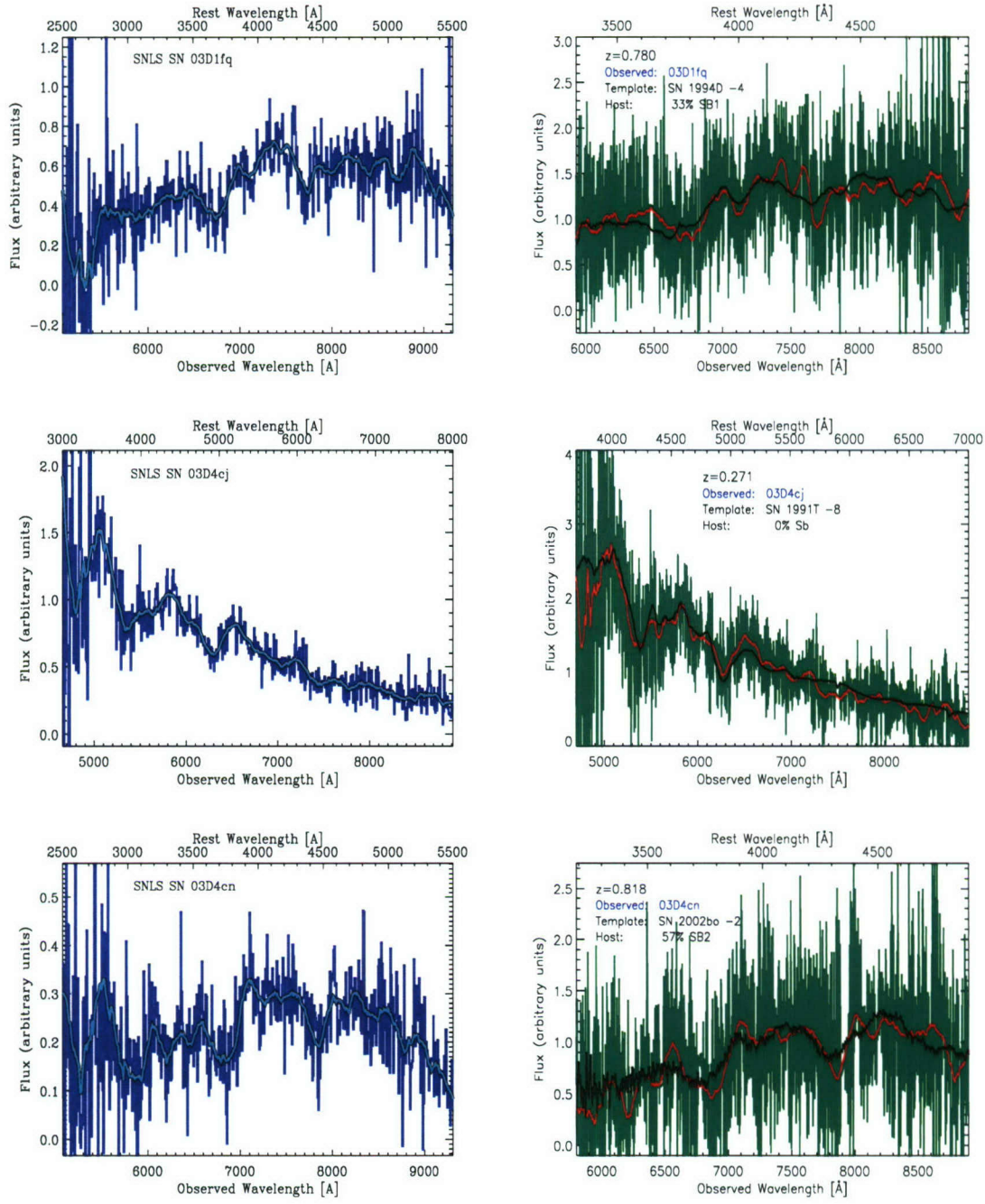

Figure A.3:
TOP: SN Ia 03D1fq **Left** - Observed spectrum **Right** - Template Fit
MIDDLE: SN Ia 03D4cj **Left** - Observed spectrum **Right** - Template Fit
BOTTOM: SN Ia 03D4cn **Left** - Observed Spectrum **Right** - Template Fit

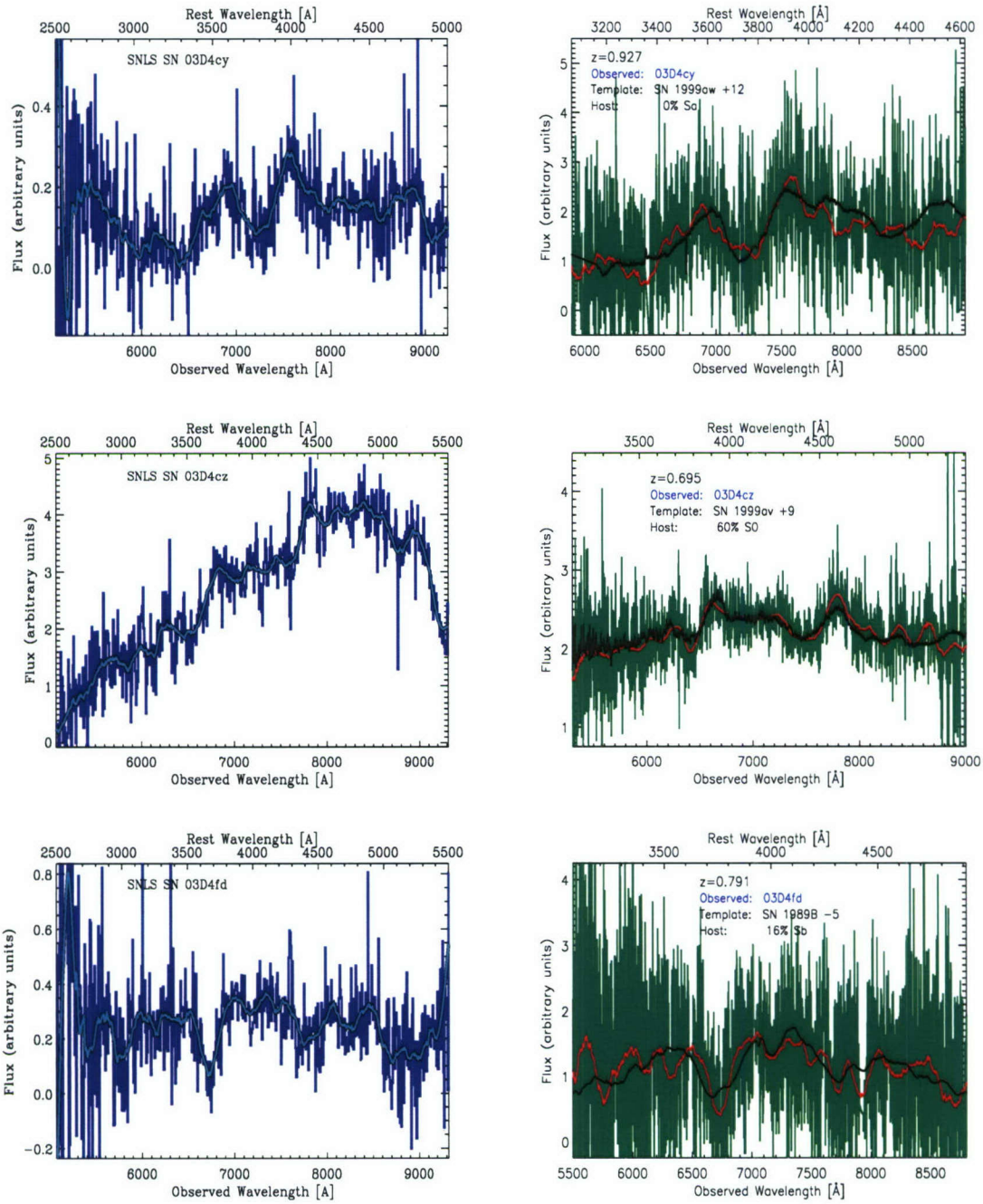

Figure A.4:
TOP: SN Ia 03D4cy **Left** - Observed spectrum **Right** - Template Fit
MIDDLE: SN Ia* 03D4cz **Left** - Observed spectrum **Right** - Template Fit
BOTTOM: SN Ia 03D4fd **Left** - Observed Spectrum **Right** - Template Fit

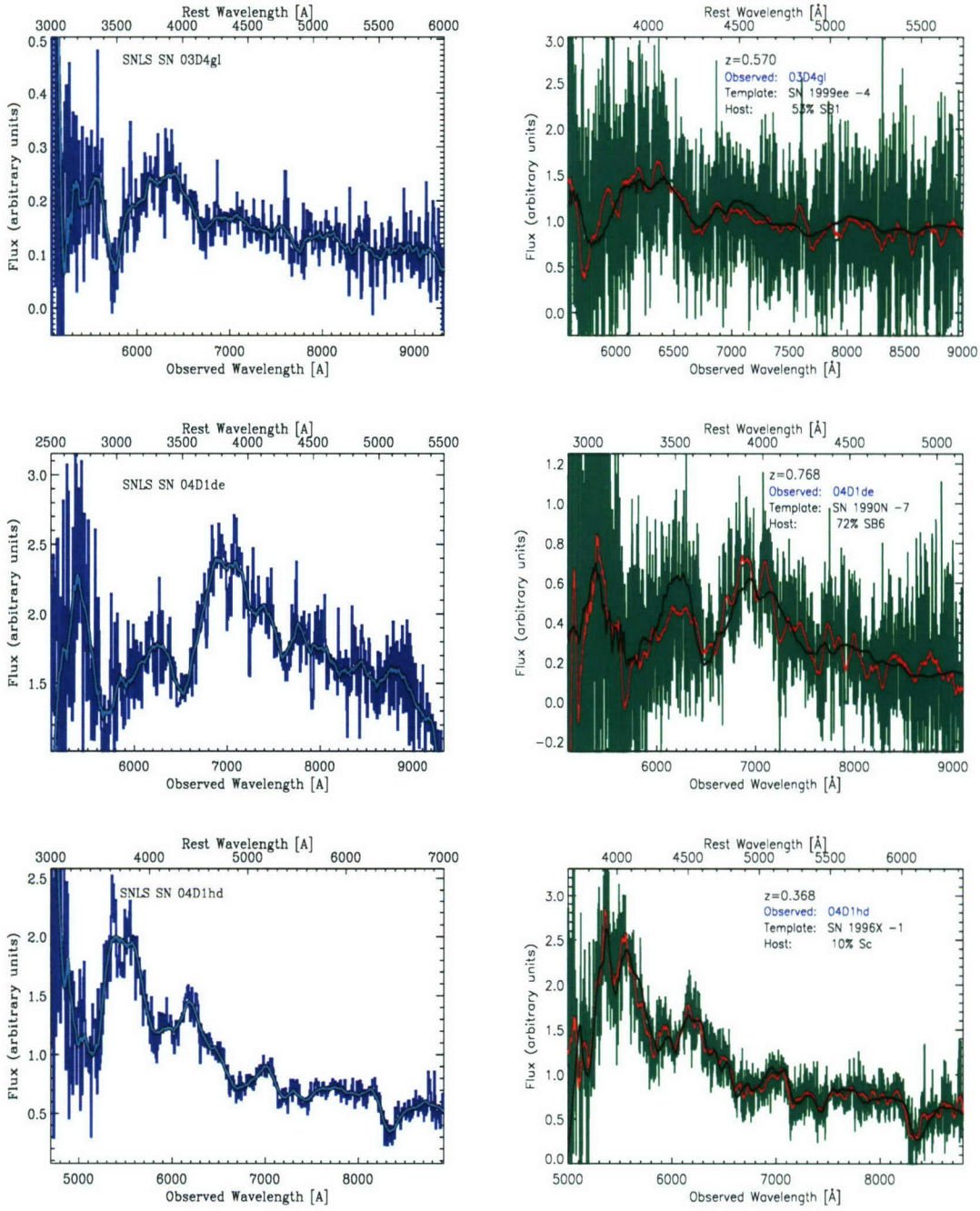

Figure A.5:
TOP: SN Ia 03D4gl **Left** - Observed spectrum **Right** - Template Fit
MIDDLE: SN Ia* 04D1de **Left** - Observed spectrum **Right** - Template Fit
BOTTOM: SN Ia 04D1hd **Left** - Observed Spectrum **Right** - Template Fit

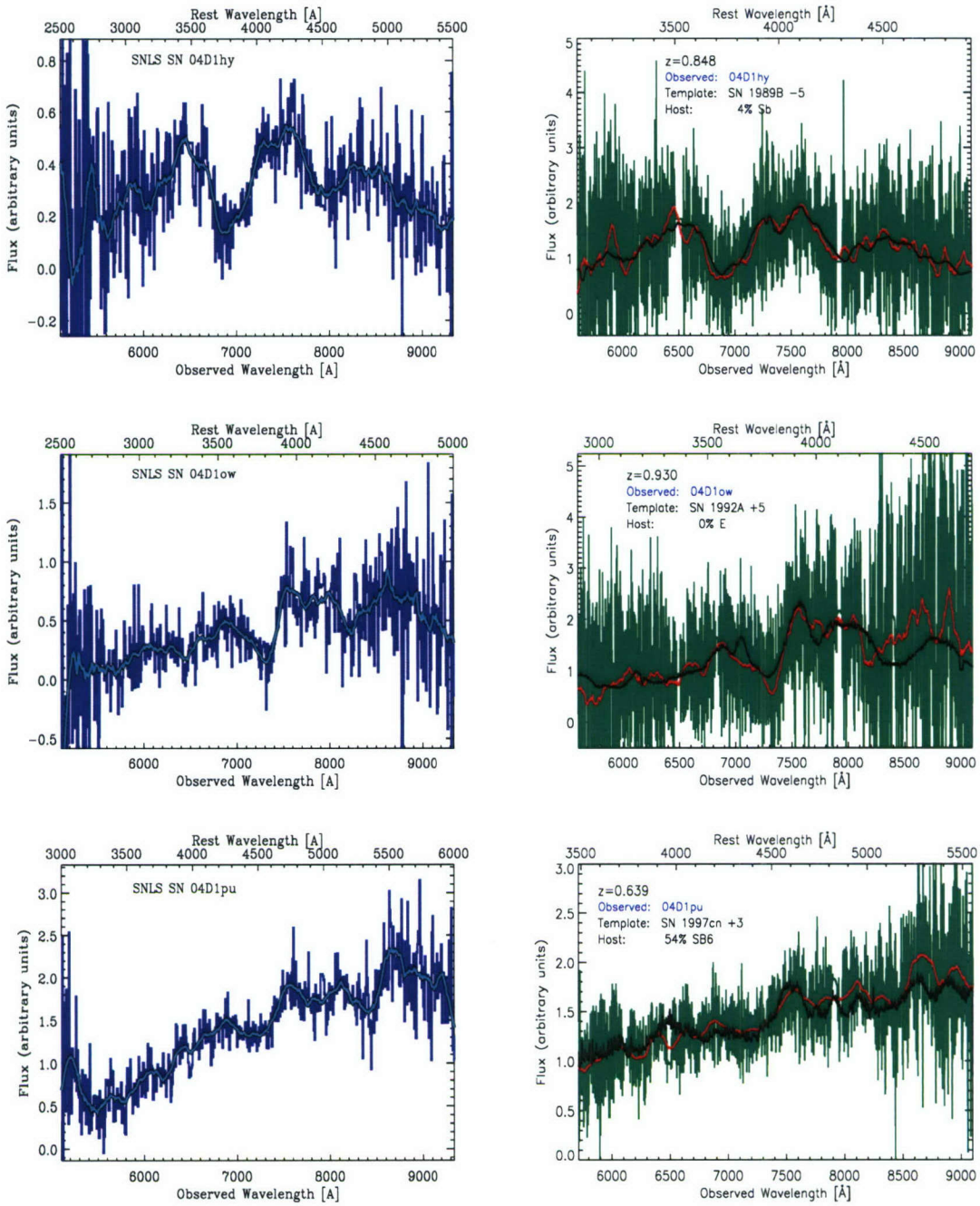

Figure A.6:
TOP: SN Ia 04D1hy **Left** - Observed spectrum **Right** - Template Fit
MIDDLE: SN Ia 04D1ow **Left** - Observed spectrum **Right** - Template Fit
BOTTOM: SN Ia* 04D1pu **Left** - Observed Spectrum **Right** - Template Fit

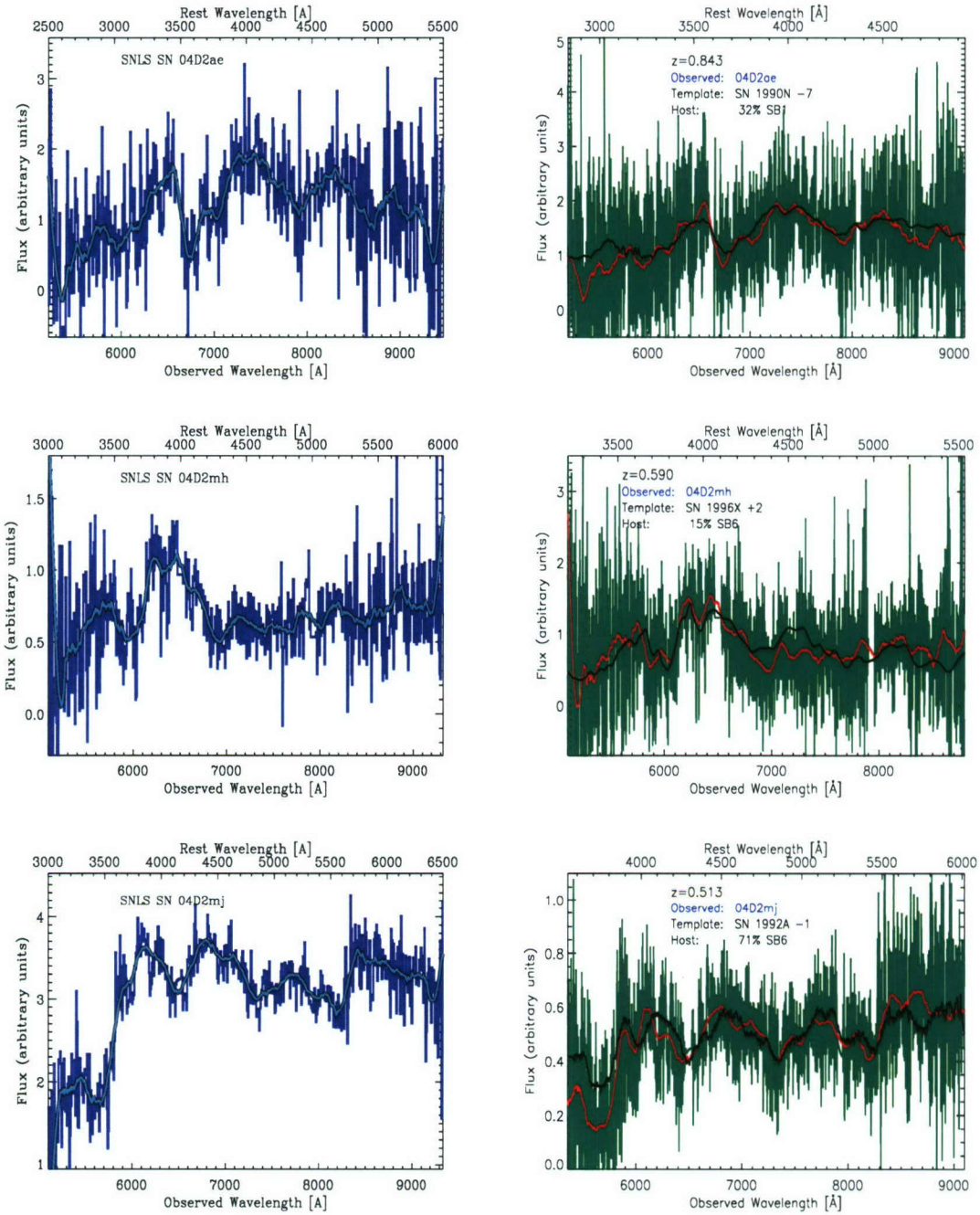

Figure A.7:
TOP: SN Ia 04D2ae **Left** - Observed spectrum **Right** - Template Fit
MIDDLE: SN Ia* 04D2mh **Left** - Observed spectrum **Right** - Template Fit
BOTTOM: SN Ia 04D2mj **Left** - Observed Spectrum **Right** - Template Fit

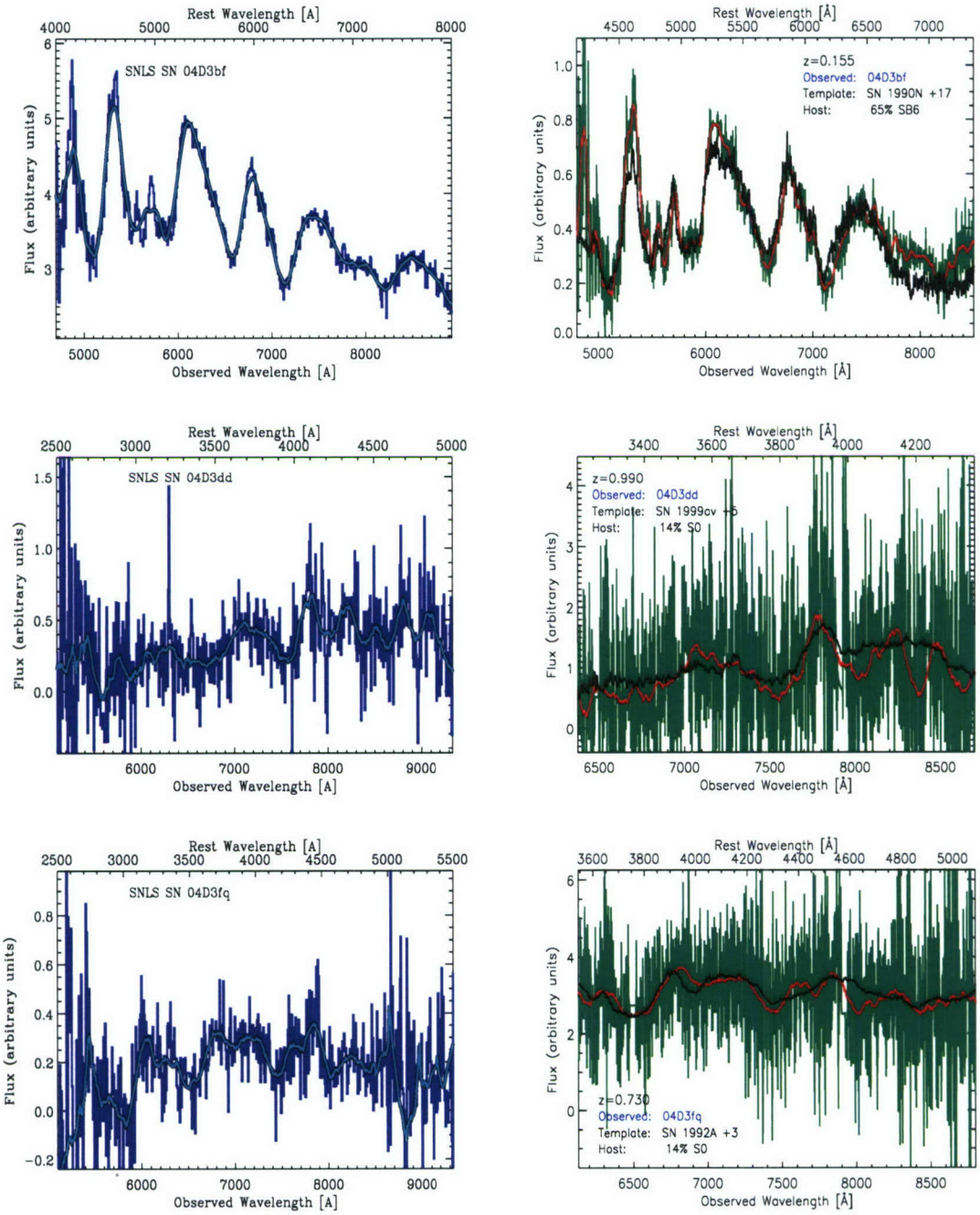

Figure A.8:
TOP: SN Ia 04D3bf **Left** - Observed spectrum **Right** - Template Fit
MIDDLE: SN Ia 04D3dd **Left** - Observed spectrum **Right** - Template Fit
BOTTOM: SN Ia 04D3fq **Left** - Observed Spectrum **Right** - Template Fit

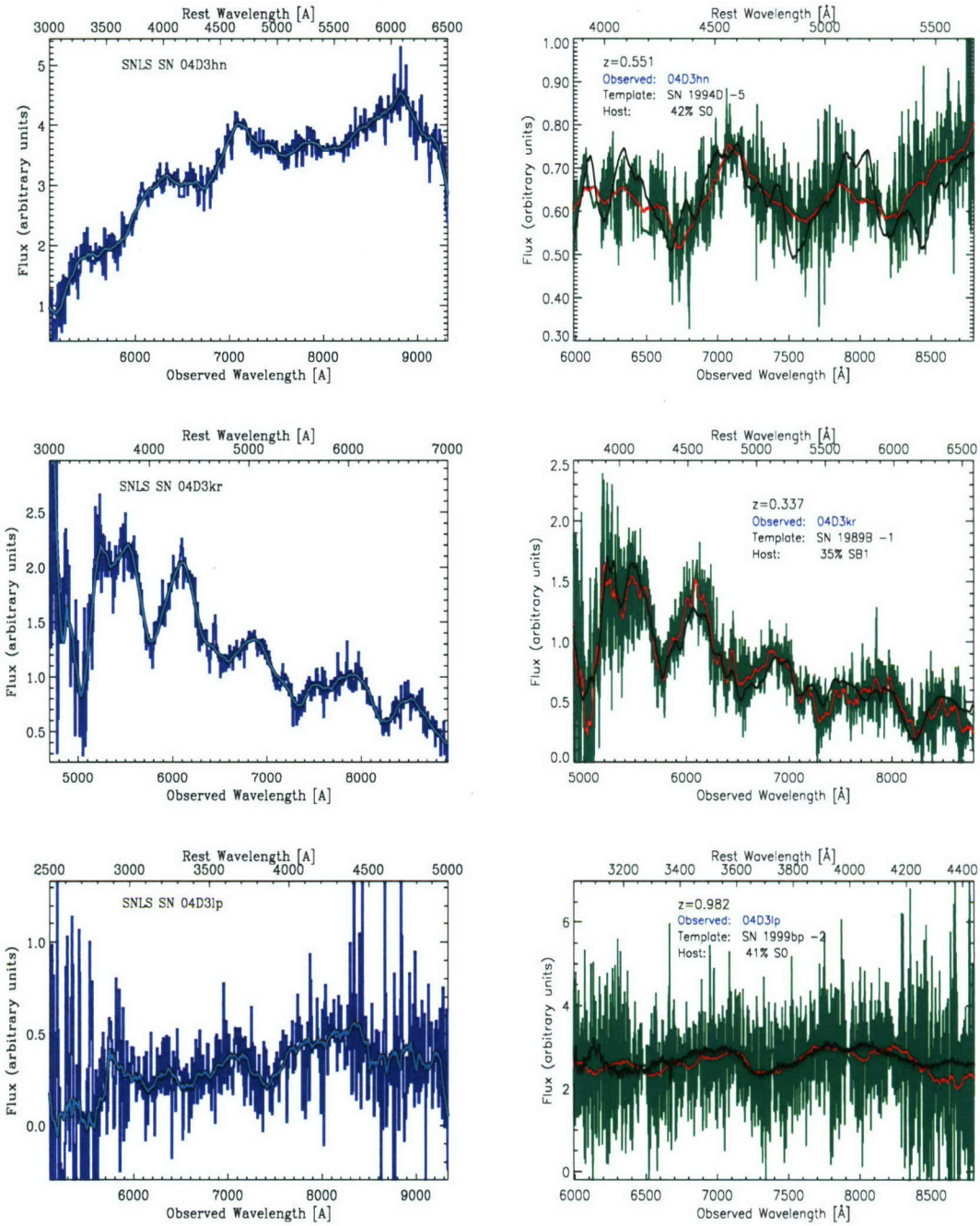

Figure A.9:

TOP:	SN Ia 04D3hn	**Left** - Observed spectrum	**Right** - Template Fit
MIDDLE:	SN Ia 04D3kr	**Left** - Observed spectrum	**Right** - Template Fit
BOTTOM:	SN Ia* 04D3lp	**Left** - Observed Spectrum	**Right** - Template Fit

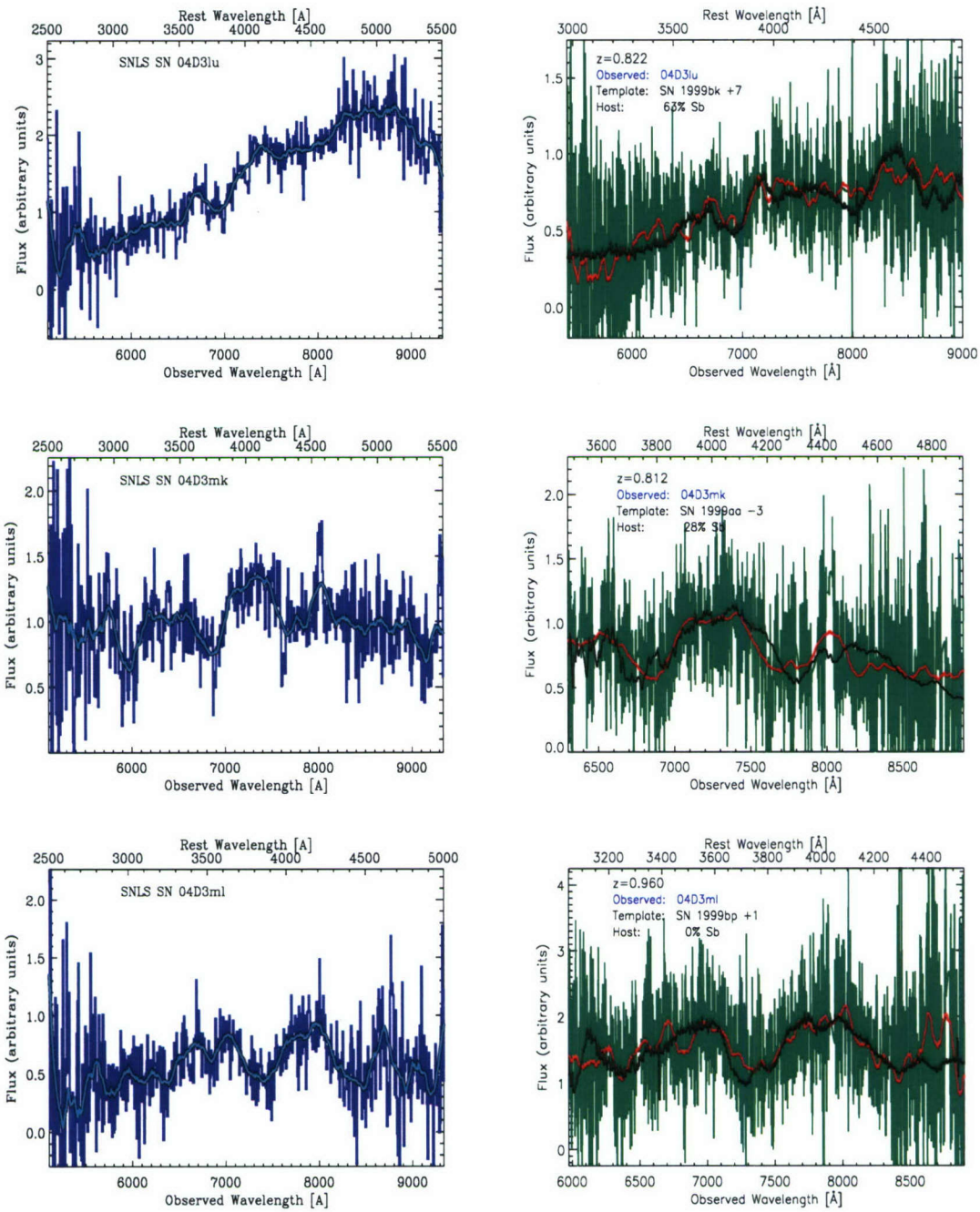

Figure A.10:
TOP: SN Ia 04D3lu **Left** - Observed spectrum **Right** - Template Fit
MIDDLE: SN Ia 04D3mk **Left** - Observed spectrum **Right** - Template Fit
BOTTOM: SN Ia 04D3ml **Left** - Observed Spectrum **Right** - Template Fit

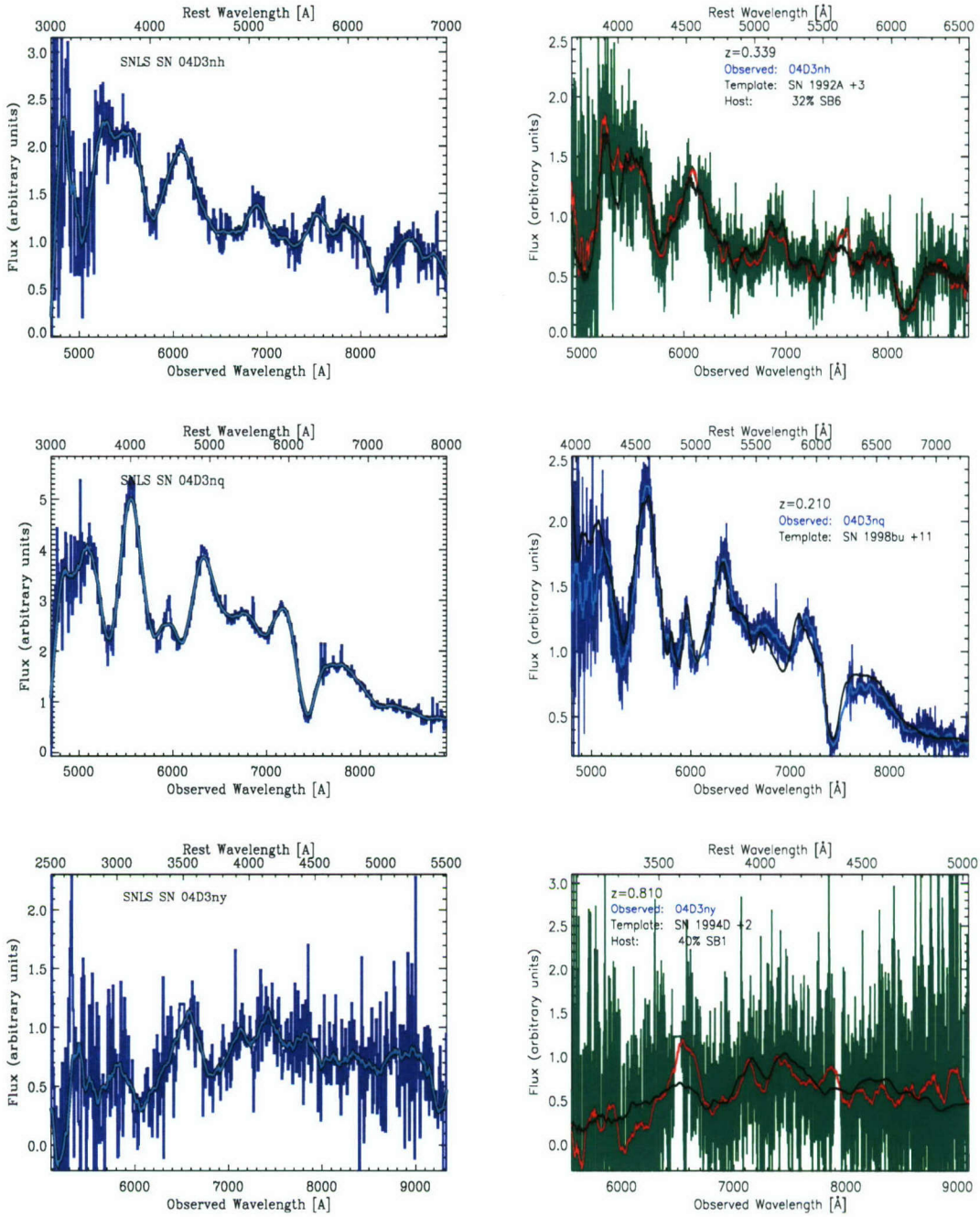

Figure A.11:
TOP: SN Ia 04D3nh **Left** - Observed spectrum **Right** - Template Fit
MIDDLE: SN Ia 04D3nq **Left** - Observed spectrum **Right** - Template Fit
BOTTOM: SN Ia 04D3ny **Left** - Observed Spectrum **Right** - Template Fit

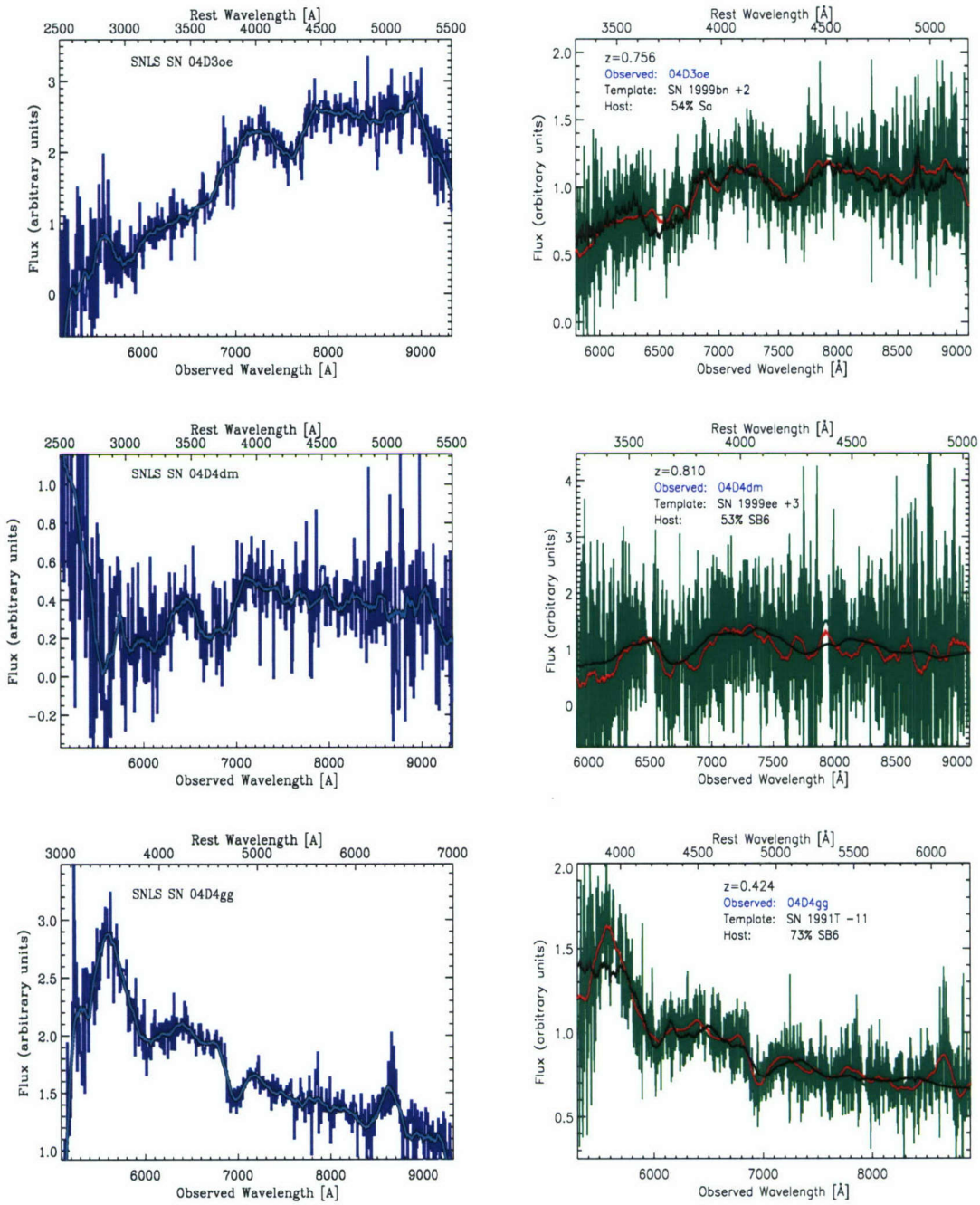

Figure A.12:
TOP: SN Ia 04D3oe **Left** - Observed spectrum **Right** - Template Fit
MIDDLE: SN Ia 04D4dm **Left** - Observed spectrum **Right** - Template Fit
BOTTOM: SN Ia 04D4gg **Left** - Observed Spectrum **Right** - Template Fit

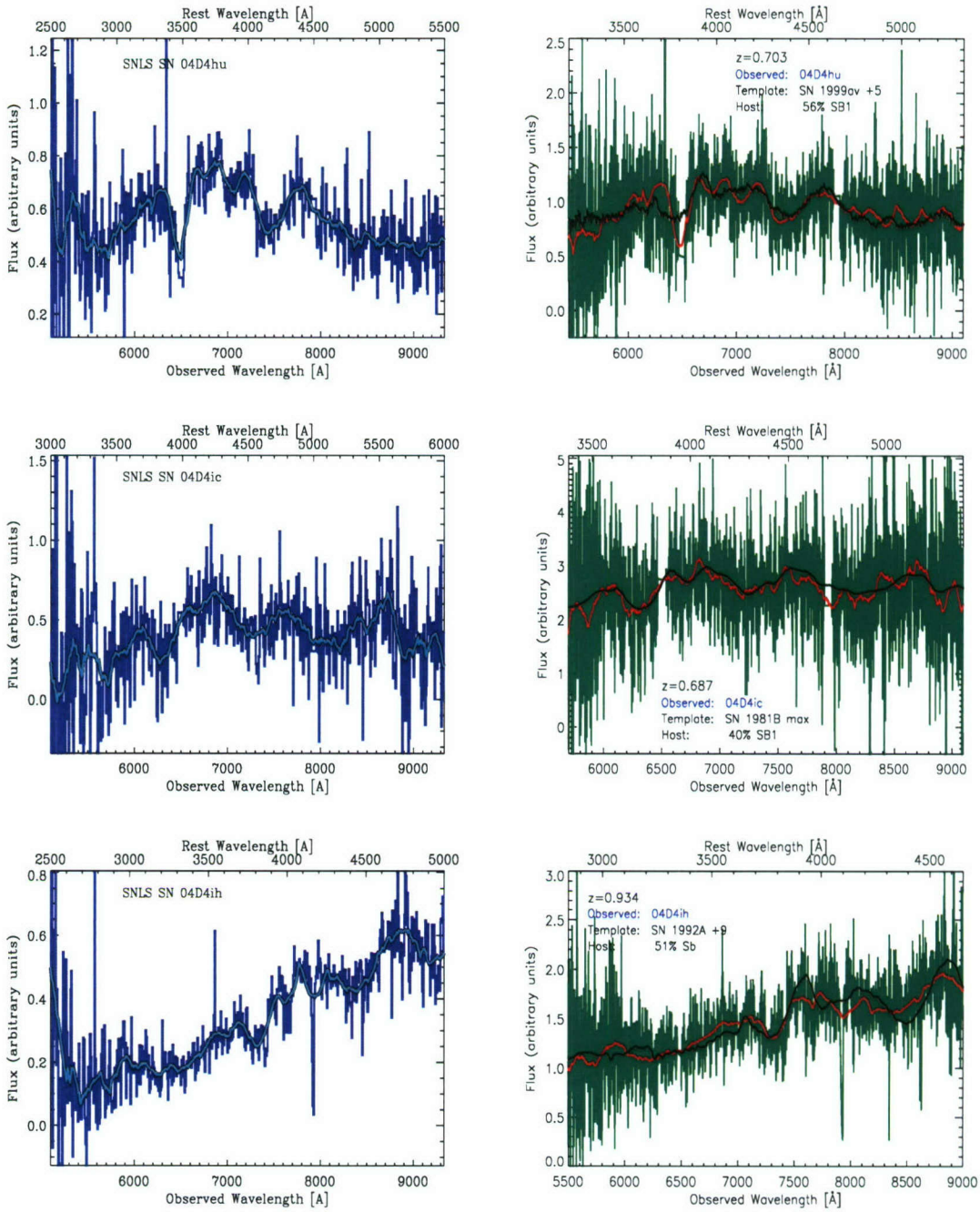

Figure A.13:
TOP: SN Ia 04D4hu **Left** - Observed spectrum **Right** - Template Fit
MIDDLE: SN Ia 04D4ic **Left** - Observed spectrum **Right** - Template Fit
BOTTOM: SN Ia 04D4ih **Left** - Observed Spectrum **Right** - Template Fit

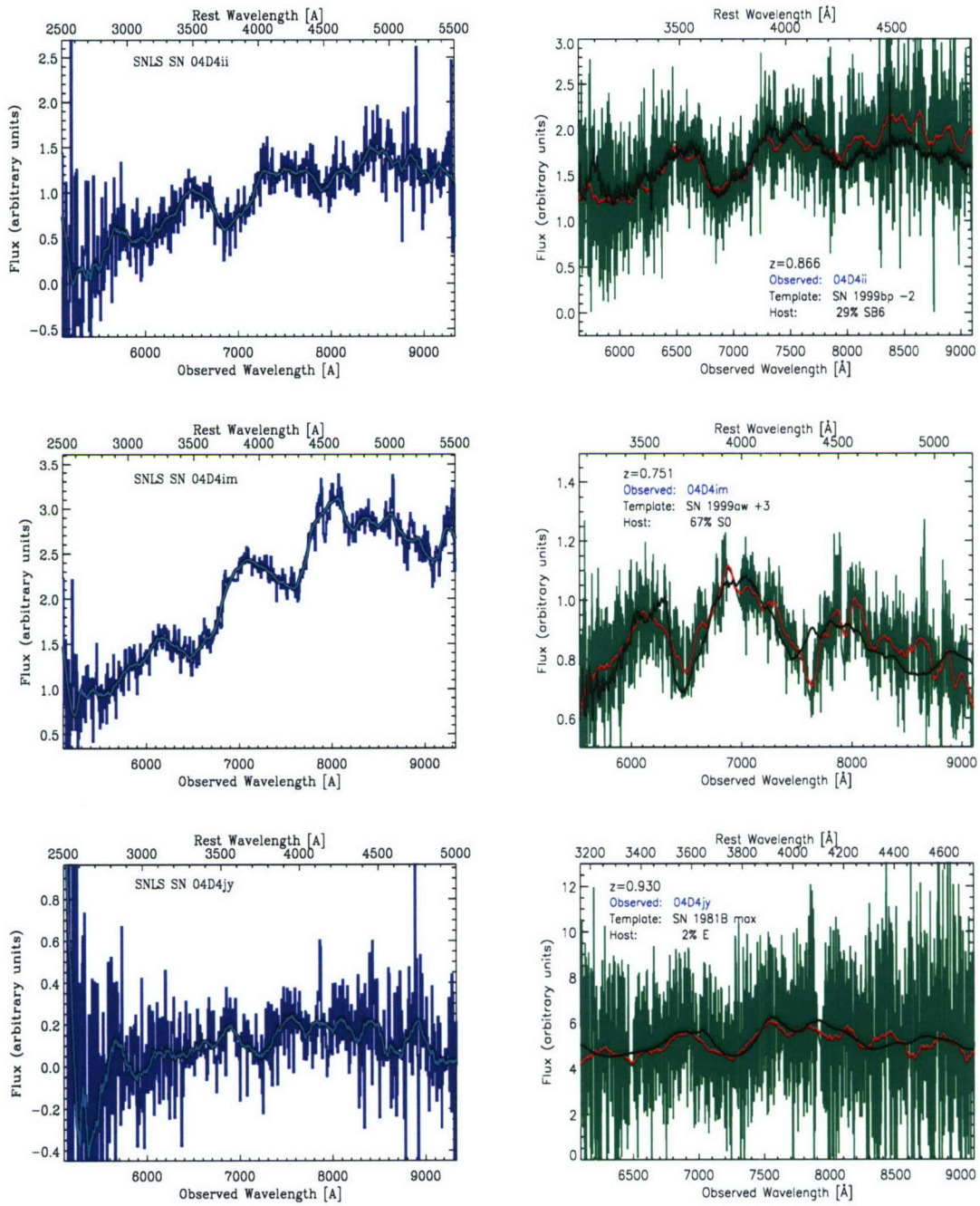

Figure A.14:
TOP: SN Ia 04D4ii **Left** - Observed spectrum **Right** - Template Fit
MIDDLE: SN Ia 04D4im **Left** - Observed spectrum **Right** - Template Fit
BOTTOM: SN Ia* 04D4jy **Left** - Observed Spectrum **Right** - Template Fit

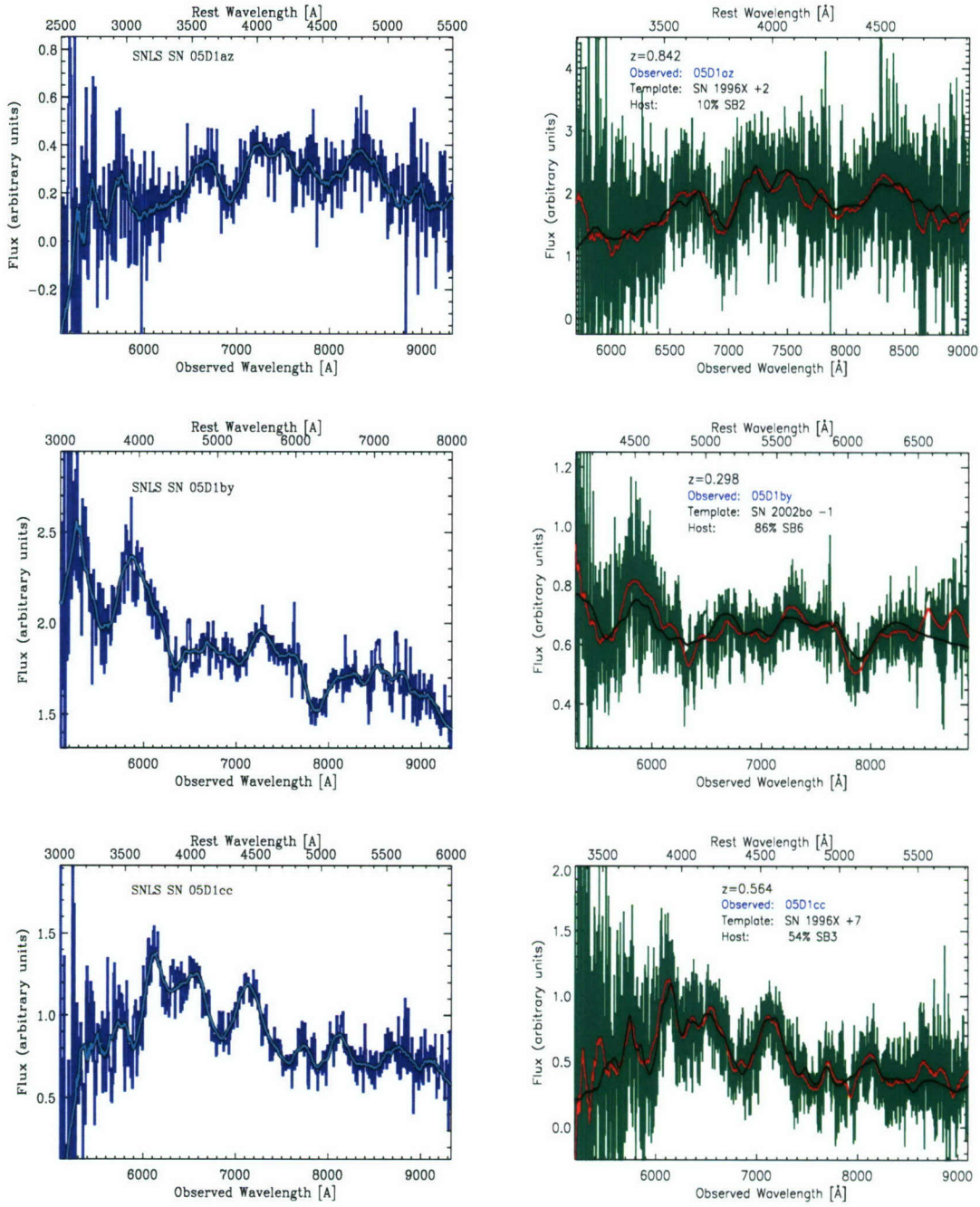

Figure A.15:
TOP: SN Ia 05D1az **Left** - Observed spectrum **Right** - Template Fit
MIDDLE: SN Ia 05D1by **Left** - Observed spectrum **Right** - Template Fit
BOTTOM: SN Ia 05D1cc **Left** - Observed Spectrum **Right** - Template Fit

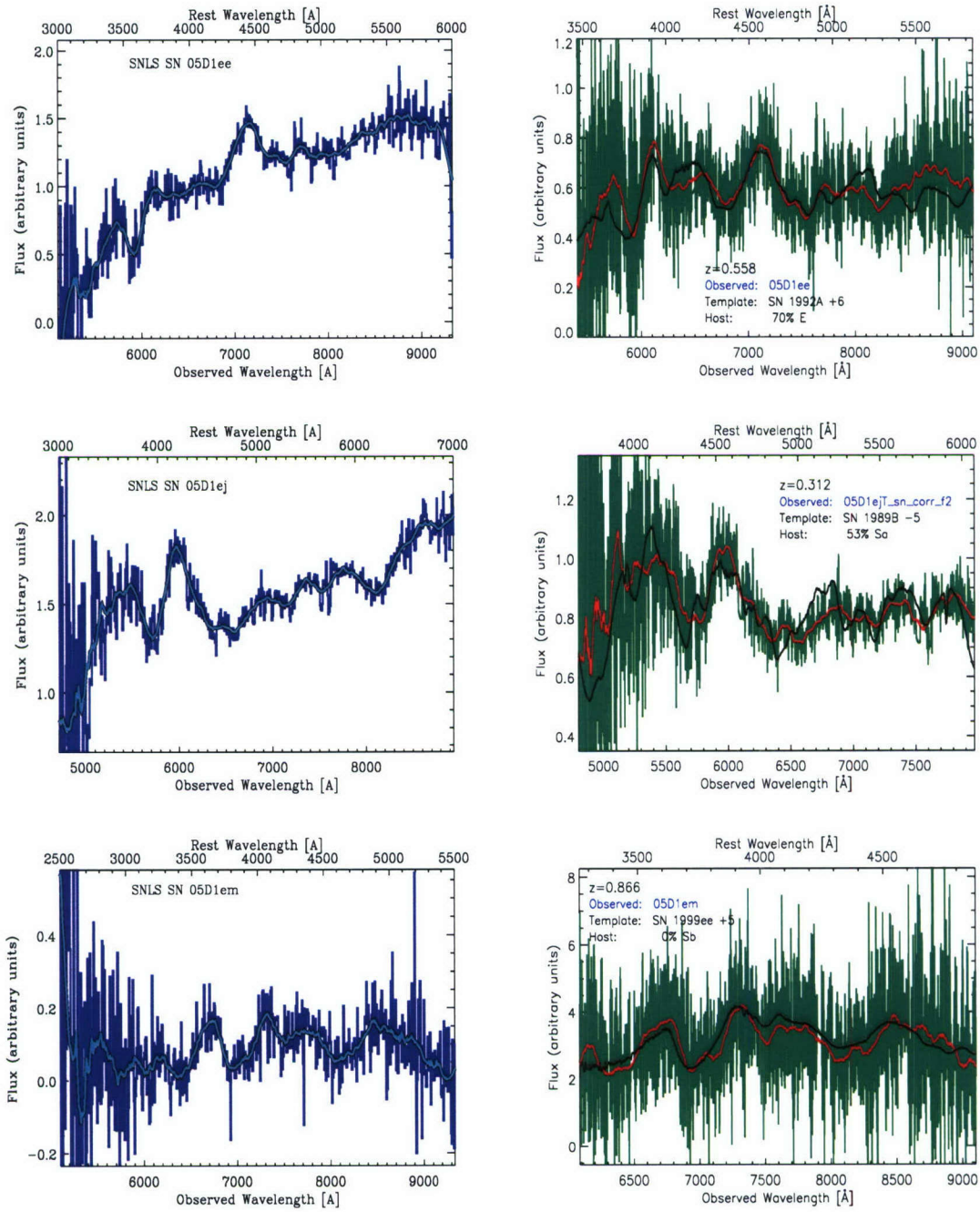

Figure A.16:

TOP:	SN Ia 05D1ee	**Left** - Observed spectrum	**Right** - Template Fit
MIDDLE:	SN Ia 05D1ej	**Left** - Observed spectrum	**Right** - Template Fit
BOTTOM:	SN Ia 05D1em	**Left** - Observed Spectrum	**Right** - Template Fit

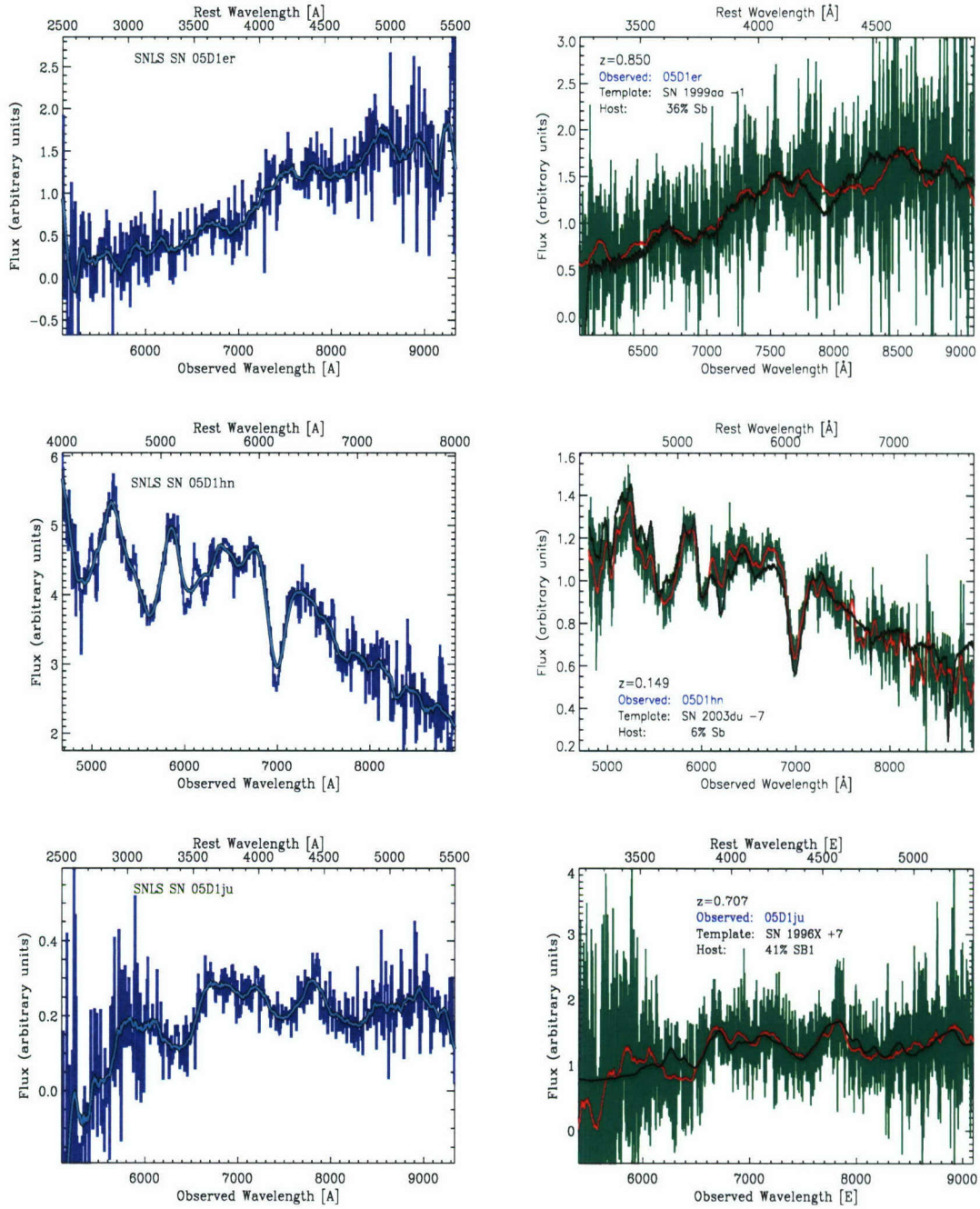

Figure A.17:

TOP:	SN Ia* 05D1er	**Left** - Observed spectrum	**Right** - Template Fit
MIDDLE:	SN Ia 05D1hn	**Left** - Observed spectrum	**Right** - Template Fit
BOTTOM:	SN Ia* 05D1ju	**Left** - Observed Spectrum	**Right** - Template Fit

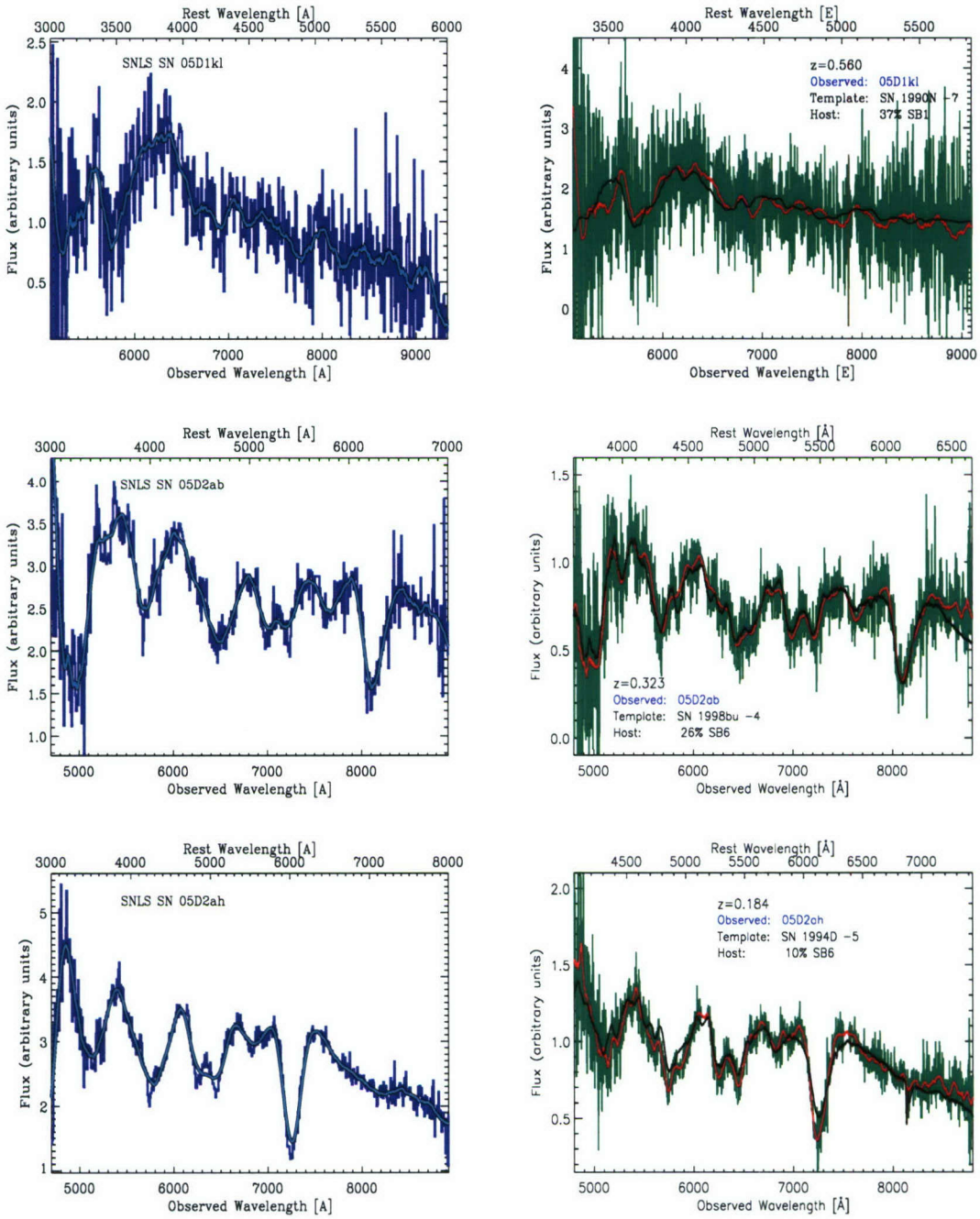

Figure A.18:

TOP:	SN Ia* 05D1kl	**Left** - Observed spectrum	**Right** - Template Fit
MIDDLE:	SN Ia 05D2ab	**Left** - Observed spectrum	**Right** - Template Fit
BOTTOM:	SN Ia 05D2ah	**Left** - Observed Spectrum	**Right** - Template Fit

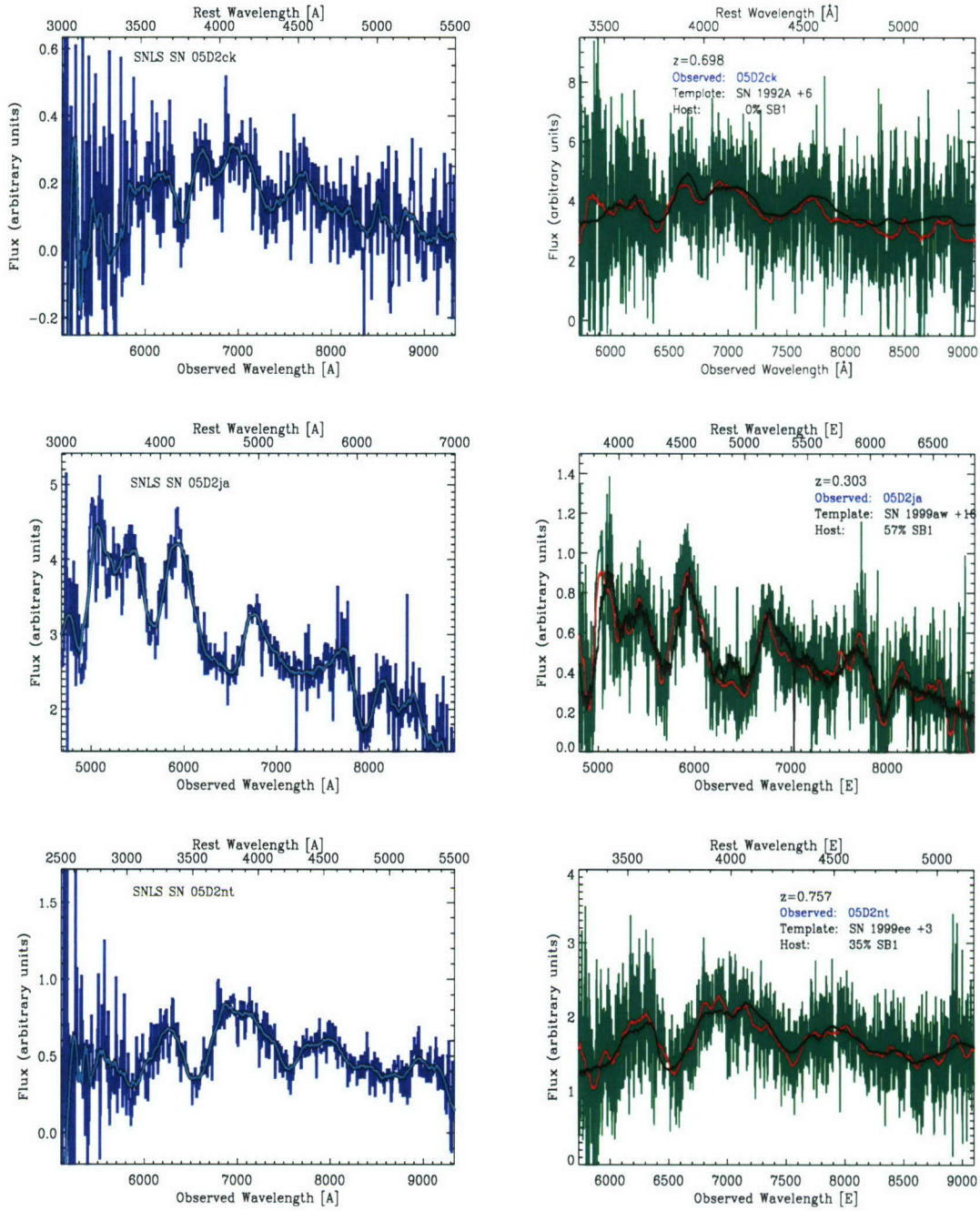

Figure A.19:
TOP: SN Ia 05D2ck **Left** - Observed spectrum **Right** - Template Fit
MIDDLE: SN Ia 05D2ja **Left** - Observed spectrum **Right** - Template Fit
BOTTOM: SN Ia 05D2nt **Left** - Observed Spectrum **Right** - Template Fit

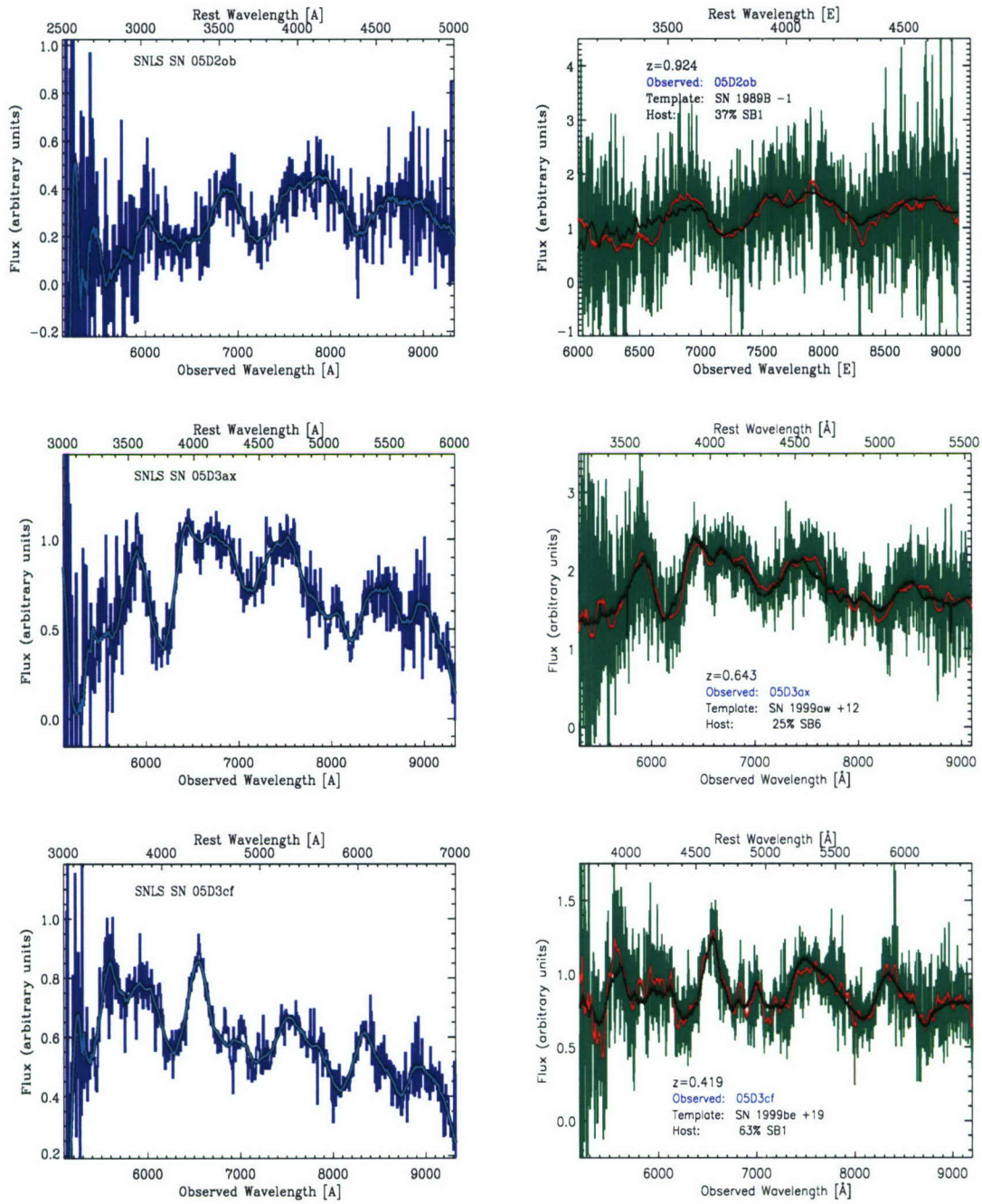

Figure A.20:
TOP: SN Ia 05D2ob **Left** - Observed spectrum **Right** - Template Fit
MIDDLE: SN Ia 05D3ax **Left** - Observed spectrum **Right** - Template Fit
BOTTOM: SN Ia 05D3cf **Left** - Observed Spectrum **Right** - Template Fit

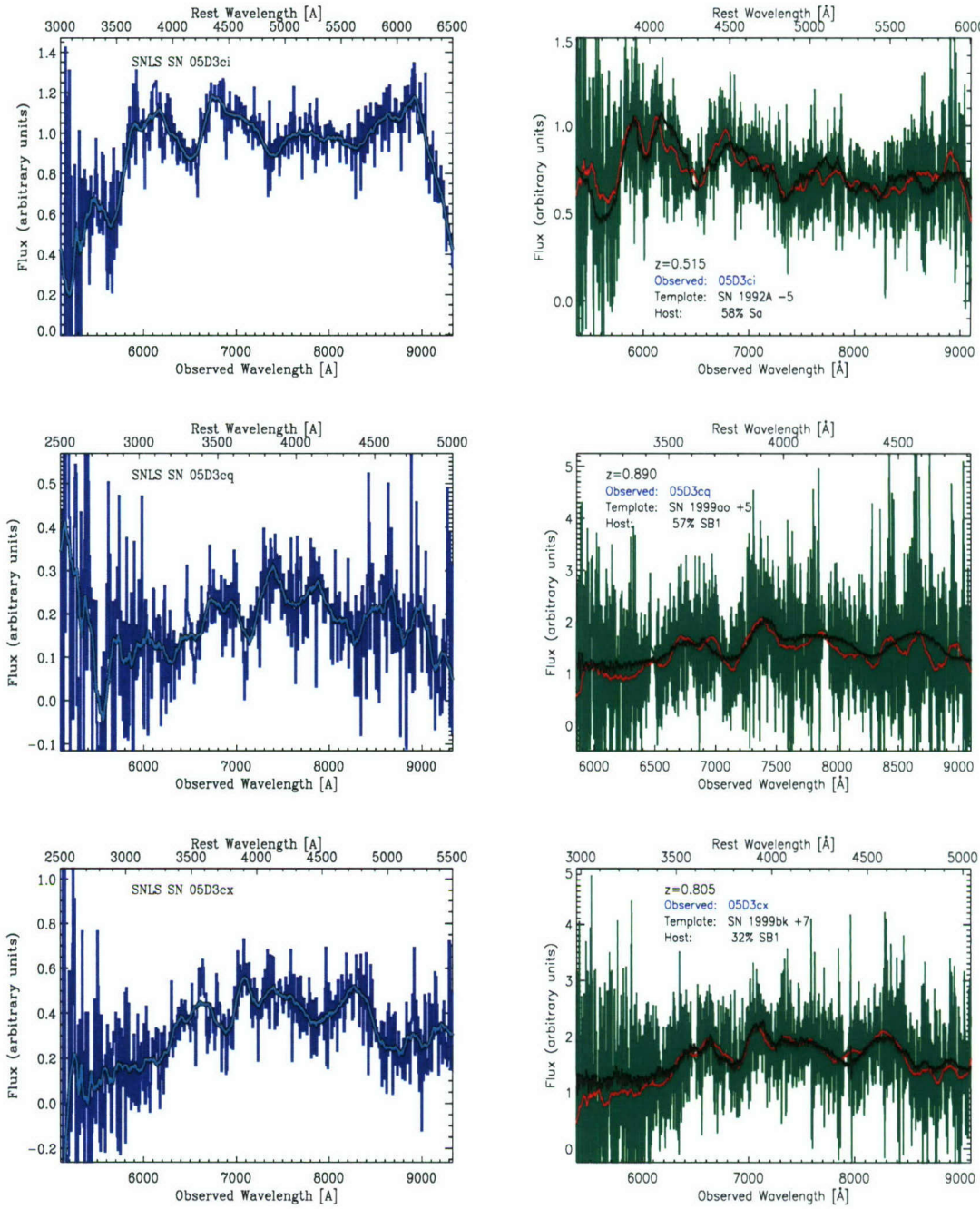

Figure A.21:
TOP: SN Ia 05D3ci **Left** - Observed spectrum **Right** - Template Fit
MIDDLE: SN Ia* 05D3cq **Left** - Observed spectrum **Right** - Template Fit
BOTTOM: SN Ia 05D3cx **Left** - Observed Spectrum **Right** - Template Fit

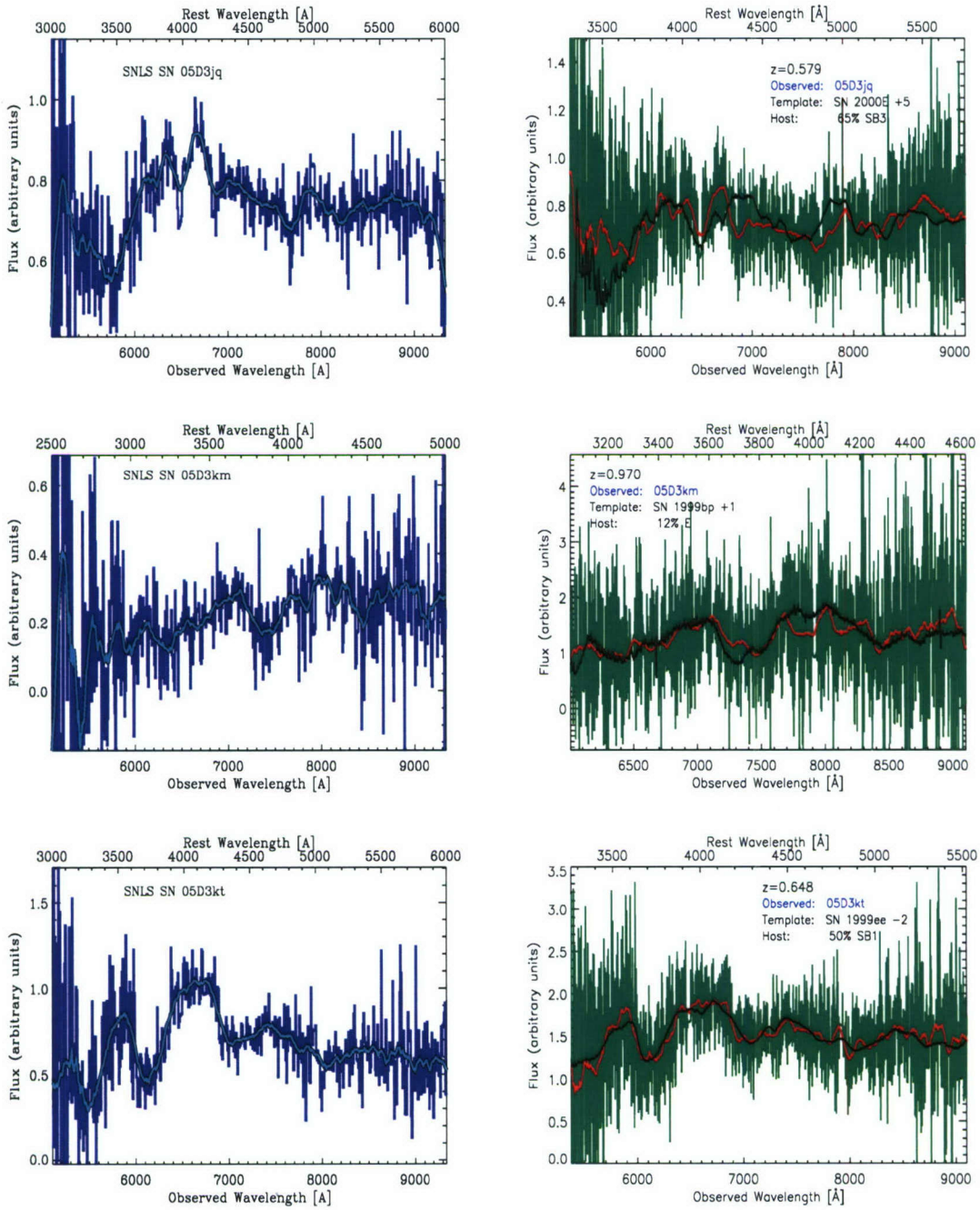

Figure A.22:
TOP: SN Ia 05D3jq **Left** - Observed spectrum **Right** - Template Fit
MIDDLE: SN Ia* 05D3km **Left** - Observed spectrum **Right** - Template Fit
BOTTOM: SN Ia 05D3kt **Left** - Observed Spectrum **Right** - Template Fit

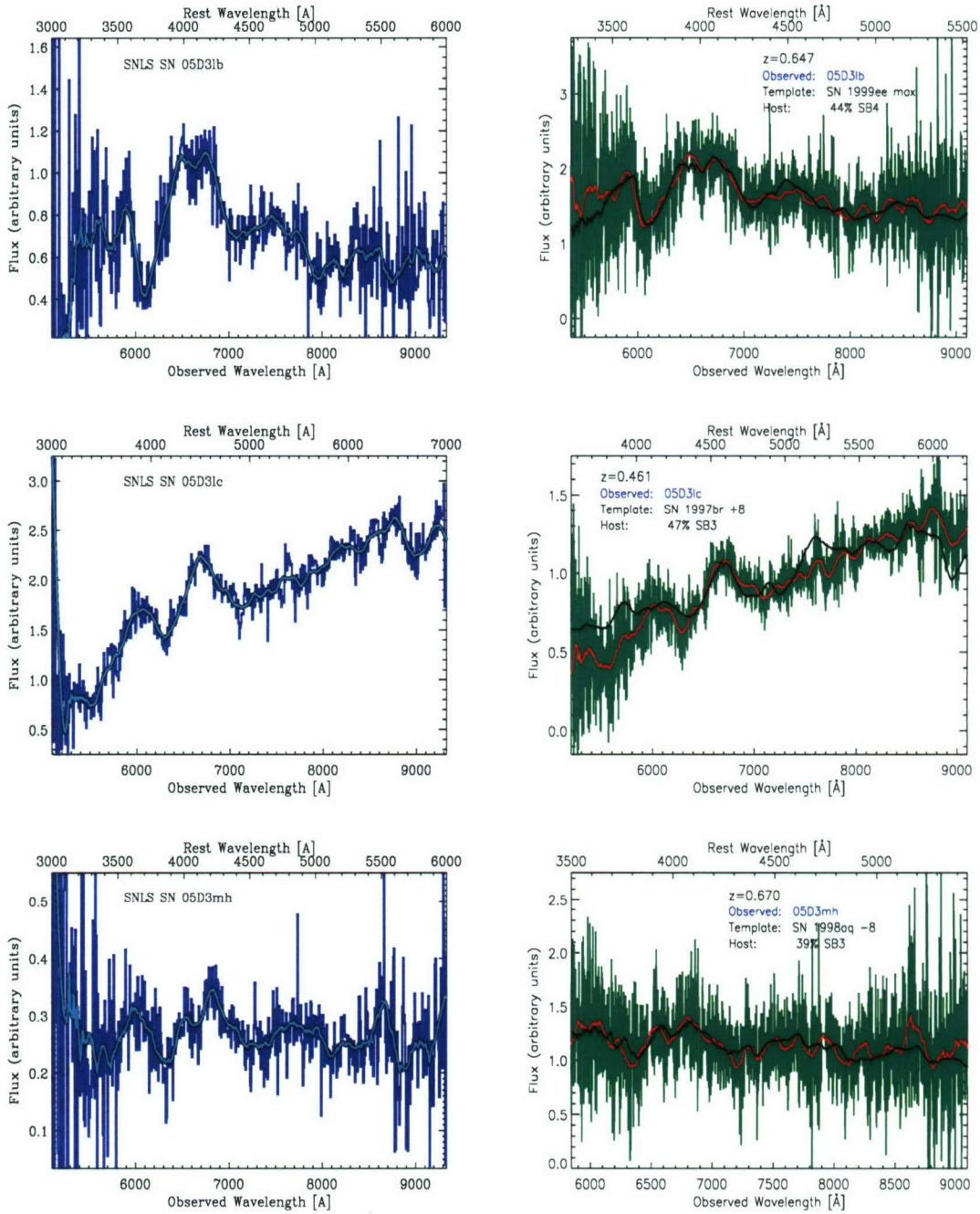

Figure A.23:
TOP: SN Ia 05D3lb **Left** - Observed spectrum **Right** - Template Fit
MIDDLE: SN Ia 05D3lc **Left** - Observed spectrum **Right** - Template Fit
BOTTOM: SN Ia 05D3mh **Left** - Observed Spectrum **Right** - Template Fit

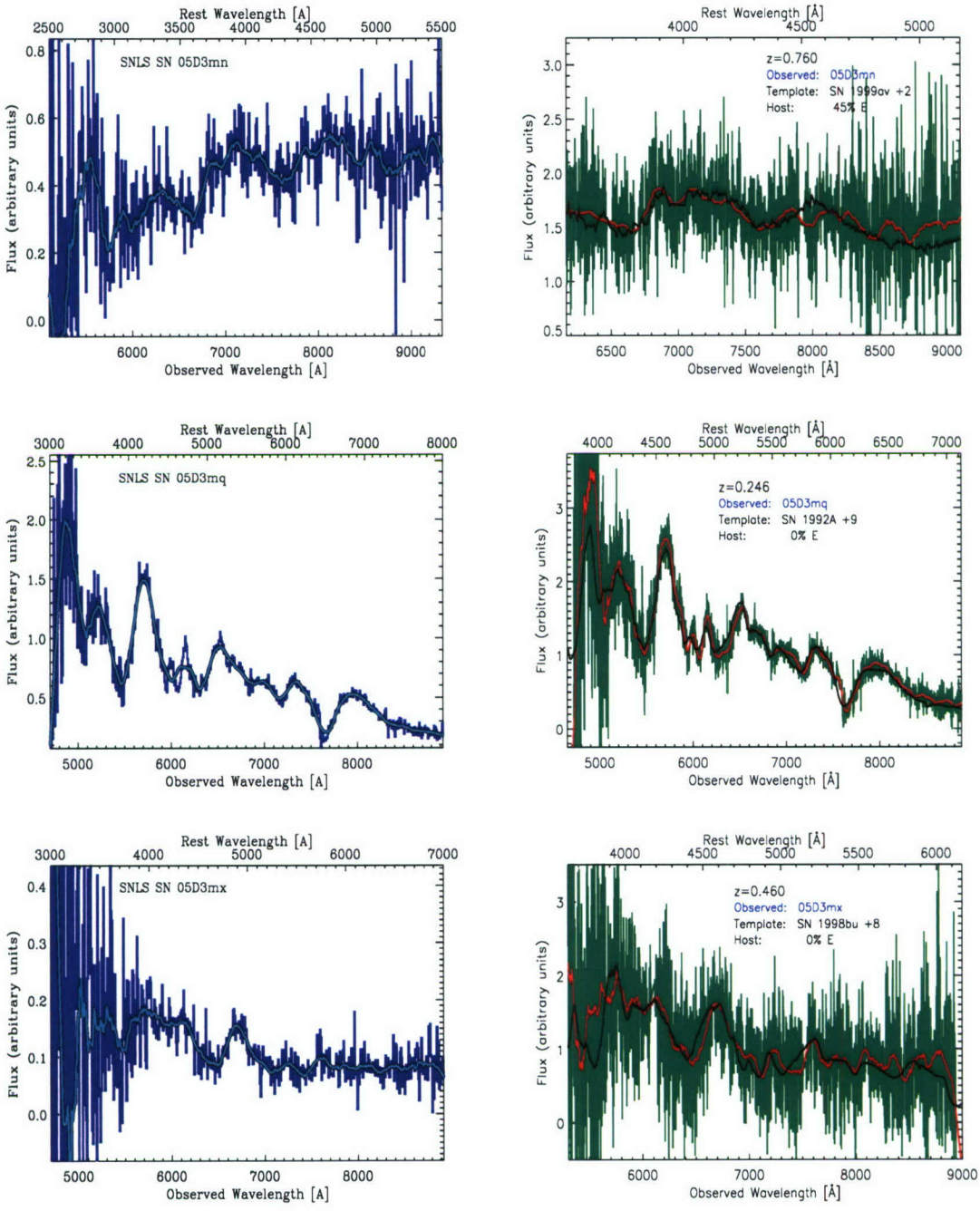

Figure A.24:

TOP:	SN Ia* 05D3mn	**Left** - Observed spectrum	**Right** - Template Fit
MIDDLE:	SN Ia 05D3mq	**Left** - Observed spectrum	**Right** - Template Fit
BOTTOM:	SN Ia 05D3mx	**Left** - Observed Spectrum	**Right** - Template Fit

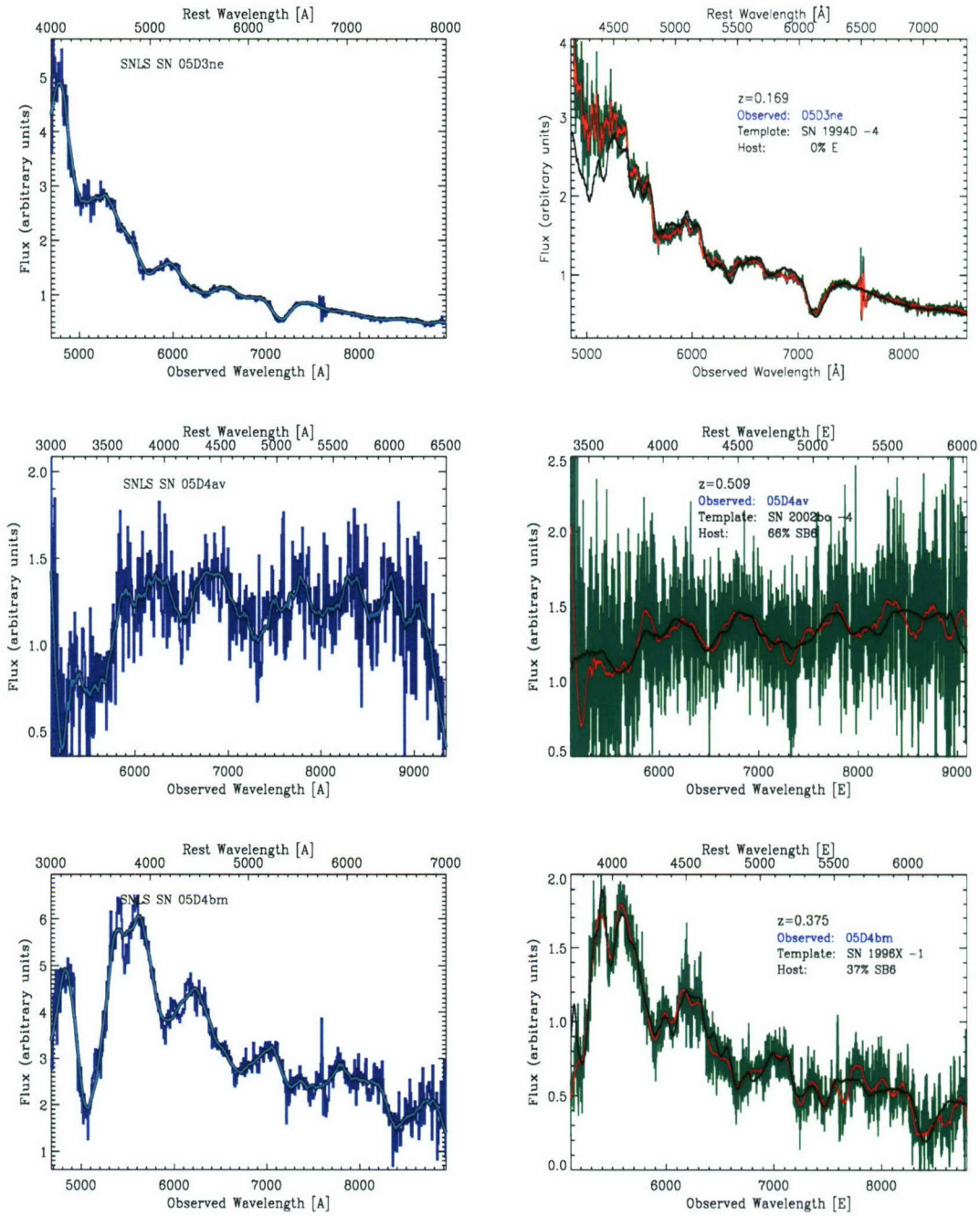

Figure A.25:

TOP:	SN Ia 05D3ne	**Left** - Observed spectrum	**Right** - Template Fit
MIDDLE:	SN Ia 05D4av	**Left** - Observed spectrum	**Right** - Template Fit
BOTTOM:	SN Ia 05D4bm	**Left** - Observed Spectrum	**Right** - Template Fit

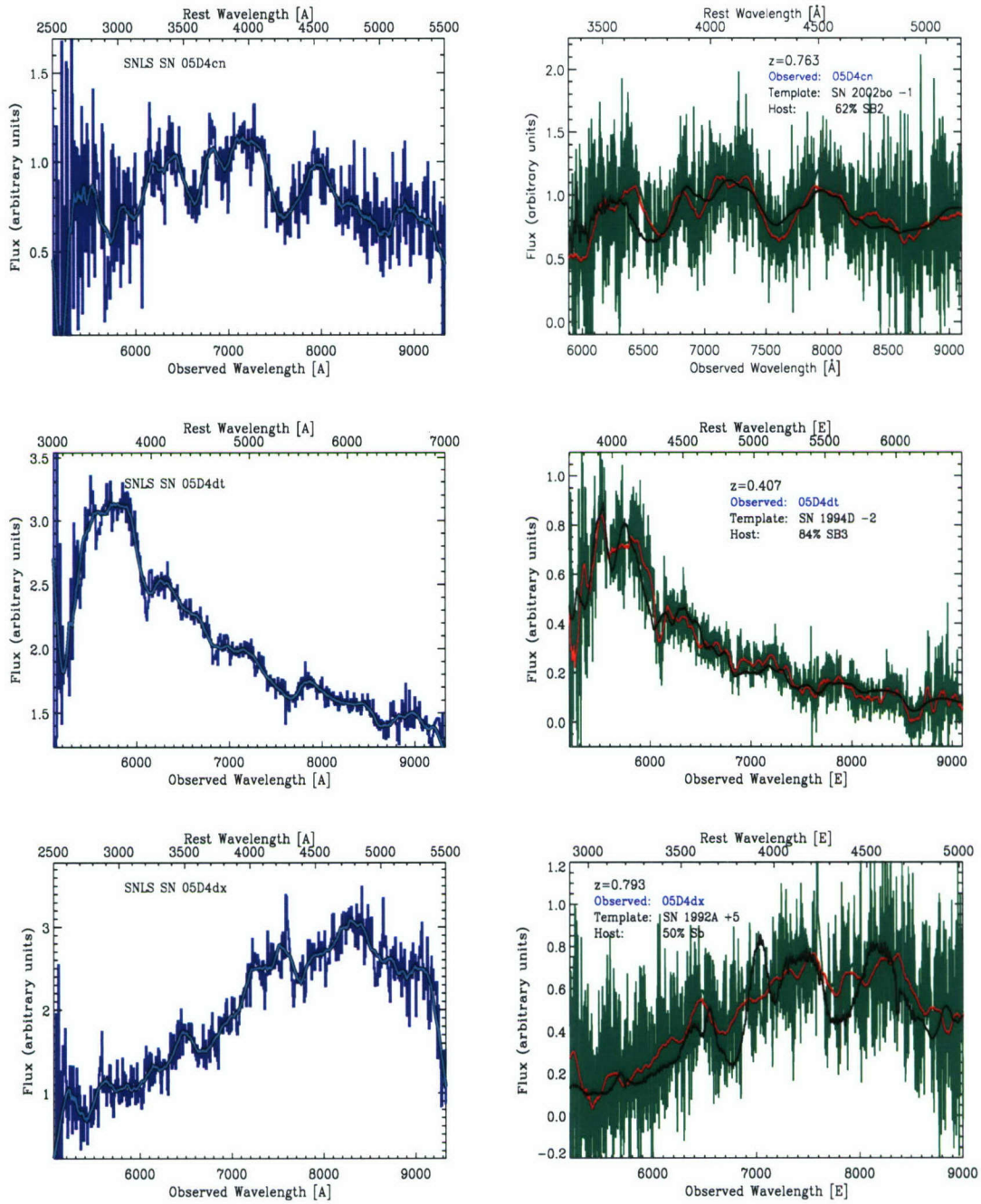

Figure A.26:

TOP:	SN Ia* 05D4cn	**Left** - Observed spectrum	**Right** - Template Fit
MIDDLE:	SN Ia 05D4dt	**Left** - Observed spectrum	**Right** - Template Fit
BOTTOM:	SN Ia 05D4dx	**Left** - Observed Spectrum	**Right** - Template Fit

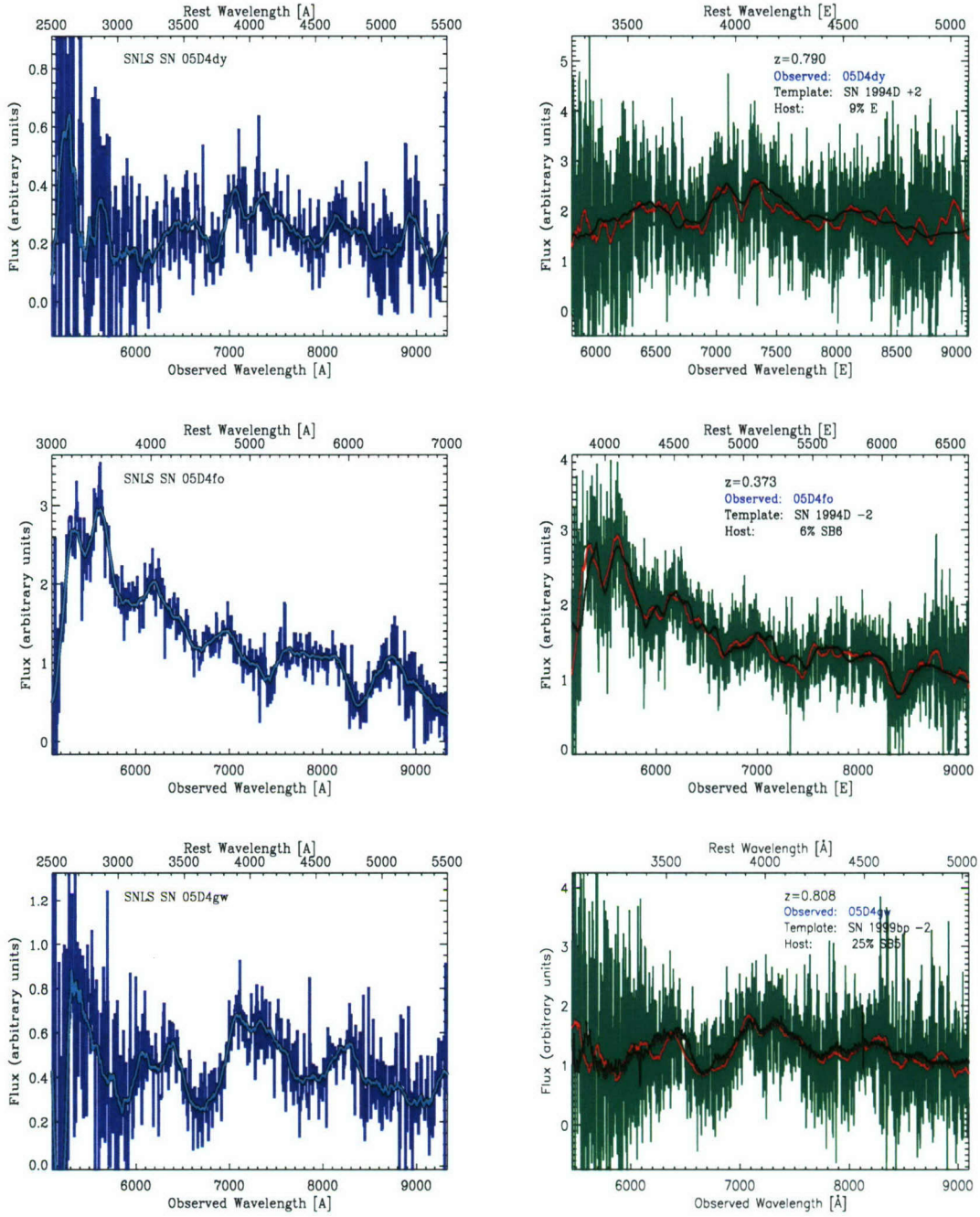

Figure A.27:

TOP:	SN Ia 05D4dy	**Left** - Observed spectrum	**Right** - Template Fit
MIDDLE:	SN Ia 05D4fo	**Left** - Observed spectrum	**Right** - Template Fit
BOTTOM:	SN Ia 05D4gw	**Left** - Observed Spectrum	**Right** - Template Fit

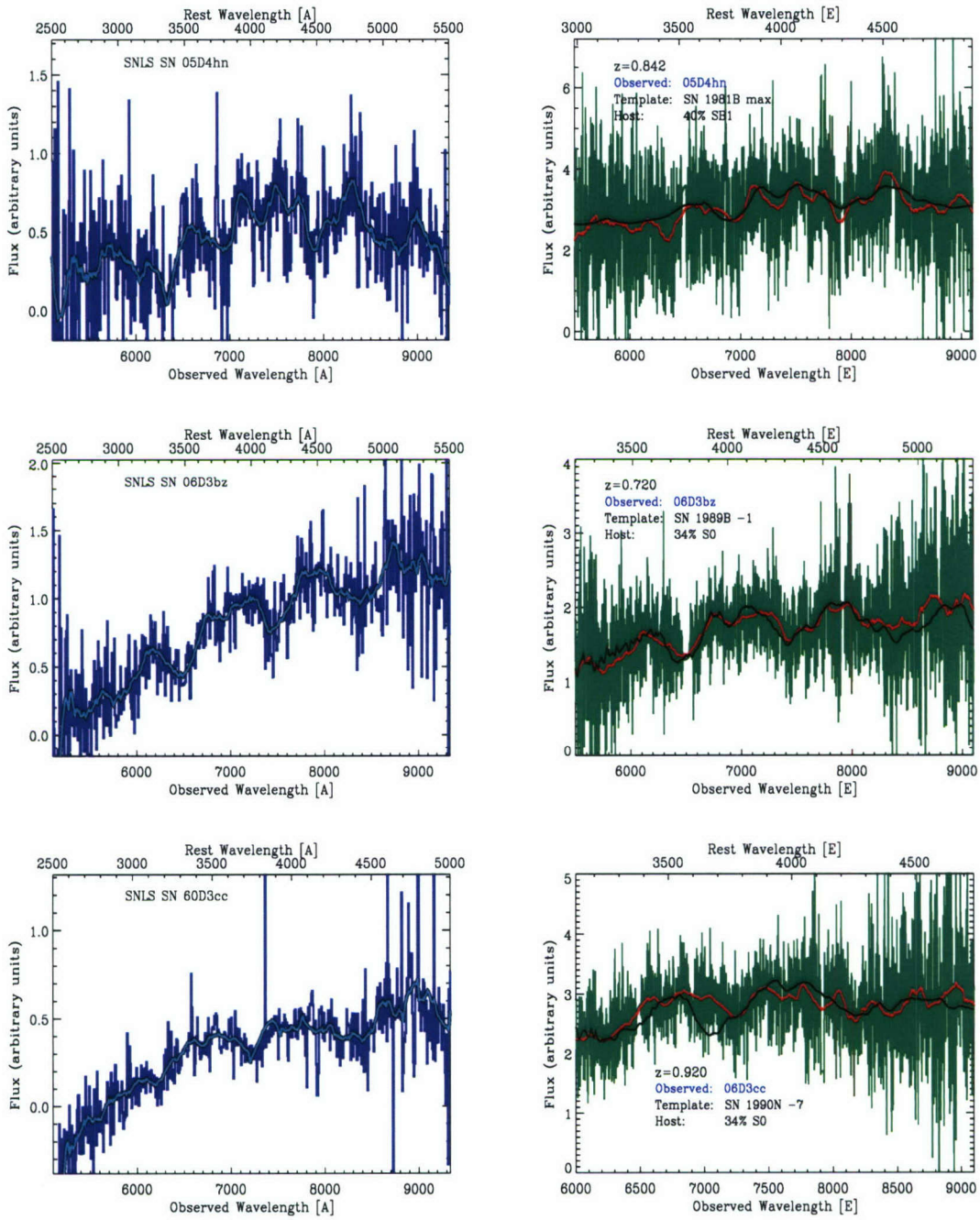

Figure A.28:
TOP: SN Ia 05D4hn **Left** - Observed spectrum **Right** - Template Fit
MIDDLE: SN Ia 06D3bz **Left** - Observed spectrum **Right** - Template Fit
BOTTOM: SN Ia* 06D3cc **Left** - Observed Spectrum **Right** - Template Fit

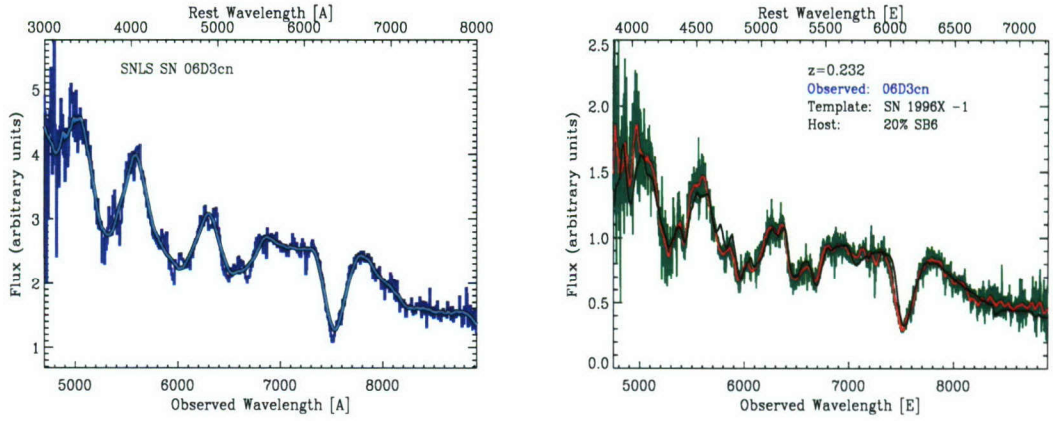

Figure A.29:
TOP: SN Ia 06D3cn **Left** - Observed spectrum **Right** - Template Fit

A.2 SNLS Supernovae Spectra - Confirmed Non-Type Ia SNe

These spectra are from SNLS SN candidates that unambiguously matched core-collapse supernovae (i.e. a Confidence Index of 0).

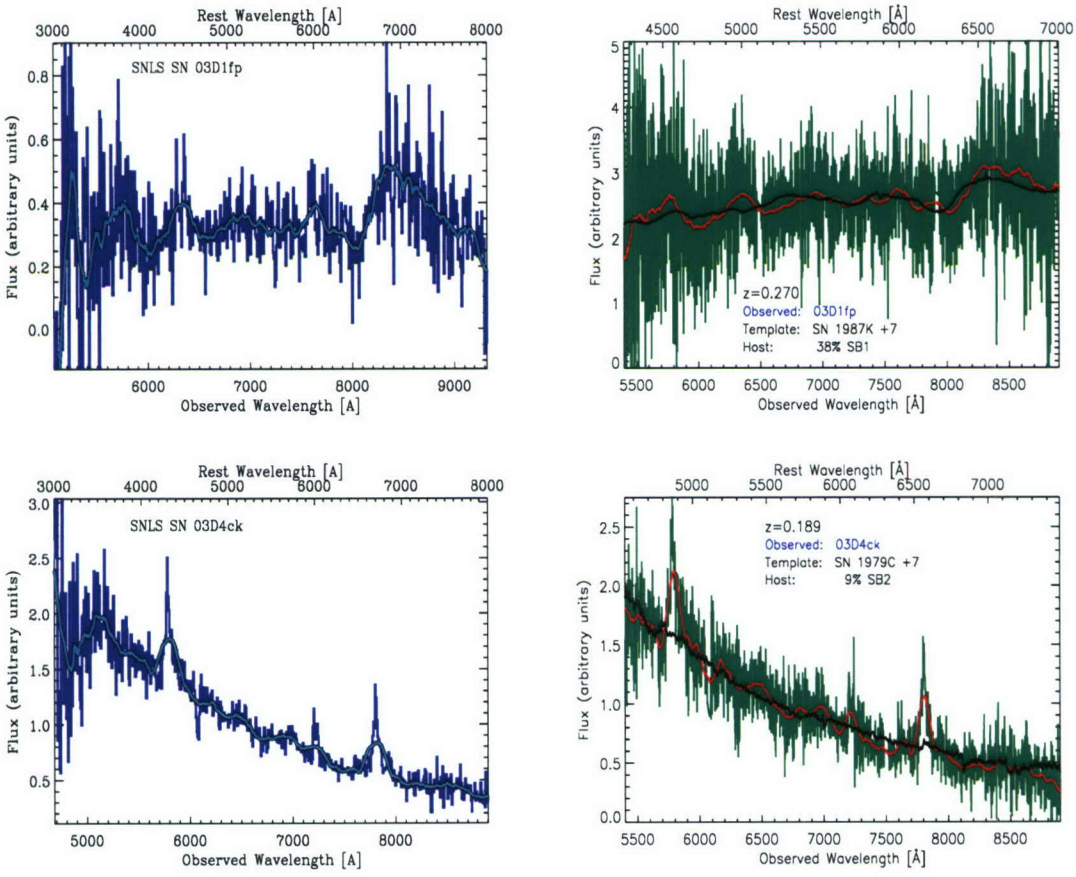

Figure A.30:
TOP: SN II 03D1fp **Left** - Observed spectrum **Right** - Template Fit
BOTTOM: SN II 03D4ck **Left** - Observed spectrum **Right** - Template Fit

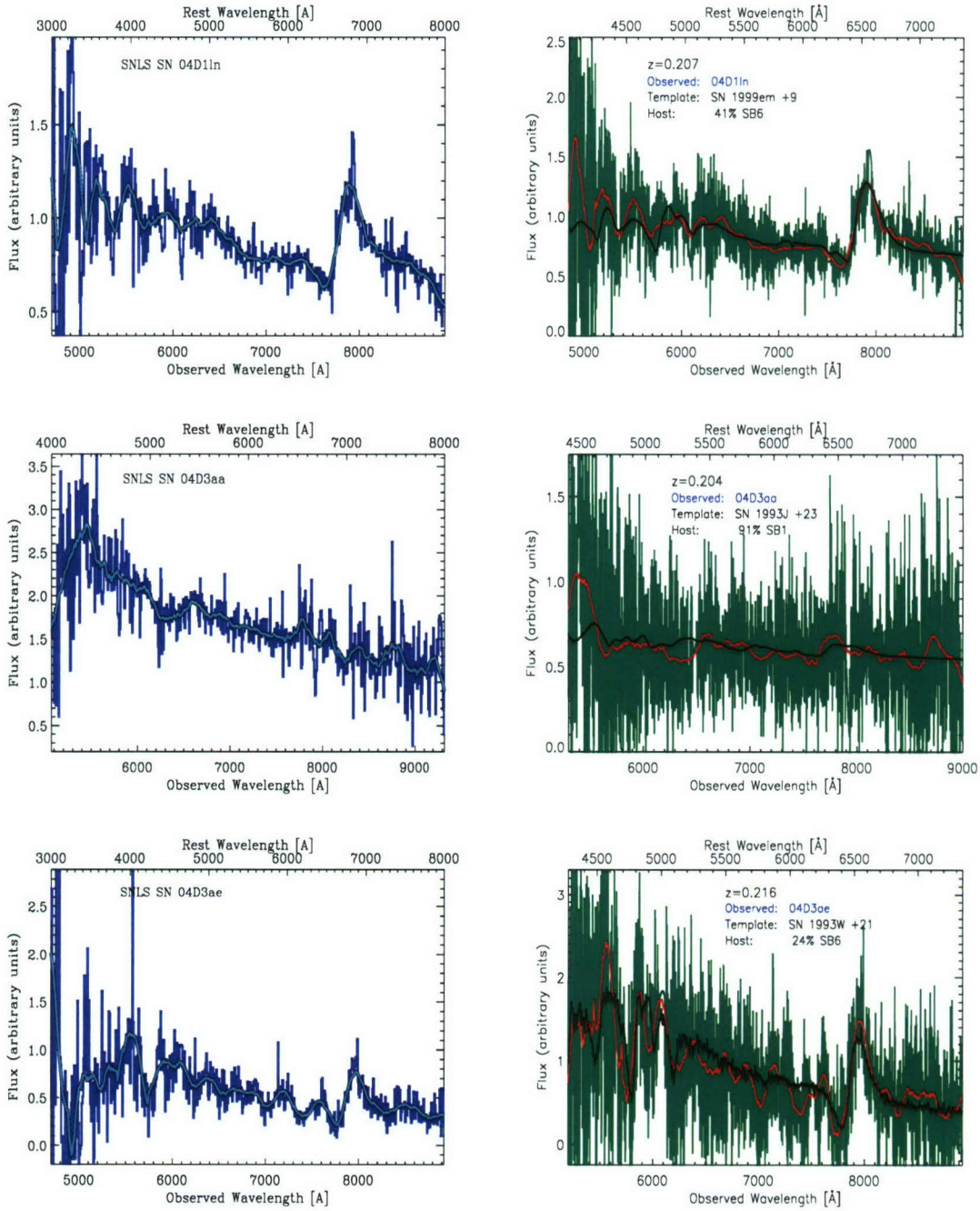

Figure A.31:

TOP:	SN II 04D1ln	**Left** - Observed spectrum	**Right** - Template Fit
MIDDLE:	SN II 04D3aa	**Left** - Observed spectrum	**Right** - Template Fit
BOTTOM:	SN II 04D3ae	**Left** - Observed spectrum	**Right** - Template Fit

A.3 SNLS Supernovae Spectra - Unknown Objects

These spectra are from SNLS SN candidates that were classified as 'Unknown' (Confidence Index = 2) or 'Probably not a Ia' (Confidence Index = 1). In many cases, the S/N in these spectra was too low or the features were too obscure to be quantitatively compared to any low-z templates with any confidence. In this case, only the 'Observed' spectrum from the object is shown. Some of these objects have estimated redshifts from host galaxy features, in these cases the rest wavelength is plotted along the top of the image. For objects with no redshift estimates only the observed wavelength axis is labeled.

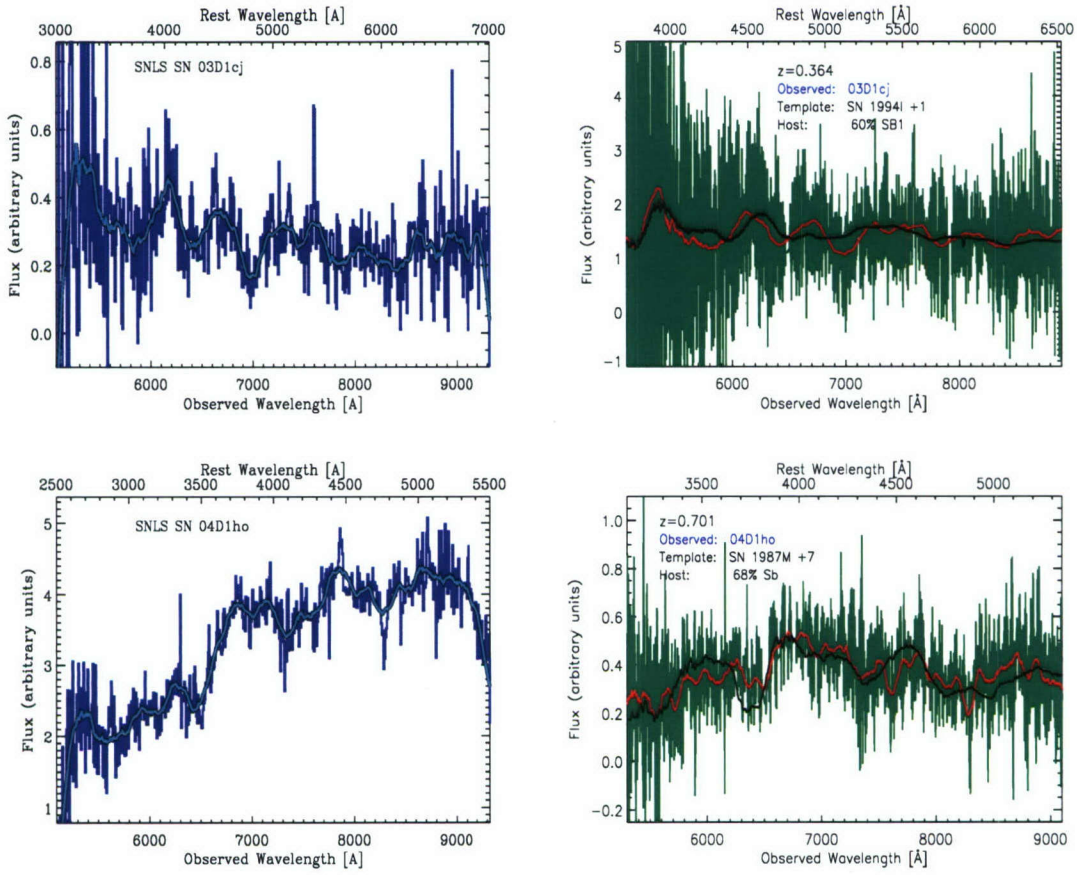

Figure A.32:
TOP: 03D1cj **Left** - Observed spectrum **Right** - Template Fit - SN Ib/c
BOTTOM: 04D1ho **Left** - Observed Spectrum **Right** - Template Fit - SN II

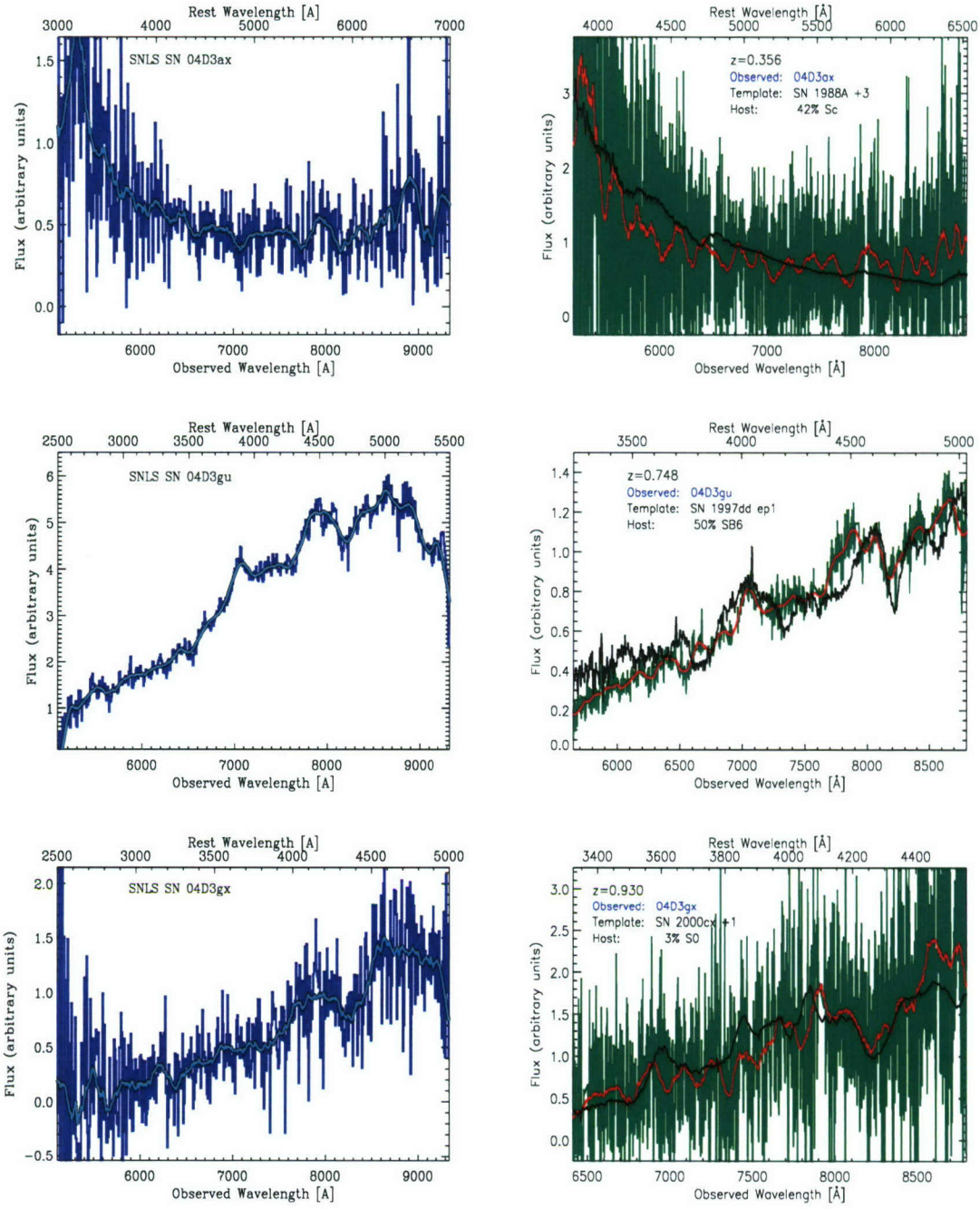

Figure A.33:
TOP: 04D3ax **Left** - Observed spectrum **Right** - Template Fit - SN II
MIDDLE: 04D3gu **Left** - Observed spectrum **Right** - Template Fit - SN Ib/c
BOTTOM: 04D3gx **Left** - Observed Spectrum **Right** - Template Fit - SN Ia

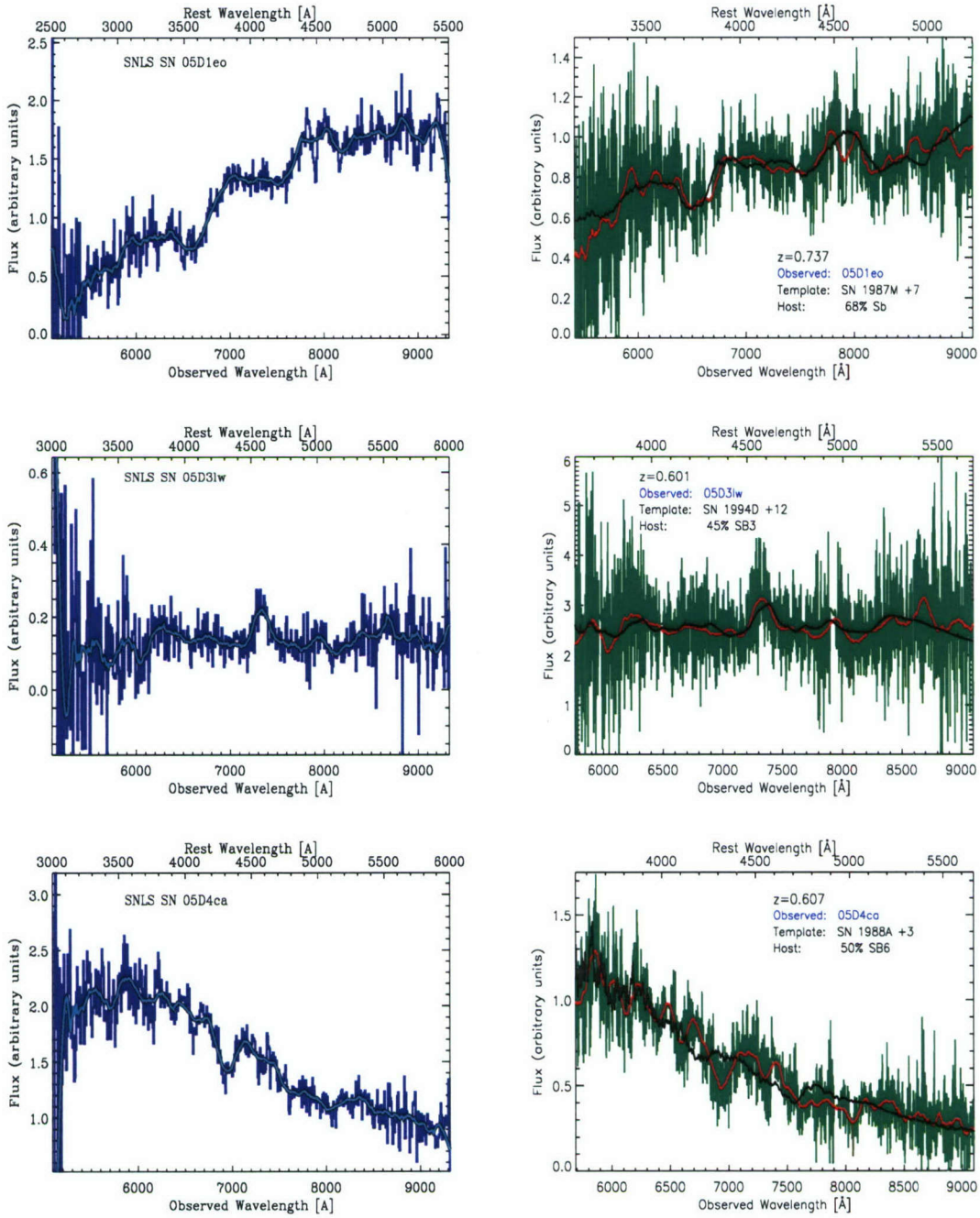

Figure A.34:
TOP: 05D1eo **Left** - Observed spectrum **Right** - Template Fit - SN Ib/c
MIDDLE: 05D3lw **Left** - Observed spectrum **Right** - Template Fit - SN Ia
BOTTOM: 05D4ca **Left** - Observed Spectrum **Right** - Template Fit - SN II

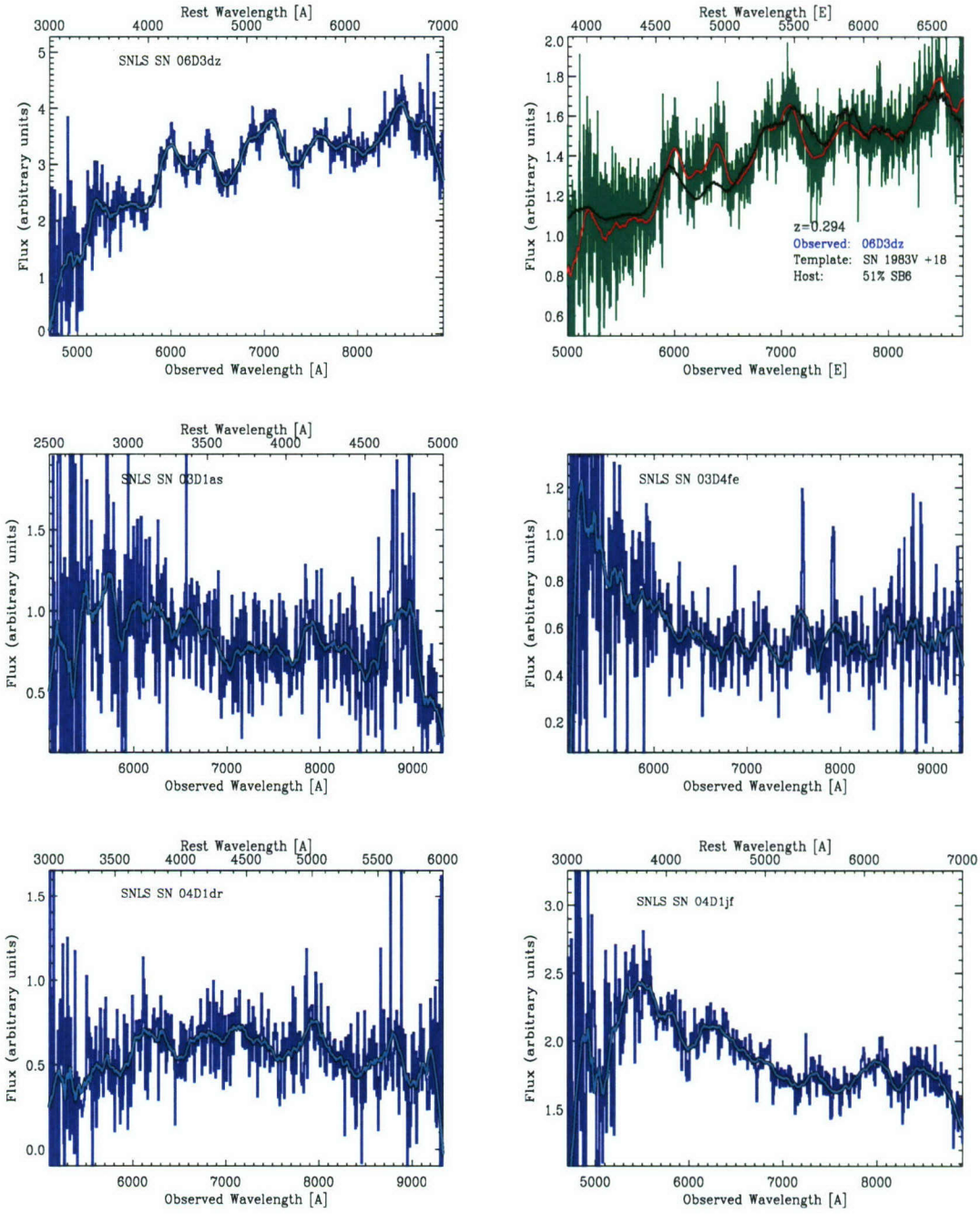

Figure A.35:
TOP: 06D3du **Left** - Observed spectrum **Right** - Template Fit SN Ib/c
MIDDLE: **Left** - 03D1as Observed spectrum **Right** - 03D4fe Observed spectrum
BOTTOM: **Left** - 04D1dr Observed spectrum **Right** - 04D1jf Observed spectrum
Template fits did not produce any reasonable matches to any of the last four objects in this image.

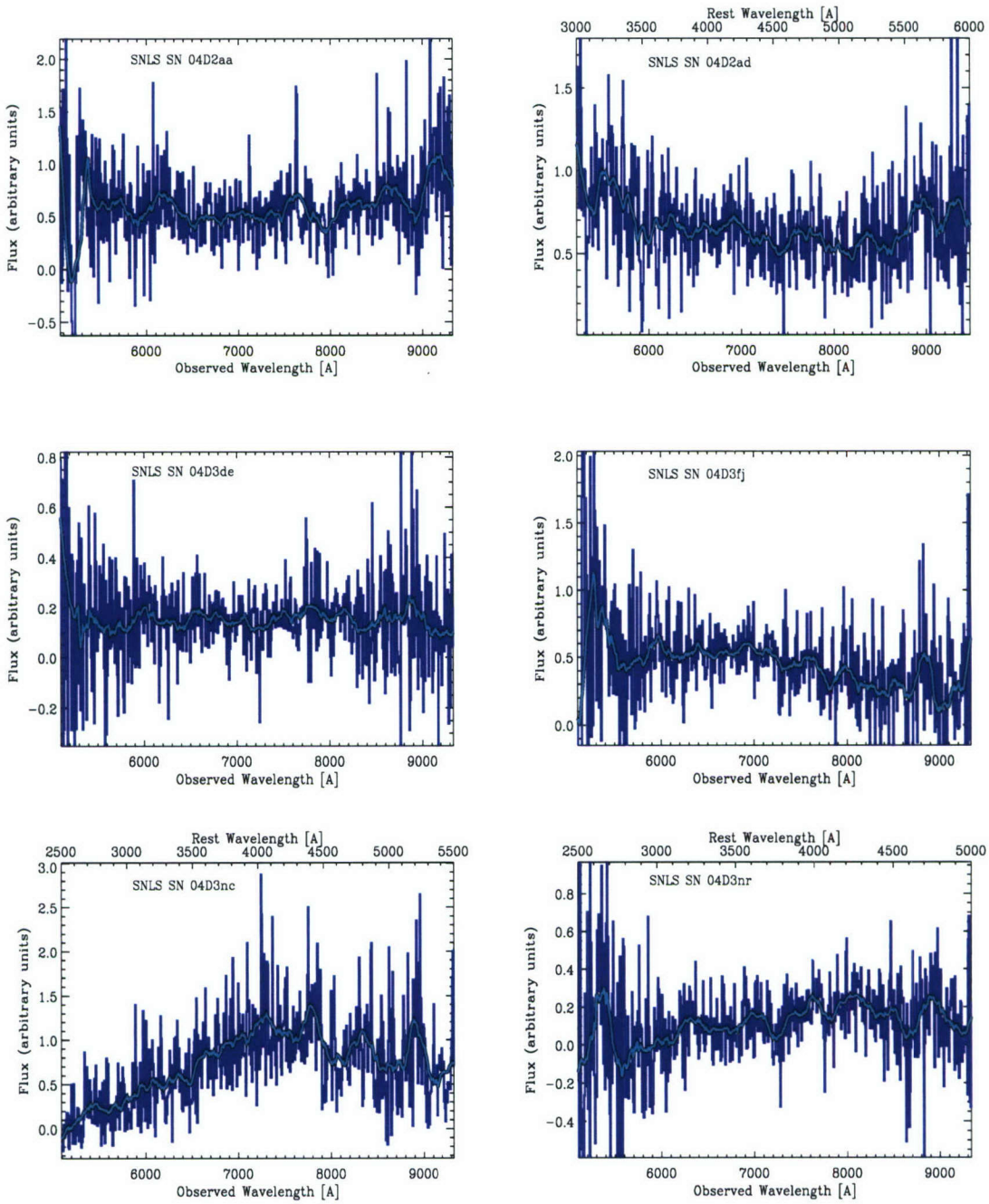

Figure A.36:
TOP: **Left** - 04D2aa **Right** - 04D2ad Observed spectrum
MIDDLE: **Left** - 04D3de Observed spectrum **Right** - 04D3fj Observed spectrum
BOTTOM: **Left** - 04D3nc Observed spectrum **Right** - 04D3nr Observed spectrum
Template fits did not produce any reasonable matches to any of these objects.

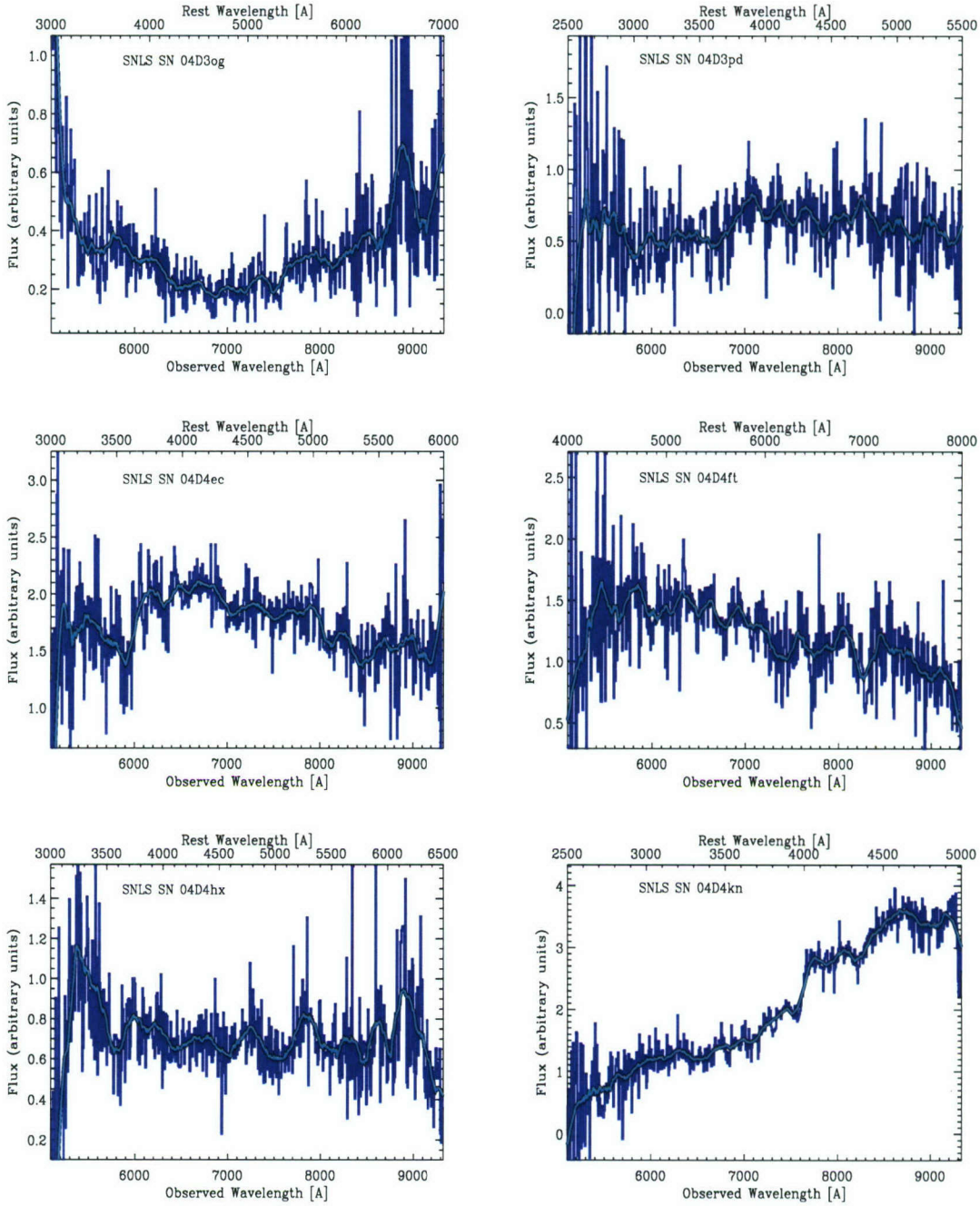

Figure A.37:
TOP: **Left** - 04D3og **Right** - 04D3pd Observed spectrum
MIDDLE: **Left** - 04D4ec Observed spectrum **Right** - 04D4ft Observed spectrum
BOTTOM: **Left** - 04D4hx Observed spectrum **Right** - 04D4kn Observed spectrum
Template fits did not produce any reasonable matches to any of these objects.

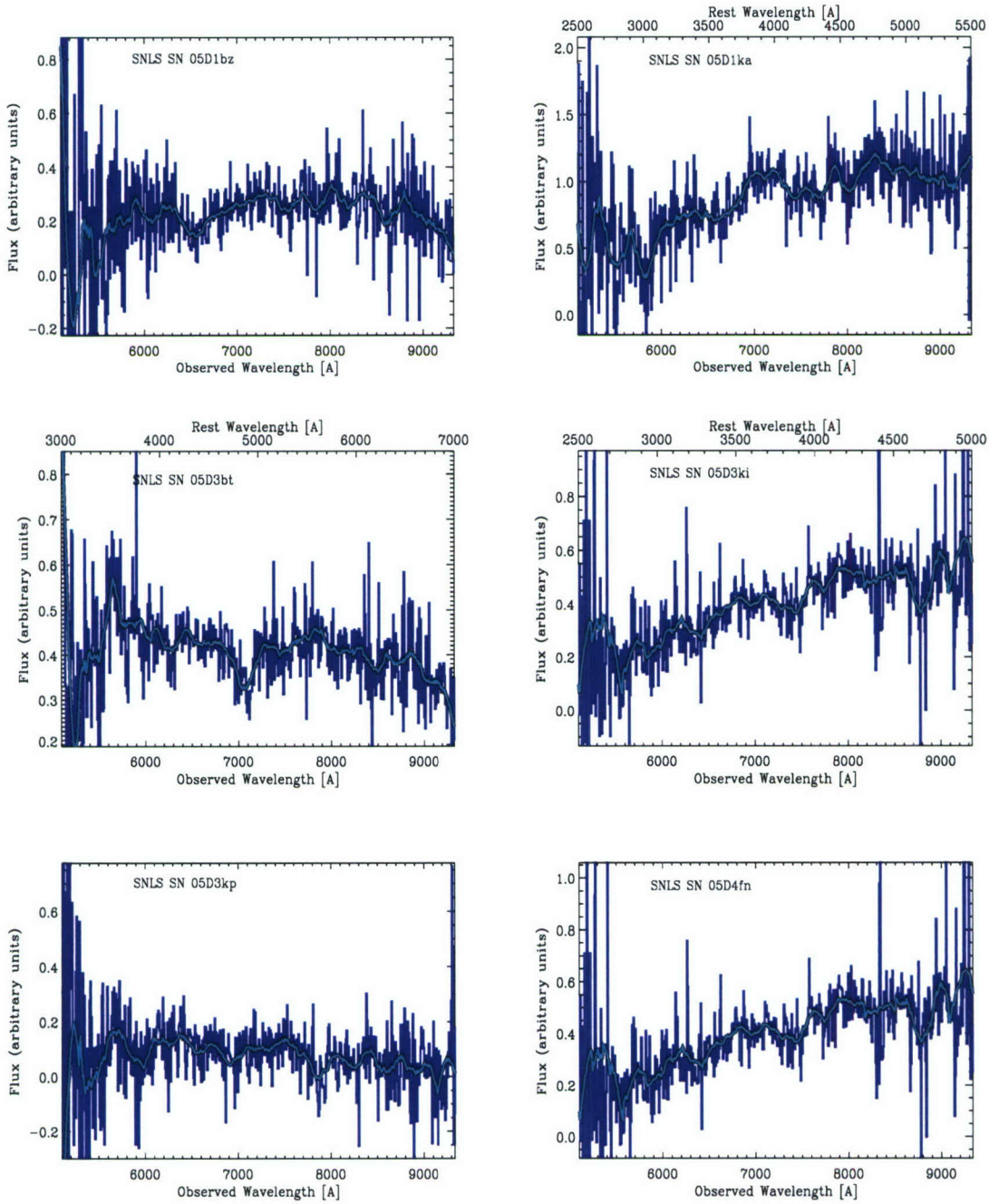

Figure A.38:
TOP: **Left** - 05D1bz **Right** - 05D1ka Observed spectrum
MIDDLE: **Left** - 05D3bt Observed spectrum **Right** - 05D3ki Observed spectrum
BOTTOM: **Left** - 05D3kp Observed spectrum **Right** - 05D4fn Observed spectrum
Template fits did not produce any reasonable matches to any of these objects.

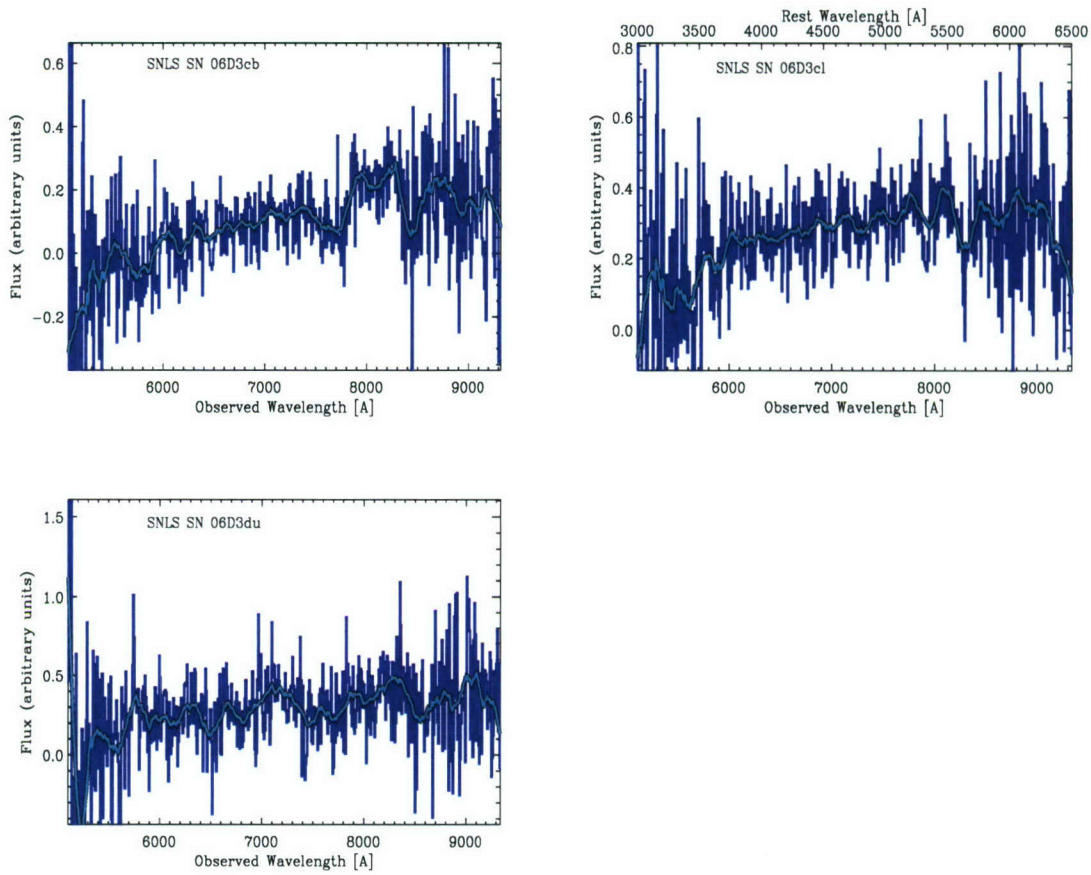

Figure A.39:
TOP: **Left** - 06D3cb **Right** - 06D3cl Observed spectrum
MIDDLE: **Left** - 06D3du Observed spectrum
Template fits did not produce any reasonable matches to any of these objects.

Bibliography

Aguirre, A.N., 1999, ApJ, 525, 583

Aguirre A.N., Haimann, Z., 2000, ApJ, 532, 28

Aldering, G., and the Nearby Supernova Factory, 2002, SPIE, 4836, 61

Aldering, G., *et al.*, 2002, SPIE, 4835, 146

Alighieri, S., Lanzoni, B., Jørgensen, I., 2006, *in press* astro-ph/0607231

Allen, S.W., Schmidt, R.W., Fabian A.C., 2002, MNRAS, 334, 11

Altavilla, G., Fiorentino, G., Marconi, M., Musella, I., Cappellaro, E., Barbon, R., Benetti, S., Pastorello, A., Riello, M., Turatto, M., Zampieri, L., 2004, MNRAS, 349, 1344

Anupama, G. C., Sahu, D. K., Jose, J., 2005, A&A, 429, 667

Appenzeller, I., *et al.* 1998, Messenger, 94, 1

Arnett, W.D., 1982, ApJ, 253, 785

Arnett, W.D., Branch, D., Wheeler, J.C., 1985, Nature, 314, 337

Arnett, D., 1996, *Supernovae and Nucleosynthesis*, Princeton: Princeton University Press

Astier, P., *et al.*, 2006, A&A, 447, 31

Balland, C., Mouchet, M., Pain, R., Walton, N.A., Amanullah, R., Astier, P., Ellis, R.S., Fabbro, S., Goobar, A., Hardin, D., Hook, I.M., Irwin, M.J., McMahon, R.G., Mendez, J.M., Ruiz-Lapuente, P., Sainton, G., Schahmaneche, K., Stanishev, V., 2006, A&A, 445, 387

Barbon, R., Benetti, S., Capellaro, E., Rosino, L., Turatto, M., 1990, A&A, 237, 79

Baron, E., Branch, D., Jeffery, D., Nugent, P., Thomas, R., Bongard, S., Hauschildt, P.H., Kasen, D., Mihalas, D., 2005, White paper submitted to the Dark Energy Task Force (astro-ph/0510166)

Baron, E., Bongard, S., Branch, D., Hauschildt, P., 2006, ApJ, 645, 480

Barris, J., et al,. 2004, ApJ, 602, 571

Basa, S., *et al.* 2006, *in prep*

Benetti, S., *et al.* 2004, MNRAS, 348, 261

Benetti, S., *et al.* 2005, ApJ, 623, 1011

Blondin, S., Walsh, J. R., Leibundgut, B., Sainton, G., 2005 A&A, 431, 757

Blondin, S., *et al.* 2006, AJ, 131, 1648

Bongard, S., Baron, E., Smadja, G., Branch, D., Hauschchildt, P.H., 2006, *in prep*

Branch, D., Lacy, C.H., McCall, M.L., Sutherland, P.G., Uomoto, A., Wheeler, J.C., Wills, B.J., 1983, ApJ, 270, 123

Branch, D., Drucker, W., Jeffery, D.J., 1988, ApJ, 330, L117

Branch, D., Tammann, G.A., 1992, ARA&A, 30, 359

Branch, D., and S. van den Bergh, 1993, AJ, 105, 2231

Branch, D., Romanishin, W., & E. Baron, 1996, ApJ, 465, 73

Branch, D., 2001, PASP, 113, 169

Branch, D., Thomas, R., Baron, E., Kasen, D., Hatano, K., Nomoto, K., Filippenko, A., Li, W., Rudy, R., 2004, ApJ, 606, 413

Branch, D., *et al.*, 2006, submitted to PASP

Bronder, T.J., *et al.*, *in prep.*

Burbidge, G.R., Burbidge, E.M., Fowler, W.A., & Hoyle, F., 1957, RvMP, 29, 547

Caldwell, R. R., Dave, R., Steinhardt, P.J., 1998, PhRvL, 80, 1582

Candia, P., *et al.*, 2003, PASP, 115, 277

Cardelli, J.A., Clayton, G.C., & Mathis, J.S. 1989, ApJ, 345, 245

Carroll, S.M., Press, W.H., & E.L. Turner, 1992, ARA&A, 30, 499

Carroll, S.M., 2004, from *Measuring and Modeling the Universe*, Carnegie Observatories Astrophysics symposium vol. 2 (W.L. Freedman, ed.), Cambridge, UK: Cambridge University Press

Coil, A., *et al.*, 2000, ApJ, 544 111

Conley, A., et al, 2006, *in prep* (astro-ph/0607363)

Conley, A., 2006, *private communication*

Dominguez, I., Chieffi, A., Limongi, M., Straniero, O., 1999, ApJ, 524, 226

Dominguez, I., Hoeflich, P., & Straniero, O. 2001, ApJ, 557, 279

Drell, P., Loredo, T., & Wasserman, I., 2000, ApJ, 530, 593

Dressler, A., 2004, *A User's Manual for IMACS* (Pasadena: Carnegie Obs.),

Eisenstein, D.J., *et al.*, 2005, ApJ, 633, 560

Ellis, R., Sullivan, M., Howell, D.A., 2006, *in prep*

Evans, A.K.D., *et al.*, 2005, A&A, 399

Fabricant, D., Cheimets, P., Caldwell, N., Geary, J., 1998, PASP, 110, 79

Filippenko, A.V., *et al.*, 1992a, ApJ, 384, L15

Filippenko, A.V., *et al.*, 1992b, AJ, 104, 1543

Filippenko, A.V., 1997, ARA&A, 35, 309

Fisher, A., Branch, D., Hoeflich, P., Khokhlov, A., 1995, AJ, 447, L73

Fisher, A., Branch, D., Hatano, K., Baron, E., 1999, MNRAS, 304, 67

Folatelli, G. 2004. PhD Thesis, University of Stockholm

Gallagher J.S., Garnavich, P.M., Berlind, P., Challis, P., Jha, S., Kirshner, R.P., 2005 ApJ, 634, 210

Gamow, G., 1970, *My World Line*, New York: Viking Press

Garavini, G., *et al.*, 2004, AJ, 128, 387

Garavini, G., *et al.*, 2006, *in prep.*

Garnavich, P. M., *et al.* 1998, ApJ, 509, 74

Gibson, B. K., *et al.*, 2000, ApJ, 529, 723

Glazebrook, Karl and Joss Bland-Hawthorne. 2001, PASP, 113, 197

Goldhaber, G., *et al.*, 2001, ApJ, 558, 359

Green, D.A., & Stephenson, F.R., 2003, from *Supernovae and Gamma Ray Bursters* (K.W. Weiler, ed.), New York: Springer-Verlag

Guy, J., Astier, P., Nobili, S., Regnault, N., Pain, R., 2005, A&A, 443, 781

Hachinger, S., Mazzali, P.A., Benetti, S., 2006, accepted for publication in MNRAS

Hamuy, M., Phillips, M.M., Suntzeff, N., Schommer, R., Maza, J., Aviles, R., 1996a, AJ, 112, 2391

Hamuy, M., *et al.*, 1996b, AJ, 112, 2408

Hamuy, M., Phillips, M. M., Suntzeff, N., Schommer, R., Maza, J., Smith, R. C., Lira, P., Aviles, R., 1996c, AJ, 112, 2438

Hamuy, M., *et al.*, 2000, AJ, 120, 1479

Harkness, R.P, Wheeler, J.C., In *Supernovae* (A.G Pettschek, ed.), New York: Springer-Verlag

Hatano, K., Branch, D., Fisher, A., Millard, J., Baron, E., 1999, ApJS, 121, 233

Hatano, K., *et al.*, 2000, ApJ, 543, L49

Hatano, K., Branch, D., Qiu, Y. L., Baron, E., Thielemann, F.-K., Fisher, A., 2002, NewAR, 7, 441

Heavens, A., Panter, B., Jimenez, R., & J. Dunlop, 2004, Nature, 428, 625

Hillebrandt, W., Niemeyer, J., 2000, ARA&A, 38, 191

Hoeflich, P., Khokhlov, A., Wheeler, J.C., Phillips, M., Suntzeff, N., Hamuy, M., 1996, ApJ, 472, L81

Hoeflich, P., Wheeler, J.C., Thielemann, F.K., 1998, ApJ, 495, 617

Hook, I., *et al.*, 2004, PASP, 116, 425

Hook, I., *et al.* 2005, AJ, 130, 2788

Horne, K., 1986, PASP, 98, 609

Howell, D. A., Wang, L., 2002, BAAS, 34, 1256

Howell, D.A., 2005, ASPC, 342, 499

Howell, D. A., *et al.* 2005, ApJ, 634, 1190

Howell, D. A., *et al.* 2006, *in prep*

Ivanov, V.D., Hamuy, M., Pinto, P.A., 2000, ApJ, 542, 588

Jeffery, D.J., *et al.* 1992 ApJ, 397, 304

Jørgensen, I., Chiboucas, K., Flint, K., Bergmann, M., Barr, J., Davies, R., 2006, ApJ, 639, 9

Kinney, A., Calzetti, D., Bohlin, R., McQuade, K., Storchi-Bergmann, T., Schmitt, H., 1996, ApJ, 467, 38

Kirshner, R., Jeffery, D., Leibundgut, B., Challis, P.M., Sonneborn, G., 1993, ApJ, 415, 589

Knop, R., *et al.* 2003, ApJ, 598, 102

Krisciunas, K., *et al.*, 2005, AJ, 130, 2453

Leibundgut, B., 2001, ARA&A, 39, 67

Lentz, E.J., Baron, E., Branch, D., 2000, ApJ, 530, 966

Levan, A., *et al.*, 2005, ApJ, 624, 880

Li, W. D., Qiu, Y. L., Qiao, Q. Y., Zhu, X. H., Hu, J. Y., Richmond, M. W., Filippenko, A. V., Treffers, R. R., Peng, C. Y., Leonard, D. C., 1999, AJ, 117, 2709

Li, W., Filippenko, A.V., & Riess, A.G., 2001a, ApJ, 546, 719

Li, W., Filippenko, A.V., Treffers, R.R., *et al.*, 2001b, ApJ, 546, 734

Li, W., Filippenko, A.V., 2003, IAU Colloquium 192 *Supernovae: 10 Years of 1993J* (J.W. Marcaide & K.W. Weiler, eds.)

Lidman, C., *et al.*, 2005, A&A, 430, 843

Livne, E., & Arnett, D., 1995, ApJ, 452, 62

Magniere, E.A & Cuillandre, J.-C. 2004, PASP, 116, 449

Matheson, T., *et al.* 2005, AJ, 129, 2352

Mazzali, P.A., Lucy, L.B., 1993, A&A, 279, 447

Mazzali, P., Danziger, I., Turatto, M., 1995, A&A, 297, 509

Mazzali, P. A., Chugai, N., Turatto, M., Lucy, L. B., Danziger, I. J., Cappellaro, E., della Valle, M., Benetti, S., 1997, MNRAS, 284, 151

Mazzali, P.A., Cappellaro, E., Danziger, I.J., Turatto, M., & S. Benetti, 1998, ApJ, 499, L49

Mazzali, P.A, Nomoto, K., Capellaro, E., Nakamura, T., Umeda, H., Iwamoto, K., 2001, ApJ, 547, 988

Mazzali, P., *et al.* 2005 ApJ, 623, 37

Mazzali, P.A., & P. Podsiadlowski, 2006, MNRAS, 369, 19

Minkowski, R., 1941, PASP, 53, 224

Mulchaey, J., 2001, LDSS-2 User's Guide (Pasadena: Carnegie Obs.),

Neill, J.D., *et al.* 2006, AJ, 132, 1126

Nørgaard-Nielsen, H., Hansen, L., Jørgensen, H., Aragon Salamanca, A., Ellis, R., 1989, Natur, 339, 553

Nomoto, K., Thielemann, F-K., & Yokoi, K., 1984, ApJ, 286, 644

North, J., 1994, *The Fontana History of Astronomy and Cosmology*, London: Fontana Press

Nugent, P., *et al.* 1995a ApJ, 455, L147

Nugent, P., *et al.* 1995b ApJ, 441, L33

Nugent, P., 1997, PhD Thesis, University of Oklahoma

Nugent, P., *et al.* 1997 ApJ, 485, 812

Nugent, P., Kim, A., Perlmutter, S., 2002, PASP, 114, 803

Nugent, P., *private communication* and `http://supernova.lbl.gov/nugent/nugent-templates.html`

Oke, J. B., *et al.* 1995, PASP, 107, 375

Patat, F., Benetti, S., Cappellaro, E., Danziger, I.J., Della Valle, M., *et al.*, 1996, MNRAS, 278, 111

Perlmutter, S., *et al.*, 1997, ApJ, 483, 565

Perlmutter, S., *et al.*, 1999, ApJ, 517, 565

Phillips, M., *et al.* 1999 AJ, 118, 1766

Phillips, M.M., 1993, ApJ, 413, 105

Phillips, M. M., Wells, L., Suntzeff, N., Hamuy, M., Leibundgut, B., Kirshner, R., Foltz, C., 1992, AJ, 103, 1632

Prieto, J.L., Rest, A, Suntzeff, N.B., 2006, ApJ, *submitted*

Pritchet, C.J., 2005, ASPC, 339, 60

Pskovskii, Iu.P., 1977, SvA, 21, 675

Reindl, B., Tamman, G.A., Sandage, A., Saha, A., 2005, ApJ, 624, 532

Riess, A.G., Press, W.H., Kirshner, R.P., 1996, ApJ, 473, 88

Riess, A.G., *et al.* 1997, AJ, 114, 722

Riess, A.G., *et al.* 1998a, AJ, 116, 1009

Riess, A.G., *et al.* 1998b, ApJ, 504, 935

Riess, A.G., Nugent, P., Filippenko, A., Kirshner, R.P., Perlmutter, S., 1998c, ApJ, 504, 935

Riess, A.G., *et al.* 2004, ApJ, 607, 665

Riess, A.G., *et al.*, 2005, ApJ, 627, 579

Roepke, F.K., Gieseler, M., Travaglio, C., Hillebrandt, W., 2006, A&A, 453, 203

Saha, A., Sandage, A., Thim, F., Labhardt, L., Tammann, G.A., Christensen, J., Panagia, N., Macchetto, F.D., 2001, ApJ, 551, 973

Sako, M., and the SDSS Collaboration, 2005, Presentation at the 22^{nd} Texas Symposium on Relativistic Astrophysics

Salvo, M.E., *et al.* 2001 MNRAS, 321, 254

Sandage, A., Obs, 88, 91

Sandage, A., PhT, 23, 34

Schmidt, G., Weymann, R., Foltz, C., 1989, PASP, 101, 713

Seljak, U., *et al.* 2005, PhRvD, 71, 3515

Sheinis, A.I., *et al.*, 2002, PASP, 114, 851

Sobolev, V.V., *Moving Envelopes of Stars*, Cambridge (USA): Harvard University Press

Spergel, D.N., et. al. 2003, ApJS, 148, 175

Spergel, D.N., *et al.* 2006, *in prep.*, submitted to ApJ (astro-ph/0603449)

Stern, D., *et al.* 2004, ApJ, 612, 690

Stritzinger, M., *et al.*, 2002, AJ, 124, 2100

Strolger, L.G., *et al.*, 2002, AJ, 124, 2905

Strolger, L.G., *et al.* 2004, ApJ, 613, 200

Sullivan, M., *et al.*, 2003, MNRAS, 340, 1057

Sullivan, M., *et al.*, 2006a, AJ, 131, 960

Sullivan, M., *et al.*, 2006b, *in prep* (astro-ph/0605455)

Sullivan, M., *private communication*, 2006

Timmes, F., Brown, E., & J.W. Truran, 2003, ApJ, 590L, 83

Tonry, J.L., Schmidt, B., *et al.*, 2003, ApJ, 594, 1

Travaglio, C., Hillebrandt, W., & M. Reinecke, 2005, A&A, 443, 1007

Tully, R.B., *Nearby Host Galaxies Catalogue*, Cambridgue University Press, Cambridge, UK

Turatto, M., Benetti, S., Cappellaro, E., Danziger, I. J., della Valle, M., Gouiffes, C., Mazzali, P. A., Patat, F., 1996, MNRAS, 283, 1

Uenishi, T., Nomoto, K., Hachisu, I., 2003, ApJ, 595, 1094

Umeda, H., Nomoto, K., Kobayashi, C., Hachisu, I., Kato, M., 1999, ApJ, 522, L43

Wang, L., Hoeflich, P., Wheeler J.C., 1997, ApJ, 483, 29

Wang, X., Wang, L., Pain, R., Zhou, X., Li, Z., 2006, ApJ, 645, 488

Wells, L.A., *et al.*, 1994, AJ, 108, 2233

Yamaoka, H., Nomoto, K., Shigeyama, T., Thielemann, F.K., 1992, ApJ, 393, L55

Yoon, S.-C., and Langer, N., 2004, A&A, 419, 623

von Hippel, T., Bothun, G.D., & R.A. Schommer, 1997, AJ, 114, 1154